The Irradiation-Driven Evolution of Gas-Giant Exoplanets

Thesis by
Shreyas Vissapragada

In Partial Fulfillment of the Requirements for the
Degree of
Ph.D. in Planetary Science

Caltech

CALIFORNIA INSTITUTE OF TECHNOLOGY
Pasadena, California

2022
Defended February 17, 2022

Shreyas Vissapragada
ORCID: 0000-0003-2527-1475

ACKNOWLEDGEMENTS

First and foremost: thank you to my advisor, Heather Knutson. Heather's unwavering support throughout graduate school has been one of the best parts of my experience at Caltech, and over the years I have really enjoyed learning how to be a scientist and a mentor from Heather's example. Thanks also to the other members of my thesis committee, Geoff Blake, Yuk Yung, and Konstantin Batygin, for your helpful input and advice over the years. Additionally, I am very grateful for the wonderful staff members across the GPS Division, especially Julie Lee, Ulrika Terrones, Margaret Carlos, Ruth Loisel, and Loreta Young.

I am incredibly lucky to have learned so much from my amazing colleagues in the Knutson Group over the past five years. I am especially thankful to have worked alongside Mike Greklek-McKeon, Jess Spake, Kim Paragas, Fei Dai, Julie Inglis, Nicole Wallack, and Yayaati Chachan. I have also had the privilege of working with a great group of collaborators including Antonija Oklopčić, Leo dos Santos, Caleb Harada, Gautam Vasisht, Dimitri Mawet, Daniel Jontof-Hutter, Tony Piro, Ian Wong, Guðmundur Stefánsson, and many others.

This thesis is entirely based on work I have completed at Palomar Observatory. None of this work would be possible without the expertise of everyone on the mountain. I would especially like to thank the telescope operators and support astronomers at Palomar: Tom Barlow, Carolyn Heffner, Paul Nied, Joel Pearman, Kajse Peffer, and Kevin Rykoski. Thank you also to Max Millar-Blanchaer, Kaew Tinyanont, Ricky Nilsson, and Avi Shporer for teaching me how to use WIRC.

Thanks to all of my officemates, colleagues, and friends in South Mudd for all of the good times, including Kyle Virgil, Griffin Mead, Qicheng Zhang, Maria Camarca, Eva Scheller, Ryleigh Davis, and many others. Also, to Mike Wong, Dana Anderson, Nancy Thomas, Nathan Stein, Ellen Leask, Ana Lobo, Siteng Fan, Elizabeth Bailey, Steve Markham, Cecilia Sanders, James Keane, Cam Buzard, and Olivia Wilkins: thank you for your kindness in welcoming me to the department, and for your friendship over the years.

A special thanks to all of my fantastic "Planet Haus" housemates, past and present. Planet Haus has been my anchor through all the trials and tribulations of graduate school, and I cannot thank Harriet Brettle, Ben Idini, Marguerite Epstein-Martin, Janosz Dewberry, Mia de los Reyes, Austin Chadwick, Jackie Pezzato, and Aida

Behmard enough for all of the fun times. I truly cannot imagine graduate school without my Planet Haus family.

Finally, thank you to my family for your love and support. Mom, Dad, and Saket – I could not have done this without you. Thank you for everything.

ABSTRACT

Nearly thirty years after their initial discovery, we now know of over five thousand extrasolar planets. Intensive efforts have been made to characterize the sizes, masses, orbits, and compositions of these new worlds, and the resulting population challenges our intuition from the Solar System. One striking feature of the exoplanet census is that the vast majority of known planets reside quite close to their host stars, with orbital periods of less than a hundred days. Our galaxy is replete with hot Jupiters, sub-Neptunes, and super-Earths orbiting their stars more quickly than Mercury orbits the Sun. These close-in planets are bombarded by high-energy stellar radiation, which heats their upper atmospheres and triggers mass loss via hydrodynamic escape. This means that planetary sizes, masses, and compositions can be substantially altered from their values at formation.

This thesis presents five studies aimed at elucidating the irradiation-driven evolution of close-in extrasolar planets. In the first study, we demonstrate a technique for high-precision ground-based infrared transit photometry using a beam-shaping diffuser in the Wide-field Infrared Camera (WIRC) on the Hale 200-inch Telescope at Palomar Observatory. We observed transits in four systems discovered by the *Kepler* mission: Kepler-29, Kepler-36, Kepler-177, and KOI-1783. The eight planets in these systems reside close to mean-motion resonances and experience detectable transit-timing variations due to their dynamical interactions. Using diffuser-assisted photometry, we measured transit light-curves for one planet in each system, and using the transit timings we refined dynamical mass estimates for the eight planets by up to a factor of three. Notably, we found that our diffuser-assisted observing mode outperforms the *Spitzer* Space Telescope in relative photometric precision for stars fainter than $J \approx 10.5$.

In the second study, we applied diffuser-assisted photometry to the study of atmospheric evolution. We commissioned a narrowband filter centered on the infrared metastable helium triplet at 1083 nm, which is a tracer of the planetary mass-loss rate and thermosphere temperature. By using this filter in concert with our beam-shaping diffuser, we were able to achieve precise constraints on helium absorption in planetary atmospheres. We used this filter to observe the gas giant exoplanets WASP-69b and WASP-52b, and found an excess absorption of $0.498 \pm 0.045\%$ for the former planet (consistent with observations by Nortmann et al., 2018) and an upper limit of $< 0.47\%$ for the latter planet. We interpreted these absorption

signals using a one-dimensional isothermal Parker wind model, and demonstrated the present-day stability of these planets' atmospheres to photoevaporation.

In the third study, we used our narrowband helium photometry technique to study three planets orbiting the young Solar analogue V1298 Tau. Atmospheric escape driven by high-energy stellar radiation is hypothesized to be most vigorous at early times, and this system is only 23 million years old, making it an excellent target for mass-loss observations. We revealed a tentative outflow signal for V1298 Tau d with $\Delta R_{\mathrm{d}}/R_{\star} = 0.0205 \pm 0.054$ across two partial transit observations; if confirmed this would be the first directly observed mass-loss signature for a transiting planet less than 100 Myr old. We also reported non-detections for planets b and c in one partial and one full transit observation, respectively. In the case of planet c, this may be due to strong ionization in the upper atmosphere, which could indicate low mass-loss efficiencies for close-in planets at early times.

In the fourth study, we described a theoretical technique for partially resolving the degeneracy between thermosphere temperature and mass-loss rate when interpreting metastable helium observations with a one-dimensional isothermal Parker wind model. The mechanical energy flux of a planetary outflow cannot exceed its energy input, and by calculating the energy input explicitly from photoionization physics we demonstrate that not all combinations of the mass-loss rate and outflow temperature satisfy energy balance. When combining this energetic constraint with metastable helium observations, we demonstrate that the present-day outflows of HAT-P-11b and WASP-69b must be relatively weak ($\dot{M} \lesssim 10^{11.5}$ g/s).

Finally, in the fifth study, we surveyed atmospheric escape in a sample of seven low-density gas giant planets using diffuser-assisted narrowband helium photometry. We strongly detect helium absorption signals for WASP-69b, HAT-P-18b, and HAT-P-26b; tentatively detect signals for WASP-52b and NGTS-5b; and do not detect signals for WASP-177b and WASP-80b. We interpret these measured excess absorption signals using grids of Parker wind models to derive mass-loss rates, which are in good agreement with predictions from the hydrodynamical outflow code ATES for all planets except WASP-52b and WASP-80b. For these two planets, the outflows are much smaller than predicted, perhaps due to confinement by magnetic fields. The rest of the sample is consistent with a mean energy-limited outflow efficiency of $\varepsilon = 0.41^{+0.16}_{-0.13}$. Even when we make the relatively conservative assumption that gas-giant planets experience energy-limited outflows at this efficiency for their entire lives, photoevaporation would still be too inefficient to carve the upper boundary of the Neptune desert. We conclude that this feature of the exoplanet population is a pristine tracer of giant planet formation and migration mechanisms.

PUBLISHED CONTENT AND CONTRIBUTIONS

Vissapragada, Shreyas, Heather A. Knutson, Leonardo A. dos Santos, et al. (Mar. 2022). "The Maximum Mass-loss Efficiency for a Photoionization-driven Isothermal Parker Wind". In: *ApJ* 927.1, 96, p. 96. DOI: 10.3847/1538-4357/ac4e8a. arXiv: 2201.09889 [astro-ph.EP].
S.V. conceived the project with input from coauthors and wrote the manuscript.

Vissapragada, Shreyas, Heather A. Knutson, Michael Greklek-McKeon, et al. (Apr. 2022). "The Upper Edge of the Neptune Desert Is Stable Against Photoevaporation". In: *arXiv e-prints*, arXiv:2204.11865, arXiv:2204.11865. arXiv: 2204.11865 [astro-ph.EP].
S.V. conceived the project with input from coauthors, performed observations, reduced data, and wrote the manuscript.

Vissapragada, Shreyas, Gudmundur Stefánsson, et al. (Nov. 2021). "A Search for Planetary Metastable Helium Absorption in the V1298 Tau System". In: *AJ* 162.5, 222, p. 222. DOI: 10.3847/1538-3881/ac1bb0. arXiv: 2108.05358 [astro-ph.EP].
S.V. conceived the project with input from coauthors, performed observations, reduced data, and wrote the manuscript.

Vissapragada, Shreyas, Daniel Jontof-Hutter, et al. (Mar. 2020). "Diffuser-assisted Infrared Transit Photometry for Four Dynamically Interacting Kepler Systems". In: *AJ* 159.3, 108, p. 108. DOI: 10.3847/1538-3881/ab65c8. arXiv: 1907.04445 [astro-ph.EP].
S.V. performed observations, reduced data, and wrote the manuscript.

Vissapragada, Shreyas, Heather A. Knutson, Nemanja Jovanovic, et al. (June 2020). "Constraints on Metastable Helium in the Atmospheres of WASP-69b and WASP-52b with Ultranarrowband Photometry". In: *AJ* 159.6, 278, p. 278. DOI: 10.3847/1538-3881/ab8e34. arXiv: 2004.13728 [astro-ph.EP].
S.V. conceived the project with input from coauthors, performed observations, reduced data, and wrote the manuscript.

TABLE OF CONTENTS

LIST OF ILLUSTRATIONS

LIST OF TABLES

Chapter 1

INTRODUCTION

1.1 The Planetary Census

The first exoplanet orbiting a Sun-like star, 51 Pegasi b, was discovered by Mayor and Queloz (1995). The 0.5 M_J mass inferred for the planet was not so surprising given the masses of giant planets in our Solar System, but the incredibly short orbital distance was: 51 Pegasi b orbits its host star every 4.2 days. This "hot Jupiter" has no counterpart in our Solar System, and its discovery raised a foundational question of for the field of exoplanets: how did this planet form and evolve?

Nearly thirty years have passed since that landmark discovery, and since then over five thousand planets have been discovered orbiting nearby stars. Most of these planets orbit their stars more quickly than Mercury orbits our Sun; we show the orbital periods and planetary masses of known planets collected by the NASA Exoplanet Archive (Akeson et al., 2013) in Figure 1.1. These results demonstrate that close-in planets are not an anomaly. Approximately 1% of Sun-like stars host a Jovian planet with $P < 100$ days (Dawson and Johnson, 2018), and that number grows substantially for sub-Neptune ($2R_\oplus < R_p < 4R_\oplus$) and super-Earth ($R_\oplus < R_p < 2R_\oplus$) planets (e.g. Fulton et al., 2017).

Despite these incredible advances in our knowledge of the planetary census, the foundational question put forward by Mayor and Queloz (1995) remains unresolved. There are three possible mechanisms that have been proposed to explain the origin of hot Jupiters (Dawson and Johnson, 2018). Though previously dismissed as a possibility, recent studies have argued that hot Jupiters could form *in situ* (close to their present locations) provided that there are sufficiently large ($\sim 10 M_\oplus$) cores capable of triggering core-nucleated accretion (Pollack et al., 1996) located in the inner protoplanetary disk well prior to its dissipation (P. Bodenheimer, Hubickyj, and Lissauer, 2000; Batygin, P. H. Bodenheimer, and Laughlin, 2016). Hot Jupiters may also have formed much further from their host stars and migrated to their present locations assisted by torques from their protoplanetary disks; most disks dissipate in less than $\sim$ 10 Myr so this process must occur relatively early in the system's lifetime (Ida and Lin, 2008). Finally, hot Jupiters may have migrated to their present locations on more leisurely timescales ($\sim$ Gyr) via high-eccentricity

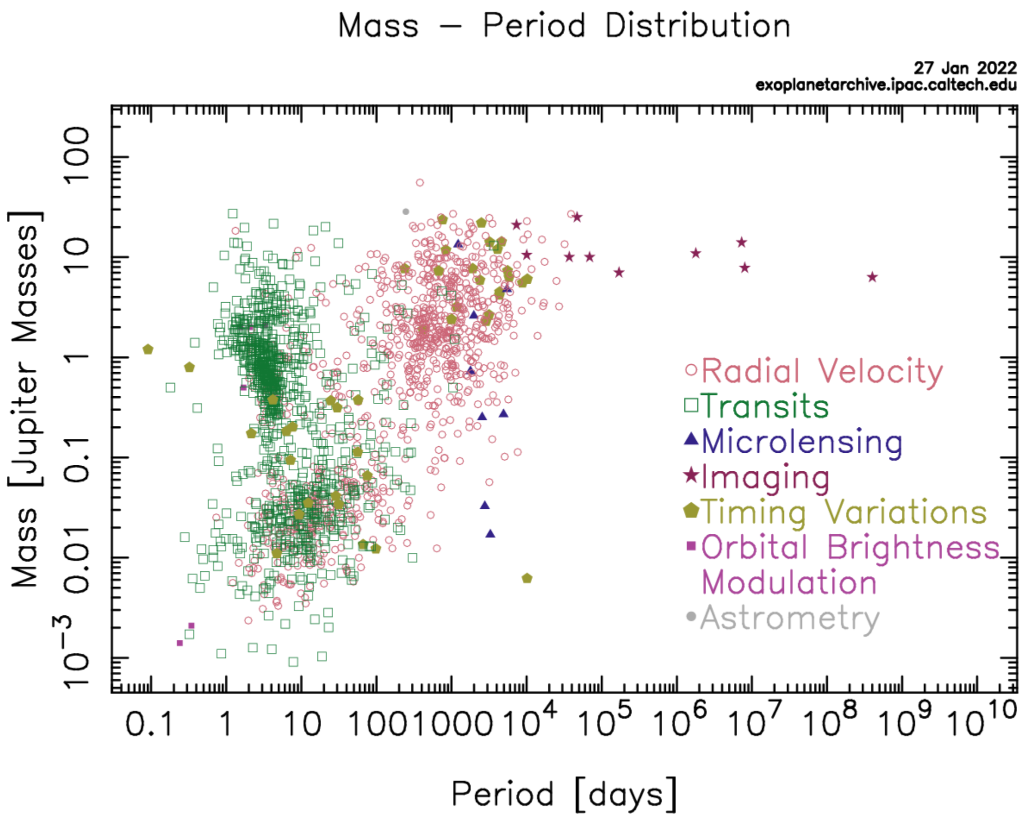

Figure 1.1: Masses and orbital periods of known exoplanets from the NASA Exoplanet Archive (Akeson et al., 2013).

migration. Some mechanism (like planet-planet scattering or the Kozai-Lidov effect) is assumed to pump the planetary eccentricity, bringing the periastron of the orbit close to the star. The orbit then tidally circularizes, leaving a hot Jupiter (Rasio and Ford, 1996).

Each of these formation mechanisms has advantages and disadvantages in explaining features of the exoplanet population. Disk migration and *in situ* formation are able to comfortably explain the existence of low-eccentricity warm ($P = 10 - 200$ days) Jupiters, the presence of Jupiter-sized planets in short orbits around young stars, and the presence of warm Jupiters with nearby super-Earths (Dawson and Johnson, 2018). However, it remains unclear whether large cores can make it to the inner gas disk before dissipation. High-eccentricity migration, on the other hand, can naturally explain warm hot Jupiters on elliptical orbits, but the eccentricity excitation mechanism remains unknown. Ngo et al. (2016) found that stellar companions are unlikely to have excited hot Jupiter progenitor eccentricities via the Kozai-Lidov effect, but Knutson et al. (2014) and Bryan et al. (2016) have shown that massive planetary companions between 1-20 au are relatively common in hot Jupiter systems.

Dynamical interactions between the hot Jupiter progenitor and these companions could have increased progenitor eccentricities to necessary values at early times.

An important demographic feature that may yield insights into the question of hot Jupiter formation and evolution is the Neptune desert, a void of Neptune mass planets on short ($P < 10$ day) orbits (Mazeh, Holczer, and Faigler, 2016). The upper boundary of the Neptune desert – equivalently, the lower boundary of the hot Jupiter population – may be a relic of high-eccentricity migration (Matsakos and Königl, 2016; Owen and Lai, 2018). Neptune-mass planets undergoing high-eccentricity migration could have had pericenter passages too close to their host stars, leading ultimately to their tidal disruption. Alternatively, if gas giants form *in situ* or migrate early via the gas disk, they experience severe high-energy irradiation for the first ~Gyr of their lives (King and Wheatley, 2021; Johnstone, Bartel, and Güdel, 2021). This radiation can heat the planetary atmospheres (via photoionization) and drive hydrodynamic escape, a process called "photoevaporation" (Murray-Clay, Chiang, and Murray, 2009). If photoevaporation is efficient enough, the Neptune desert could be cleared by atmospheric loss (Kurokawa and Nakamoto, 2014).

1.2 The Transit Technique

The most successful technique to date for detecting extrasolar planets is the transit technique, which is employed by the planet-hunting missions *Kepler* (Borucki et al., 2010) and *TESS* (Ricker et al., 2015). By chance, the orbits of some extrasolar planets are aligned with our line of sight ($i \sim 90°$). When this happens, the planets pass in front of their host stars and block out some of their light. The fractional amount of light blocked out is referred to as the "transit depth". In the simplest picture of a hard-sphere planet transiting a static, uniform-brightness star, the transit depth can be written as a ratio of the sky-projected surface areas of the planet and star, or equivalently, as the square of the radius ratio:

$$\delta = \frac{\pi R_{\mathrm{p}}^2}{\pi R_\star^2} = \left(\frac{R_{\mathrm{p}}}{R_\star}\right)^2. \tag{1.1}$$

The transit depth can change as a function of wavelength due to limb-darkening effects in the host star. Atomic and molecular absorption also cause the transit depth to change with wavelength; if an atom or molecule is abundant in the planetary atmosphere, it may absorb substantial amounts of light, increasing the transit depth. The amount of extra absorption is proportional to the isothermal scale height of the atmosphere (e.g. Sara Seager, 2010):

$$H = \frac{k_B T}{\mu g}, \tag{1.2}$$

where k_B is Boltzmann's constant, T is the atmospheric temperature (usually taken to be the equilibrium temperature), μ is the mean particle mass for the atmosphere measured in grams, and g is the surface gravity of the planet.

1.3 Atmospheric Escape

Insights into the second part of the question from Mayor and Queloz (1995) came relatively quickly: planetary atmospheres *are* affected by their intense radiation environments, as first revealed by the strong Lyman-α detection for HD 209458b. This planet transits its host star, blocking out 1.5% of the star's light at optical wavelengths (Charbonneau et al., 2000). However, in the ultraviolet Lyman-α line at 121.6 nm, the planet blocks out a whopping 15±4% of its stars light (Vidal-Madjar et al., 2003). Lyman-α absorption occurs when ground-state neutral hydrogen atoms encounter and absorb radiation at 121.6 nm. Equation 1.1 tells us that this absorption comes from hydrogen atoms at an altitude of $\sqrt{\frac{15\%}{1.5\%}} R_p \approx 3R_p$. We can compare this to the Roche lobe distance, beyond which material is unbound from the planet:

$$R_{\text{Roche}} \approx a \left(\frac{M_p}{3M_\star} \right)^{1/3}. \tag{1.3}$$

For HD 209458b, the Roche radius is $2.7R_p$. Thus, some of the neutral hydrogen atoms observed in Lyman-α must be escaping the planet.

The qualitative conclusion from these early Lyman-α observations was that atmospheric mass loss is occurring, but the question of *how much* mass loss remained unanswered for some time. It turns out that Lyman-α is a rather poor observational tracer for the mass-loss rate $\dot{M}$ (Owen, Murray-Clay, et al., 2021). Additionally, the core of the line (where most of the absorption occurs) is typically obscured by interstellar absorption and geocoronal emission, obfuscating the physical processes in action.

A viable path towards estimating planetary mass-loss rates was finally demonstrated by Antonija Oklopčić and Hirata (2018). These authors considered the metastable helium feature, a triplet of lines near 1083 nm arising from an excited state of the helium atom. While S. Seager and Sasselov (2000) were the first to propose that helium absorption may be observable in planetary atmospheres, Antonija Oklopčić and Hirata (2018) established the critical connection between the metastable helium triplet and planetary outflows. They used a one-dimensional isothermal Parker wind model (parameterized by a mass-loss rate $\dot{M}$ and a thermosphere temperature T_0) to estimate the density structure of a planetary outflow and computed the steady-state level populations for helium in the outflow to arrive at relatively large metastable helium signal.

Remarkably, around the same time this methodology was established, Spake, Sing, et al. (2018) discovered helium in the outflowing atmosphere of WASP-107b. Using observations from the *Hubble Space Telescope* Wide-Field Camera 3, these authors reported that the planet appeared to block out excess light at 1083 nm compared to other wavelengths. They deduced that at high resolving power, the outflow probably filled a substantial fraction of the planetary Roche lobe, which has since been confirmed many times over (Allart et al., 2019; Kirk et al., 2020; Spake, A. Oklopčić, and Hillenbrand, 2021).

Together, the insights of Spake, Sing, et al. (2018) and Antonija Oklopčić and Hirata (2018) give a methodology for systematically and quantitatively constraining the mass-loss rates of extrasolar planets: measure the strength of the absorption in the metastable helium line, and interpret that absorption using a one-dimensional isothermal Parker wind model. The majority of this thesis is inspired by those two works in a quest to better understand the physics of mass loss in gas-giant exoplanets.

References

Akeson, R. L. et al. (Aug. 2013). "The NASA Exoplanet Archive: Data and Tools for Exoplanet Research". In: *PASP* 125.930, p. 989. DOI: 10.1086/672273. arXiv: 1307.2944 [astro-ph.IM].

Allart, R. et al. (Mar. 2019). "High-resolution confirmation of an extended helium atmosphere around WASP-107b". In: *A&A* 623, A58, A58. DOI: 10.1051/0004-6361/201834917. arXiv: 1901.08073 [astro-ph.EP].

Batygin, Konstantin, Peter H. Bodenheimer, and Gregory P. Laughlin (Oct. 2016). "In Situ Formation and Dynamical Evolution of Hot Jupiter Systems". In: *ApJ* 829.2, 114, p. 114. DOI: 10.3847/0004-637X/829/2/114. arXiv: 1511.09157 [astro-ph.EP].

Bodenheimer, Peter, Olenka Hubickyj, and Jack J. Lissauer (Jan. 2000). "Models of the in Situ Formation of Detected Extrasolar Giant Planets". In: *Icarus* 143.1, pp. 2–14. DOI: 10.1006/icar.1999.6246. arXiv: 2111.08776 [astro-ph.EP].

Borucki, William J. et al. (Feb. 2010). "Kepler Planet-Detection Mission: Introduction and First Results". In: *Science* 327.5968, p. 977. DOI: 10.1126/science.1185402.

Bryan, Marta L. et al. (Apr. 2016). "Statistics of Long Period Gas Giant Planets in Known Planetary Systems". In: *ApJ* 821.2, 89, p. 89. DOI: 10.3847/0004-637X/821/2/89. arXiv: 1601.07595 [astro-ph.EP].

Charbonneau, David et al. (Jan. 2000). "Detection of Planetary Transits Across a Sun-like Star". In: *ApJL* 529.1, pp. L45–L48. DOI: 10.1086/312457. arXiv: astro-ph/9911436 [astro-ph].

Dawson, Rebekah I. and John Asher Johnson (Sept. 2018). "Origins of Hot Jupiters". In: *ARA&A* 56, pp. 175–221. DOI: 10.1146/annurev-astro-081817-051853. arXiv: 1801.06117 [astro-ph.EP].

Fulton, Benjamin J. et al. (Sept. 2017). "The California-Kepler Survey. III. A Gap in the Radius Distribution of Small Planets". In: *AJ* 154.3, 109, p. 109. DOI: 10.3847/1538-3881/aa80eb. arXiv: 1703.10375 [astro-ph.EP].

Ida, S. and D. N. C. Lin (Jan. 2008). "Toward a Deterministic Model of Planetary Formation. IV. Effects of Type I Migration". In: *ApJ* 673.1, pp. 487–501. DOI: 10.1086/523754. arXiv: 0802.1114 [astro-ph].

Johnstone, C. P., M. Bartel, and M. Güdel (May 2021). "The active lives of stars: A complete description of the rotation and XUV evolution of F, G, K, and M dwarfs". In: *A&A* 649, A96, A96. DOI: 10.1051/0004-6361/202038407. arXiv: 2009.07695 [astro-ph.SR].

King, George W. and Peter J. Wheatley (Jan. 2021). "EUV irradiation of exoplanet atmospheres occurs on Gyr time-scales". In: *MNRAS* 501.1, pp. L28–L32. DOI: 10.1093/mnrasl/slaa186. arXiv: 2007.13731 [astro-ph.EP].

Kirk, James et al. (Mar. 2020). "Confirmation of WASP-107b's Extended Helium Atmosphere with Keck II/NIRSPEC". In: *AJ* 159.3, 115, p. 115. DOI: 10.3847/1538-3881/ab6e66. arXiv: 2001.07667 [astro-ph.EP].

Knutson, Heather A. et al. (Apr. 2014). "Friends of Hot Jupiters. I. A Radial Velocity Search for Massive, Long-period Companions to Close-in Gas Giant Planets". In: *ApJ* 785.2, 126, p. 126. DOI: 10.1088/0004-637X/785/2/126. arXiv: 1312.2954 [astro-ph.EP].

Kurokawa, H. and T. Nakamoto (Mar. 2014). "Mass-loss Evolution of Close-in Exoplanets: Evaporation of Hot Jupiters and the Effect on Population". In: *ApJ* 783.1, 54, p. 54. DOI: 10.1088/0004-637X/783/1/54. arXiv: 1401.2511 [astro-ph.EP].

Matsakos, Titos and Arieh Königl (Mar. 2016). "On the Origin of the Sub-Jovian Desert in the Orbital-period-Planetary-mass Plane". In: *ApJL* 820.1, L8, p. L8. DOI: 10.3847/2041-8205/820/1/L8. arXiv: 1603.00414 [astro-ph.EP].

Mayor, Michel and Didier Queloz (Nov. 1995). “A Jupiter-mass companion to a solar-type star”. In: *Nature* 378.6555, pp. 355–359. DOI: 10.1038/378355a0.

Mazeh, T., T. Holczer, and S. Faigler (May 2016). “Dearth of short-period Neptunian exoplanets: A desert in period-mass and period-radius planes”. In: *A&A* 589, A75, A75. DOI: 10.1051/0004-6361/201528065. arXiv: 1602.07843 [astro-ph.EP].

Murray-Clay, Ruth A., Eugene I. Chiang, and Norman Murray (Mar. 2009). “Atmospheric Escape From Hot Jupiters”. In: *ApJ* 693.1, pp. 23–42. DOI: 10.1088/0004-637X/693/1/23. arXiv: 0811.0006 [astro-ph].

Ngo, Henry et al. (Aug. 2016). “Friends of Hot Jupiters. IV. Stellar Companions Beyond 50 au Might Facilitate Giant Planet Formation, but Most are Unlikely to Cause Kozai-Lidov Migration”. In: *ApJ* 827.1, 8, p. 8. DOI: 10.3847/0004-637X/827/1/8. arXiv: 1606.07102 [astro-ph.EP].

Oklopčić, Antonija and Christopher M. Hirata (Mar. 2018). “A New Window into Escaping Exoplanet Atmospheres: 10830 Å Line of Helium”. In: *ApJL* 855.1, L11, p. L11. DOI: 10.3847/2041-8213/aaada9. arXiv: 1711.05269 [astro-ph.EP].

Owen, James E. and Dong Lai (Oct. 2018). “Photoevaporation and high-eccentricity migration created the sub-Jovian desert”. In: *MNRAS* 479.4, pp. 5012–5021. DOI: 10.1093/mnras/sty1760. arXiv: 1807.00012 [astro-ph.EP].

Owen, James E., Ruth A. Murray-Clay, et al. (Nov. 2021). “The fundamentals of Lyman-alpha exoplanet transits”. In: *arXiv e-prints*, arXiv:2111.06094, arXiv:2111.06094. arXiv: 2111.06094 [astro-ph.EP].

Pollack, James B. et al. (Nov. 1996). “Formation of the Giant Planets by Concurrent Accretion of Solids and Gas”. In: *Icarus* 124.1, pp. 62–85. DOI: 10.1006/icar.1996.0190.

Rasio, Frederic A. and Eric B. Ford (Nov. 1996). “Dynamical instabilities and the formation of extrasolar planetary systems”. In: *Science* 274, pp. 954–956. DOI: 10.1126/science.274.5289.954.

Ricker, George R. et al. (Jan. 2015). “Transiting Exoplanet Survey Satellite (TESS)”. In: *Journal of Astronomical Telescopes, Instruments, and Systems* 1, 014003, p. 014003. DOI: 10.1117/1.JATIS.1.1.014003.

Seager, S. and D. D. Sasselov (July 2000). “Theoretical Transmission Spectra during Extrasolar Giant Planet Transits”. In: *ApJ* 537.2, pp. 916–921. DOI: 10.1086/309088. arXiv: astro-ph/9912241 [astro-ph].

Seager, Sara (2010). *Exoplanet Atmospheres: Physical Processes*.

Spake, J. J., A. Oklopčić, and L. A. Hillenbrand (Dec. 2021). “The Posttransit Tail of WASP-107b Observed at 10830 Å”. In: *AJ* 162.6, 284, p. 284. DOI: 10.3847/1538-3881/ac178a. arXiv: 2107.08999 [astro-ph.EP].

Spake, J. J., D. K. Sing, et al. (May 2018). “Helium in the eroding atmosphere of an exoplanet”. In: *Nature* 557.7703, pp. 68–70. DOI: 10.1038/s41586-018-0067-5. arXiv: 1805.01298 [astro-ph.EP].

Vidal-Madjar, A. et al. (Mar. 2003). “An extended upper atmosphere around the extrasolar planet HD209458b”. In: *Nature* 422.6928, pp. 143–146. DOI: 10.1038/nature01448.

Chapter 2

DIFFUSER-ASSISTED INFRARED TRANSIT PHOTOMETRY FOR FOUR DYNAMICALLY INTERACTING *KEPLER* SYSTEMS

Vissapragada, Shreyas et al. (Mar. 2020). "Diffuser-assisted Infrared Transit Photometry for Four Dynamically Interacting Kepler Systems". In: *AJ* 159.3, 108, p. 108. DOI: 10.3847/1538-3881/ab65c8. arXiv: 1907.04445 [astro-ph.EP].

2.1 Introduction

The *Kepler* mission (Borucki et al., 2010) has revealed thousands of transiting exoplanets and exoplanet candidates over the past decade, many of which reside in multi-planet systems. Dynamical interactions between planets in these systems cause deviations from the expected Keplerian behavior that can change both the timing and duration of transits (Agol, J. Steffen, et al., 2005; Holman and Murray, 2005; Agol and Fabrycky, 2018). In systems where planetary periods are close to integer multiples of each other – in other words, for planets close to or occupying mean motion resonances – the amplitude of transit timing variations (TTVs) and transit duration variations (TDVs) may become observable and reveal the dynamical architecture of the system. Approximately 10% of Kepler Objects of Interest (KOIs) exhibit significant long-term TTVs (Tomer Holczer et al., 2016). Most of these planets are on $\lesssim$ 100 day orbits, with eccentricities of a few percent and sizes ranging from 1-10 $R_\oplus$ (Tomer Holczer et al., 2016; Hadden and Lithwick, 2017).

TTV analyses have yielded a wealth of information about the properties of *Kepler* multi-planet systems, but arguably their most valuable contribution to date has been estimates of planet masses and densities for systems that are not amenable to characterization using the radial velocity (RV) technique (e.g. Wu and Lithwick, 2013; Jontof-Hutter, Ford, et al., 2016; Hadden and Lithwick, 2017). These density constraints are especially critical for interpreting the bimodal radius distribution observed for close-in planets, which peaks at approximately 1.3 and 2.5 $R_\oplus$ (Fulton, Petigura, et al., 2017; Fulton and Petigura, 2018). It has been suggested that this distribution is well-matched by models in which a subset of highly irradiated rocky planets have lost their primordial atmospheres while more distant planets retain modest (few percent in mass) hydrogen-rich atmosphere that inflate their observed radii (Owen and Wu, 2013; Lopez and Jonathan J. Fortney, 2013; Lopez and Jonathan J. Fortney, 2014; Fulton, Petigura, et al., 2017; Owen and Wu, 2017; Fulton and Petigura, 2018). Measuring the bulk density of planets in this size regime is thus a direct test of these photoevaporative models.

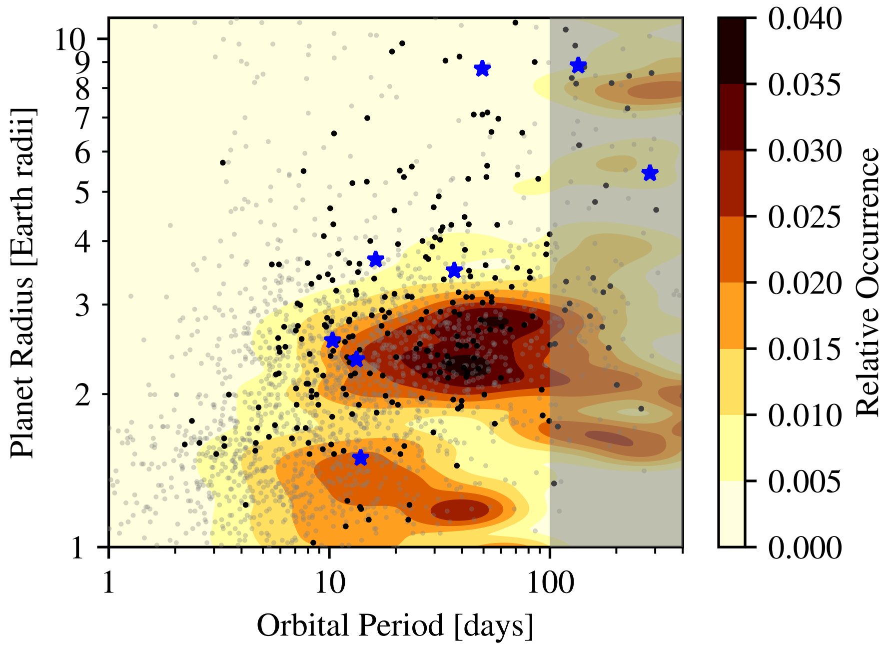

Figure 2.1: Planet radius as a function of orbital period for all non-TTV *Kepler* planets (gray points) and the *Kepler* TTV sample (black points), along with the dynamically interacting planets with improved masses from this work (blue stars). The colored contours are the relative planet occurrence contours calculated by Fulton and Petigura (2018), and the gray highlighted region denotes the region of low completeness at $P > 100$ days.

In Figure 2.1, we plot all confirmed *Kepler* planets (with those exhibiting TTVs specially marked) on the radius-period plane, following Fulton, Petigura, et al. (2017). In general, the TTV sample allows for characterization of planets that are $1.75R_\oplus$ and larger (on the sub-Neptune side of the bimodal radius distribution), with periods longer than a week. While the radial velocity technique is most sensitive to short-period planets with relatively high densities, TTV observations are well-suited to characterizing long period and/or low-density planets, making it an important tool for probing this region of parameter space (J. H. Steffen, 2016; Mills and Tsevi Mazeh, 2017). Indeed, this technique has already revealed the existence of a separate sub-population of "super-puffs," a rare class of super-Earths with very low bulk densities and relatively long orbital periods (Masuda, 2014; Jontof-Hutter, Lissauer, et al., 2014). Unlike the broader super-Earth population, which some studies argue could have formed in situ, it is thought that these planets may have accreted their envelopes at large stellocentric distances and then migrated inward to their current locations in resonant chains (Ikoma and Hori, 2012; Lee, Chiang, and Ormel, 2014; Ginzburg, Schlichting, and Sari, 2016; Lee and Chiang, 2016; Schlichting, 2018).

These previous studies showcase the crucial role of *Kepler* TTVs in testing theories of planet formation and evolution. The failure of *Kepler*'s second reaction wheel in 2013, however, effectively limited the baseline of these TTV analyses to four years. This makes it particularly challenging to constrain masses and bulk densities for long-period planets with a relatively small set of measured transits during this four-year period. In addition, uncertainties in the orbital solutions grow over time, making future in-transit observations (for instance, those aimed at atmospheric characterization) increasingly difficult to schedule with confidence.

These problems can be ameliorated with ground- or space-based follow-up observations (Petigura, Björn Benneke, et al., 2018; S. Wang et al., 2018). However, many of the *Kepler* planets exhibiting TTVs orbit faint ($V > 12$) stars, making it difficult to achieve the required photometric precision using existing space-based facilities with small apertures, such as the *Spitzer Space Telescope*. Additionally, *Spitzer* will be decommissioned in January 2020, necessitating an alternative approach to follow-up observations. Although ongoing observations by the *Transiting Exoplanet Survey Satellite* (*TESS*; Ricker et al., 2015) are expected to recover a few hundred *Kepler* planets (Christ, Montet, and Fabrycky, 2019), short-cadence data from the nominal mission will only improve the mass uncertainties for 6-14 of the $\sim$150 currently known *Kepler* TTV planets (Goldberg et al., 2019). This is due to the limited photometric precision and relatively short baseline of *TESS* relative to *Kepler*. While *TESS* is expected to recover additional transits in an extended mission scenario, these detections will still constitute less than 20% of the overall *Kepler* TTV sample (Goldberg et al., 2019).

Ground-based observatories can in principle recover transits for faint *Kepler* stars with long period planets, and coordinated multi-observatory campaigns have shown promise in achieving the requisite phase coverage (Freudenthal et al., 2018; von Essen, A. Ofir, et al., 2018; S. Wang et al., 2018). However, their photometric precisions are typically limited by low observing efficiencies and the presence of time-correlated noise due to imperfect guiding and point-spread function (PSF) variations (Zhao et al., 2014; Croll et al., 2015; Gudmundur Stefansson, Mahadevan, et al., 2017). These difficulties can be mitigated by using diffusers to control the shape of the point spread function (PSF) and spread out light from the star over a larger area. Diffusers have already been installed on several ground-based telescopes and have been shown to achieve significantly better photometric precision than more traditional observing techniques (Gudmundur Stefansson, Mahadevan, et al., 2017; Gudmundur Stefansson, Li, et al., 2018; von Essen, G. Stefansson, et al., 2019).

Here, we present diffuser-assisted TTV follow-up observations of four *Kepler* planets in dynamically interacting systems. We discuss our sample selection methodology and our observations of the four-planet sample with the Wide-field InfraRed Camera (WIRC; J. C. Wilson et al., 2003) in Section 2.2. In Section 2.3, we describe our image calibration, data reduction, light curve modeling, and dynamical modeling methods. We then present our results for each system in Section 2.4, along with some brief comments on the general performance of our instrument. In Section 2.5, we discuss some of the scientific implications of our new dynamical mass constraints within the broader exoplanet population, and we conclude with a summary of our results and a look towards future possibilities in Section 2.6.

2.2 Observations

Sample Selection

In this study we focused on the set of multi-planet systems from the original *Kepler* survey. We began by estimating the expected TTV signal strength for all planet pairs in order to identify the systems most likely to exhibit strong transit timing variations. We estimated the minimum mass of a planet from its radius, and then estimated the chopping signal and near-first order resonant TTV signal for planet pairs given their orbital periods. We then use the number of transits and the transit timing uncertainty to estimate a minimum TTV signal-to-noise ratio (SNR) in the limit of circular orbits. For systems exhibiting TTVs with high SNRs, we performed dynamical fits to the long cadence transit times in Rowe and Thompson (2015). We fit five parameters per planet, including the orbital period and phase at a chosen epoch, the two eccentricity vector components, and the dynamical mass. We then mapped the resulting posterior using Differential Evolution Markov Chain Monte Carlo sampling (Jontof-Hutter, Ford, et al., 2016). Since mutual inclinations are a second-order effect for the TTV amplitude, we assumed coplanarity in our models (Lithwick, J. Xie, and Wu, 2012; Nesvorný and Vokrouhlický, 2014; Jontof-Hutter, Ford, et al., 2016). We then forward modeled sample solutions for each system in order to identify those with the most strongly diverging TTV predictions. A detailed report of our forward modeling is in preparation.

We selected targets for our WIRC program from the subset of systems with strongly detected TTVs and dynamical solutions that diverged measurably in the years following the end of the primary *Kepler* mission. We excluded systems where the 1σ range of predicted transit times at the epoch of our proposed WIRC observation was greater than one hour, as this meant that there was a significant possibility that the transit might occur outside our window of observability. In order to ensure that the measured transit time was likely to provide a useful constraint on the dynamical fit we also calculated the expected timing precision of a new WIRC observation and excluded systems where this uncertainty was greater than the 1σ range in predicted transit times.

Within this sample of systems, we searched for targets with an ingress and/or egress visible from Palomar between August 2017 and May 2018. We then ranked the targets in our sample based on predicted signal-to-noise ratio (SNR) scaled from early WIRC commissioning data (Gudmundur Stefansson, Mahadevan, et al., 2017), and prioritized observations of the highest SNR targets. We ultimately obtained high-quality light curves for four confirmed and candidate planets from this ranked list, including: Kepler-29b, Kepler-36c, KOI-1783.01, and Kepler-177c. The predicted mid-transit times for these planets are shown in Table 2.1.

Table 2.1: Observational parameters for our four nights of data collection.

Star	J mag[a]	Date (UTC)	Start Time (UTC)	End Time (UTC)	Event Time[b] (UTC)	Event Duration (hr)	Start/Min/End Airmass	Exposure Time (s)
Kepler-29	14.13	2017 August 25	05:35:24	11:57:00	08:26:53	3.046	1.03/1.03/3.01	25
Kepler-36	11.12	2017 September 27	03:06:20	08:55:42	09:52:34	7.461	1.04/1.04/2.50	16[c]
KOI-1783	12.92	2018 April 21	08:19:42	12:04:05	07:07:51	5.871	1.73/1.05/1.05	20
Kepler-177	13.86	2018 May 4	07:17:36	12:09:04	10:30:49	5.245	1.73/1.02/1.02	75[d]

[a]: J band magnitudes from the 2MASS catalogue (Cutri et al., 2003).
[b]: Predicted mid-transit time.
[c]: 4 co-adds of 4 second exposures.
[d]: 3 co-adds of 25 second exposures.

New WIRC Observations

We observed our four selected systems in *J* band with WIRC, which is located at the prime focus of the Hale 200" telescope at Palomar Observatory (J. C. Wilson et al., 2003). The current 2048 × 2048 pixel Hawaii-II HgCdTe detector was installed in January 2017, along with 32-channel readout electronics that allow for a read time of 0.92 s (Tinyanont et al., 2019). The instrument has an $8\farcm7 \times 8\farcm7$ field of view with a pixel scale of $0\farcs2487$, ensuring that (at least for the magnitude range in our sample) there are always on the order of ten stars with comparable brightness contained within the same field of view as our target star.

We utilize the custom near-infrared Engineered Diffuser described in Gudmundur Stefansson, Mahadevan, et al. (2017) to mitigate time-correlated noise from PSF variations and improve our observing efficiency. The diffuser delivers a top-hat PSF with a full width at half maximum (FWHM) of $3''$. We also minimize the time-correlated noise contribution from flat-fielding errors by utilizing precision guiding software (Zhao et al., 2014). WIRC does not have a separate guide camera, but instead guides on science images by fitting 2D Gaussian profiles to comparison stars and determining guiding offsets on each image. For these observations, we find that the position of the star typically varies by less than 2-3 pixels over the course of the night, with the largest position drift occurring at high airmass where accurate centroid measurements become more challenging.

Dates, times, and airmasses for each observation are reported in Table 2.1. For Kepler-29, Kepler-36, and Kepler-177, we observed continuously during the observation windows. During our observation of KOI-1783 there were three breaks in data acquisition due to a malfunctioning torque motor causing a temporary loss of telescope pointing.

Exposure times are also reported in Table 2.1, and were chosen to keep the detector in the linear regime. WIRC commissioning tests have shown the detector to be linear to $\sim 0.5\%$ at 22,000 ADU (Tinyanont et al., 2019). When choosing exposure times, we aimed to keep the maximum count level at or below 20,000 ADU in order to accommodate potential changes in airmass and sky background. In some cases, frames were co-added during the night to increase observing efficiency as noted in Table 2.1.

2.3 Data Reduction and Model Fits

Image Calibration and Photometry

For each night, we construct a median dark frame and a flat field. During the construction of the dark and flat, we also construct a global bad pixel map with the procedure described by Tinyanont et al. (2019). Each image is dark subtracted and flat-fielded, and each bad pixel is replaced with the median of the 5 pixel $\times$ 5 pixel box surrounding the errant value. The total number of bad pixels is approximately 0.6% of the full array (Tinyanont et al., 2019). During the calibration sequence, mid-exposure times are converted to Barycentric Julian Date in the Barycentric Dynamical Time standard ($\mathrm{BJD_{TDB}}$), following the recommendation of Eastman, Siverd, and Gaudi (2010). All of the above steps are performed by the WIRC Data Reduction Pipeline, which was originally developed to automatically handle large sets of polarimetric data (Tinyanont et al., 2019).

We perform aperture photometry using the `photutils` package (Bradley et al., 2016). We begin by using the first science image as a "finding frame" and detect sources using the `DAOStarFinder` function (based on Stetson, 1987). Sources that are close to the detector edge and those with overlapping apertures are removed automatically. The target star is registered by comparison to an Aladin Lite finding chart (Bonnarel et al., 2000; Boch and Fernique, 2014). We then perform the photometry using a range of circular apertures with radii ranging between 6 and 18 pixels in one pixel steps, using the same aperture for all stars in each image. With WIRC's $\sim 0''.25$/pixel scale, the diffuser is expected to deliver stellar PSFs with a FWHM of 12 pixels, but the actual FWHM changes with stellar brightness. For each image, we calculate and subtract the median background via iterative 3σ clipping with the `sigma_clipped_stats` function in `astropy` with a five-iteration maximum specified (Astropy Collaboration, Robitaille, et al., 2013; Astropy Collaboration, Price-Whelan, et al., 2018). After this, we re-calculate the source centroids via iterative flux-weighted centroiding and shift apertures accordingly for each individual image. The local sky background is then estimated using an annular region around each source with inner radius of 20 pixels and outer radius of 50 pixels. We find that iterative sigma-clipping of this background region (this time with a 2σ threshold) is sufficient to reconstruct the mean local background, even though the fields are fairly crowded.

After raw light curves are obtained for each aperture size, we choose the ten comparison stars that best track the time-varying flux of the target star (i.e. those that have the minimal variance from the target star). We clean the target and comparison light curves by applying a moving median filter (of width 10 data points) to the target star dataset and removing 3σ outliers. We then select the optimal aperture by minimizing the root mean square (RMS) scatter after the light curve fitting described in the next section. Our optimal aperture radii were 8 pixels for Kepler-29b, 14 pixels for Kepler-36c, 10 pixels for KOI-1783.01, and 10 pixels for Kepler-177c. We find that our preferred apertures for each target increase in size with increasing stellar brightness, and all preferred apertures are comparable in size to the aforementioned 12 pixel FWHM expected for the diffuser.

Kepler Light Curves

Of the four planets in our sample, only one (Kepler-29b) had a transit duration short enough to allow us to observe a full transit; for the other three planets our observations spanned ingress or egress, but not both. This introduces a degeneracy between the mid-transit time and transit duration (parameterized here by the inclination and semi-major axis) in our fits to these four transits. We resolve this degeneracy by carrying out joint fits with the original *Kepler* photometry, where we assume common values for the transit depth $(R_\mathrm{p}/R_\star)^2$, the inclination i, and the scaled semi-major axis $a/R_\star$. Although we would expect the transit depth to vary as a function of wavelength if any of these planets have atmospheres, the maximum predicted magnitude for this variation (corresponding to a cloud-free, hydrogen-rich atmosphere) is much smaller than our expected measurement uncertainty for the change in transit depth $(R_\mathrm{p}/R_\star)^2$ between the optical *Kepler* band and our J band photometry. This effect would be strongest for the low-density planet Kepler-177c, but even then, the maximal variation is of order 200 ppm versus our WIRC J band precision of roughly 1300 ppm. We found that constraining the transit depth to the *Kepler* value resulted in smaller transit timing uncertainties for our partial transit observations, which otherwise exhibited correlations between the transit depth, the transit time, and the linear trend in time.

We processed the *Kepler* long-cadence simple aperture photometry (SAP) light curves for each star in our sample using the `kepcotrend` function in the `PyKE` package (Still and Barclay, 2012). To avoid errors in light curve shape introduced by assuming a linear ephemeris, we cut out individual light curves from the cotrended *Kepler* data using lists of individual transit times from Tomer Holczer et al. (2016) when possible and otherwise using Rowe and Thompson, 2015. We selected our trim window to provide two transit durations of both pre-ingress and post-egress baseline. After dividing out a linear trend fit to the out-of-transit baseline for each light curve, we combined all transits into a single transit light curve with flux as a function of time from transit center.

This process assumes that TDVs do not strongly bias our retrieved transit shapes. For systems with large amplitude TDVs it may become necessary to perform photodynamical modeling in order to properly treat the time-varying transit shape (e.g. Freudenthal et al., 2018). However, Tomer Holczer et al., 2016 examined data spanning the full length of the *Kepler* mission and did not detect TDVs for any of the targets in our sample. To further justify our assumption that TDVs have a negligible impact on the measured signals, we calculated the expected TDV amplitude for Kepler-177c (a planet with long period and large impact parameter that is more prone to nodal precession). The maximum TDV amplitude is of order 0.1 hr over the 10 year baseline. The WIRC data alone are not sensitive to transit duration changes on this timescale, since we only detect ingress or egress for most transits. Additionally, the precision on the transit timing in the joint fits tend to be much more uncertain than 0.1 hr, meaning that TDV effects will not compromise our final TTV constraints. We conclude that we can safely ignore TDVs in our treatment of these data.

Light Curve Fitting

To fit the *Kepler* and WIRC light curves, we first constructed light curve models defined by observed quantities and fit parameters. We then constructed appropriate likelihood and prior functions and sampled the resultant posterior probability numerically to obtain estimates of the best-fit parameters and their associated uncertainties. The outputs of the WIRC photometry pipeline are an array of times $\vec{t} = (t_1, t_2, ..., t_n)$, the target data array $\vec{y} = (y_1, y_2, ..., y_n)$ (with y_i referring to the measurement at time t_i), and comparison star arrays $\vec{x}_j = (x_1, x_2, ..., x_n)$. Collectively, the comparison stars define a matrix $\mathbf{X}$, with one comparison star $\vec{x}_j$ in each row of the matrix.

We aim to fit the target $\vec{y}$ with a model $\vec{M}$ that depends on the depth of the transit $(R_\mathrm{p}/R_\star)^2$, the transit center time t_0, the inclination i, the ratio of semi-major axis to stellar radius $a/R_\star$, and a linear trend in time α. That model can be written as follows (loosely following the notation of Diamond-Lowe et al., 2018):

$$\vec{M} = [\alpha\vec{t} + \vec{S}] \times \vec{T}_{\mathrm{WIRC}}((R_\mathrm{p}/R_\star)^2, t_0, i, a/R_\star), \tag{2.1}$$

where $\vec{S}$ is the systematics model, $\vec{T}_{\mathrm{WIRC}}$ is the transit model, and the multiplication is meant to denote a pointwise product. We use the `batman` code to construct the transit model (Kreidberg, 2015) and fix the planet eccentricities to zero. The eccentricities of multi-planet *Kepler* systems are typically small, with a population mean of $\bar{e} = 0.04^{+0.03}_{-0.04}$ (J.-W. Xie et al., 2016), and the effect of these eccentricities on the shape of the transit light curve is negligible for these data. We use four-parameter nonlinear limb darkening coefficients from Claret and Bloemen (2011), assuming stellar parameter values from Petigura, Howard, et al. (2017) that are reproduced in Table 2.2.

Table 2.2: Stellar parameters for the stars in our sample.

Target	T_{eff} (K)	[Fe/H] (dex)	$\log(g)$ ($\log(\mathrm{cm/s^2})$)	$M_\star$ ($M_\odot$)	$R_\star$ ($R_\odot$)
Kepler-29	5378^{+60}_{-60}	$-0.44^{+0.04}_{-0.04}$	$4.6^{+0.1}_{-0.1}$	$0.761^{+0.024}_{-0.028}$	$0.732^{+0.033}_{-0.031}$
Kepler-36	5979^{+60}_{-60}	$-0.18^{+0.04}_{-0.04}$	$4.1^{+0.1}_{-0.1}$	$1.034^{+0.022}_{-0.022}$	$1.634^{+0.042}_{-0.040}$
KOI-1783	5922^{+60}_{-60}	$0.11^{+0.04}_{-0.04}$	$4.3^{+0.1}_{-0.1}$	$1.076^{+0.036}_{-0.032}$	$1.143^{+0.031}_{-0.030}$
Kepler-177	5732^{+60}_{-60}	$-0.11^{+0.04}_{-0.04}$	$4.1^{+0.1}_{-0.1}$	$0.921^{+0.025}_{-0.023}$	$1.324^{+0.053}_{-0.051}$

Spectroscopic parameters (T_{eff}, [Fe/H], and $\log(g)$) are taken from Fulton, Petigura, et al. (2017), and physical parameters ($M_\star$ and $\mathrm{R}_\star$) are from Fulton and Petigura (2018).

For ground-based observations, we expect the measured flux from each star to vary as a function of the airmass, centroid drift, seeing changes, transparency variations, and other relevant parameters. However, all of the stars on our wide-field detector should respond similarly to changes in the observing conditions. In particular, we expect that stars of approximately the same J magnitude and color will track closely with the light curve of our target star. We therefore define our systematics model as a linear combination of comparison star light curves. This allows us to empirically model these effects without explicitly relating them to the relevant atmospheric and telescope state parameters via a parametric model. We determine the coefficients for the linear combination via a linear regression fit to the target light curve after dividing out the transit light curve model (which we call the "target systematics" $\vec{S}_{\mathrm{target}}$). We calculate new linear coefficients every time the transit light curve is modified. Mathematically, the target systematics can be written:

$$\vec{S}_{\mathrm{target}} = \frac{\vec{y}}{\vec{T}_{\mathrm{WIRC}}((R_{\mathrm{p}}/R_\star)^2, t_0, i, a/R_\star)} - \alpha\vec{t}, \tag{2.2}$$

where division is meant to be pointwise, and the linear regression defining the systematics model can be written:

$$\vec{S} = \mathbf{P}\vec{S}_{\mathrm{target}}, \tag{2.3}$$

where the projection matrix **P** comes from the comparison stars and can be written:

$$\mathbf{P} = \mathbf{X}^T(\mathbf{X}\mathbf{X}^T)^{-1}\mathbf{X} \tag{2.4}$$

Equations (2.1)–(2.4) thus define the model $\vec{M}$ solely as a function of the observed quantities $\{\vec{t}, \vec{y}, \mathbf{X}\}$ and the fit parameters $\{(R_{\mathrm{p}}/R_\star)^2, t_0, \alpha, i, a/R_\star\}$. To give a sense for how our systematics removal looks in practice, in Figure 2.2 we show the raw and detrended light curves for KOI-1783.01 along with the best systematics and transit models.

As discussed in §2.3, we fit the WIRC photometry jointly with the *Kepler* photometry in order to avoid a strong degeneracy between mid-transit time and transit duration. The *Kepler* photometry consists of an array of times $\vec{t}_{Kep} = (t_1, t_2, ..., t_n)$ and the corresponding detrended target data array $\vec{y}_{Kep} = (y_1, y_2, ..., y_n)$. Because these data are already detrended and phased together, the model $\vec{M}_{Kep}$ for the *Kepler* data is simply a `batman` transit model:

$$\vec{M}_{Kep} = \vec{T}_{Kep}((R_{\mathrm{p}}/R_\star)^2, i, a/R_\star) \tag{2.5}$$

We supersampled the *Kepler* light curves to 1 min cadence, and used four-parameter nonlinear limb darkening coefficients from Sing (2010) calculated specifically for the *Kepler* bandpass.

Having defined our models, we can now define our likelihood function. We assume measurements to be Gaussian-distributed and uncorrelated (correlated noise is considered briefly in §2.4) such that the likelihood takes the form:

$$\begin{aligned}\log(\mathcal{L}) = &-\frac{1}{2}\sum_i \log(2\pi\sigma_i^2) - \frac{1}{2}\sum_i\left(\frac{y_i - M_i}{\sigma_i}\right)^2 \\ &-\frac{1}{2}\sum_i \log(2\pi\sigma_{Kep,i}^2) \\ &-\frac{1}{2}\sum_i\left(\frac{y_{Kep,i} - M_{Kep,i}}{\sigma_{Kep,i}}\right)^2,\end{aligned} \tag{2.6}$$

where the uncertainties σ_i and $\sigma_{Kep,i}$ are quadrature sums of the Poisson noise from the target star and extra noise terms that can be fitted:

$$\vec{\sigma} = \sqrt{\vec{\sigma}^2_{\text{phot,WIRC}} + \sigma^2_{\text{extra,WIRC}}} \tag{2.7}$$

$$\vec{\sigma}_{Kep} = \sqrt{\vec{\sigma}^2_{\text{phot},Kep} + \sigma^2_{\text{extra},Kep}}. \tag{2.8}$$

Because the extra noise terms are always positive, we fit for $\log(\sigma_{\text{extra,WIRC}})$ and $\log(\sigma_{\text{extra},Kep})$ as a numerical convenience. Also, rather than fitting for t_0 itself, we define all times relative to the predicted transit times in Table 2.1, and fit for the offset from that time Δt_0.

We impose priors on all parameters. They are either Gaussian, taking the functional form:

$$\log(\mathcal{P}_k) = -\frac{1}{2}\log(2\pi\sigma_k^2) - \frac{1}{2}\left(\frac{k-\mu_k}{\sigma_k}\right)^2, \tag{2.9}$$

or uniform, taking the functional form:

$$\begin{aligned}\log(\mathcal{P}_k) = & \log\left(\frac{1}{k_{\max} - k_{\min}}\right), \quad k_{\min} < k < k_{\max}; \\ & -\infty \text{ otherwise.}\end{aligned} \tag{2.10}$$

We placed physically motivated Gaussian priors on $a/R_\star$ calculated from the stellar parameters reported by Fulton and Petigura (2018), and used uniform priors for all other variables. We list our priors for the physical fit parameters in Table 2.4.

With the likelihood and priors defined, we can finally write the posterior probability with Bayes' Theorem (up to a constant proportional to the evidence):

$$\log(\text{Prob}) = \log(\mathcal{L}) + \sum_k \log(\mathcal{P}_k) \tag{2.11}$$

Then, we seek a solution for the fit parameters $(R_\text{p}/R_\star)^2, \Delta t_0, i, a/R_\star, \alpha, \log(\sigma_{\text{extra,WIRC}})$, and $\log(\sigma_{\text{extra},Kep})$ that maximizes log(Prob). We carry out an initial fit using `scipy`'s Powell minimizer (Virtanen et al., 2020) and use this solution as a starting point for the affine-invariant ensemble Markov chain Monte Carlo sampler `emcee` (Foreman-Mackey et al., 2013). We burn the chains in for 2×10^3 steps and then run for 10^5 steps. This corresponds to at least 500 integrated autocorrelation times for each parameter. The maximum *a posteriori* parameter estimates with associated 68% confidence intervals for all model parameters aside from α, $\log(\sigma_{\mathrm{extra,WIRC}})$, and $\log(\sigma_{\mathrm{extra},Kep})$ are given in Table 2.4. The best-fit light curves are shown in Appendix 2.7. Additionally, we plot the posterior distributions for these parameters in Appendix 2.8.

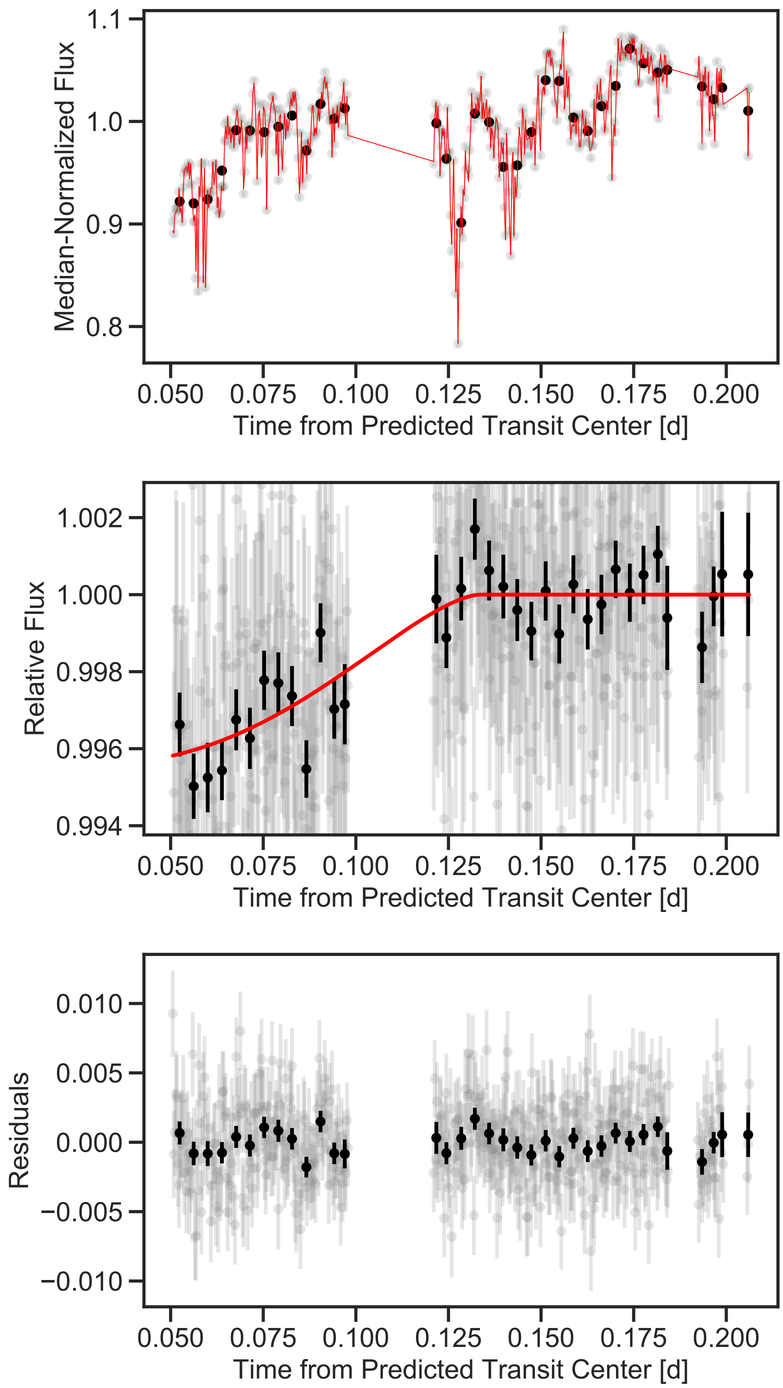

Figure 2.2: (Top) Median-normalized photometry for KOI-1783.01, with unbinned data in gray and data binned by a factor of 10 in black. The breaks in data acquisition were due to a malfunctioning torque motor. The best-fit systematic noise model is shown as a red curve. (Middle) Detrended photometry of KOI-1783.01, with the best-fit light curve model now shown in red. (Bottom) Residuals from the light curve fitting of the detrended photometry.

Table 2.3: Photometric quality statistics for the observations presented in this work.

Planet	WIRC Transit Coverage (%)	*Kepler* RMS (ppm)	WIRC RMS (ppm)	WIRC RMS ($\times$ photon noise)	WIRC Binned RMS ($\times$ photon noise)	$\log(\sigma_{\mathrm{extra,WIRC}})$
Kepler-29b	100	504	4222	1.20	1.27	-2.627
Kepler-36c	41.8	75	1305	2.10	2.46	-2.943
KOI-1783.01	33.7	157	2862	1.48	1.29	-2.680
Kepler-177c	66.9	320	2403	1.22	1.46	-2.851

For the binned RMS values, data are binned to 10 minute cadence. Additionally, the Carter and Winn (2009) β factor quantifying correlated noise is the binned RMS divided by the unbinned RMS in this parameterization, since both are provided in terms of the photon noise.

Table 2.4: System parameters for the joint photometric fits.

Parameter	Symbol	Values				Units	Source
		Kepler-29b	Kepler-36c	KOI-1783.01	Kepler-177c		
Fixed Parameters							
Orbital period	P	10.3392924	16.23192004	134.4786723	49.41117582	d	(1, 2)
Predicted transit time	t_0	2457990.852	2458023.9115	2458229.7971125	2458242.93807	BJD	—
Eccentricity	e	0.	0.	0.	0.	—	—
Kepler limb darkening coefficients	a_1	0.4959	0.4639	0.6034	0.5716	—	(3)
	a_2	0.0222	0.3045	-0.1382	-0.1145	—	(3)
	a_3	0.5708	0.0751	0.6330	0.6579	—	(3)
	a_4	-0.3485	-0.1251	-0.3506	-0.3667	—	(3)
WIRC limb darkening coefficients	b_1	0.3634	0.3982	0.4832	0.4421	—	(4)
	b_2	0.5846	0.5452	0.2998	0.3993	—	(4)
	b_3	-0.6152	-0.6817	-0.3634	-0.4523	—	(4)
	b_4	0.1997	0.2508	0.1152	0.1474	—	(4)
Fit Priors							
Transit depth prior	$\mathcal{P}_{(R_p/R_\star)^2}$	$\mathcal{U}(0, 2000)$	$\mathcal{U}(0, 1000)$	$\mathcal{U}(0, 10000)$	$\mathcal{U}(0, 8000)$	ppm	—
Transit timing offset prior	$\mathcal{P}_{\Delta t_0}$	$\mathcal{U}(-100, 100)$	$\mathcal{U}(-100, 100)$	$\mathcal{U}(-100, 100)$	$\mathcal{U}(-100, 100)$	min	—
Inclination prior	$\mathcal{P}_i$	$\mathcal{U}(85, 90)$	$\mathcal{U}(85, 90)$	$\mathcal{U}(85, 90)$	$\mathcal{U}(85, 90)$	°	—
Scaled semi-major axis prior	$\mathcal{P}_{a/R_\star}$	$\mathcal{N}(24.906, 1.125)$	$\mathcal{N}(16.696, 0.436)$	$\mathcal{N}(99.030, 2.840)$	$\mathcal{N}(41.649, 1.674)$	—	(5)
Fit Posteriors							
Transit depth	$(R_p/R_\star)^2$	1020^{+31}_{-34}	$425.3^{+3.8}_{-3.5}$	5044^{+87}_{-64}	3643^{+55}_{-57}	ppm	—
Transit timing offset	Δt_0	$-14.3^{+16.7}_{-2.7}$	$-17.9^{+11.8}_{-4.7}$	16^{+10}_{-11}	$45.2^{+8.7}_{-7.1}$	min	—
Inclination	i	$89.13^{+0.45}_{-0.23}$	$89.36^{+0.45}_{-0.29}$	$89.4413^{+0.0076}_{-0.0082}$	$88.795^{+0.037}_{-0.035}$	°	—
Scaled semi-major axis	$a/R_\star$	$24.95^{+1.34}_{-0.91}$	$16.69^{+0.26}_{-0.31}$	$94.8^{+1.1}_{-1.1}$	$42.08^{+1.04}_{-0.94}$	—	—
Derived Parameters							
Planet-star radius ratio	$R_p/R_\star$	$0.03194^{+0.00048}_{-0.00054}$	$0.02062^{+0.00009}_{-0.00009}$	$0.07102^{+0.00061}_{-0.00045}$	$0.06036^{+0.00045}_{-0.00047}$	–	–
Impact Parameter	b	$0.379^{+0.083}_{-0.185}$	$0.186^{+0.080}_{-0.131}$	$0.9239^{+0.0026}_{-0.0023}$	$0.8848^{+0.0056}_{-0.0065}$	–	–
Transit duration	T_{14}	$3.041^{+0.045}_{-0.052}$	$7.46^{+0.021}_{-0.017}$	$5.874^{+0.039}_{-0.040}$	$5.243^{+0.054}_{-0.054}$	hr	–

(1) Morton et al. (2016), (2) Thompson et al. (2018), (3) Sing (2010), (4) Claret and Bloemen (2011), (5) Fulton and Petigura (2018). Also, $\mathcal{N}(a, b)$ indicates a normal (Gaussian) prior with mean a and standard deviation b described by Equation (2.9), whereas $\mathcal{U}(a, b)$ indicates a uniform prior with lower bound a and upper bound b described by Equation (2.10).

Dynamical Modeling

Our fits to the ground-based WIRC photometry typically resulted in a non-Gaussian posterior for the mid-transit time. We accounted for these skewed distributions in our dynamical fits by dividing the posteriors into twenty bins and normalized the probability density to give a likelihood for each bin, as illustrated in the marginalized timing distributions from Appendix 2.8. We then ran two sets of dynamical fits for each system using either these skewed timing posteriors or a symmetric Gaussian distribution with a width equal to the average of our positive and negative uncertainties.

We fitted dynamical models to the transit timing data using a Differential Evolution Markov Chain Monte Carlo algorithm (Ter Braak, 2006; Nelson, Ford, and Payne, 2014; Jontof-Hutter, Rowe, et al., 2015; Jontof-Hutter, Ford, et al., 2016). We used uniform priors for the orbital period and phase and uniform positive definite priors for the dynamical masses. For each eccentricity vector component, we assumed a Gaussian distribution centered on 0 with a width of 0.1 for the prior. This is wider than the inferred eccentricity distribution among *Kepler*'s multi-planet systems (Fabrycky, Lissauer, et al., 2014; Hadden and Lithwick, 2014), but TTV modeling is subject to an eccentricity-eccentricity degeneracy whereby aligned orbits can have larger eccentricities than allowed by our prior with little effect on the relative eccentricity (Jontof-Hutter, Ford, et al., 2016). The results of our dynamical modeling are given in Table 2.5. This table includes orbital periods (solved at our chosen epoch of BJD = 2455680), masses, and eccentricity vectors for retrievals with only the *Kepler* data, retrievals including the new WIRC transit time with a Gaussian uncertainty distribution, and retrievals using the skewed WIRC timing posterior. We find that our fits using Gaussian posteriors are generally in good agreement with results from fits utilizing the skewed transit timing posteriors.

2.4 Results

We determine the significance of each detection in the WIRC data by re-running the joint fit and allowing the WIRC transit depth to vary independent of the *Kepler* transit depth. The confidence is then estimated using the width of the posterior on the WIRC transit depth. We detect transit signals for all four of our targets with 3σ or greater confidence in the WIRC data alone.

We show various quality statistics for each night of photometry in Table 2.3 (see Section 2.4 for additional details). Our results for the photometric fits to each

Table 2.5: Results from our dynamical analysis.

Planet	Dataset	P [days]	$\left(\frac{M_p}{M_\oplus}\right)\left(\frac{M_\odot}{M_\star}\right)$	$e\cos(\omega)$	$e\sin(\omega)$
Kepler-29b	Kep LC	$10.33838^{+0.00030}_{-0.00027}$	$4.6^{+1.4}_{-1.5}$	$-0.060^{+0.072}_{-0.071}$	$-0.030^{+0.072}_{-0.072}$
	Kep LC + WIRC (G)	$10.33974^{+0.00014}_{-0.00015}$	$3.7^{+1.3}_{-1.3}$	$0.013^{+0.071}_{-0.071}$	$-0.016^{+0.056}_{-0.063}$
	Kep LC + WIRC (S)	$10.33966^{+0.00015}_{-0.00017}$	$3.8^{+1.1}_{-1.0}$	$0.003^{+0.068}_{-0.070}$	$-0.088^{+0.059}_{-0.058}$
Kepler-29c	Kep LC	$13.28843^{+0.00048}_{-0.00053}$	$4.07^{+2.87}_{-2.29}$	$0.007^{+0.063}_{-0.062}$	$-0.022^{+0.063}_{-0.063}$
	Kep LC + WIRC (G)	$13.28613^{+0.00026}_{-0.00021}$	$3.28^{+1.06}_{-1.08}$	$-0.023^{+0.061}_{-0.062}$	$-0.022^{+0.045}_{-0.055}$
	Kep LC + WIRC (S)	$13.28633^{+0.00031}_{-0.00027}$	$3.39^{+0.86}_{-0.84}$	$-0.007^{+0.059}_{-0.061}$	$-0.085^{+0.051}_{-0.051}$
Kepler-36b	Kep LC	$13.86834^{+0.00050}_{-0.00051}$	$3.990^{+0.093}_{-0.092}$	$0.050^{+0.023}_{-0.025}$	$-0.026^{+0.034}_{-0.033}$
	Kep LC + WIRC (G)	$13.86825^{+0.00050}_{-0.00050}$	$3.972^{+0.078}_{-0.074}$	$0.041^{+0.019}_{-0.020}$	$-0.011^{+0.018}_{-0.018}$
	Kep LC + WIRC (S)	$13.86821^{+0.00049}_{-0.00049}$	$3.964^{+0.077}_{-0.068}$	$0.037^{+0.019}_{-0.018}$	$-0.004^{+0.012}_{-0.015}$
Kepler-36c	Kep LC	$16.21867^{+0.00010}_{-0.00010}$	$7.456^{+0.167}_{-0.168}$	$0.053^{+0.021}_{-0.023}$	$-0.039^{+0.031}_{-0.031}$
	Kep LC + WIRC (G)	$16.21865^{+0.00010}_{-0.00010}$	$7.397^{+0.104}_{-0.107}$	$0.046^{+0.017}_{-0.018}$	$-0.026^{+0.017}_{-0.017}$
	Kep LC + WIRC (S)	$16.21865^{+0.00010}_{-0.00010}$	$7.371^{+0.092}_{-0.093}$	$0.042^{+0.017}_{-0.016}$	$-0.019^{+0.012}_{-0.014}$
KOI-1783.01	Kep LC	$134.4622^{+0.0035}_{-0.0038}$	$90.2^{+30.3}_{-23.2}$	$0.0079^{+0.0080}_{-0.0050}$	$-0.039^{+0.012}_{-0.021}$
	Kep LC + WIRC (G)	$134.4628^{+0.0033}_{-0.0035}$	$78.1^{+15.1}_{-12.9}$	$0.0073^{+0.0067}_{-0.0046}$	$-0.048^{+0.014}_{-0.015}$
	Kep LC + WIRC (S)	$134.4629^{+0.0033}_{-0.0036}$	$76.4^{+11.8}_{-9.6}$	$0.0072^{+0.0067}_{-0.0045}$	$-0.049^{+0.014}_{-0.012}$
KOI-1783.02	Kep LC	$284.230^{+0.044}_{-0.031}$	$17.1^{+5.1}_{-4.3}$	$0.018^{+0.018}_{-0.015}$	$-0.011^{+0.027}_{-0.032}$
	Kep LC + WIRC (G)	$284.215^{+0.026}_{-0.021}$	$16.2^{+4.7}_{-3.8}$	$0.017^{+0.015}_{-0.015}$	$-0.020^{+0.034}_{-0.028}$
	Kep LC + WIRC (S)	$284.212^{+0.024}_{-0.018}$	$16.1^{+4.6}_{-3.8}$	$0.017^{+0.015}_{-0.014}$	$-0.020^{+0.034}_{-0.026}$
Kepler-177b	Kep LC	$36.8591^{+0.0019}_{-0.0017}$	$5.76^{+0.84}_{-0.81}$	$-0.026^{+0.074}_{-0.075}$	$-0.014^{+0.065}_{-0.068}$
	Kep LC + WIRC (G)	$36.8601^{+0.0015}_{-0.0014}$	$5.44^{+0.78}_{-0.75}$	$0.017^{+0.052}_{-0.054}$	$-0.001^{+0.062}_{-0.063}$
	Kep LC + WIRC (S)	$36.8601^{+0.0013}_{-0.0012}$	$5.38^{+0.78}_{-0.74}$	$0.020^{+0.047}_{-0.048}$	$0.005^{+0.061}_{-0.061}$
Kepler-177c	Kep LC	$49.40964^{+0.00097}_{-0.00097}$	$14.6^{+2.7}_{-2.5}$	$-0.027^{+0.064}_{-0.065}$	$-0.014^{+0.056}_{-0.059}$
	Kep LC + WIRC (G)	$49.40926^{+0.00078}_{-0.00077}$	$13.9^{+2.7}_{-2.5}$	$0.010^{+0.045}_{-0.046}$	$-0.003^{+0.053}_{-0.054}$
	Kep LC + WIRC (S)	$49.40921^{+0.00072}_{-0.00074}$	$13.5^{+2.5}_{-2.3}$	$0.013^{+0.040}_{-0.041}$	$0.003^{+0.052}_{-0.053}$

In the Dataset column, "Kep LC" refers to the transit timings from the *Kepler* long-cadence light curves, "WIRC (G)" refers to the transit timing from our observations when assumed to have Gaussian uncertainties, and "WIRC (S)" refers to the transit timing from our observations taking into account the skewed shape of our timing posteriors. Also, the orbital period P is solved for at our chosen epoch of BJD = 2455680.

observed planet are given in Table 2.4, and the resulting orbital periods, masses, and eccentricity vectors are presented in Table 2.5. We combine our photometric and dynamical results with previously computed stellar parameters to yield the physical planet parameters we report in Table 2.6. Below we discuss WIRC's overall photometric performance as well as results for each individual system.

Instrument Performance

Our best photometric performance is for Kepler-177c, where we were only $\sim 20\%$ above the shot noise. We also investigate how well WIRC mitigates time-correlated noise, which can lead to underestimated uncertainties in reported transit times. We calculate the RMS versus bin size for each observation and show the corresponding

Table 2.6: Physical parameters for the planets in this study.

Planet	M_p $[M_\oplus]^a$	R_p $[R_\oplus]^b$	ρ_p [g/cm^3]	$F_\mathrm{in}\,[F_\oplus]$ ^{c}
Kepler-29b	$5.0^{+1.5}_{-1.3}$	$2.55^{+0.12}_{-0.12}$	$1.65^{+0.53}_{-0.49}$	$55.9^{+6.5}_{-4.8}$
Kepler-29c^d	$4.5^{+1.1}_{-1.1}$	$2.34^{+0.12}_{-0.11}$	$1.91^{+0.57}_{-0.54}$	$34.4^{+3.8}_{-3.8}$
Kepler-36b^d	$3.83^{+0.11}_{-0.10}$	$1.498^{+0.061}_{-0.049}$	$6.26^{+0.79}_{-0.64}$	247^{+32}_{-32}
Kepler-36c	$7.13^{+0.18}_{-0.18}$	$3.679^{+0.096}_{-0.091}$	$0.787^{+0.065}_{-0.062}$	$191.0^{+9.7}_{-10.4}$
KOI-1783.01	$71.0^{+11.2}_{-9.2}$	$8.86^{+0.25}_{-0.24}$	$0.560^{+0.101}_{-0.085}$	$5.70^{+0.27}_{-0.27}$
KOI-1783.02^d	$15.0^{+4.3}_{-3.6}$	$5.44^{+0.52}_{-0.30}$	$0.51^{+0.21}_{-0.15}$	$2.49^{+0.35}_{-0.35}$
Kepler-177b^d	$5.84^{+0.86}_{-0.82}$	$3.50^{+0.19}_{-0.15}$	$0.75^{+0.16}_{-0.14}$	$30.4^{+4.0}_{-4.0}$
Kepler-177c	$14.7^{+2.7}_{-2.5}$	$8.73^{+0.36}_{-0.34}$	$0.121^{+0.027}_{-0.025}$	$25.4^{+1.6}_{-1.6}$

[a] Calculated from our dynamical masses and the stellar masses of Fulton and Petigura (2018).
[b] Calculated from either our measured $R_\mathrm{p}/R_\star$ or that from Thompson et al. (2018) and stellar radii from Fulton and Petigura (2018).
[c] Calculated in the low-eccentricity ($e^2 << 1$) approximation via $F_\mathrm{in} = 4.62{\times}10^4 F_\oplus \left(\frac{T_\mathrm{eff}}{T_\odot}\right)^4 \left(\frac{a}{R_\star}\right)^{-2}$ (Jontof-Hutter, Ford, et al., 2016), with effective temperatures from Fulton, Petigura, et al. (2017) and scaled semi-major axes from our measurements or Thompson et al. (2018).
[d] Radius ratio and scaled semi-major axis taken from Thompson et al. (2018).

plots in the bottom right panels of Figures 2.7–2.10. We find that Kepler-29b and KOI-1783.01 appear to have minimal time-correlated noise (see the bottom right panels in Figures 2.7 and 2.9, respectively). Kepler-36c has some time-correlated trends on longer timescales, and for Kepler-177c, quasi-periodic noise is readily visible in both the best-fit residual plot and in the RMS versus bin size plot (see also the bottom right panel in Figures 2.8 and 2.10, respectively). We tried adding sinusoids to our fits for these planets, but found that this had a negligible effect on the overall quality of the fits and the resulting transit timing posteriors.

To derive a representative noise statistic for WIRC, we first calculated the scatter in 10 minute bins for each of our observations. These statistics were then scaled to the equivalent values for observations of a 14th magnitude star. In some of our earliest observations we used a sub-optimal co-addition strategy, resulting in relatively inefficient observations (for Kepler-36c, this increased the noise by 31.1% relative to a more optimal strategy). We therefore applied an additional correction factor to to rescale the noise for these inefficient observations to the expected value for better-optimized observations. Averaging these corrected noise statistics together, we find that WIRC can deliver 1613 ppm photometry per 10 minute bin on a $J = 14$ magnitude star. If we assume that we are able to collect two hours of data in transit and two hours out of transit, this equates to a precision of 659 ppm on the transit depth measurement for planets around a $J = 14$ magnitude star. To highlight the range of parameter space that this precision opens up, we plot transit depths for all confirmed transiting exoplanets against host star J magnitude in Figure 2.3 along with the 3σ detection thresholds of WIRC and *Spitzer*. While *Spitzer* performs better for brighter stars, WIRC begins to out-perform *Spitzer* for stars fainter than ~ 10 magnitude, doing a factor of 1.6 better at $J = 14$. In practice, the achieved photometric precision will also depend on factors such as atmospheric background, amount of baseline obtained, diurnal constraints, and the number of available comparison stars of comparable magnitude, but the first-order considerations in Figure 2.3 suggest that ground-based, diffuser-assisted infrared photometry can indeed outperform some current space-based facilities for typical *Kepler* transiting planet systems.

Kepler-29

Kepler-29b is sub-Neptune near the 5:4 and 9:7 mean-motion resonances with the sub-Neptune Kepler-29c. Both low-density planets were originally confirmed by Fabrycky, Ford, et al. (2012) using TTVs; subsequent dynamical analyses have shown that the pair may actually be in the second-order 9:7 resonance (Migaszewski, Goździewski, and Panichi, 2017), but the TTV curve is likely also affected by proximity to the first-order 5:4 resonance (Jontof-Hutter, Ford, et al., 2016). We detect a transit of Kepler-29b at 3.5σ confidence in the WIRC data. The final detrended *Kepler* and WIRC light curves, models, residuals, and RMS binning plots for Kepler-29b are shown in Figure 2.7 and the corresponding posterior probability distributions are shown in Figure 2.11. Although the transit shape is poorly constrained by the WIRC data alone, both ingress and egress are visible by eye in the WIRC light curve and the relative timing of these two events provides a solid estimate of the transit time when we constrain the transit shape using the *Kepler* photometry. We find that the resulting posterior distribution for our new WIRC transit time is fairly asymmetric, with the final timing offset determined to -14^{+17}_{-3} min.

Our new observation was obtained in an epoch where the Kepler-only dynamical fits yield substantially divergent transit times, and as a result our new transit time provides an improved constraint on the planet masses and eccentricities as shown in Figure 2.15. We find that the dynamical mass estimate for Kepler-29c has improved by almost a factor of three in our updated fits. Our new results favor dynamical

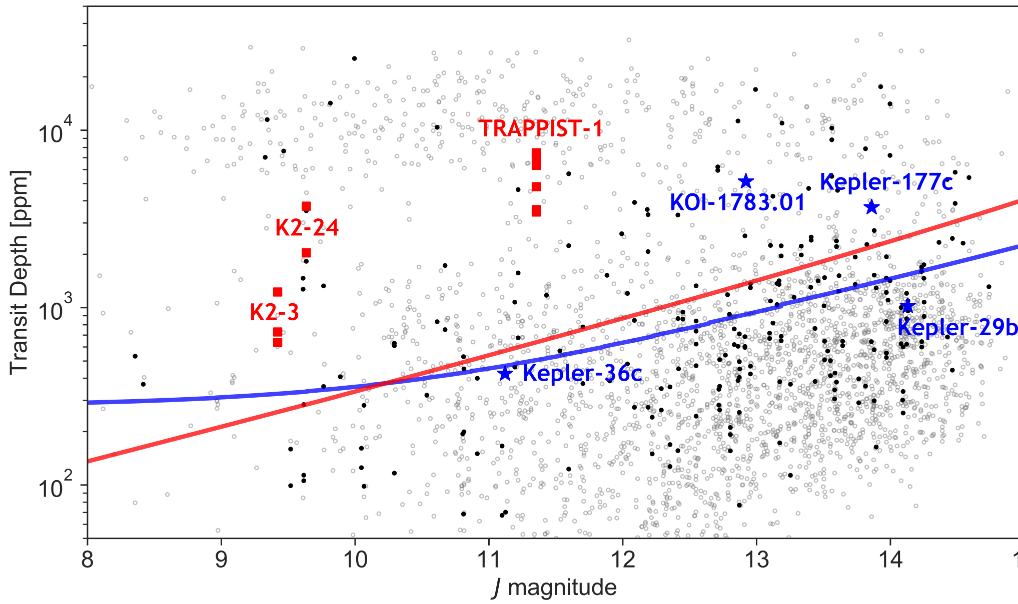

Figure 2.3: Transit depth as a function of host star magnitude for non-TTV (grey points) and TTV (black points) systems, taken from the NASA Exoplanet Archive. Also noted are approximate 3σ detection thresholds with *Spitzer* (red curve), which is scaled with magnitude from the photometric scatter obtained by Björn Benneke et al. (2017) with a slight nonlinear correction at higher magnitudes fit to the brown dwarf survey results of Metchev et al. (2015), and the 3σ detection threshold with WIRC assuming the optimal co-addition strategy (blue curve). The systems investigated in this work are marked with labeled blue stars, while a few sample TTV systems investigated by *Spitzer* (K2-3, K2-24, TRAPPIST-1) are given marked with labeled red squares (Beichman et al., 2016; Delrez et al., 2018; Petigura, Björn Benneke, et al., 2018). The WIRC detection threshold levels off for brighter stars due to decreasing observing efficiency, and the slight discontinuities in the curve are artifacts of discrete changes in the number of co-additions.

masses on the low side of (but not incompatible with) the mass distributions inferred by Jontof-Hutter, Ford, et al. (2016) for Kepler-29b and c.

Despite these decreased masses our updated densities for these planets (1.7±0.5 and 1.9±0.5 g/cm^3, respectively) are larger than the densities reported by Jontof-Hutter, Ford, et al. (2016). This is because we utilize updated stellar parameters of $M = 0.761^{+0.024}_{-0.028}\ M_\odot$ and $R = 0.732^{+0.033}_{-0.031}\ R_\odot$ from Fulton and Petigura (2018), which are smaller than the values of $M = 0.979 \pm 0.052\ M_\odot$ and $R = 0.932 \pm 0.060\ M_\odot$ adopted by Jontof-Hutter, Ford, et al. (2016). For a fixed planet-star radius ratio, a smaller stellar radius implies a correspondingly smaller planet radius. Similarly, a smaller stellar mass implies a larger planet mass for the same best-fit dynamical mass ratio. Both changes therefore act to increase the measured planetary density. Even with these increased density estimates, it is likely that both of these planets have retained a modest hydrogen-rich atmosphere (see §2.5). The masses and radii of both planets also remain quite similar, in good agreement with the "peas in a pod" trend wherein multi-planet *Kepler* systems tend to host planets that are similar in both size and bulk density (Millholland, S. Wang, and Laughlin, 2017; Weiss, Marcy, et al., 2018).

Kepler-36

The Kepler-36 system includes two planets with strikingly dissimilar densities: Kepler-36b is a rocky super-Earth close to 7:6 mean-motion resonance with the low-density sub-Neptune Kepler-36c (Carter, Agol, et al., 2012). The latter planet was included in our sample, and we detect it with a significance of 5.3σ. We present the final light curves and associated statistics for our new transit observation of Kepler-36c in Figure 2.8, and plot the corresponding posteriors in Figure 2.12. The posterior distribution on the WIRC transit time is again fairly asymmetric, with the offset constrained to -18^{+12}_{-5} minutes. We obtain masses and densities for both planets consistent with previous investigations (though on the low side for Kepler-36b; Carter, Agol, et al., 2012; Hadden and Lithwick, 2017). In Figure 2.16, we provide updated dynamical masses, eccentricity vectors, and transit timing for this system. Future constraints from *TESS* should allow for improved mass estimates in this system, especially for Kepler-36c (Goldberg et al., 2019).

The RMS scatter achieved for this measurement was 2$\times$ the photon noise limit (see bottom right panel of Figure 2.8), which is higher than any of the other observations presented in this work. This is due in part to scintillation noise (Gudmundur Stefansson, Mahadevan, et al., 2017), as Kepler-36 was our brightest target and we used correspondingly short integration times. For this star, the scintillation noise at an airmass of 1.5 is $\sim$ 650 ppm, which is comparable to the shot noise. Our use of short integration times also limited our observing efficiency, resulting in higher photometric scatter than might otherwise have been expected for this relatively bright star. Both problems could be mitigated by increasing the number of co-adds, resulting in a longer effective integration time and higher overall observing efficiency.

KOI-1783

As we will discuss in §2.5, there is already compelling evidence in the literature establishing the planetary nature of this system, which contains two long-period (134 and 284 days, respectively) gas giant planet candidates located near a 2:1 period commensurability. We present the final light curves and associated statistics for our new transit observation of KOI-1783.01 in Figure 2.9, and plot the corresponding posteriors in Figure 2.13. This planet is detected with a significance of 5.9σ in the WIRC data, and we achieve a timing precision of about 10 minutes. These results are in good agreement with a model of the KOI-1783 system that assumes the source of TTVs to be near-resonant planet-planet perturbations. In Figure 2.17, we present updated constraints on dynamical masses, eccentricities, and transit timing for KOI-1783. Our new transit observation reduces the uncertainty on the dynamical mass of KOI-1783.01 by approximately a factor of two. When combined with the stellar parameters from Fulton and Petigura (2018), these new constraints provide the most detailed picture of this system to date. We find that KOI-1783.01 is slightly smaller than Saturn, with $R_{\mathrm{p}} = 8.9^{+0.3}_{-0.2} R_{\oplus}$ and $M_{\mathrm{p}} = 71^{+11}_{-9} M_{\oplus}$. This corresponds to a density of $\rho = 0.56^{+0.10}_{-0.09}$ g/cm^3, consistent with the presence of a substantial gaseous envelope; we discuss the corresponding implications for this planet's bulk composition in more detail in §2.5. KOI 1783.02 has a mass of $M_{\mathrm{p}} = 15^{+4}_{-4} M_{\oplus}$, a radius of $R_{\mathrm{p}} = 5.4^{+0.5}_{-0.3} R_{\oplus}$, and a density of $\rho = 0.5^{+0.2}_{-0.2}$g/cm^3, again indicative of a substantial gaseous envelope. Both planets appear to have low orbital eccentricities ($e \lesssim 0.05$), in agreement with the overall *Kepler* TTV sample (Fabrycky, Lissauer, et al., 2014; Hadden and Lithwick, 2014; J.-W. Xie et al., 2016). Additionally, we note that the uncertainty on $e\cos(\omega)$ for KOI-1783.01 is an order of magnitude lower than for the other planets in this study, corresponding to a $\pm 1\sigma$ uncertainty of approximately 13 hours in the secondary eclipse phase. Although this is quite good for a planet on a 134 day orbit, the star's faintness and the planet's low equilibrium temperature make this a challenging target for secondary eclipse observations.

Kepler-177

The Kepler-177 system contains a low-density sub-Neptune (Kepler-177b) and a very-low-density sub-Neptune (Kepler-177c) located near the 4:3 mean motion resonance. This system was initially confirmed via TTVs by J.-W. Xie (2014) and subsequently re-analyzed by Jontof-Hutter, Ford, et al. (2016) and Hadden and Lithwick (2017). Our final light curves and associated statistics for Kepler-177c are given in Figure 2.10, and the posteriors are given in Figure 2.14. We detect the transit at 5.5σ significance and measure the corresponding transit time with a 1σ uncertainty of approximately 10 minutes. Although our new dynamical fits for this system result in modestly lower mass uncertainties, our transit observation was taken close to one TTV super-period away from the *Kepler* data, where diverging solutions re-converge and thus our new observations provided limited leverage to constrain these dynamical models. If the *TESS* mission is extended it should provide additional transit observations that would further reduce the mass uncertainties in this system (Goldberg et al., 2019), but our observations demonstrate that this system is also accessible to ground-based follow-up at a more favorable epoch.

2.5 Discussion

Confirmation of the KOI-1783 System

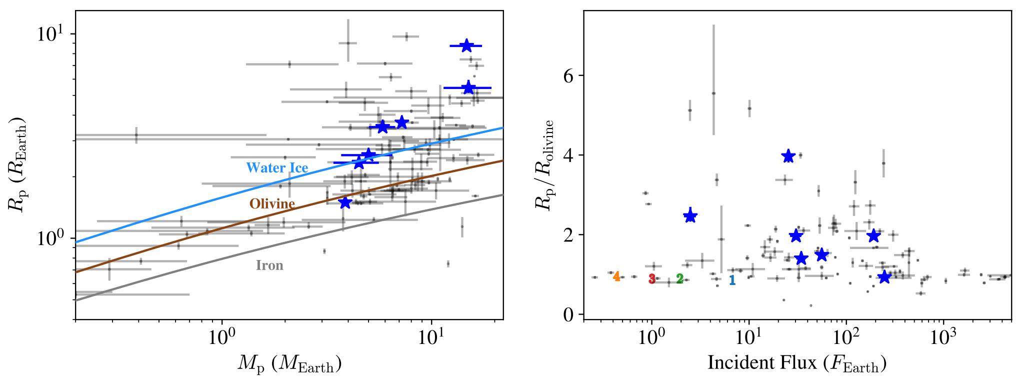

Figure 2.4: (Left) Masses and radii of the sub-Neptune planets studied in this work (blue stars) compared to all $M < 20M_\oplus$ planets from the NASA Exoplanet Archive (gray points). The blue, brown, and grey curves show the mass-radius relation for planets made of pure water ice, olivine, and iron (J. J. Fortney, Marley, and Barnes, 2007). (Right) Planetary radius relative to that of a pure-rock planet of the same mass is plotted as a function of incident flux for our systems (blue stars) and all $M < 17M_\oplus$ planets on the NASA Exoplanet Archive (gray points). Also noted are the Solar System planets with the colored numbers (Mercury is 1, Venus is 2, Earth is 3, and Mars is 4).

As the only unverified planet candidate in our sample, KOI 1783.01 represents a special case for this program. A transiting planet candidate around KOI-1783 (KIC 10005758) was first reported by Batalha et al. (2013), and a second candidate in the system was identified by the Planet Hunters citizen science collaboration (Lintott et al., 2013). While the *a priori* probability of both transit signals being false positives is quite low (Lissauer, Ragozzine, et al., 2011; Lissauer, Marcy, Rowe, et al., 2012; Lintott et al., 2013; Lissauer, Marcy, Bryson, et al., 2014; Rowe, Bryson, et al., 2014), a few characteristics of this system precluded a quick confirmation. First, the transit signals for both candidates are near-grazing (the grazing parameter $X = b + R_{\rm p}/R_\star$ is $0.9949^{+0.0032}_{-0.0027}$ for KOI-1783.01 from our posteriors, and $0.932^{+0.065}_{-0.015}$ for KOI-1783.02 from the Thompson et al. (2018) catalog), with "V"-shaped morphologies that Batalha et al. (2013) noted as being potentially diagnostic of an eclipsing binary. Additionally, the *Kepler* Data Validation reports show a fairly large offset ($\sim 0''.25$) of the stellar centroid during the transit relative to the KIC position, which is also typical of stellar blends.

The two transit candidates in this system have a period ratio of 2.11, near the 2:1 commensurability. Such an architecture can generate detectable TTVs, which previous studies have used to confirm the planetary nature of transit candidates (J. H. Steffen et al., 2013; Nesvorný, D. Kipping, et al., 2013). Early analyses of the transit times of KOI-1783.01 (Ford et al., 2012; Tsevi Mazeh et al., 2013) noted the potential presence of TTVs, but concluded that the significance of the deviation from a linear ephemeris was too low to be conclusive. As *Kepler* continued to observe this target, evidence for TTVs of both planet candidates in this system grew stronger (Rowe, Bryson, et al., 2014; Tomer Holczer et al., 2016). An independent analysis of this system by the Hunt for Exomoons with Kepler Project found evidence for dynamical interactions (D. M. Kipping et al., 2015), selecting a TTV model over a linear ephemeris model by 17.2σ for KOI-1783.02. The spectral TTV analysis of Aviv Ofir, J.-W. Xie, et al. (2018) also found evidence of dynamical interactions, yielding $\Delta\chi^2$ values for the TTV signals over a linear model of 49 and 264 for KOI-1783.01 and .02, respectively (the authors note that $\Delta\chi^2 \gtrsim 20$ is a reliable detection threshold).

For non-dynamically interacting systems, it is common to use statistical arguments to establish that the planetary hypothesis is the most likely explanation for a given transit signal using codes such as the publicly-available false-positive probability (FPP) calculator `vespa` (Morton, 2012; Morton, 2015). The `vespa` package has been used to statistically validate more than a thousand exoplanet candidates from *Kepler* and *K2* thus far (Crossfield et al., 2016; Morton et al., 2016; Livingston, Endl, et al., 2018; Livingston, Crossfield, et al., 2018; Mayo et al., 2018), although refutation of some previously validated planets suggests that caution is necessary when validating with limited follow-up data (Santerne et al., 2016; Cabrera et al., 2017; Shporer et al., 2017). Morton et al. (2016) obtained FPPs for all KOIs, including KOI-1783.01 (FPP = 0.680 ± 0.014) and KOI-1783.02 (FPP = 0.200 ± 0.012). However, TTVs were not considered in the construction of the light curves for these planets, which can inflate the FPP by making the transits look more "V"-shaped. Additionally, Morton et al. (2016) found four confirmed planets with anomalously high FPPs: three exhibited TTVs, and the other had grazing transits. Our analysis suggests that KOI-1783 system is a near-grazing TTV system, making it very likely to have an overestimated FPP.

In a six-year campaign, Santerne et al. (2016) performed RV observations of a sample of 125 KOI stars, including KOI-1783. They observed KOI-1783 two times with SOPHIE and detected no RV variation. Additionally, they establish 99% upper limits on the RV semi-amplitude ($K < 81.3$ m/s) and corresponding mass ($M < 2.83\ M_\mathrm{J}$). While these upper limits were derived by fitting a circular orbit with no TTVs, the lack of detected RV variations rule out the eclipsing binary false positive mode to very high confidence.

In addition to high-resolution spectroscopic follow-up, three ground-based adaptive optics (AO) follow-up observations of KOI-1783 have been performed to date, as listed by Furlan et al. (2017) and the Exoplanet Follow-up Observing Program. The Robo-AO team observed this star in their LP600 filter with the Palomar 60" telescope, achieving a contrast of $\Delta M = 4.00$ mag at $0''.30$ (Law et al., 2014). Additionally, J. Wang et al. (2015) observed KOI-1783 in K_s band with PHARO on the Hale 200" telescope at Palomar Observatory, achieving a contrast of $\Delta M = 4.33$ mag at $0''.50$. More stringent contrast constraints of $\Delta M = 7.96$ mag at $0''.50$ were obtained with NIRC2 on the Keck II Telescope using the Brγ filter (Furlan et al., 2017). These observations demonstrate that there are no nearby stars that might explain the $0''.25$ offset noted in the Data Validation Report.

Published RV data rule out the existence of an eclipsing binary, and AO imaging data rule out the existence of companions. Combined with the aforementioned multiple independent analyses all supporting dynamical interactions between the bodies in the system, these follow-up constraints lead us to conclude that the two transit candidates in the KOI-1783 system should be confirmed as bona fide planets.

Population-Level Trends

TTVs Probe Warm Sub-Neptune-Sized Planets

There are currently very few sub-Neptune-sized transiting planets with well-measured masses at large orbital distances ($P > 100$ days); these systems are quite rare to begin with, and most are too small and faint to be amenable to RV follow-up (Jontof-

Hutter, 2019). TTV studies that probe this regime are thus quite valuable, as planets that receive low incident fluxes are much more likely to retain their primordial atmospheres than their more highly-irradiated counterparts (e.g. Owen and Wu, 2013; T. Mazeh, T. Holczer, and Faigler, 2016). Even if mass loss is common for these longer-period planets, the mechanism by which it occurs may be quite different. For highly irradiated exoplanets, atmospheric mass loss is primarily driven by thermal escape processes as the intense XUV flux heats the upper atmospheres (e.g. Owen, 2019). However for planets on more distant orbits, non-thermal processes are competitive with or dominant over photoevaporative escape; this is, for instance, the present case for terrestrial planets like Mars (F. Tian et al., 2013; Feng Tian, 2015). Density constraints for this population of long-period extrasolar planets at low ($\lesssim 100 F_{\oplus}$) incident fluxes are therefore critical for building a holistic understanding of atmospheric mass loss in the regime relevant for potentially habitable terrestrial planets.

In Figure 2.4, we plot the masses and radii of our sub-Neptune-sized sample ($M < 17 M_{\oplus}$) along with those from the NASA Exoplanet Archive and compare their radii to their incident fluxes. Other than the rocky super-Earth Kepler-36b (Carter, Agol, et al., 2012), all of the planets in our sample are more inflated than they would be if they were purely composed of silicate rock (J. J. Fortney, Marley, and Barnes, 2007), implying that they possess at least modest volatile-rich envelopes. Even after allowing for water-rich compositions, our bulk density estimates for the planets in Table 2.6 are still too low, and likely require a modest hydrogen-rich atmosphere. For Kepler-29b, Kepler-29c, Kepler-36c, and Kepler-177b, the grids of Lopez and Jonathan J. Fortney (2014) suggest hydrogen-helium envelope fractions of 2-5% in mass. For the more massive sub-Neptunes KOI-1783.02 and Kepler-177c, these grids suggest hydrogen-helium envelope fractions greater than 10% in mass. In the following section, we explore the bulk composition of KOI-1783.01, KOI-1783.02, and Kepler-177c in more detail.

Bulk Metallicities of the Giant Planets KOI-1783.01, KOI-1783.02, and Kepler-177c

TTVs can also deliver masses and radii for giant planets in the low-insolation regime. This is crucial for estimates of bulk metallicity, as gas giants hotter than approximately 1000 K appear to have inflated radii that are inconsistent with predictions from standard interior models (e.g., Laughlin, Crismani, and Adams, 2011; D. P.

Thorngren, Jonathan J. Fortney, et al., 2016; D. P. Thorngren and Jonathan J. Fortney, 2018). Relatively cool, dynamically interacting planets such as KOI-1783.01 are not expected to be affected by this inflation mechanism and are therefore ideal candidates for these studies.

We measure the mass of the gas giant KOI-1783.01 to $\sim$ 15% precision and its radius to $\sim$ 3%, as this star has relatively accurate stellar parameters from Fulton and Petigura (2018). When combined with our incident flux constraints and stellar age estimates from Fulton and Petigura (2018), these parameters yield a bulk metallicity of $Z_{\rm p} = 0.30 \pm 0.03$ for KOI-1783.01 using the statistical model of D. Thorngren and Jonathan J. Fortney (2019). Using the stellar metallicity from Table 2.2 and the $Z_{\rm star} = 0.014 \times 10^{\rm [Fe/H]}$ prescription from D. P. Thorngren, Jonathan J. Fortney, et al. (2016), this corresponds to $Z_{\rm p}/Z_{\rm star} = 16.6^{+2.4}_{-2.2}$. We note that when masses and radii are constrained to this level of precision we should also consider the additional uncertainties introduced by the choice of models, which are not accounted for in these error bars (D. P. Thorngren, Jonathan J. Fortney, et al., 2016; D. Thorngren and Jonathan J. Fortney, 2019). This bulk metallicity value is nevertheless in excellent agreement with the mass-metallicity relation previously inferred for gas giant planets at higher incident fluxes (D. P. Thorngren, Jonathan J. Fortney, et al., 2016; D. Thorngren and Jonathan J. Fortney, 2019), as shown in Figure 2.5.

This bulk metallicity also yields an upper limit on the atmospheric metallicity, as the metallicity observable in a planetary atmosphere will always be less than the total metal content of the planet (D. Thorngren and Jonathan J. Fortney, 2019). For KOI-1783.01, this (95th percentile) upper limit is $Z_{\rm atm} \leq 79\times$ solar, where “solar” refers to the Asplund et al. (2009) photospheric metal fraction of 1.04×10^{-3}. This calculation assumes an average mean molecular mass of 18 (that of water) for this heavy element component; if this is not the case, then the true upper limit on the atmospheric metallicity should be scaled by $18/\mu_Z$ (D. Thorngren and Jonathan J. Fortney, 2019).

We calculate comparable bulk composition estimates for the two sub-Neptunes in our sample, KOI-1783.02 and Kepler-177c. In this mass regime, differences in equation of state between rock and water ice become important, adding another degree of freedom to the calculation. We construct models composed of a rock layer, a water layer, and low-density H/He layer enriched to Neptune’s metallicity (90× solar) by borrowing water from the water layer. We do not include mass loss in our simulation, and we assume negligible amounts of iron in the calculation. We

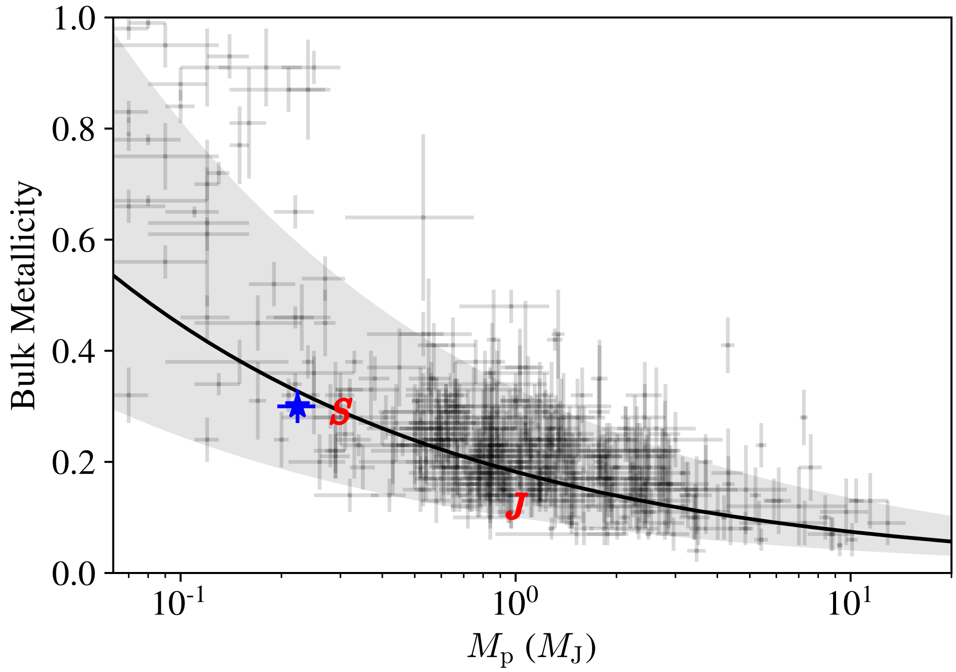

Figure 2.5: Bulk metallicity of KOI-1783.01 (blue star) compared to the metallicities of the D. Thorngren and Jonathan J. Fortney (2019) sample (grey points). The best-fit mass-metallicity relation obtained by D. P. Thorngren, Jonathan J. Fortney, et al. (2016) is shown in black, with $\pm 1\sigma$ uncertainties denoted by the grey shaded region. The red "J" and "S" correspond to Jupiter and Saturn.

use constraints on the mass, radius, host star age, and incident flux to retrieve the composition, including the relative amounts of rock, water, and H/He. Although we are not able to place strong constraints on the relative amounts of rock versus water as the radius is still fairly insensitive to the core composition details (Lopez and Jonathan J. Fortney, 2014; Petigura, Sinukoff, et al., 2017), we are able to place a strong constraint on the total bulk metallicity Z_p and the corresponding the H/He fraction $f_\mathrm{H/He} = 1 - Z_\mathrm{p}$.

As hinted at by their low bulk densities, these two planets have large H/He mass fractions: $f_\mathrm{H/He} = 0.31 \pm 0.08$ for KOI-1783.02 and $f_\mathrm{H/He} = 0.74 \pm 0.04$ for Kepler-177c. The value for Kepler-177c is somewhat problematic from a planet formation perspective, as it implies a maximum core mass of just 4 $M_\oplus$. Depending on the planet's formation location, it may be difficult to explain how such a small core could have accreted such a massive gas envelope. One explanation is that the core formed outside 1 au and experienced relatively dust-free accretion, as is typically invoked for super-puffs (Lee and Chiang, 2016). We note, however, that super-puffs are a few times less massive than Kepler-177c despite having similar inferred core masses, implying that the gas-to-core mass ratio of Kepler-177c exceeds that of a typical super-puff. Although it is possible that our estimate of this maximum core mass might have been biased by assumptions made in our models, accounting for atmospheric mass loss would have preferentially removed hydrogen and helium, and including iron in the model would have increased the $f_{\mathrm{H/He}}$. We conclude that these assumptions are unlikely to explain the large inferred H/He mass fraction for this planet. The MIST isochrone-derived age estimate for this planet from Fulton and Petigura (2018) appears to be quite secure, with $\log(\mathrm{age}) = 10.07 \pm 0.04$, so it is unlikely that this planet's radius is inflated by residual heat from formation.

Can Kepler-177c be inflated by internal heating mechanisms such as Ohmic dissipation (Pu and Valencia, 2017) or obliquity tides (Millholland, 2019)? Its large total mass and low insolation makes this scenario unlikely. We assess the scenario of Kepler-177c having a core mass of $14.5 M_\oplus$ and an envelope mass of $0.2 M_\oplus$ (envelope mass fraction of 1%). Its estimated equilibrium temperature is $\sim$800K, too low for Ohmic dissipation to puff up Kepler-177c to $\gtrsim 8 R_\oplus$ (see Figures 8 and 9 of Pu and Valencia, 2017). Next, we assess heating by obliquity tides. Even if we assume maximal obliquity, the expected thickness of the envelope is $\sim 0.48 R_\oplus$ (see equation 13 of Millholland, 2019). If the composition of Kepler-177c core is similar to that of Earth, we expect its core size to be $\sim 1.95 R_\oplus$ (assuming $R \propto M^{1/4}$), so that the expected total radii of the planet is only $\sim 2.43 R_\oplus$, far too small to explain the measured $8.73 R_\oplus$. Even at gas-to-core mass ratio of 10%, the expected total radii is just $3.74 R_\oplus$.

A Possible Formation Scenario for Kepler-177

We conclude that Kepler-177c rightfully belongs in the small sample of $\sim 15 M_\oplus$ planets with extremely low bulk densities (and thus extremely large envelope fractions). This sample also includes Kepler-18d (Cochran et al., 2011; Petigura, Sinukoff, et al., 2017) and K2-24c (Petigura, Björn Benneke, et al., 2018). Petigura, Björn Benneke, et al. (2018) suggest a formation scenario for the latter planet wherein the disk dissipates just as the planet begins to enter runaway accretion. Lee (2019) show that the sub-Saturn population can indeed be explained by the timing of disk dispersal, but they note as a prerequisite that their cores must be massive enough to trigger runaway accretion during the disk lifetime, $\gtrsim 10 M_\oplus$. For cores less massive than this, the maximum gas-to-core mass ratio (GCR) is set by the amount of gas that can be accreted by cooling. In Figure 2.6, we reproduce the Lee (2019) GCR plot as a function of core mass and accretion time, which highlights the different regimes dictating the maximum envelope fraction for a given core mass. While KOI-1783.01 and KOI-1783.02 can largely be explained within the framework of disk dispersal timing relative to the onset of runaway accretion, Kepler-177c cannot, nor can K2-24c or Kepler-18d. These low-density $15M_\oplus$ planets are outliers, lying above their theoretical maximum GCRs, as are the super-puffs Kepler-51b (Masuda, 2014), Kepler-223e (Mills, Fabrycky, et al., 2016), Kepler-87c (Aviv Ofir, Dreizler, et al., 2014), and Kepler-79d (Jontof-Hutter, Lissauer, et al., 2014).

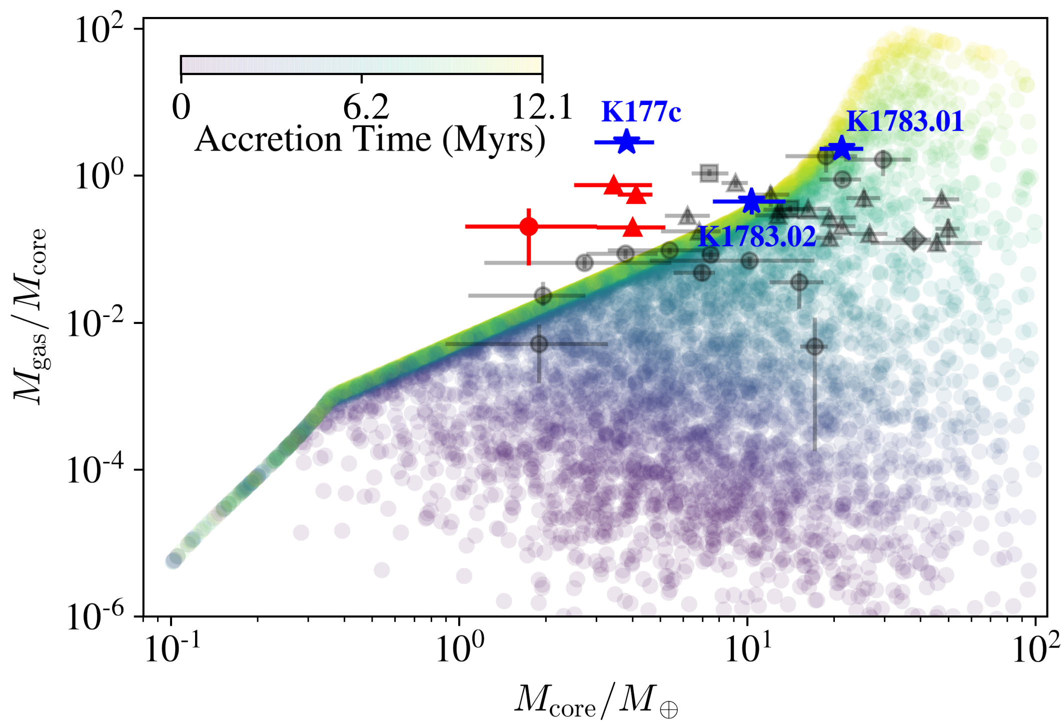

Figure 2.6: The Lee (2019) gas-to-core mass ratio (GCR) plot as a function of core mass $M_{\rm core}$ and accretion time (color-coded) for their best-fit model ensemble of core masses (log-normal with $\mu = 4.3M_\oplus$ and $\sigma = 1.3$). Overplotted on this theoretically-derived distribution are observational GCR constraints on real planets, denoted by gray circles (Lopez and Jonathan J. Fortney, 2014), gray triangles (Petigura, Sinukoff, et al., 2017), gray diamonds (Dressing et al., 2018), gray squares (Petigura, Björn Benneke, et al., 2018), and blue stars (this work). Previously identified super-puffs (Kepler-51b, Kepler-223e, Kepler-87c, and Kepler-79d) are marked in red. Note that Kepler-177c has a larger GCR than these super-puffs despite having a similar core mass.

As a result, Lee (2019) suggests that these more massive low-density planets may share a formation pathway with the less-massive super-puffs. Super-puffs likely accreted their envelopes farther from their star and then migrated inwards (Ikoma and Hori, 2012; Lee, Chiang, and Ormel, 2014; Ginzburg, Schlichting, and Sari, 2016; Lee and Chiang, 2016; Schlichting, 2018), and additionally should have experienced "dust-free" accretion, meaning that dust did not contribute much to the overall opacity due to e.g. grain growth or sedimentation (Lee and Chiang, 2015; Lee and Chiang, 2016). To test the feasibilty of this hypothesis, we can estimate the amount of time that Kepler-177c must have spent undergoing dust-free accretion and compare to typical disk lifetimes. If this timescale is longer than the typical disk dispersal timescale, then a mechanism other than dust-free accretion is necessary; if it is comparable or shorter, then dust-free accretion may be feasible. For Kepler-177c ($M_{\rm core} \approx 3.8 M_\oplus$, GCR ≈ 2.8), we can approximate the dust-free accretion time necessary to achieve the observed GCR beyond 1 au in a gas-rich disk using the analytic scaling relation of Lee and Chiang (2015, see their Equation 24):

$$t \sim 1\ \mathrm{kyr} \left[\left(\frac{\mathrm{GCR}}{0.1} \right) \left(\frac{5 M_\oplus}{M_{\rm core}} \right) \right]^{2.5} \approx 8.2\ \mathrm{Myr}, \tag{2.12}$$

where for simplicity we have assumed their nominal values for the f factor, the nebular gas metallicity Z, the adiabatic gradient $\nabla_{\rm ad}$, and the temperature and mean molecular weight at the radiative-convective boundary $T_{\rm rcb} = 200$ K and $\mu_{\rm rcb}$. The outer layers of dust-free envelopes are largely isothermal so the adopted temperature corresponds to the nebular temperature at the formation location. The estimated accretion timescale required to build Kepler-177c is comparable to typical disk lifetimes (~ 5 Myr; see, e.g. Alexander et al., 2014, and references therein). We note that Equation 2.12 is derived assuming the self-gravity of the envelope is negligible compared to the gravity of the core. The rate of accretion starts to accelerate once GCR $\gtrsim 0.5$, so a more careful calculation would provide an even shorter timescale. We suggest that $15 M_\oplus$ planets with large GCRs may indeed share a dust-free accretion history with their lower-mass super-puff counterparts. As such, detailed characterization of Neptune-mass planets with low ($\rho \lesssim 0.3$ g/cm^3) bulk densities may provide invaluable insights into super-puff formation processes.

2.6 Conclusions and Future Prospects

We presented infrared photometry for four dynamically interacting *Kepler* systems. With precise telescope guiding and the use of an engineered diffuser, we achieved a precision with WIRC that is comparable to or better than *Spitzer* for stars fainter than $J = 9.5$. Most of the planets we observed have host stars that are too faint for standard Doppler-based follow-up, but their masses can be measured to a high relative precision by fitting their transit timing variations. Our new transit measurements demonstrate that a single, well-timed follow-up observation taken years after the *Kepler* mission's conclusion can improve mass estimates by almost a factor of three. Perhaps unsurprisingly, we found that observing in epochs of maximally divergent transit times for differing dynamical solutions yields the largest improvements in mass estimates. The potential information gain is also larger for long-period systems with relatively few transits observed during the original *Kepler* mission. The systems we have studied highlight the diverse range of science cases made possible by diffuser-assisted photometry, including the confirmation of long-period planet candidates in TTV systems as well as bulk composition studies for relatively cool planets ranging in size from sub-Neptunes to gas giants.

WIRC's demonstrated infrared photometric precision opens up multiple new opportunities for ground-based studies of transiting planets and brown dwarfs. For dynamically interacting systems bright enough for RV observations, diffuser-assisted transit observations can provide an extended TTV baseline for joint RV-TTV modeling. These kinds of studies can constrain the structures of planetary systems without reliance on stellar models (Almenara, Díaz, Mardling, et al., 2015; Almenara, Díaz, Bonfils, et al., 2016; Agol and Fabrycky, 2018; Weiss, Deck, et al., 2017; Almenara, Díaz, Hébrard, et al., 2018; Petigura, Björn Benneke, et al., 2018). For highly irradiated gas giant planets, WIRC can be used to complement existing space-based emission and transmission spectroscopy from *Spitzer* and the *Hubble Space Telescope* by observing photometric transits and secondary eclipses at wavelengths that are inaccessible to these telescopes. This extended wavelength coverage is important for reducing degeneracies in atmospheric retrievals (e.g. Bjoern Benneke and Seager, 2012; Line, Zhang, et al., 2012; Line, Wolf, et al., 2013; Line, Knutson, et al., 2014). WIRC can also measure low-amplitude rotational variability in brown dwarfs at infrared wavelengths. Current ground-based infrared measurements can constrain variability at the $\sim 0.7\%$ level (P. A. Wilson, Rajan, and Patience, 2014; Radigan, 2014) in these objects; for the brighter (J = 14-15) variable brown dwarfs, WIRC will be able to push these limiting amplitudes below 0.1%. We are only beginning to explore the parameter space made available by diffuser-assisted photometry, but the prospects for new ground-based studies of brown dwarfs and transiting planets are promising.

2.7 Appendix A: *Kepler* and WIRC Light Curves

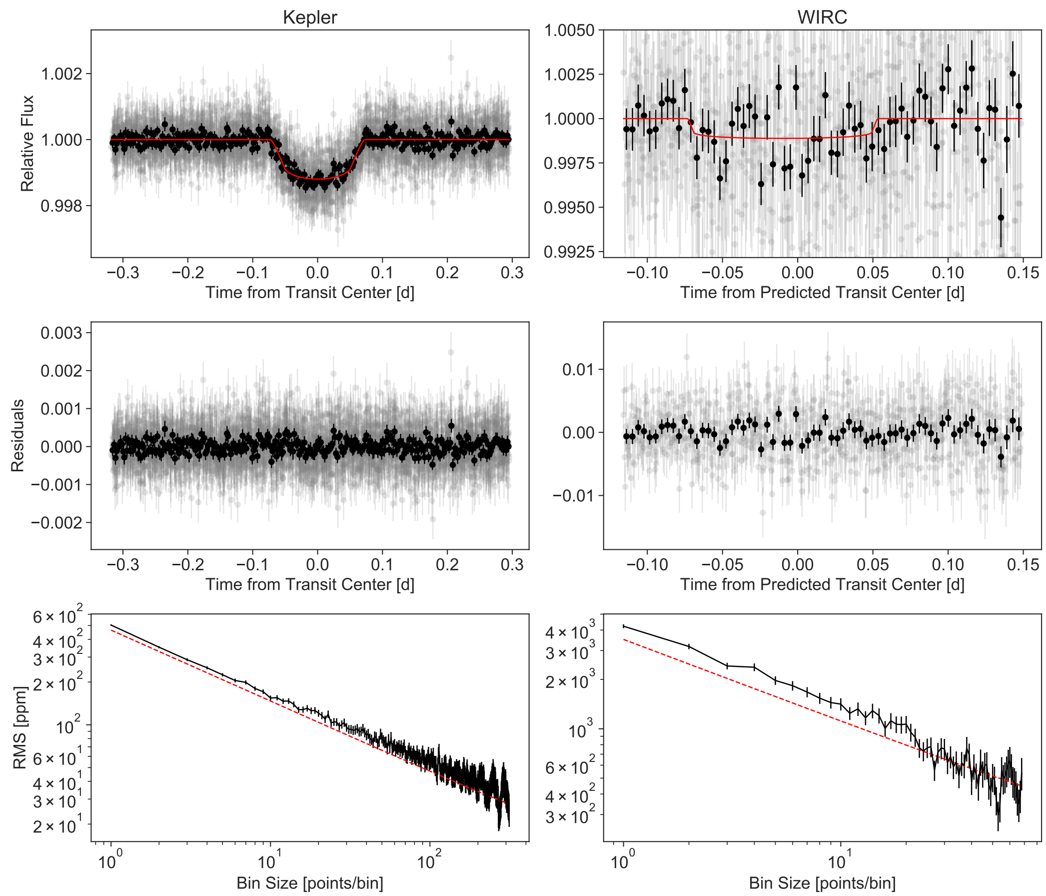

Figure 2.7: *Kepler* (left) and WIRC (right) light curves and best-fit models (top), residuals (middle), and RMS as a function of bin size (bottom) for Kepler-29b. In the top and middle plots, the unbinned data are shown as gray filled circles, and the light curves binned by a factor of 10 are shown as black filled circles. The red lines in the top plots denote our best-fit light curve model. The transit is detected at 3.5σ confidence in the WIRC data, and we constrain the transit timing offset to be -14^{+17}_{-3} minutes (from the predicted time in Table 2.1). For continuous data acquisition with WIRC, a bin size of 24 points is equivalent to 10 minutes in the lower right plot.

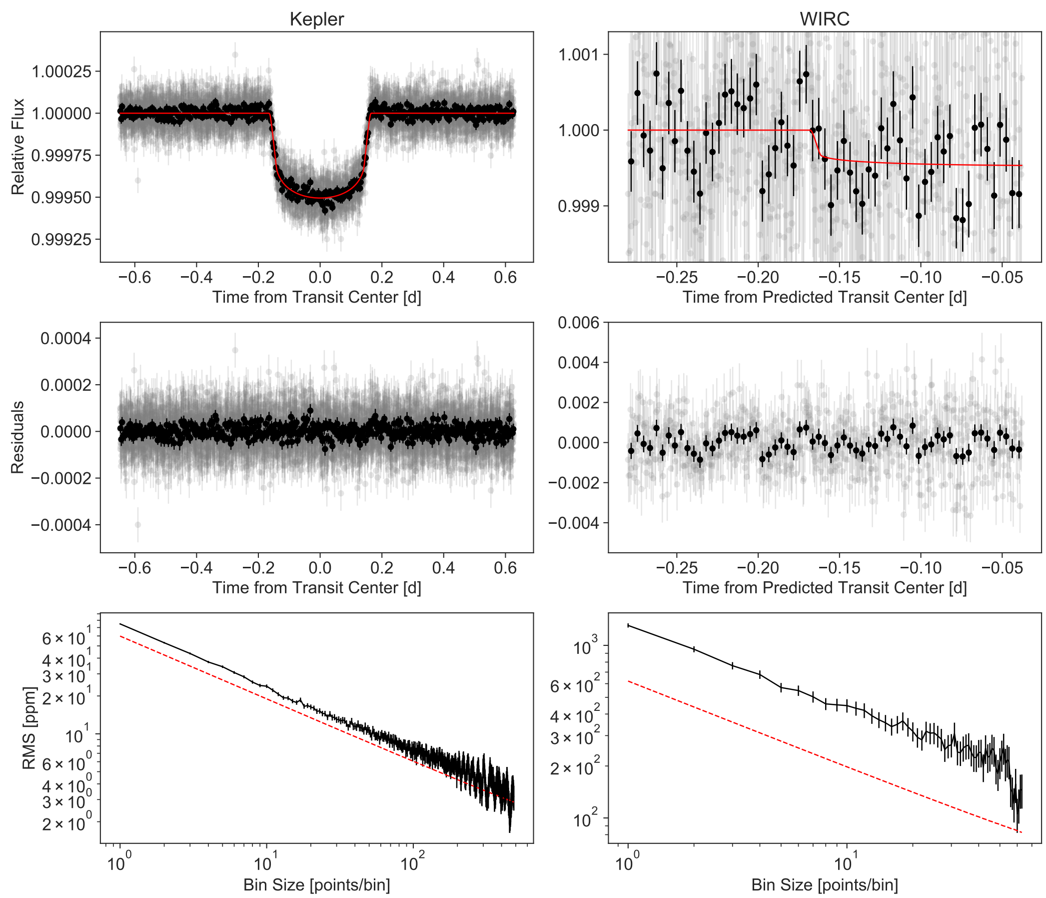

Figure 2.8: Same as Figure 2.7, but for Kepler-36c. The transit is detected at 5.3σ confidence in the WIRC data, and we constrain the transit timing offset to be -18^{+12}_{-5} minutes (from the predicted time in Table 2.1). For continuous data acquisition with WIRC, a bin size of 38 points is approximately equivalent to 10 minutes in the lower right plot.

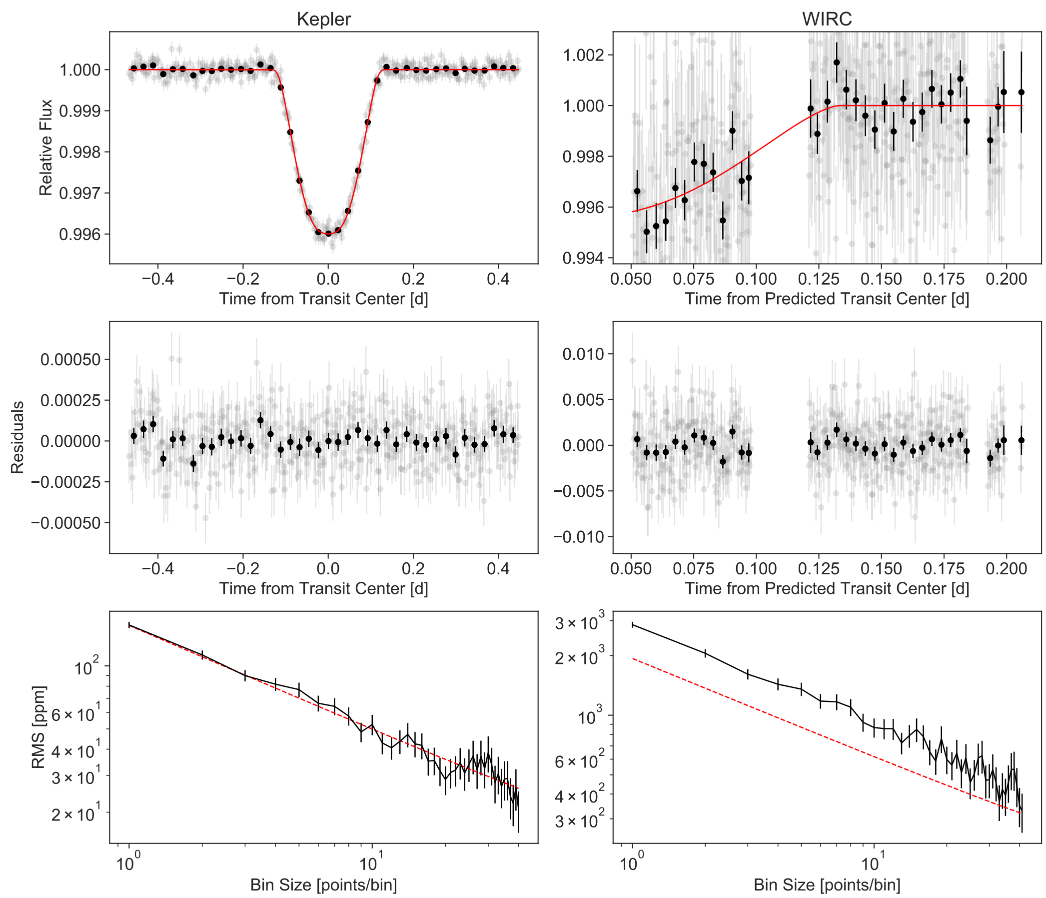

Figure 2.9: Same as Figure 2.7, but for KOI-1783.01. The transit is detected at 5.9σ confidence in the WIRC data, and we constrain the transit timing offset to be 16^{+10}_{-11} minutes (from the predicted time in Table 2.1). For continuous data acquisition with WIRC, a bin size of 30 points is equivalent to 10 minutes in the lower right plot (note however the breaks in data acquisition).

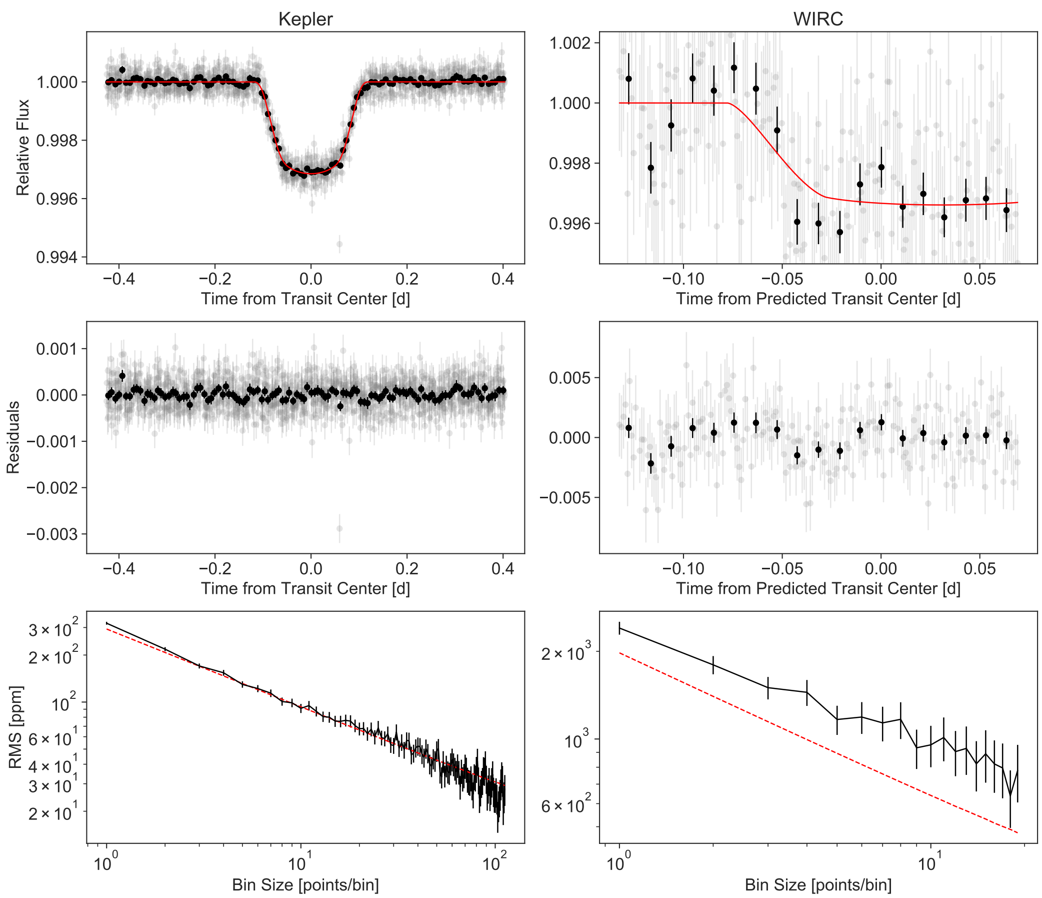

Figure 2.10: Same as Figure 2.7, but for Kepler-177c. The transit is detected at 5.5σ confidence in the WIRC data, and we constrain the transit timing offset to be 45^{+9}_{-7} minutes (from the predicted time in Table 2.1). For continuous data acquisition with WIRC, a bin size of 8 points is equivalent to 10 minutes in the lower right plot (note however the breaks in data acquisition in this observation).

2.8 Appendix B: Posterior Probability Distributions

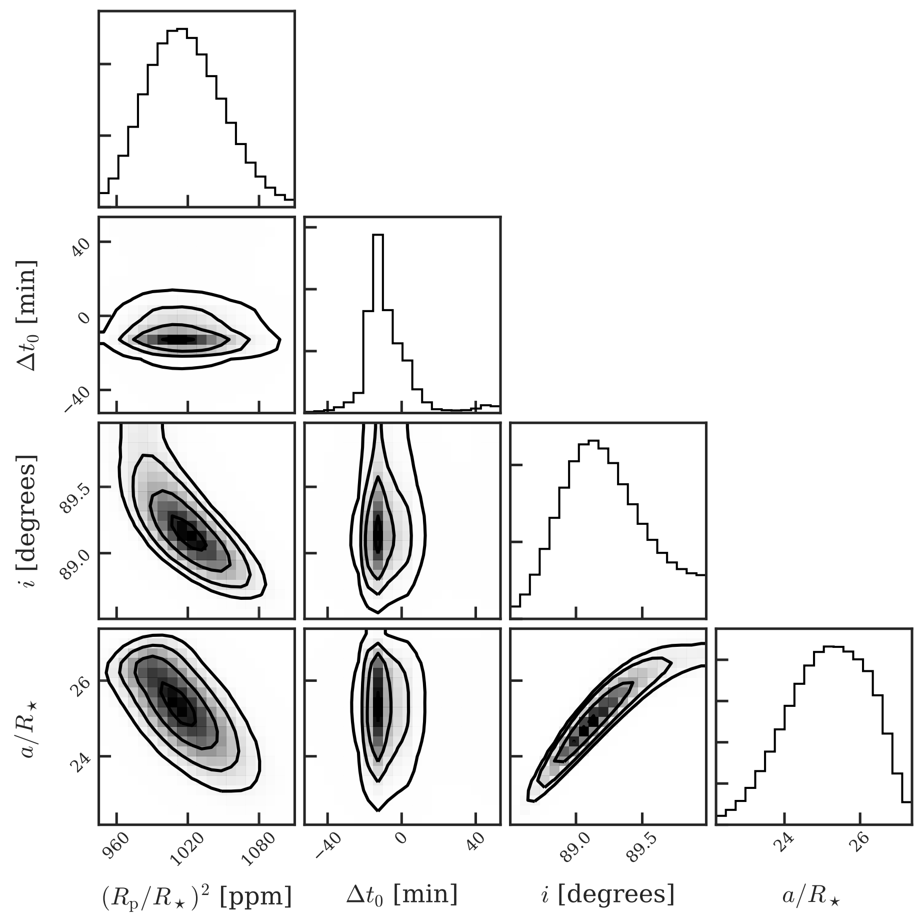

Figure 2.11: The posterior probability distributions for our fit to Kepler-29b. For ease of viewing, only the middle 99 percent of the samples are shown for each distribution, and the contours denote 1, 2, and 3σ boundaries.

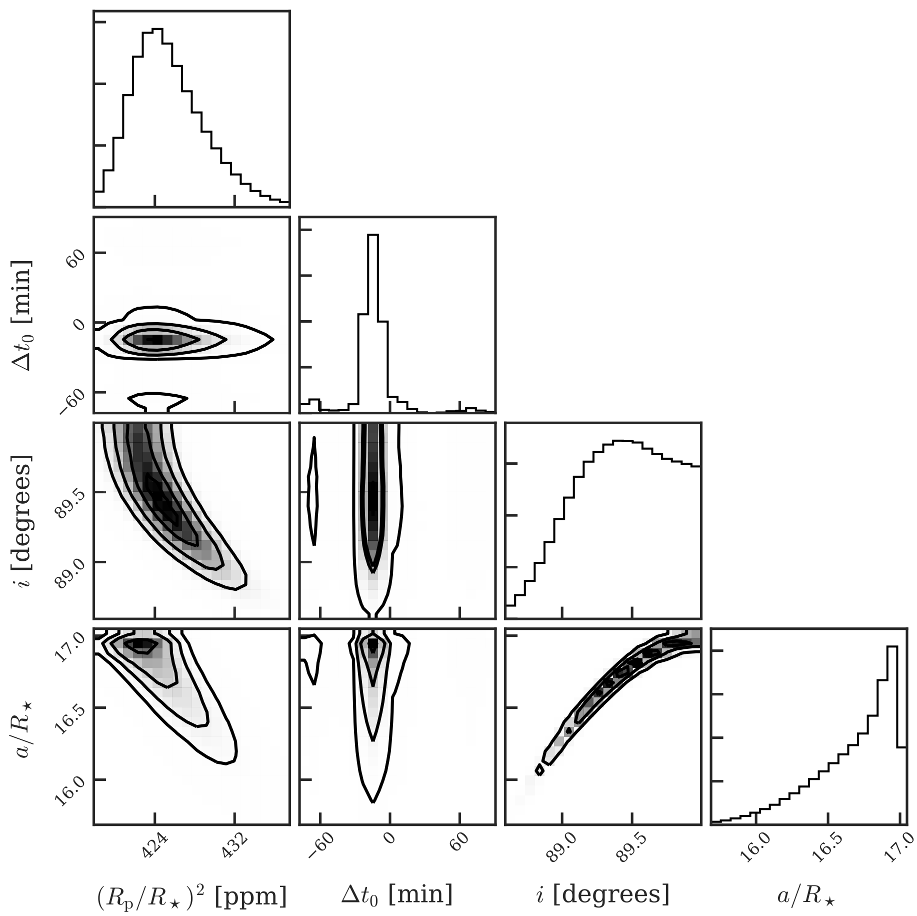

Figure 2.12: Same as Figure 2.11, but for Kepler-36c.

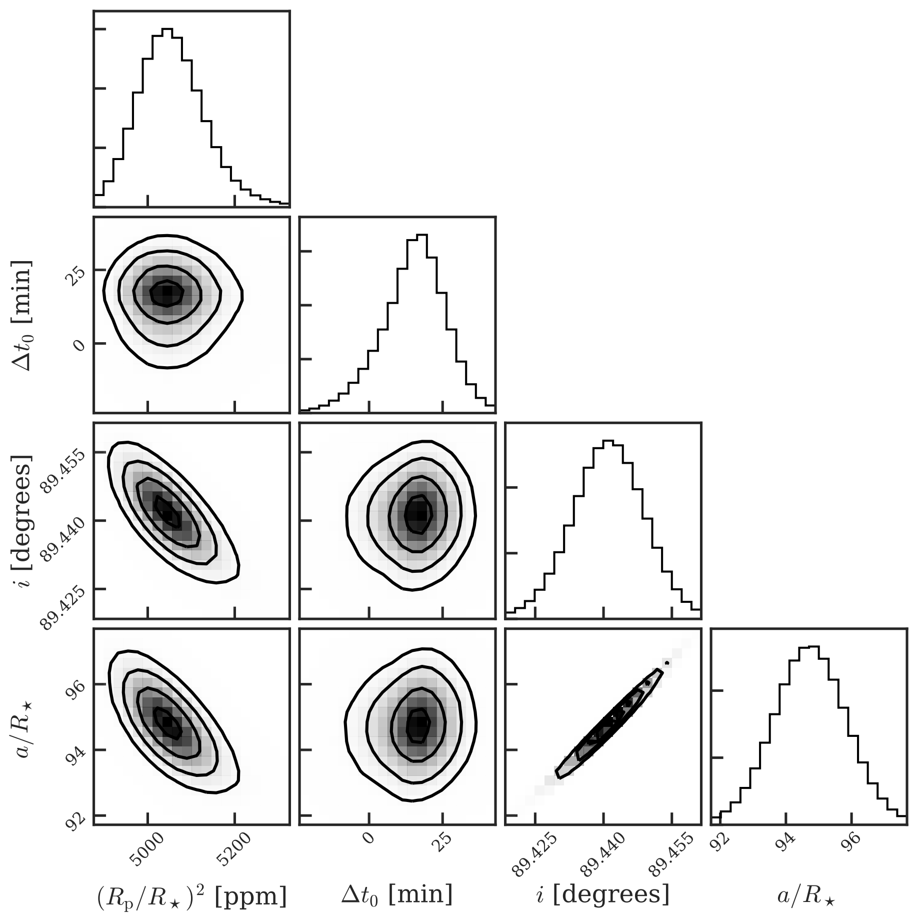

Figure 2.13: Same as Figure 2.11, but for KOI-1783.01.

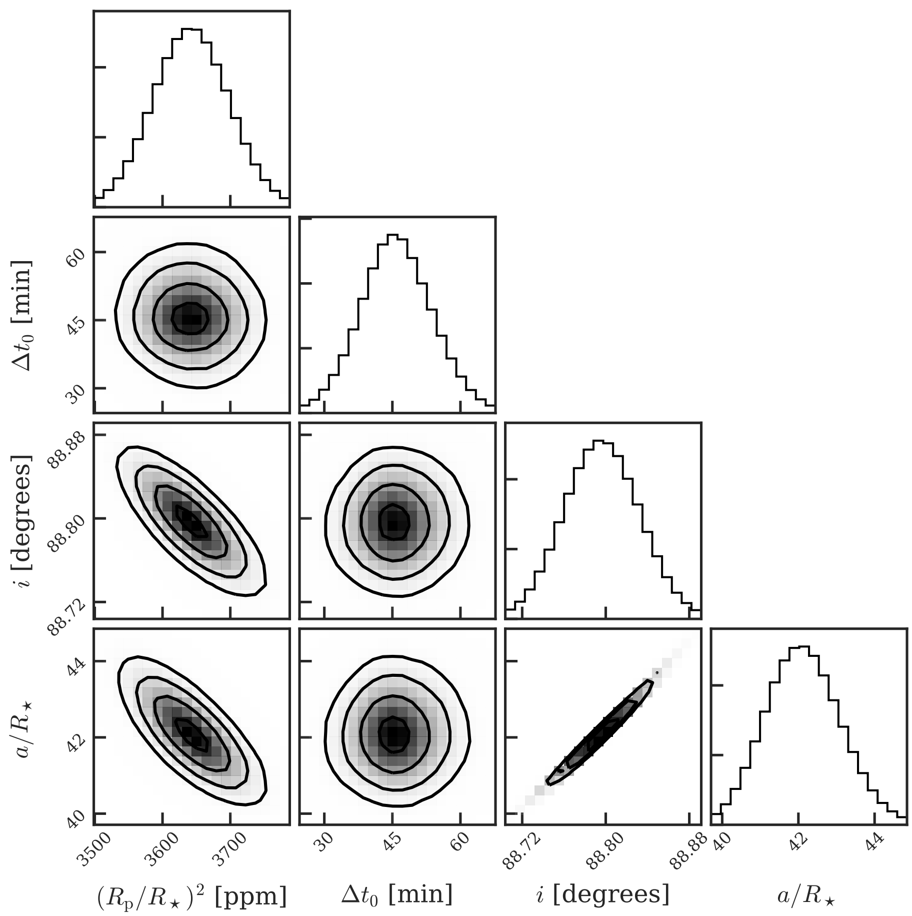

Figure 2.14: Same as Figure 2.11, but for Kepler-177c.

2.9 Appendix C: Dynamical Modeling Results

References

Agol, Eric and Daniel C. Fabrycky (2018). “Transit-Timing and Duration Variations for the Discovery and Characterization of Exoplanets”. In: *Handbook of Exoplanets*. Ed. by Hans J. Deeg and Juan Antonio Belmonte, 7, p. 7. DOI: 10.1007/978-3-319-55333-7_7.

Agol, Eric, Jason Steffen, et al. (May 2005). “On detecting terrestrial planets with timing of giant planet transits”. In: *MNRAS* 359.2, pp. 567–579. DOI: 10.1111/j.1365-2966.2005.08922.x.

Alexander, R. et al. (Jan. 2014). “The Dispersal of Protoplanetary Disks”. In: *Protostars and Planets VI*. Ed. by Henrik Beuther et al., p. 475. DOI: 10.2458/azu_uapress_9780816531240-ch021. arXiv: 1311.1819 [astro-ph.EP].

Almenara, J. M., R. F. Díaz, X. Bonfils, et al. (Oct. 2016). “Absolute densities, masses, and radii of the WASP-47 system determined dynamically”. In: *A&A* 595, L5, p. L5. DOI: 10.1051/0004-6361/201629770. arXiv: 1610.09533 [astro-ph.EP].

Almenara, J. M., R. F. Díaz, G. Hébrard, et al. (July 2018). “SOPHIE velocimetry of Kepler transit candidates. XVIII. Radial velocity confirmation, absolute masses and radii, and origin of the Kepler-419 multiplanetary system”. In: *A&A* 615, A90, A90. DOI: 10.1051/0004-6361/201732500. arXiv: 1804.01869 [astro-ph.EP].

Almenara, J. M., R. F. Díaz, R. Mardling, et al. (Nov. 2015). “Absolute masses and radii determination in multiplanetary systems without stellar models”. In: *MNRAS* 453.3, pp. 2644–2652. DOI: 10.1093/mnras/stv1735. arXiv: 1508.06596 [astro-ph.EP].

Asplund, Martin et al. (Sept. 2009). “The Chemical Composition of the Sun”. In: *ARA&A* 47.1, pp. 481–522. DOI: 10.1146/annurev.astro.46.060407.145222. arXiv: 0909.0948 [astro-ph.SR].

Astropy Collaboration, A. M. Price-Whelan, et al. (Sept. 2018). “The Astropy Project: Building an Open-science Project and Status of the v2.0 Core Package”. In: *AJ* 156.3, 123, p. 123. DOI: 10.3847/1538-3881/aabc4f. arXiv: 1801.02634 [astro-ph.IM].

Astropy Collaboration, Thomas P. Robitaille, et al. (Oct. 2013). “Astropy: A community Python package for astronomy”. In: *A&A* 558, A33, A33. DOI: 10.1051/0004-6361/201322068. arXiv: 1307.6212 [astro-ph.IM].

Batalha, Natalie M. et al. (Feb. 2013). “Planetary Candidates Observed by Kepler. III. Analysis of the First 16 Months of Data”. In: *ApJS* 204.2, 24, p. 24. DOI: 10.1088/0067-0049/204/2/24. arXiv: 1202.5852 [astro-ph.EP].

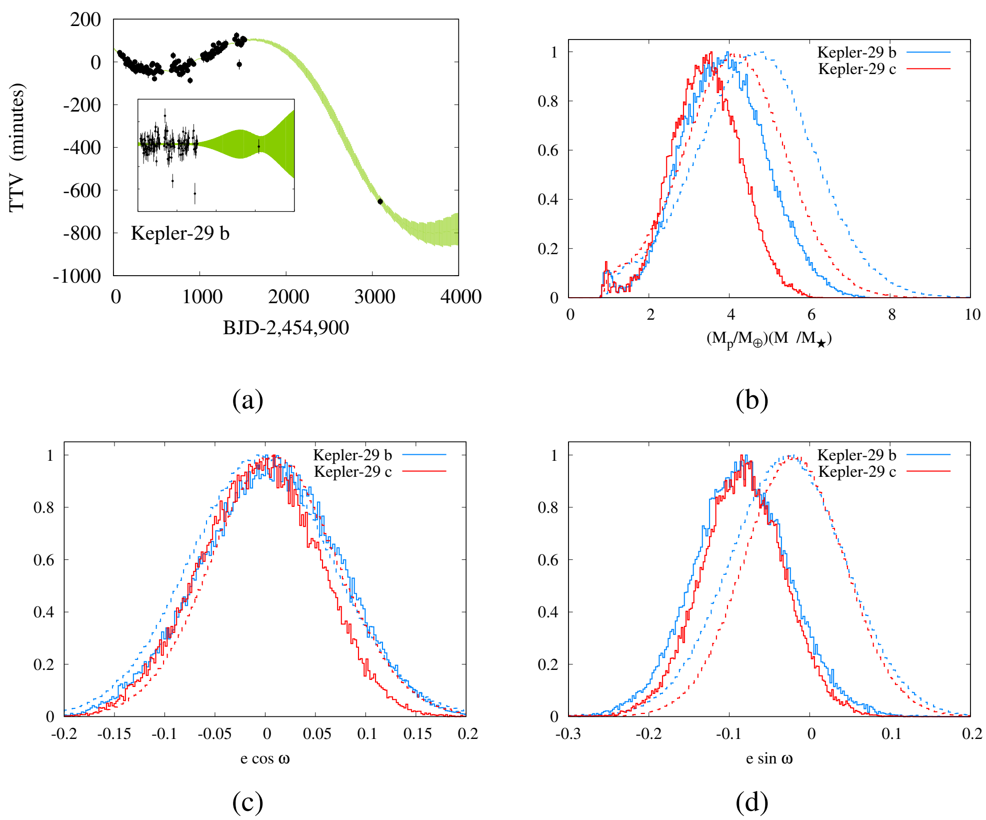

Figure 2.15: Updated dynamical modeling of the Kepler-29 system based on fits to *Kepler* and WIRC transit times. (a) The measured transit timing variations (i.e., deviations from a constant ephemeris using the period derived from our TTV modeling) for Kepler-29b from the *Kepler* and WIRC transit observations (black filled circles); we also overplot the 1σ range in predicted TTVs for each epoch from the updated dynamical model in green. We include an inset of the residuals from the best fit TTV model to show how our new measurement compares to the *Kepler* uncertainties. (b) The dynamical mass posteriors for both planets in the system. (c and d) The posteriors on both components of the eccentricity vectors. Posteriors from TTV modeling of the *Kepler* data are shown as dashed lines, and those from joint modeling of the *Kepler* and WIRC data are shown as solid lines.

Beichman, Charles et al. (May 2016). "Spitzer Observations of Exoplanets Discovered with the Kepler K2 Mission". In: *ApJ* 822.1, 39, p. 39. doi: 10.3847/0004-637X/822/1/39. arXiv: 1603.01934 [astro-ph.EP].

Benneke, Bjoern and Sara Seager (July 2012). "Atmospheric Retrieval for Super-Earths: Uniquely Constraining the Atmospheric Composition with Transmission Spectroscopy". In: *ApJ* 753.2, 100, p. 100. doi: 10.1088/0004-637X/753/2/100. arXiv: 1203.4018 [astro-ph.EP].

Benneke, Björn et al. (Jan. 2017). "Spitzer Observations Confirm and Rescue the Habitable-zone Super-Earth K2-18b for Future Characterization". In: *ApJ* 834.2, 187, p. 187. doi: 10.3847/1538-4357/834/2/187. arXiv: 1610.07249 [astro-ph.EP].

Boch, T. and P. Fernique (May 2014). "Aladin Lite: Embed your Sky in the Browser". In: *Astronomical Data Analysis Software and Systems XXIII*. Ed. by N. Manset and P. Forshay. Vol. 485. Astronomical Society of the Pacific Conference Series, p. 277.

Bonnarel, F. et al. (Apr. 2000). "The ALADIN interactive sky atlas. A reference tool for identification of astronomical sources". In: *A&AS* 143, pp. 33–40. doi: 10.1051/aas:2000331.

Borucki, William J. et al. (Feb. 2010). "Kepler Planet-Detection Mission: Introduction and First Results". In: *Science* 327.5968, p. 977. doi: 10.1126/science.1185402.

Bradley, Larry et al. (Sept. 2016). *Photutils: Photometry tools*. ascl: 1609.011.

Cabrera, J. et al. (Oct. 2017). "Disproving the validated planets K2-78b, K2-82b, and K2-92b. The importance of independently confirming planetary candidates". In: *A&A* 606, A75, A75. doi: 10.1051/0004-6361/201731233. arXiv: 1707.08007 [astro-ph.IM].

Carter, Joshua A., Eric Agol, et al. (Aug. 2012). "Kepler-36: A Pair of Planets with Neighboring Orbits and Dissimilar Densities". In: *Science* 337.6094, p. 556. doi: 10.1126/science.1223269. arXiv: 1206.4718 [astro-ph.EP].

Carter, Joshua A. and Joshua N. Winn (Oct. 2009). "Parameter Estimation from Time-series Data with Correlated Errors: A Wavelet-based Method and its Application to Transit Light Curves". In: *ApJ* 704.1, pp. 51–67. doi: 10.1088/0004-637X/704/1/51. arXiv: 0909.0747 [astro-ph.EP].

Christ, Callista N., Benjamin T. Montet, and Daniel C. Fabrycky (June 2019). "Observations of the Kepler Field with TESS: Predictions for Planet Yield and Observable Features". In: *AJ* 157.6, 235, p. 235. doi: 10.3847/1538-3881/ab1aae. arXiv: 1810.02826 [astro-ph.EP].

Claret, A. and S. Bloemen (May 2011). "Gravity and limb-darkening coefficients for the Kepler, CoRoT, Spitzer, uvby, UBVRIJHK, and Sloan photometric systems". In: *A&A* 529, A75, A75. doi: 10.1051/0004-6361/201116451.

Cochran, William D. et al. (Nov. 2011). "Kepler-18b, c, and d: A System of Three Planets Confirmed by Transit Timing Variations, Light Curve Validation, Warm-Spitzer Photometry, and Radial Velocity Measurements". In: *ApJS* 197.1, 7, p. 7. DOI: 10.1088/0067-0049/197/1/7. arXiv: 1110.0820 [astro-ph.EP].

Croll, Bryce et al. (Mar. 2015). "Near-infrared Thermal Emission Detections of a Number of Hot Jupiters and the Systematics of Ground-based Near-infrared Photometry". In: *ApJ* 802.1, 28, p. 28. DOI: 10.1088/0004-637X/802/1/28. arXiv: 1410.4286 [astro-ph.EP].

Crossfield, Ian J. M. et al. (Sept. 2016). "197 Candidates and 104 Validated Planets in K2's First Five Fields". In: *ApJS* 226.1, 7, p. 7. DOI: 10.3847/0067-0049/226/1/7. arXiv: 1607.05263 [astro-ph.EP].

Cutri, R. M. et al. (June 2003). "VizieR Online Data Catalog: 2MASS All-Sky Catalog of Point Sources (Cutri+ 2003)". In: *VizieR Online Data Catalog*, II/246, pp. II/246.

Delrez, L. et al. (Apr. 2018). "Early 2017 observations of TRAPPIST-1 with Spitzer". In: *MNRAS* 475.3, pp. 3577–3597. DOI: 10.1093/mnras/sty051. arXiv: 1801.02554 [astro-ph.EP].

Diamond-Lowe, Hannah et al. (Aug. 2018). "Ground-based Optical Transmission Spectroscopy of the Small, Rocky Exoplanet GJ 1132b". In: *AJ* 156.2, 42, p. 42. DOI: 10.3847/1538-3881/aac6dd. arXiv: 1805.07328 [astro-ph.EP].

Dressing, Courtney D. et al. (Aug. 2018). "Characterizing K2 Candidate Planetary Systems Orbiting Low-mass Stars. III. A High Mass and Low Envelope Fraction for the Warm Neptune K2-55b". In: *AJ* 156.2, 70, p. 70. DOI: 10.3847/1538-3881/aacf99. arXiv: 1804.05148 [astro-ph.EP].

Eastman, Jason, Robert Siverd, and B. Scott Gaudi (Aug. 2010). "Achieving Better Than 1 Minute Accuracy in the Heliocentric and Barycentric Julian Dates". In: *PASP* 122.894, p. 935. DOI: 10.1086/655938. arXiv: 1005.4415 [astro-ph.IM].

Fabrycky, Daniel C., Eric B. Ford, et al. (May 2012). "Transit Timing Observations from Kepler. IV. Confirmation of Four Multiple-planet Systems by Simple Physical Models". In: *ApJ* 750.2, 114, p. 114. DOI: 10.1088/0004-637X/750/2/114. arXiv: 1201.5415 [astro-ph.EP].

Fabrycky, Daniel C., Jack J. Lissauer, et al. (Aug. 2014). "Architecture of Kepler's Multi-transiting Systems. II. New Investigations with Twice as Many Candidates". In: *ApJ* 790.2, 146, p. 146. DOI: 10.1088/0004-637X/790/2/146. arXiv: 1202.6328 [astro-ph.EP].

Ford, Eric B. et al. (Sept. 2012). "Transit Timing Observations from Kepler. V. Transit Timing Variation Candidates in the First Sixteen Months from Polynomial Models". In: *ApJ* 756.2, 185, p. 185. DOI: 10.1088/0004-637X/756/2/185. arXiv: 1201.1892 [astro-ph.EP].

Foreman-Mackey, Daniel et al. (Mar. 2013). "emcee: The MCMC Hammer". In: *PASP* 125.925, p. 306. DOI: 10.1086/670067. arXiv: 1202.3665 [astro-ph.IM].

Fortney, J. J., M. S. Marley, and J. W. Barnes (Apr. 2007). "Planetary Radii across Five Orders of Magnitude in Mass and Stellar Insolation: Application to Transits". In: *ApJ* 659.2, pp. 1661–1672. DOI: 10.1086/512120. arXiv: astro-ph/0612671 [astro-ph].

Freudenthal, J. et al. (Oct. 2018). "Kepler Object of Interest Network. II. Photodynamical modelling of Kepler-9 over 8 years of transit observations". In: *A&A* 618, A41, A41. DOI: 10.1051/0004-6361/201833436. arXiv: 1807.00007 [astro-ph.EP].

Fulton, Benjamin J. and Erik A. Petigura (Dec. 2018). "The California-Kepler Survey. VII. Precise Planet Radii Leveraging Gaia DR2 Reveal the Stellar Mass Dependence of the Planet Radius Gap". In: *AJ* 156.6, 264, p. 264. DOI: 10.3847/1538-3881/aae828. arXiv: 1805.01453 [astro-ph.EP].

Fulton, Benjamin J., Erik A. Petigura, et al. (Sept. 2017). "The California-Kepler Survey. III. A Gap in the Radius Distribution of Small Planets". In: *AJ* 154.3, 109, p. 109. DOI: 10.3847/1538-3881/aa80eb. arXiv: 1703.10375 [astro-ph.EP].

Furlan, E. et al. (Feb. 2017). "The Kepler Follow-up Observation Program. I. A Catalog of Companions to Kepler Stars from High-Resolution Imaging". In: *AJ* 153.2, 71, p. 71. DOI: 10.3847/1538-3881/153/2/71. arXiv: 1612.02392 [astro-ph.SR].

Ginzburg, Sivan, Hilke E. Schlichting, and Re'em Sari (July 2016). "Super-Earth Atmospheres: Self-consistent Gas Accretion and Retention". In: *ApJ* 825.1, 29, p. 29. DOI: 10.3847/0004-637X/825/1/29. arXiv: 1512.07925 [astro-ph.EP].

Goldberg, Max et al. (Apr. 2019). "Prospects for Refining Kepler TTV Masses Using TESS Observations". In: *AJ* 157.4, 142, p. 142. DOI: 10.3847/1538-3881/ab06c9. arXiv: 1810.02852 [astro-ph.EP].

Hadden, Sam and Yoram Lithwick (May 2014). "Densities and Eccentricities of 139 Kepler Planets from Transit Time Variations". In: *ApJ* 787.1, 80, p. 80. DOI: 10.1088/0004-637X/787/1/80. arXiv: 1310.7942 [astro-ph.EP].

– (July 2017). "Kepler Planet Masses and Eccentricities from TTV Analysis". In: *AJ* 154.1, 5, p. 5. DOI: 10.3847/1538-3881/aa71ef. arXiv: 1611.03516 [astro-ph.EP].

Holczer, Tomer et al. (July 2016). "Transit Timing Observations from Kepler. IX. Catalog of the Full Long-cadence Data Set". In: *ApJS* 225.1, 9, p. 9. DOI: 10.3847/0067-0049/225/1/9. arXiv: 1606.01744 [astro-ph.EP].

Holman, Matthew J. and Norman W. Murray (Feb. 2005). "The Use of Transit Timing to Detect Terrestrial-Mass Extrasolar Planets". In: *Science* 307.5713, pp. 1288–1291. DOI: 10.1126/science.1107822. arXiv: astro-ph/0412028 [astro-ph].

Ikoma, M. and Y. Hori (July 2012). “In Situ Accretion of Hydrogen-rich Atmospheres on Short-period Super-Earths: Implications for the Kepler-11 Planets”. In: *ApJ* 753.1, 66, p. 66. doi: 10.1088/0004-637X/753/1/66. arXiv: 1204.5302 [astro-ph.EP].

Jontof-Hutter, Daniel (May 2019). “The Compositional Diversity of Low-Mass Exoplanets”. In: *Annual Review of Earth and Planetary Sciences* 47, pp. 141–171. doi: 10.1146/annurev-earth-053018-060352. arXiv: 1911.04598 [astro-ph.EP].

Jontof-Hutter, Daniel, Eric B. Ford, et al. (Mar. 2016). “Secure Mass Measurements from Transit Timing: 10 Kepler Exoplanets between 3 and 8 $M_\oplus$ with Diverse Densities and Incident Fluxes”. In: *ApJ* 820.1, 39, p. 39. doi: 10.3847/0004-637X/820/1/39. arXiv: 1512.02003 [astro-ph.EP].

Jontof-Hutter, Daniel, Jack J. Lissauer, et al. (Apr. 2014). “Kepler-79’s Low Density Planets”. In: *ApJ* 785.1, 15, p. 15. doi: 10.1088/0004-637X/785/1/15. arXiv: 1310.2642 [astro-ph.EP].

Jontof-Hutter, Daniel, Jason F. Rowe, et al. (June 2015). “The mass of the Mars-sized exoplanet Kepler-138 b from transit timing”. In: *Nature* 522.7556, pp. 321–323. doi: 10.1038/nature14494. arXiv: 1506.07067 [astro-ph.EP].

Kipping, D. M. et al. (Nov. 2015). “The Hunt for Exomoons with Kepler (HEK): V. A Survey of 41 Planetary Candidates for Exomoons”. In: *ApJ* 813.1, 14, p. 14. doi: 10.1088/0004-637X/813/1/14. arXiv: 1503.05555 [astro-ph.EP].

Kreidberg, Laura (Nov. 2015). “batman: BAsic Transit Model cAlculatioN in Python”. In: *PASP* 127.957, p. 1161. doi: 10.1086/683602. arXiv: 1507.08285 [astro-ph.EP].

Laughlin, Gregory, Matteo Crismani, and Fred C. Adams (Mar. 2011). “On the Anomalous Radii of the Transiting Extrasolar Planets”. In: *ApJL* 729.1, L7, p. L7. doi: 10.1088/2041-8205/729/1/L7. arXiv: 1101.5827 [astro-ph.EP].

Law, Nicholas M. et al. (Aug. 2014). “Robotic Laser Adaptive Optics Imaging of 715 Kepler Exoplanet Candidates Using Robo-AO”. In: *ApJ* 791.1, 35, p. 35. doi: 10.1088/0004-637X/791/1/35. arXiv: 1312.4958 [astro-ph.EP].

Lee, Eve J. (June 2019). “The Boundary between Gas-rich and Gas-poor Planets”. In: *ApJ* 878.1, 36, p. 36. doi: 10.3847/1538-4357/ab1b40. arXiv: 1904.10470 [astro-ph.EP].

Lee, Eve J. and Eugene Chiang (Sept. 2015). “To Cool is to Accrete: Analytic Scalings for Nebular Accretion of Planetary Atmospheres”. In: *ApJ* 811.1, 41, p. 41. doi: 10.1088/0004-637X/811/1/41. arXiv: 1508.05096 [astro-ph.EP].

– (Feb. 2016). “Breeding Super-Earths and Birthing Super-puffs in Transitional Disks”. In: *ApJ* 817.2, 90, p. 90. doi: 10.3847/0004-637X/817/2/90. arXiv: 1510.08855 [astro-ph.EP].

Lee, Eve J., Eugene Chiang, and Chris W. Ormel (Dec. 2014). "Make Super-Earths, Not Jupiters: Accreting Nebular Gas onto Solid Cores at 0.1 AU and Beyond". In: *ApJ* 797.2, 95, p. 95. DOI: 10.1088/0004-637X/797/2/95. arXiv: 1409.3578 [astro-ph.EP].

Line, Michael R., Heather Knutson, et al. (Mar. 2014). "A Systematic Retrieval Analysis of Secondary Eclipse Spectra. II. A Uniform Analysis of Nine Planets and their C to O Ratios". In: *ApJ* 783.2, 70, p. 70. DOI: 10.1088/0004-637X/783/2/70. arXiv: 1309.6663 [astro-ph.EP].

Line, Michael R., Aaron S. Wolf, et al. (Oct. 2013). "A Systematic Retrieval Analysis of Secondary Eclipse Spectra. I. A Comparison of Atmospheric Retrieval Techniques". In: *ApJ* 775.2, 137, p. 137. DOI: 10.1088/0004-637X/775/2/137. arXiv: 1304.5561 [astro-ph.EP].

Line, Michael R., Xi Zhang, et al. (Apr. 2012). "Information Content of Exoplanetary Transit Spectra: An Initial Look". In: *ApJ* 749.1, 93, p. 93. DOI: 10.1088/0004-637X/749/1/93. arXiv: 1111.2612 [astro-ph.EP].

Lintott, Chris J. et al. (June 2013). "Planet Hunters: New Kepler Planet Candidates from Analysis of Quarter 2". In: *AJ* 145.6, 151, p. 151. DOI: 10.1088/0004-6256/145/6/151. arXiv: 1202.6007 [astro-ph.EP].

Lissauer, Jack J., Geoffrey W. Marcy, Stephen T. Bryson, et al. (Mar. 2014). "Validation of Kepler's Multiple Planet Candidates. II. Refined Statistical Framework and Descriptions of Systems of Special Interest". In: *ApJ* 784.1, 44, p. 44. DOI: 10.1088/0004-637X/784/1/44. arXiv: 1402.6352 [astro-ph.EP].

Lissauer, Jack J., Geoffrey W. Marcy, Jason F. Rowe, et al. (May 2012). "Almost All of Kepler's Multiple-planet Candidates Are Planets". In: *ApJ* 750.2, 112, p. 112. DOI: 10.1088/0004-637X/750/2/112. arXiv: 1201.5424 [astro-ph.EP].

Lissauer, Jack J., Darin Ragozzine, et al. (Nov. 2011). "Architecture and Dynamics of Kepler's Candidate Multiple Transiting Planet Systems". In: *ApJS* 197.1, 8, p. 8. DOI: 10.1088/0067-0049/197/1/8. arXiv: 1102.0543 [astro-ph.EP].

Lithwick, Yoram, Jiwei Xie, and Yanqin Wu (Dec. 2012). "Extracting Planet Mass and Eccentricity from TTV Data". In: *ApJ* 761.2, 122, p. 122. DOI: 10.1088/0004-637X/761/2/122. arXiv: 1207.4192 [astro-ph.EP].

Livingston, John H., Ian J. M. Crossfield, et al. (Dec. 2018). "Sixty Validated Planets from K2 Campaigns 5-8". In: *AJ* 156.6, 277, p. 277. DOI: 10.3847/1538-3881/aae778. arXiv: 1810.04074 [astro-ph.EP].

Livingston, John H., Michael Endl, et al. (Aug. 2018). "44 Validated Planets from K2 Campaign 10". In: *AJ* 156.2, 78, p. 78. DOI: 10.3847/1538-3881/aaccde. arXiv: 1806.11504 [astro-ph.EP].

Lopez, Eric D. and Jonathan J. Fortney (Oct. 2013). "The Role of Core Mass in Controlling Evaporation: The Kepler Radius Distribution and the Kepler-36 Density Dichotomy". In: *ApJ* 776.1, 2, p. 2. DOI: 10.1088/0004-637X/776/1/2. arXiv: 1305.0269 [astro-ph.EP].

– (Sept. 2014). "Understanding the Mass-Radius Relation for Sub-neptunes: Radius as a Proxy for Composition". In: *ApJ* 792.1, 1, p. 1. DOI: 10.1088/0004-637X/792/1/1. arXiv: 1311.0329 [astro-ph.EP].

Masuda, Kento (Mar. 2014). "Very Low Density Planets around Kepler-51 Revealed with Transit Timing Variations and an Anomaly Similar to a Planet-Planet Eclipse Event". In: *ApJ* 783.1, 53, p. 53. DOI: 10.1088/0004-637X/783/1/53. arXiv: 1401.2885 [astro-ph.EP].

Mayo, Andrew W. et al. (Mar. 2018). "275 Candidates and 149 Validated Planets Orbiting Bright Stars in K2 Campaigns 0-10". In: *AJ* 155.3, 136, p. 136. DOI: 10.3847/1538-3881/aaadff. arXiv: 1802.05277 [astro-ph.EP].

Mazeh, T., T. Holczer, and S. Faigler (May 2016). "Dearth of short-period Neptunian exoplanets: A desert in period-mass and period-radius planes". In: *A&A* 589, A75, A75. DOI: 10.1051/0004-6361/201528065. arXiv: 1602.07843 [astro-ph.EP].

Mazeh, Tsevi et al. (Oct. 2013). "Transit Timing Observations from Kepler. VIII. Catalog of Transit Timing Measurements of the First Twelve Quarters". In: *ApJS* 208.2, 16, p. 16. DOI: 10.1088/0067-0049/208/2/16. arXiv: 1301.5499 [astro-ph.EP].

Metchev, Stanimir A. et al. (Feb. 2015). "Weather on Other Worlds. II. Survey Results: Spots are Ubiquitous on L and T Dwarfs". In: *ApJ* 799.2, 154, p. 154. DOI: 10.1088/0004-637X/799/2/154. arXiv: 1411.3051 [astro-ph.SR].

Migaszewski, Cezary, Krzysztof Goździewski, and Federico Panichi (Feb. 2017). "The origin and 9:7 MMR dynamics of the Kepler-29 system". In: *MNRAS* 465.2, pp. 2366–2380. DOI: 10.1093/mnras/stw2866. arXiv: 1609.09135 [astro-ph.EP].

Millholland, Sarah (Nov. 2019). "Tidally Induced Radius Inflation of Sub-Neptunes". In: *ApJ* 886.1, 72, p. 72. DOI: 10.3847/1538-4357/ab4c3f. arXiv: 1910.06794 [astro-ph.EP].

Millholland, Sarah, Songhu Wang, and Gregory Laughlin (Nov. 2017). "Kepler Multi-planet Systems Exhibit Unexpected Intra-system Uniformity in Mass and Radius". In: *ApJL* 849.2, L33, p. L33. DOI: 10.3847/2041-8213/aa9714. arXiv: 1710.11152 [astro-ph.EP].

Mills, Sean M., Daniel C. Fabrycky, et al. (May 2016). "A resonant chain of four transiting, sub-Neptune planets". In: *Nature* 533.7604, pp. 509–512. DOI: 10.1038/nature17445. arXiv: 1612.07376 [astro-ph.EP].

Mills, Sean M. and Tsevi Mazeh (Apr. 2017). "The Planetary Mass-Radius Relation and Its Dependence on Orbital Period as Measured by Transit Timing Variations and Radial Velocities". In: *ApJL* 839.1, L8, p. L8. doi: 10.3847/2041-8213/aa67eb. arXiv: 1703.07790 [astro-ph.EP].

Morton, Timothy D. (Dec. 2012). "An Efficient Automated Validation Procedure for Exoplanet Transit Candidates". In: *ApJ* 761.1, 6, p. 6. doi: 10.1088/0004-637X/761/1/6. arXiv: 1206.1568 [astro-ph.EP].

– (Mar. 2015). *VESPA: False positive probabilities calculator*. ascl: 1503.011.

Morton, Timothy D. et al. (May 2016). "False Positive Probabilities for all Kepler Objects of Interest: 1284 Newly Validated Planets and 428 Likely False Positives". In: *ApJ* 822.2, 86, p. 86. doi: 10.3847/0004-637X/822/2/86. arXiv: 1605.02825 [astro-ph.EP].

Nelson, Benjamin, Eric B. Ford, and Matthew J. Payne (Jan. 2014). "RUN DMC: An Efficient, Parallel Code for Analyzing Radial Velocity Observations Using N-body Integrations and Differential Evolution Markov Chain Monte Carlo". In: *ApJS* 210.1, 11, p. 11. doi: 10.1088/0067-0049/210/1/11. arXiv: 1311.5229 [astro-ph.EP].

Nesvorný, David, David Kipping, et al. (Nov. 2013). "KOI-142, The King of Transit Variations, is a Pair of Planets near the 2:1 Resonance". In: *ApJ* 777.1, 3, p. 3. doi: 10.1088/0004-637X/777/1/3. arXiv: 1304.4283 [astro-ph.EP].

Nesvorný, David and David Vokrouhlický (July 2014). "The Effect of Conjunctions on the Transit Timing Variations of Exoplanets". In: *ApJ* 790.1, 58, p. 58. doi: 10.1088/0004-637X/790/1/58. arXiv: 1405.7433 [astro-ph.EP].

Ofir, Aviv, Stefan Dreizler, et al. (Jan. 2014). "An independent planet search in the Kepler dataset. II. An extremely low-density super-Earth mass planet around Kepler-87". In: *A&A* 561, A103, A103. doi: 10.1051/0004-6361/201220935. arXiv: 1310.2064 [astro-ph.EP].

Ofir, Aviv, Ji-Wei Xie, et al. (Jan. 2018). "A Spectral Approach to Transit Timing Variations". In: *ApJS* 234.1, 9, p. 9. doi: 10.3847/1538-4365/aa9f2b. arXiv: 1710.10930 [astro-ph.EP].

Owen, James E. (May 2019). "Atmospheric Escape and the Evolution of Close-In Exoplanets". In: *Annual Review of Earth and Planetary Sciences* 47, pp. 67–90. doi: 10.1146/annurev-earth-053018-060246. arXiv: 1807.07609 [astro-ph.EP].

Owen, James E. and Yanqin Wu (Oct. 2013). "Kepler Planets: A Tale of Evaporation". In: *ApJ* 775.2, 105, p. 105. doi: 10.1088/0004-637X/775/2/105. arXiv: 1303.3899 [astro-ph.EP].

– (Sept. 2017). "The Evaporation Valley in the Kepler Planets". In: *ApJ* 847.1, 29, p. 29. doi: 10.3847/1538-4357/aa890a. arXiv: 1705.10810 [astro-ph.EP].

Petigura, Erik A., Björn Benneke, et al. (Sept. 2018). "Dynamics and Formation of the Near-resonant K2-24 System: Insights from Transit-timing Variations and Radial Velocities". In: *AJ* 156.3, 89, p. 89. DOI: 10.3847/1538-3881/aaceac. arXiv: 1806.08959 [astro-ph.EP].

Petigura, Erik A., Andrew W. Howard, et al. (Sept. 2017). "The California-Kepler Survey. I. High-resolution Spectroscopy of 1305 Stars Hosting Kepler Transiting Planets". In: *AJ* 154.3, 107, p. 107. DOI: 10.3847/1538-3881/aa80de. arXiv: 1703.10400 [astro-ph.EP].

Petigura, Erik A., Evan Sinukoff, et al. (Apr. 2017). "Four Sub-Saturns with Dissimilar Densities: Windows into Planetary Cores and Envelopes". In: *AJ* 153.4, 142, p. 142. DOI: 10.3847/1538-3881/aa5ea5. arXiv: 1702.00013 [astro-ph.EP].

Pu, Bonan and Diana Valencia (Sept. 2017). "Ohmic Dissipation in Mini-Neptunes". In: *ApJ* 846.1, 47, p. 47. DOI: 10.3847/1538-4357/aa826f. arXiv: 1709.01642 [astro-ph.EP].

Radigan, Jacqueline (Dec. 2014). "An Independent Analysis of the Brown Dwarf Atmosphere Monitoring (BAM) Data: Large-amplitude Variability is Rare Outside the L/T Transition". In: *ApJ* 797.2, 120, p. 120. DOI: 10.1088/0004-637X/797/2/120. arXiv: 1408.5919 [astro-ph.SR].

Ricker, George R. et al. (Jan. 2015). "Transiting Exoplanet Survey Satellite (TESS)". In: *Journal of Astronomical Telescopes, Instruments, and Systems* 1, 014003, p. 014003. DOI: 10.1117/1.JATIS.1.1.014003.

Rowe, Jason F., Stephen T. Bryson, et al. (Mar. 2014). "Validation of Kepler's Multiple Planet Candidates. III. Light Curve Analysis and Announcement of Hundreds of New Multi-planet Systems". In: *ApJ* 784.1, 45, p. 45. DOI: 10.1088/0004-637X/784/1/45. arXiv: 1402.6534 [astro-ph.EP].

Rowe, Jason F. and Susan E. Thompson (Apr. 2015). "Uniform Modeling of KOIs: MCMC Data Release Notes". In: *arXiv e-prints*, arXiv:1504.00707, arXiv:1504.00707. arXiv: 1504.00707 [astro-ph.EP].

Santerne, A. et al. (Mar. 2016). "SOPHIE velocimetry of Kepler transit candidates. XVII. The physical properties of giant exoplanets within 400 days of period". In: *A&A* 587, A64, A64. DOI: 10.1051/0004-6361/201527329. arXiv: 1511.00643 [astro-ph.EP].

Schlichting, Hilke E. (2018). "Formation of Super-Earths". In: *Handbook of Exoplanets*. Ed. by Hans J. Deeg and Juan Antonio Belmonte, 141, p. 141. DOI: 10.1007/978-3-319-55333-7_141.

Shporer, Avi et al. (Oct. 2017). "Three Statistically Validated K2 Transiting Warm Jupiter Exoplanets Confirmed as Low-mass Stars". In: *ApJL* 847.2, L18, p. L18. DOI: 10.3847/2041-8213/aa8bff. arXiv: 1708.08455 [astro-ph.SR].

Sing, D. K. (Feb. 2010). “Stellar limb-darkening coefficients for CoRot and Kepler”. In: *A&A* 510, A21, A21. DOI: 10.1051/0004-6361/200913675. arXiv: 0912.2274 [astro-ph.EP].

Stefansson, Gudmundur, Yiting Li, et al. (Dec. 2018). “Diffuser-assisted Photometric Follow-up Observations of the Neptune-sized Planets K2-28b and K2-100b”. In: *AJ* 156.6, 266, p. 266. DOI: 10.3847/1538-3881/aae6ca. arXiv: 1807.04420 [astro-ph.EP].

Stefansson, Gudmundur, Suvrath Mahadevan, et al. (Oct. 2017). “Toward Space-like Photometric Precision from the Ground with Beam-shaping Diffusers”. In: *ApJ* 848.1, 9, p. 9. DOI: 10.3847/1538-4357/aa88aa. arXiv: 1710.01790 [astro-ph.IM].

Steffen, Jason H. (Apr. 2016). “Sensitivity bias in the mass-radius distribution from transit timing variations and radial velocity measurements”. In: *MNRAS* 457.4, pp. 4384–4392. DOI: 10.1093/mnras/stw241. arXiv: 1510.04750 [astro-ph.EP].

Steffen, Jason H. et al. (Jan. 2013). “Transit timing observations from Kepler - VII. Confirmation of 27 planets in 13 multiplanet systems via transit timing variations and orbital stability”. In: *MNRAS* 428.2, pp. 1077–1087. DOI: 10.1093/mnras/sts090. arXiv: 1208.3499 [astro-ph.EP].

Stetson, Peter B. (Mar. 1987). “DAOPHOT: A Computer Program for Crowded-Field Stellar Photometry”. In: *PASP* 99, p. 191. DOI: 10.1086/131977.

Still, Martin and Tom Barclay (Aug. 2012). *PyKE: Reduction and analysis of Kepler Simple Aperture Photometry data*. ascl: 1208.004.

Ter Braak, Cajo J. F. (Sept. 2006). “A Markov Chain Monte Carlo version of the genetic algorithm Differential Evolution: easy Bayesian computing for real parameter spaces”. In: *Statistics and Computing* 16.3, pp. 239–249. DOI: 10.1007/s11222-006-8769-1.

Thompson, Susan E. et al. (Apr. 2018). “Planetary Candidates Observed by Kepler. VIII. A Fully Automated Catalog with Measured Completeness and Reliability Based on Data Release 25”. In: *ApJS* 235.2, 38, p. 38. DOI: 10.3847/1538-4365/aab4f9. arXiv: 1710.06758 [astro-ph.EP].

Thorngren, Daniel and Jonathan J. Fortney (Apr. 2019). “Connecting Giant Planet Atmosphere and Interior Modeling: Constraints on Atmospheric Metal Enrichment”. In: *ApJL* 874.2, L31, p. L31. DOI: 10.3847/2041-8213/ab1137. arXiv: 1811.11859 [astro-ph.EP].

Thorngren, Daniel P. and Jonathan J. Fortney (May 2018). “Bayesian Analysis of Hot-Jupiter Radius Anomalies: Evidence for Ohmic Dissipation?” In: *AJ* 155.5, 214, p. 214. DOI: 10.3847/1538-3881/aaba13. arXiv: 1709.04539 [astro-ph.EP].

Thorngren, Daniel P., Jonathan J. Fortney, et al. (Nov. 2016). "The Mass-Metallicity Relation for Giant Planets". In: *ApJ* 831.1, 64, p. 64. DOI: 10.3847/0004-637X/831/1/64. arXiv: 1511.07854 [astro-ph.EP].

Tian, F. et al. (2013). "Atmospheric Escape and Climate Evolution of Terrestrial Planets". In: *Comparative Climatology of Terrestrial Planets*. Ed. by Stephen J. Mackwell et al., pp. 567–582. DOI: 10.2458/azu_uapress_9780816530595-ch023.

Tian, Feng (May 2015). "Atmospheric Escape from Solar System Terrestrial Planets and Exoplanets". In: *Annual Review of Earth and Planetary Sciences* 43, pp. 459–476. DOI: 10.1146/annurev-earth-060313-054834.

Tinyanont, Samaporn et al. (Feb. 2019). "WIRC+Pol: A Low-resolution Near-infrared Spectropolarimeter". In: *PASP* 131.996, p. 025001. DOI: 10.1088/1538-3873/aaef0f. arXiv: 1811.03138 [astro-ph.IM].

Virtanen, Pauli et al. (2020). "SciPy 1.0: Fundamental Algorithms for Scientific Computing in Python". In: *Nature Methods* 17, pp. 261–272. DOI: 10.1038/s41592-019-0686-2.

von Essen, C., A. Ofir, et al. (July 2018). "Kepler Object of Interest Network. I. First results combining ground- and space-based observations of Kepler systems with transit timing variations". In: *A&A* 615, A79, A79. DOI: 10.1051/0004-6361/201732483. arXiv: 1801.06191 [astro-ph.EP].

von Essen, C., G. Stefansson, et al. (Aug. 2019). "First light of engineered diffusers at the Nordic Optical Telescope reveal time variability of the optical eclipse depth of WASP-12b". In: *A&A* 628, A115, A115. DOI: 10.1051/0004-6361/201935312. arXiv: 1904.05362 [astro-ph.EP].

Wang, Ji et al. (June 2015). "Influence of Stellar Multiplicity On Planet Formation. III. Adaptive Optics Imaging of Kepler Stars With Gas Giant Planets". In: *ApJ* 806.2, 248, p. 248. DOI: 10.1088/0004-637X/806/2/248. arXiv: 1505.05363 [astro-ph.EP].

Wang, Songhu et al. (Feb. 2018). "Transiting Exoplanet Monitoring Project (TEMP). III. On the Relocation of the Kepler-9 b Transit". In: *AJ* 155.2, 73, p. 73. DOI: 10.3847/1538-3881/aaa253. arXiv: 1712.06297 [astro-ph.EP].

Weiss, Lauren M., Katherine M. Deck, et al. (June 2017). "New Insights on Planet Formation in WASP-47 from a Simultaneous Analysis of Radial Velocities and Transit Timing Variations". In: *AJ* 153.6, 265, p. 265. DOI: 10.3847/1538-3881/aa6c29. arXiv: 1612.04856 [astro-ph.EP].

Weiss, Lauren M., Geoffrey W. Marcy, et al. (Jan. 2018). "The California-Kepler Survey. V. Peas in a Pod: Planets in a Kepler Multi-planet System Are Similar in Size and Regularly Spaced". In: *AJ* 155.1, 48, p. 48. DOI: 10.3847/1538-3881/aa9ff6. arXiv: 1706.06204 [astro-ph.EP].

Wilson, John C. et al. (Mar. 2003). “A Wide-Field Infrared Camera for the Palomar 200-inch Telescope”. In: *Instrument Design and Performance for Optical/Infrared Ground-based Telescopes*. Ed. by Masanori Iye and Alan F. M. Moorwood. Vol. 4841. Society of Photo-Optical Instrumentation Engineers (SPIE) Conference Series, pp. 451–458. DOI: 10.1117/12.460336.

Wilson, P. A., A. Rajan, and J. Patience (June 2014). “The brown dwarf atmosphere monitoring (BAM) project. I. The largest near-IR monitoring survey of L and T dwarfs”. In: *A&A* 566, A111, A111. DOI: 10.1051/0004-6361/201322995. arXiv: 1404.4633 [astro-ph.SR].

Wu, Yanqin and Yoram Lithwick (July 2013). “Density and Eccentricity of Kepler Planets”. In: *ApJ* 772.1, 74, p. 74. DOI: 10.1088/0004-637X/772/1/74. arXiv: 1210.7810 [astro-ph.EP].

Xie, Ji-Wei (Feb. 2014). “Transit Timing Variation of Near-resonance Planetary Pairs. II. Confirmation of 30 Planets in 15 Multiple-planet Systems”. In: *ApJS* 210.2, 25, p. 25. DOI: 10.1088/0067-0049/210/2/25. arXiv: 1309.2329 [astro-ph.EP].

Xie, Ji-Wei et al. (Oct. 2016). “Exoplanet orbital eccentricities derived from LAMOST-Kepler analysis”. In: *Proceedings of the National Academy of Science* 113.41, pp. 11431–11435. DOI: 10.1073/pnas.1604692113. arXiv: 1609.08633 [astro-ph.EP].

Zhao, Ming et al. (Dec. 2014). “Characterization of the Atmosphere of the Hot Jupiter HAT-P-32Ab and the M-dwarf Companion HAT-P-32B”. In: *ApJ* 796.2, 115, p. 115. DOI: 10.1088/0004-637X/796/2/115. arXiv: 1410.0968 [astro-ph.EP].

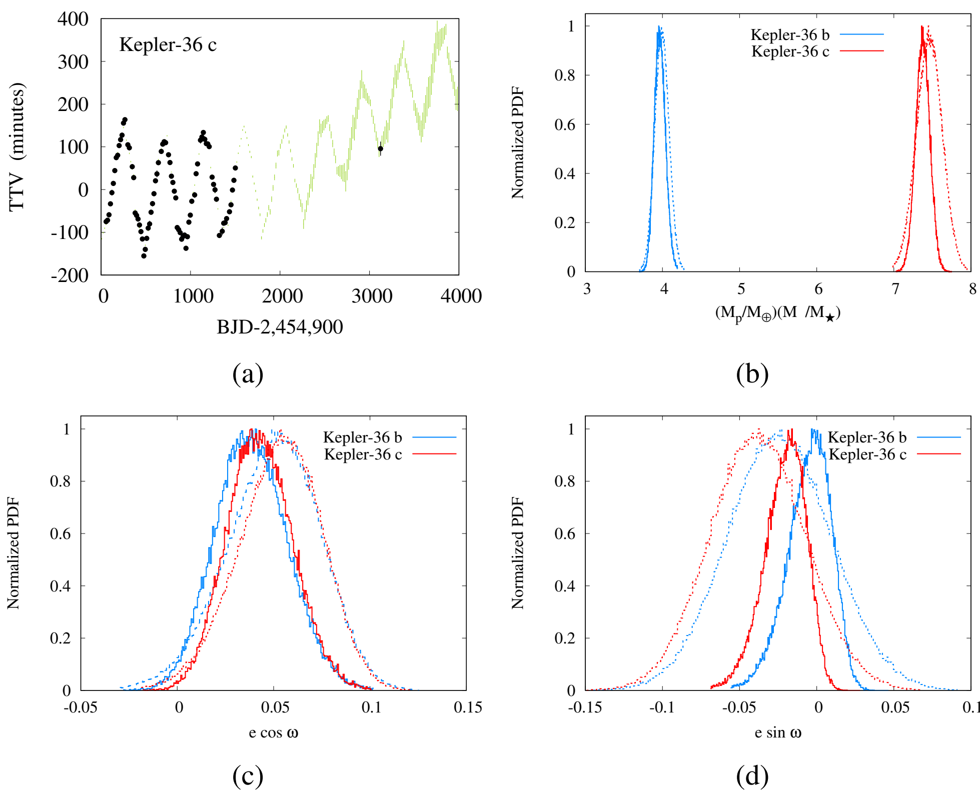

Figure 2.16: Same as Figure 2.15, but for Kepler-36.

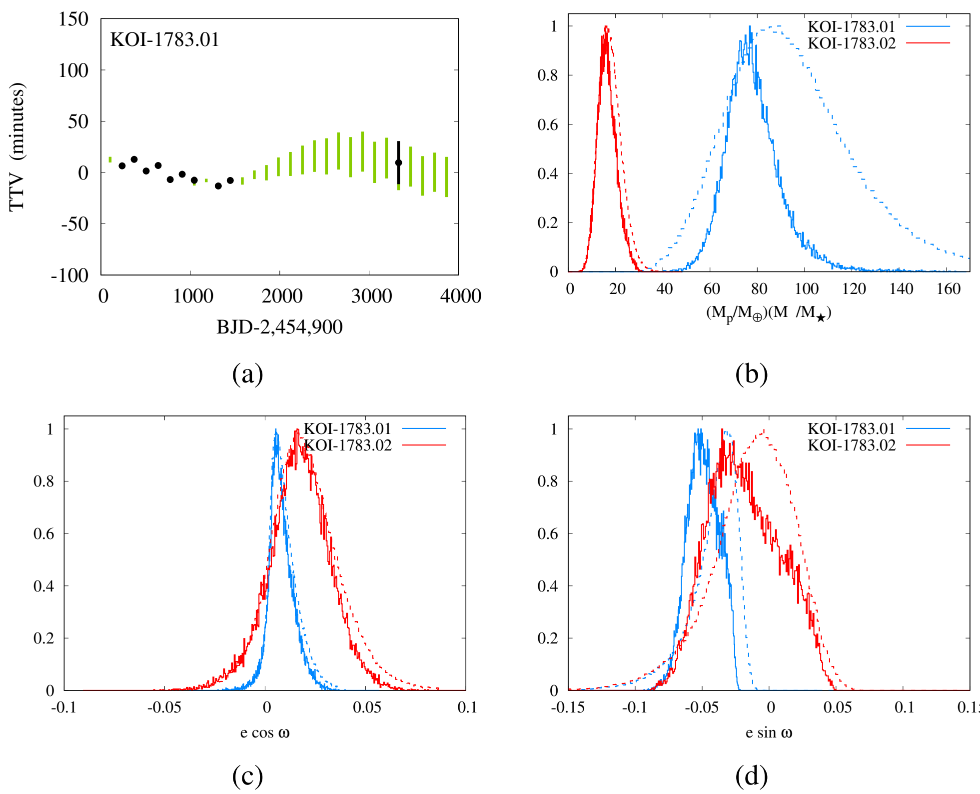

Figure 2.17: Same as Figure 2.15, but for KOI-1783.

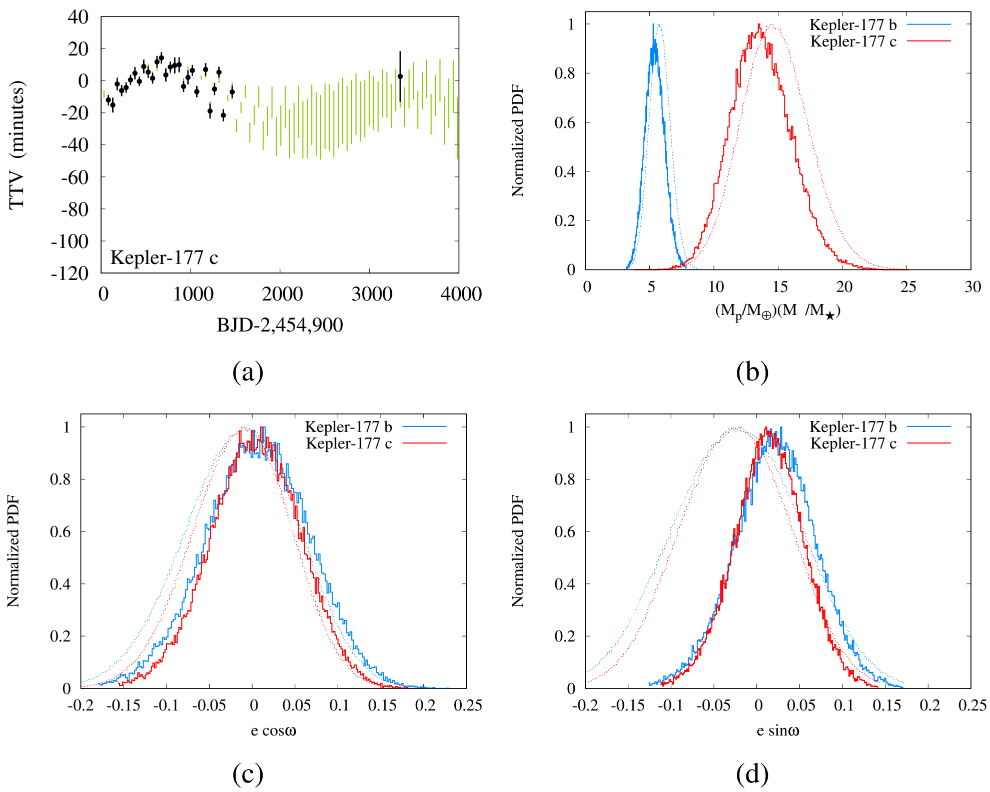

Figure 2.18: Same as Figure 2.15, but for Kepler-177.

Chapter 3

CONSTRAINTS ON METASTABLE HELIUM IN THE ATMOSPHERES OF WASP-69B AND WASP-52B WITH ULTRA-NARROWBAND PHOTOMETRY

Vissapragada, Shreyas et al. (June 2020). "Constraints on Metastable Helium in the Atmospheres of WASP-69b and WASP-52b with Ultranarrowband Photometry". In: *AJ* 159.6, 278, p. 278. DOI: 10.3847/1538-3881/ab8e34. arXiv: 2004.13728 [astro-ph.EP].

3.1 Introduction

Many of the currently known exoplanets are on short-period orbits and thus experience severe insolation. Such extreme environments can radically alter planetary evolution, potentially driving atmospheric mass loss via thermal escape (e.g. Tian, 2015; Owen, 2019). Mass loss can in turn leave substantial imprints on observed planetary statistics, such as the dearth of planets between 1.5 and 2 Earth radii (the "radius gap" or "evaporation valley") and the so-called "Neptune desert" in the radius-period plane (Lopez and Fortney, 2013; Owen and Wu, 2013; Owen and Wu, 2017; Fulton, Petigura, et al., 2017; Van Eylen et al., 2018; Fulton and Petigura, 2018; Cloutier and Menou, 2020; Hardegree-Ullman et al., 2020). Over the past two decades, most measurements of mass loss rates for close-in planets have been conducted at ultraviolet wavelengths, with Lyman-α detections for HD 209458b (Vidal-Madjar et al., 2003), HD 189733b (Lecavelier Des Etangs et al., 2010; Lecavelier des Etangs et al., 2012), GJ 436b (Kulow et al., 2014; David Ehrenreich et al., 2015; Lavie et al., 2017), and GJ 3470b (Bourrier, Lecavelier des Etangs, et al., 2018); tentative/marginal signals for TRAPPIST-1b and c (Bourrier, D. Ehrenreich, Wheatley, et al., 2017), Kepler-444e and f (Bourrier, D. Ehrenreich, Allart, et al., 2017), and K2-18b (dos Santos et al., 2020); and non-detections for 55 Cnc e (D. Ehrenreich et al., 2012), HD 97658b (Bourrier, D. Ehrenreich, King, et al., 2017), GJ 1132 b (Waalkes et al., 2019), and π Men c (García Muñoz et al., 2020). While in theory the large cross-section of this line should result in strong absorption during exoplanet transits, in practice geocoronal emission and interstellar absorption effectively mask out the line core for most stars, requiring these studies to study the absorption in the line's extended wings.

The neutral helium triplet (with vacuum wavelengths near 1083.3 nm) offers a way to circumvent the limitations of Lyman-α observations (Seager and Sasselov, 2000; Oklopčić and Hirata, 2018) by shifting to infrared wavelengths where both the Earth's atmosphere and the interstellar medium (e.g. Indriolo et al., 2009) are effectively transmissive. Spake et al. (2018) were the first to successfully observe an enhanced transit depth in He I for WASP-107b with Wide-Field Camera 3 (WFC3) on the *Hubble Space Telescope* (*HST*). Soon after, ground-based observations with the CARMENES high-resolution ($R \sim 80,000$) spectrograph on the 3.5 m telescope at Calar Alto Observatory have confirmed the absorption signal and measured the He I line shape for HAT-P-11b (Allart, Bourrier, Lovis, D. Ehrenreich, Spake, et al., 2018) and WASP-107b (Allart, Bourrier, Lovis, D. Ehrenreich, Aceituno, et al., 2019), and have additionally revealed excess helium absorption signals for HD 189733b (Salz, Czesla, Schneider, Nagel, et al., 2018), HD 209458b (Alonso-Floriano et al., 2019), and WASP-69b (Nortmann et al., 2018). *HST* WFC3 observations were also used to identify He I absorption for HAT-P-11b (Mansfield et al., 2018), and recently Keck II/NIRSPEC and the Habitable-zone Planet Finder have observed helium in the atmospheres of WASP-107b (James Kirk et al., 2020) and GJ 3470b (Ninan et al., 2020), respectively. We note also the reported non-detections of helium in the atmospheres of KELT-9b, GJ 436b (both Nortmann et al., 2018), WASP-12b (Kreidberg and Oklopčić, 2018), GJ 1214b (Crossfield et al., 2019), and K2-100b (Gaidos et al., 2020). Due to its observational accessibility for ground- and space-based facilities, the helium triplet has been firmly established as a window into the upper atmospheres of exoplanets.

Here, we introduce ultra-narrowband helium photometry, a ground-based technique complementary to high-resolution spectroscopy that is specifically crafted to measure the helium absorption depth using an ultra-narrow bandpass filter. In this work, we benchmark our new technique on the Wide-field Infrared Camera (WIRC), at the prime focus of the Hale 200" telescope at Palomar Observatory. We first measure the He I light curve of WASP-69b, a 1000 K, Saturn-mass, and Jupiter-size planet orbiting a K5 host star with $J = 8$ (Anderson et al., 2014). We compare our results to those of Nortmann et al. (2018), and show that our results agree well with theirs. We then present the first He I light curve of the slightly warmer (1300 K), larger (1.27 R_{J}), and heavier (0.46 M_{J}) planet WASP-52b, which orbits a K2 host star with $J = 10.5$ (Hébrard et al., 2013). In Section 3.2, we detail the experimental design of our ultra-narrowband helium photometer. We discuss our observations and data reduction techniques in Section 3.3. We present our results in Section 3.4, and conclude with a look towards future applications of ultra-narrowband photometry in Section 3.5.

3.2 Experimental Design

Our experiment is analogous to broad-band transit photometry performed previously (Vissapragada et al., 2020) with the Wide-field InfraRed Camera (WIRC; Wilson et al., 2003) on the Hale 200" telescope at Palomar Observatory. The sole difference is that we use an ultra-narrowband filter (manufactured by Alluxa) that is centered on the helium feature. We used a combination of identifiable telluric OH emission lines as well as a helium lamp (naturally producing the feature in emission) to calibrate out refractive effects and ensure our knowledge of the filter transmission profile is accurate.

Filter Properties

Specifically, our filter has a center wavelength of 1083.3 nm in vacuum, at 77 K, and at an angle of incidence (AOI) of 7°; a full width at half maximum (FWHM) of 0.635 nm; and a maximum transmission of 95.6% (averaged across five positions on the filter). To cover the full spectral range to which our 2.5 μm cutoff Hawaii-II detector is sensitive, the filter also has OD4 absolute out-of-band blocking (i.e. a transmission less than 0.01% everywhere outside the passband) from 500 to 3000 nm. We additionally utilize an Engineered Diffuser (located in a separate filter wheel from the helium filter) that molds the stellar point-spread functions (PSFs) into a top-hat shape with a FWHM of 3″. The diffuser increases observing efficiency and limits systematics related to PSF variations. When combined with our guiding software, which can keep pointing stable to within 2-3 pixels (equivalent to 0.″5-0.″75) over an entire night, this setup allows for powerful control of time-correlated systematics (Stefansson et al., 2017). With this setup in place, we have recently demonstrated a precision of 0.16% per 10 minute bin for $J = 14$ magnitude stars (Vissapragada et al., 2020).

Consideration of refractive effects is critical for such a narrowband filter, especially with a wide-field camera (e.g. Ghinassi et al., 2002; Tinyanont et al., 2019). Critically, the filter wheels in WIRC are fixed at a 7° tilt to minimize ghosting (Wilson et al., 2003), and the filters cannot be angle-tuned. Because most rays forming the image encounter the filter at non-normal incidence due to the filter tilt (as well as the diversity of angles for each field point), they experience a different passband. As a result, different positions on the detector correspond to different filter transmission

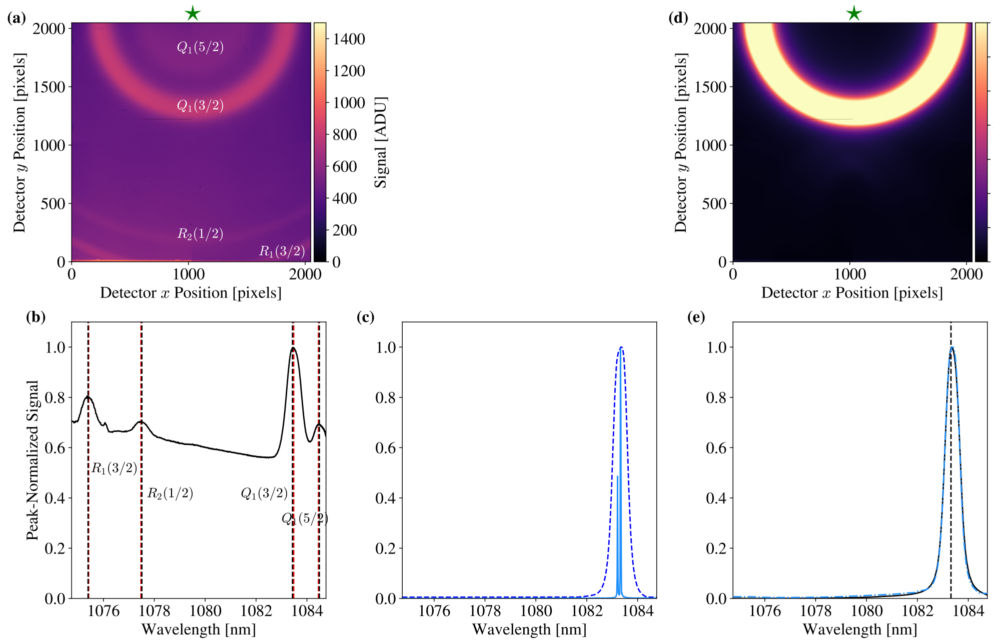

Figure 3.1: Experiment calibration. (a) 2048 by 2048 image of the sky background observed through WIRC and the helium filter. Telluric OH emission lines appear as arcs, and each strong line from the $\nu = 5-2$ band of ground-state OH is labeled. The green star indicates the zero point of the filter at $(x_0, y_0) = (1037, 2120)$. (b) The reconstructed spectrum of the sky from (a). Known positions of the telluric OH features are labeled and marked with black dashed lines, and line positions from the best-fit wavelength solution are marked with red dashed lines, which are effectively superimposed on the black dashed lines with small offsets. (c) Laboratory measurements of the helium lamp spectrum (light blue) and the helium filter transmission profile (dashed blue). (d) 2048 by 2048 image of the helium lamp observed through WIRC and the helium filter. The metastable helium triplet appears as a single bright arc due to convolution with the filter transmission profile. The green star again indicates the zero point of the filter. (e) The reconstructed spectrum of the helium arc lamp from (d), shown with a solid black line, compared to the laboratory spectrum of the helium arc lamp convolved with the filter transmission profile (dashed light blue) and the known wavelength of the feature (dashed black).

profiles. While this effect is noticeable even for broadband filters (Ghinassi et al., 2002; Tinyanont et al., 2019), the amplitude of the shift in wavelength space is small compared to the width of the bandpass, and thus it is typically ignored without consequence. For ultra-narrowband filters however, this shift can easily be larger than the bandwidth of the filter itself (e.g. Baker, Blake, and Halverson, 2019). The success of our experiment therefore depended largely on the success of our wavelength calibration.

Wavelength Calibration with Telluric OH Lines

To begin calibrating refractive effects, we used known telluric emission lines in the sky background to construct a model for the position-dependent wavelength shift. We used a sky background frame (constructed with a four-point dither near WASP-69) shown in Figure 3.1a. Rays that pass through the filter at the same angle of incidence trace out semi-circular arcs across the detector, and telluric OH emission lines thus appear as bright arcs on the detector. The offset center of the circles towards the top of the image is due to the aforementioned 7° tilt of the filter wheel; if the filter wheel was not tilted, the circles would be centered on the detector (see e.g. Sing et al., 2011). Instead, the center of the circle to which the arcs belong is the "zero point" of the filter; i.e., where rays encounter the filter at normal incidence. The best-fitting circular arcs to the emission features give the detector position for the zero point: $(x_0, y_0) = (1037, 2120)$, where the origin of the coordinate system is the bottom left corner of the image. The angle of incidence on the filter at detector position (x, y) can be written as a function of the radial distance from the zero point $r = \sqrt{(x - x_0)^2 + (y - y_0)^2}$:

$$
\begin{aligned}
\theta(r) &= (\text{pixel scale})(\text{magnification})r \\
&= (0.''25/\text{px})\left(\frac{5.08\ \text{m}}{5.2364 \times 10^{-2}\ \text{m}}\right)r \\
&= (24.''3/\text{px})r,
\end{aligned}
\tag{3.1}
$$

where the magnification is calculated as the primary mirror diameter over the beam diameter. By extracting the median count value in radial steps outward from the zero point, we construct a spectrum of the sky. To convert the spectrum into more useful wavelength units, we note that the OH emission lines in the image can be individually identified as Q and R branch lines from the $v = 5 - 2$ band for ground state ($X^2\Pi$) OH (Bernath and Colin, 2009; Oliva et al., 2015). Using the known wavelengths of these lines, we can fit to the equation for wavelength shift as a function of angle of incidence θ (e.g. Ghinassi et al., 2002):

$$
\lambda(\theta) = \lambda_0 \sqrt{1 - \frac{\sin^2(\theta)}{n_{\text{eff}}^2}},
\tag{3.2}
$$

where λ_0 is the central wavelength of the filter at normal incidence, and n_{eff} is the effective index of refraction for the filter. A non-linear least-squares fit to the known wavelengths of the telluric lines gives $\lambda_0 = 1084.80$ nm and $n_{\text{eff}} = 1.948$. Combined with Equation (3.1), this fully specifies the wavelength solution for every pixel on the detector as a function of the distance r from (x_0, y_0) = (1037, 2120). The spectrum of the sky background constructed with this transformation is given in Figure 3.1b.

Helium Arc Lamp Calibration

We used a helium arc lamp, which is a natural source of the He I triplet in vacuum, to confirm our wavelength solution and test our knowledge of the filter transmission profile. First, we measured the spectrum of the arc lamp and the transmission spectrum of the helium filter (back-lit by white light) using an Optical Spectrum Analyzer (OSA, ThorLabs #OSA202C). The OSA uses Fourier transform spectroscopy to deliver laboratory spectra at high resolving power ($R \sim 75,000$). We show the laboratory spectra in Figure 3.1c, where the two-component structure of the helium feature is clear (the two lines on the red side of the triplet are blended even at this resolution).

We then installed the helium arc lamp at the Hale 200" and used it to uniformly illuminate the region of the dome normally used for flat fields. When the helium lamp is observed through WIRC, the resultant bright arc (Figure 3.1d) is where the filter transmission profile maximally overlaps with the triplet helium feature, so during science observations we place the target within the region delineated by this arc. In practice, we take an arc lamp calibration frame before each observation, and we move the target star to a spot with a count level within 5% of the peak counts in the calibration frame. Since there is a semicircular locus on the detector that satisfies this criterion, the exact location is selected during observations to optimize the number of reference stars and avoid detector regions with many bad pixels or defects. Using the same procedure as detailed in Section 3.2, we extract the spectrum from the image in Figure 3.1d, and use the wavelength solution from Equation (3.2) to convert from AOI to nm. The resulting spectrum (Figure 3.1e) peaks at 1083.3 nm, indicating that our empirical wavelength solution correctly predicts the location of the helium triplet as measured by the lamp observation. Finally, as a test of the filter transmission profile, we convolve the laboratory measurements of the helium feature and the filter transmission profile, and overplot the result on the WIRC spectrum in Figure 3.1e. The laboratory measurements (dot-dashed blue curve) and observations (black curve) show very good agreement.

3.3 Observations

Data Collection

We observed WASP-69b through our helium filter and beam-shaping diffuser on August 16, 2019 (UT), and we observed WASP-52b with the same setup on September 17, 2019 (UT). Before beginning both science observations, we constructed a sky background frame with a simple four-point dither. Images in the dither sequence were first sigma-clipped to remove the sources, then median scaled to the first image in the stack, and finally median stacked to produce the sky background frame. We then collected science data, choosing exposure times to keep the maximum count level for the sources and comparison stars ($\sim 12,000$ ADU) well within the linearity regime for our detector while maintaining a good observing efficiency. For WASP-69b, we collected science data from UT 04:26:06 to 11:00:00 with an exposure time of 60 seconds; our observations began at airmass 1.73, reached a minimum airmass of 1.28, and then rose again until we stopped collecting data at airmass 2.49. For WASP-52b, we collected science data from UT 03:16:57 to 11:14:49 with an exposure time of 90 seconds; our observations began at airmass 2.04, reached a minimum airmass of 1.10, and then rose again until we stopped collecting data at airmass 1.96.

Data Reduction

Image Calibration

We show an example science image for WASP-69b in Figure 3.2. All science data were dark-subtracted and flat-fielded, and during this procedure bad pixels were flagged and corrected using the process described by Tinyanont et al. (2019) and Vissapragada et al. (2020). Unlike the case in Vissapragada et al. (2020), however, the background is not uniform across the detector. Contamination from telluric OH emission is clearly visible, but because these lines have a very unique spatial structure their contribution can be identified and removed. Presently, we do not correct for telluric water during image calibration. We note that the water line at 1083.507 nm (vacuum wavelength in the observer rest frame) can potentially affect the observations, though it is diluted by a minimum of $\sim$20% by the filter transmission at the target position. This line does not encroach upon the helium triplet unless the triplet is redshifted by $48.7 \text{ km/s} < v < 83.6 \text{ km/s}$ relative to the observer. This does not occur for WASP-69b and WASP-52b (and in fact we do not observe targets at such velocity shifts because the helium signal would be spatially shifted from the positions set by the calibration lamp) so our measurements are not

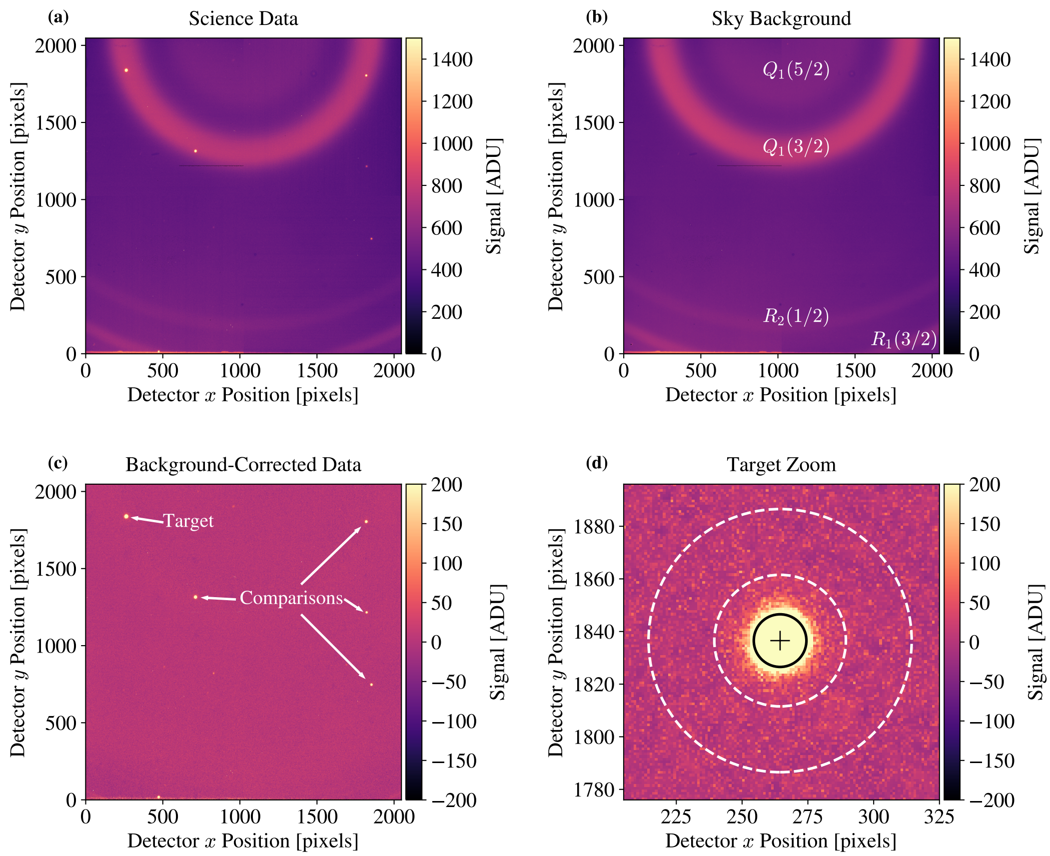

Figure 3.2: Example of the data reduction process. (a) A calibrated science frame from the WASP-69 observations before background correction. (b) The dithered sky background frame, with telluric lines indicated (see also Figure 3.1). (c) The background-corrected science frame, with target and comparison stars marked. (d) A zoomed image of the target star in the background-corrected science frame (with flux-weighted centroid given by the black cross, the optimized 10 pixel aperture by the black circle, and the annulus used for residual background estimation by the white dashed circles).

directly biased by telluric water. Variations in the water column, however, may indirectly affect observations by manifesting as additional noise in our light curves. Due to the narrow width of the water line (~ 0.03 nm FWHM Allart, Bourrier, Lovis, D. Ehrenreich, Spake, et al., 2018; Nortmann et al., 2018; Salz, Czesla, Schneider, Nagel, et al., 2018; Allart, Bourrier, Lovis, D. Ehrenreich, Aceituno, et al., 2019; Alonso-Floriano et al., 2019), relative to the filter (0.635 nm FWHM), variations would need to be large (~10%) on timescales comparable to our exposure times (~1 min) to manifest above the photometric noise as extra white noise. Smaller variations over long timescales could manifest as a time-correlated trend in our photometric data. If warranted by the data in the future, we could correct such time-correlated variations with a Gaussian process, but we see little evidence of this effect in our final light curves.

To correct for telluric OH emission in each image, we median-scaled our sky background frame to the sigma-clipped science data in 10 pixel steps radially outwards from the filter zero point (where, as in Equation 3.1 above, the pixel scale is $0\farcs25$). This procedure removed a majority of the telluric background as shown in Figure 3.2, but in some images left a small amount of residual local structure with maximum amplitude of 10 ADU/pixel, perhaps due to spatial variation of OH emission on the sky. Because even these residuals were locally quite stable, we estimated and removed the remaining background during aperture photometry using an annular region around each source as described below. This local background varies quite slowly in time and we find that this procedure reliably eliminates time-correlated noise from sky background and tellurics.

Aperture Photometry

We detected and registered the positions of the target and comparison stars using Aladin Lite (Bonnarel et al., 2000; Boch and Fernique, 2014) as described in Vissapragada et al. (2020). For both WASP-69 and WASP-52, we registered four comparison stars in addition to the target; for WASP-69, the target and comparison stars are visible in the background-corrected image in Figure 3.2. We performed aperture photometry on each source in each image with the `photutils` package (Bradley et al., 2016) where we stepped through a range of circular apertures (from 7 to 15 pixels in radius in one pixel steps). The positions of the aperture centers were allowed to shift to trace telescope pointing drift. For WASP-69 and associated comparison stars, these varied by less than 2 pixels over most of the night, but a guiding error compromised the last hour of data collection. Excluding this last hour did not change our final answers but substantially decreased the correlated noise, so we choose to exclude these images from the final photometry. For WASP-52 we encountered a guiding jump of about 6 pixels an hour from the start of the observation, and again an hour from the end of the observation. These jumps were purely in the RA direction and are thus likely related to a known issue with the RA guiding on the telescope. Including the data marred by guiding errors substantially increased the correlated noise in the final light curve, so we opted to leave them out for our analysis of WASP-52b.

We estimated the residual local background by measuring the sigma-clipped median for an annulus around each source with an inner radius of 25 pixels and an outer radius of 50 pixels. We then trimmed outliers in the raw light curves using the moving median procedure from Vissapragada et al. (2020). We determined the optimal photometric aperture size by minimizing the RMS of the residuals after the light-curve modeling described in the next section. Our optimal apertures were 10 and 8 pixels in radius for WASP-69 and WASP-52, respectively. A zoomed-in view of WASP-69 with flux-weighted centroid, best-aperture, and background annulus overplotted is shown in Figure 3.2. It is clear from this figure that a 10 pixel aperture misses some flux from the target star. However, when the aperture size increases to encompass all of the flux from the target star, the comparison star light curves decrease in quality due to increased noise from the sky background. We tested the impact of using different aperture sizes for each source and found that this sharply degraded the quality of the final light curve, likely because PSF changes due to seeing variations impact each aperture differently. We therefore chose to continue with the selected optimal apertures in our final light-curve modeling. Raw light curves in the optimized apertures are given in Figure 3.3 for both planets.

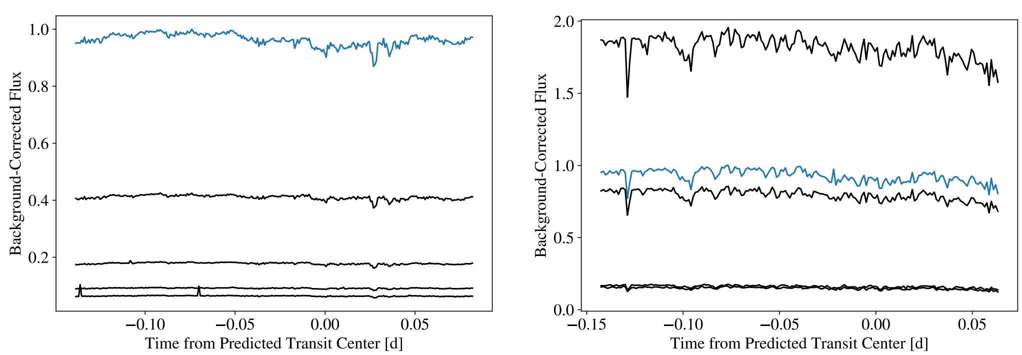

(a) (b)

Figure 3.3: Raw light curves for stars in the WASP-69 field (a) and WASP-52 field (b). In both plots, the target light curve is shown in blue, comparison light curves are shown in black, and all light curves have been normalized to the target light curve maximum.

Light-Curve Modeling

We modeled the light curves with a procedure similar to that used in Vissapragada et al. (2020), which we briefly summarize here for completeness. Each target light curve is modeled as a transit light-curve model (which is computed with `batman`; Kreidberg, 2015) multiplied by a systematics model. The systematics are further modeled as a linear trend in time plus a linear combination of the comparison star light curves, with new best-fitting linear coefficients chosen every time the transit light curve is modified. As in Vissapragada et al. (2020), our six fit parameters were the transit depth $(R_\mathrm{p}/R_\star)^2$, a timing offset from the predicted mid-transit time Δt_0, a linear trend in time α, the inclination i, the scaled semi-major axis $a/R_\star$, and a parameter describing the photometric scatter in excess of shot noise $\log(\sigma_\mathrm{extra})$. The excess scatter that we calculate is added in quadrature to the photometric error bars on each data point to give the final errors. We calculated custom quadratic limb darkening coefficients u_1 and u_2 in our bandpass using `ldtk` (Husser et al., 2013; Parviainen and Aigrain, 2015) and the stellar parameters from Anderson et al. (2014) and Hébrard et al. (2013) for WASP-69 and WASP-52, respectively. These coefficients are reported in Table 3.1. We additionally explored the possibility of fitting the quadratic limb darkening coefficients using the triangular sampling algorithm from Kipping (2013), but found that this did not make a substantive difference in our final results, so we chose to leave these coefficients fixed.

We first fit the data using the Powell minimizer from `scipy` (Virtanen et al., 2020), and we use this initial solution as a starting point for a Markov Chain Monte Carlo investigation with `emcee` (Foreman-Mackey et al., 2013). We run 50 chains for 10^3 steps to burn in, and then 10^4 steps (which corresponds to at least 150 integrated autocorrelation times for each parameter) for the actual run. The posteriors from these light-curve fits are summarized in Table 3.1, and they are visualized in Appendix 3.6.

3.4 Results and Discussion

WASP-69b

Our helium light curve for WASP-69b, along with best-fit model, residuals, and Allan deviation plot for the residuals are shown in Figure 3.4a, and a corner plot summarizing the fit posteriors is shown in Figure 3.7. We measure a transit depth of 2.152±0.045%. As a reference value, we use the *HST* WFC3 spectrum obtained by Tsiaras et al. (2018), who report an average transit depth of 1.6538 ± 0.0045% between 1110.8 nm and 1141.6 nm. Our transit depth exceeds the reference value by 11.1σ, indicating a secure detection of helium in the atmosphere of WASP-69b. We prefer a transit timing solution slightly earlier than, but not incompatible with, the ephemeris from Baştürk et al. (2019). Our constraints on i and $a/R_\star$ are compatible with those from Anderson et al. (2014). We note, however, slight covariances between these parameters and the transit depth in Figure 3.7. Updated knowledge on these parameters may allow us to better constrain the transit depth in the future.

Table 3.1: Light-Curve Fitting Results

Parameter	Prior		Posterior		Note
	WASP-69b	WASP-52b	WASP-69b	WASP-52b	
P (days)	3.86814098	1.74978179	(fixed)	(fixed)	(1), (2)
t_0 (BJD_{TDB})	2458711.8300727	2458743.8135163	(fixed)	(fixed)	(1), (2)
u_1	0.3975	0.3635	(fixed)	(fixed)	(3), (4), (5)
u_2	0.1156	0.1229	(fixed)	(fixed)	(3), (4), (5)
e	0.	0.	(fixed)	(fixed)	(4), (5)
$(R_p/R_\star)^2$ (%)	$\mathcal{U}(0.0, 3.0)$	$\mathcal{U}(0.0, 6.0)$	$2.152^{+0.045}_{-0.045}$	$2.97^{+0.13}_{-0.13}$	–
Δt_0 (min)	$\mathcal{N}(0.0, 0.70)$	$\mathcal{N}(0.0, 0.65)$	$-0.57^{+0.42}_{-0.42}$	$-0.39^{+0.54}_{-0.54}$	(1), (2)
i (°)	$\mathcal{N}(86.71, 0.20)$	$\mathcal{N}(85.17, 0.13)$	$86.63^{+0.15}_{-0.15}$	$85.20^{+0.12}_{-0.12}$	(4), (6)
$a/R_\star$	$\mathcal{N}(12.00, 0.46)$	$\mathcal{N}(7.22, 0.07)$	$11.82^{+0.25}_{-0.25}$	$7.207^{+0.062}_{-0.062}$	(4), (6)
α	$\mathcal{U}(-0.2, 0.2)$	$\mathcal{U}(-0.2, 0.2)$	$0.0160^{+0.0026}_{-0.0025}$	$0.0811^{+0.0012}_{-0.0012}$	–
$\log(\sigma_{extra})$	$\mathcal{U}(-3.5, -2.0)$	$\mathcal{U}(-3.5, -2.0)$	$-2.711^{+0.025}_{-0.025}$	$-2.422^{+0.060}_{-0.070}$	–

(1) WASP-69b ephemerides from Baştürk et al. (2019); (2) WASP-52b ephemerides from Baluev et al. (2019); (3) Quadratic limb darkening coefficients calculated with `ldtk` (Husser et al., 2013; Parviainen and Aigrain, 2015) (4) Stellar parameters (for limb darkening calculations), e, i, and $a/R_\star$ from Anderson et al. (2014) for WASP-69b; (5) Stellar parameters (for limb darkening calculations) and e from Hébrard et al. (2013) for WASP-52b; (6) i and $a/R_\star$ from Alam et al. (2018) for WASP-52b. Note also that $\mathcal{N}(a, b)$ denotes a Gaussian distribution centered on a with standard deviation b, and $\mathcal{U}(a, b)$ denotes a uniform distribution between a and b.

We achieved a per-point rms of 8.21 ppm/pt across 271 points. The final scatter in our residuals was 2.0× the shot noise (the noise floor set by Poisson statistics on our total detected photon counts, of which approximately 25% are background counts due to OH emission). A small correlated component to the noise appears on 10 minute timescales (see Figure 3.4a); we obtain a Carter and Winn (2009) β factor of 1.08. This is noticeably larger scatter (relative to shot noise) than what we have typically achieved in the past for targets of similar apparent brightness (Vissapragada et al., 2020). We observed this target at high efficiency (collecting light 87.6% of the time we were on sky), and the long exposure times make scintillation noise an unlikely culprit (Stefansson et al., 2017). This may be a signature of variation in the stellar He I line itself (Sanz-Forcada and Dupree, 2008; Andretta et al., 2017; Salz, Czesla, Schneider, Nagel, et al., 2018), but if such variations occur on long timescales (e.g. from spots on the stellar surface), then they would be corrected by our linear detrending model, and if they occur on short timescales, they would manifest as strong red noise in the light curve, which we do not observe. Rather, the likely explanation for our photometric performance is a paucity of good comparison stars in the field. WASP-69 inhabits a fairly sparse field already, and to compound the issue we are limited in target placement to the arc shown in Figure 3.1d, which may put otherwise accessible comparison stars outside the field of view. Thus, we are limited in our ability to obtain many good comparison stars for this technique, which here is likely the ultimate limiting factor in our photometry.

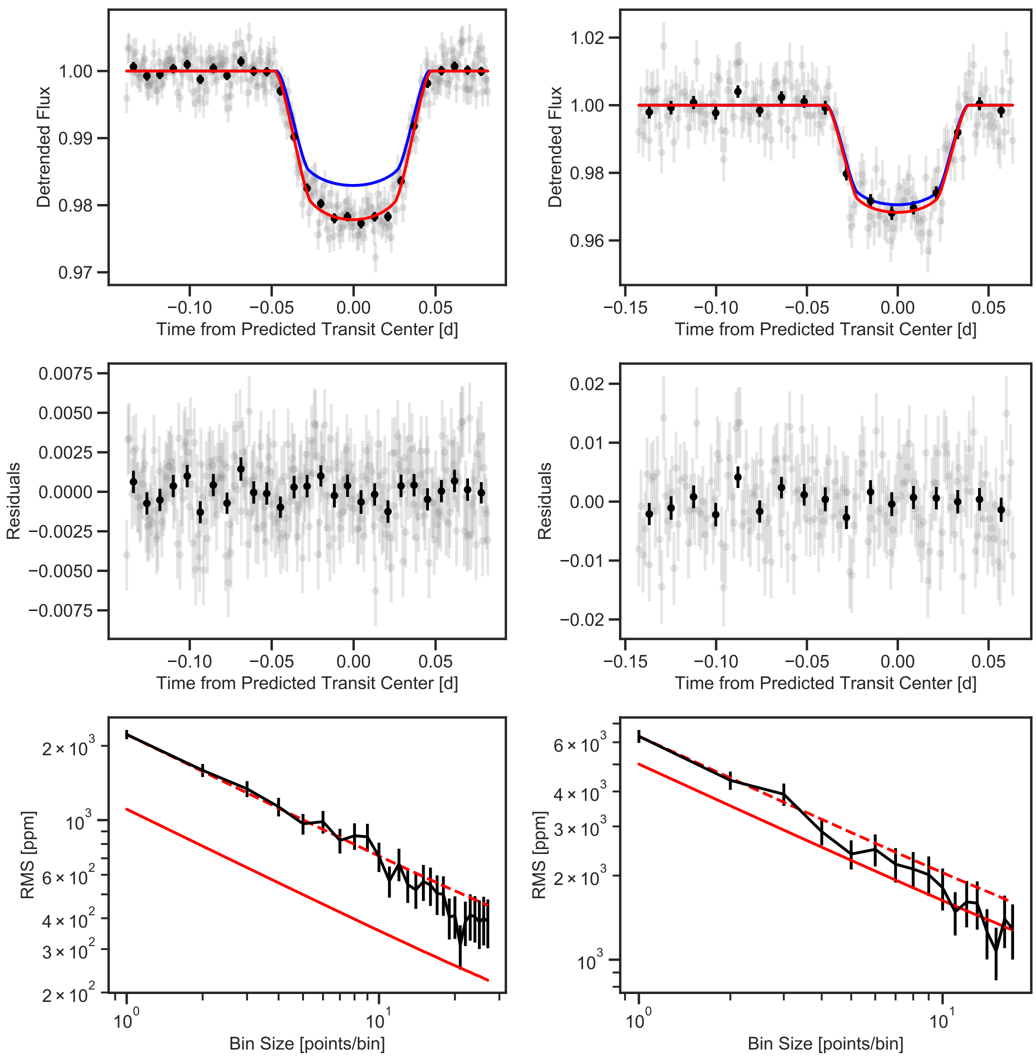

(a) (b)

Figure 3.4: Results for WASP-69b in (a) and WASP-52b in (b). Top: helium light curves, with unbinned data in gray and data binned to a 10 minute cadence in black, with best-fit models shown by the red curves. The blue curves indicate reference transit depths from Tsiaras et al. (2018) for WASP-69b and Alam et al. (2018) for WASP-52b. Middle: fit residuals, with unbinned data in gray and binned to 10 minute cadence in black. Bottom: Allan deviation plot of the residuals (black curve) along with the photon noise limit (red curve) and the predicted behavior of our residuals assuming white noise statistics (red dashed line). We find that the scatter in these data is 2.0× the photon noise limit for WASP-69b and 1.3× the photon noise limit for WASP-52b.

We now assess how our transit measurement compares to the spectroscopic measurement of Nortmann et al. (2018). We took their reduced stellar spectra gathered over two nights of observation and converted these from the planet rest frame (in which the reduced data were provided) back to the telluric rest frame. For each spectrum (which we label $f_{i,\lambda}$, where i indexes time and λ indexes wavelength), we calculated the excess absorption signal f_i in our bandpass using our measured transmission function T_λ via

$$f_i = \frac{\int f_{i,\lambda} T_\lambda d\lambda}{\int T_\lambda d\lambda}. \tag{3.3}$$

The timeseries f then represents the excess absorption in the helium line during the transit as would be measured by CARMENES through our helium filter. To this we added the broadband light curve (calculated with the parameters of Tsiaras et al., 2018) which gave the total light curve as would have been observed by WIRC. We repeated this procedure for both nights of CARMENES data collection (with 35 spectra in night 1 and 31 spectra in night 2), and we present our results compared to the two CARMENES timeseries in Figure 3.5a. Our data show good agreement with those collected by Nortmann et al. (2018).

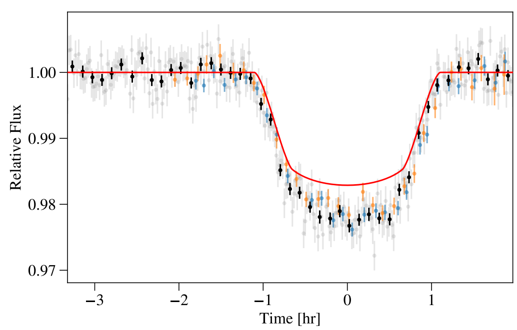

(a)

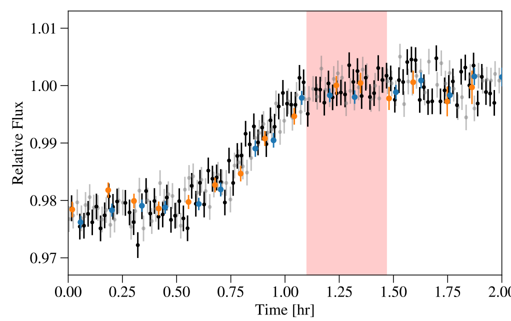

(b)

Figure 3.5: (a) WIRC light curve of WASP-69b (unbinned in gray and binned to 7 minute cadence in black) compared to CARMENES light curves (computed by integrating CARMENES spectra against our transmission function) from Nortmann et al. (2018) in blue and orange (their first and second nights of data collections, respectively). The comparison light curve from Tsiaras et al. (2018) is shown in red. (b) Mirrored, unbinned WIRC light curve, with ingress shown in gray and egress shown in black. Data from CARMENES are again shown in blue and orange for the first and second nights of data collection (Nortmann et al., 2018). The post-egress absorption reported by Nortmann et al. (2018) would fall within the red region. We do not see significant evidence for it here, but the asymmetry is also washed out in the calculated CARMENES light curve due to our wide bandpass (relative to the CARMENES resolution element).

Nortmann et al. (2018) also report the detection of an asymmetric transit in He I, with egress extending about half an hour past ingress. We do not find strong evidence for this effect in our light curve. In Figure 3.5b, we show our WASP-69b light curve mirrored across our best-fit mid-transit time; there is no visible absorption in the post-egress window where Nortmann et al. (2018) report an extended tail. While we do not see strong evidence for this effect in our light curve, however, we cannot rule it out. The amplitude of the reported post-egress absorption is of order 0.5%; when diluted through our transmission function this becomes a 500 ppm effect which we are not significantly sensitive to on a 22 min timescale (our rms on this timescale is 388 ppm). Repeated observations of WASP-69b may allow us to constrain the transit asymmetry in the future.

WASP-52b

Our helium light curve for WASP-52b, along with best-fit model, residuals, and Allan deviation plot for the residuals are shown in Figure 3.4b, and a corner plot summarizing the fit posteriors is shown in Figure 3.8. We measure a transit depth of $2.97^{+0.13}_{-0.13}$%, which exceeds the spot-uncorrected transit depth between 898.5 nm and 1030.0 nm (2.76 ± 0.021%) from Alam et al. (2018) by 1.6σ. Assuming the same line structure shape as is observed for WASP-69b (Nortmann et al., 2018), this converts to an amplitude of 1.31 ± 0.94% in the deepest line of the triplet. This is meant only to give a sense of what one might expect at high resolution; in reality, lineshapes can vary from planet to planet, and there is no guarantee that assuming the line shape of WASP-69b is correct (Nortmann et al., 2018; Allart, Bourrier, Lovis, D. Ehrenreich, Spake, et al., 2018; Salz, Czesla, Schneider, Nagel, et al., 2018; Allart, Bourrier, Lovis, D. Ehrenreich, Aceituno, et al., 2019; Alonso-Floriano et al., 2019; James Kirk et al., 2020). We obtained a per-point RMS of 35.6 ppm/pt across 177 points. The scatter in the light curve was 1.3× the photon noise limit, binning down like white noise (see bottom panel of Figure 3.4). This performance is comparable to what we have achieved in the past for similar targets (Vissapragada et al., 2020), despite the fact that there were only four comparison stars in the field of view.

WASP-52 is a young ($0.4^{+0.3}_{-0.2}$ Gyr), active host star, with a $\log R'_{\mathrm{HK}}$ index of -4.4 ± 0.2 (Hébrard et al., 2013) and many authors observing and analyzing the effects of spots and plages (J. Kirk et al., 2016; Chen, Pallé, et al., 2017; Louden et al., 2017; Mancini et al., 2017; Alam et al., 2018; Bruno, Lewis, Stevenson, et al., 2018; May et al., 2018; Bruno, Lewis, Alam, et al., 2020). Considering the proposed relationship between planetary metastable helium absorption and stellar activity (Nortmann et al., 2018; Alonso-Floriano et al., 2019), WASP-52 remains a high-priority target for future work. Follow-up observations with high-resolution spectroscopic facilities on larger telescopes should be able to detect absorption and quantify the line shape (which we must assume here) for this rather challenging target. We note that confident detections of Na, K, and Hα absorption in the atmosphere of this planet recently required three transits with the ESPRESSO high-resolution spectrograph on the VLT (Chen, Casasayas-Barris, et al., 2020). Though its host star is relatively faint, WASP-52b is well worth additional observations in metastable helium, as the other detected atomic species will provide some context for modeling the upper atmosphere of this planet.

Mass Loss Modeling

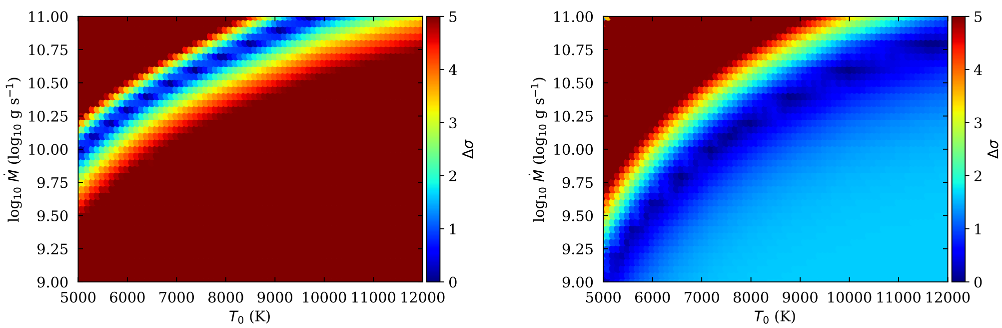

(a) (b)

Figure 3.6: Mass loss modeling for WASP-69b in (a) and WASP-52b in (b). Each point (T_0, $\dot{M}$) corresponds to a different mass loss model, and the color of the point indicates the σ discrepancy between that model and the data presented in Figure 3.5.

We interpret our observations of WASP-69b and WASP-52b using the Oklopčić and Hirata (2018) model. Despite our lack of a significant detection for WASP-52b, we model potential outflows from this planet to set an upper limit on the mass loss rate corresponding to our upper limit on the excess absorption. As WASP-52b is a high-priority target for future observations (James Kirk et al., 2020), this is a particularly important constraint that we can obtain from our light curve.

We first computed grids of atmospheric mass loss models; following Oklopčić and Hirata (2018) and Mansfield et al. (2018), we computed 1D density and velocity profiles for a 90%–10% hydrogen–helium atmosphere losing mass to an isothermal Parker wind. These profiles spanned 5,000–12,000 K in thermosphere temperature T_0 and 10^9–10^{11} g/s in mass loss rate $\dot{M}$, with the ranges motivated by hydrodynamics simulations of atmospheric escape (Salz, Czesla, Schneider, and Schmitt, 2016). Level populations for hydrogen and helium were then computed for each profile. As there are no measurements of the stellar UV spectra (required for computing photoionization rates) for WASP-69 and WASP-52, we used UV spectra from MUSCLES (France et al., 2016) of stars with similar spectral type. For WASP-69, we used HD 85512 (K6) and for WASP-52 we used ϵ Eri (K2).

The resulting density profiles of 2^3S He were then used to compute the transit depth in the line given our filter transmission function, and the model transit depths were compared to those that we report in Table 3.1. We opted to compare only the transit depths from the outflow models to our data rather than the full light curve, as the full computation is substantially more expensive for a marginal gain in accuracy for the model comparison (relative to our photometric uncertainties). In Figure 3.6, we show how the model grids compare to our data, parameterized by the number of standard deviations away from our data. For WASP-69b we obtain a curved contour of best-fit solutions, indicating a known degeneracy between mass loss rate and thermosphere temperature due to our inability to resolve line shapes (Mansfield et al., 2018).

To summarize the contours in Figure 3.6, we quote our constraints on the mass loss rate at two possible thermosphere temperatures. At $T_0 = 7,000$ K (12,000 K) we obtain a corresponding mass loss rate of $\dot{M} = 10^{10.50^{+0.05}_{-0.04}}$ g/s ($\dot{M} = 10^{11.30^{+0.08}_{-0.08}}$ g/s). This translates to $5.25^{+0.65}_{-0.46} \times 10^{-4}$ M_J/Gyr ($3.32^{+0.67}_{-0.56} \times 10^{-3}$ M_J/Gyr). The mass loss rate for WASP-69b is therefore very similar to those reported for HAT-P-11b and WASP-107b (Allart, Bourrier, Lovis, D. Ehrenreich, Spake, et al., 2018; Mansfield et al., 2018; Spake et al., 2018; Allart, Bourrier, Lovis, D. Ehrenreich, Aceituno, et al., 2019; James Kirk et al., 2020), which should be typical for planets at similar distances and gravitational potentials (Salz, Czesla, Schneider, and Schmitt, 2016). For WASP-52b, we can set a 95th-percentile upper limit of $\dot{M} < 10^{10.1}$ g/s ($10^{11.1}$ g/s) at $T_0 = 7,000$ K (12,000 K). This translates to 2.1×10^{-4} M_J/Gyr (2.1×10^{-3} M_J/Gyr). We conclude from these measurements that, barring substantial changes in orbital distance and stellar irradiation, WASP-69b ($M_\mathrm{p} = 0.26 M_\mathrm{J}$) and WASP-52b ($M_\mathrm{p} = 0.46 M_\mathrm{J}$) will survive over the lifetime of their host stars (losing at most a few percent in envelope mass), and their compositions will not be substantially impacted by mass loss.

3.5 Conclusions

In this work, we have presented a new photometric technique to observe the metastable 2^3S helium absorption feature near 1083.3 nm using an ultra-narrowband filter and a beam-shaping diffuser. We benchmarked this new technique by observing WASP-69b, a planet for which the shape of the helium feature has been measured with high-resolution spectroscopy (Nortmann et al., 2018). Our technique detects helium absorption to 11.1σ confidence (a single-transit S/N comparable to that achieved with CARMENES) in this planet's atmosphere, at a level consistent with previous observations. Additionally, for WASP-52b we set a 95th-percentile upper limit on excess absorption in the helium bandpass of 0.47%. We find that the quality of our photometry relative to the photon noise limit depends sensitively on the availability of comparison sources. Interpreting our results with atmospheric mass loss modeling allows us to constrain the mass loss rate for WASP-69b to $5.25^{+0.65}_{-0.46} \times 10^{-4}$ $M_{\mathrm{J}}/\mathrm{Gyr}$ ($3.32^{+0.67}_{-0.56} \times 10^{-3}$ $M_{\mathrm{J}}/\mathrm{Gyr}$) at 7,000 K (12,000 K), and additionally we set an upper limit to the mass loss rate for WASP-52b at these temperatures of 2.1×10^{-4} $M_{\mathrm{J}}/\mathrm{Gyr}$ (2.1×10^{-3} $M_{\mathrm{J}}/\mathrm{Gyr}$). These values are typical for other gaseous planets at similar gravitational potentials and orbital periods, and we conclude that both of these planets' atmospheres will not be substantially affected by mass loss for many Gyr.

Diffuser-assisted, ultra-narrowband photometry on a wide-field camera is a unique way to study exoplanet atmospheres, but it also comes with challenges. For the experimental setup detailed here, we sometimes have to settle for sub-optimal photometry on brighter targets because we are observing in sparse fields with relatively few suitable comparison stars, and also because of the constraints imposed by the AOI shift effect. Additionally, the lack of a comparison bandpass means that we must rely on high-precision infrared transit measurements taken by other groups (or simultaneous measurements with different instruments) to establish the magnitude of the excess absorption in the helium line, rather than doing so in our own experimental setup. Both of these challenges could be overcome with photometers like those presented in Baker, Blake, and Halverson (2019), which allow for simultaneous photometry of a target star in two adjacent passbands. Though our restricted instrumental setup does not presently allow us to use this method, or other multicolor imaging methods requiring dichroics (e.g. Dhillon et al., 2016), we believe these are fruitful avenues for future exploration in the context of narrow atomic and molecular features.

Despite the challenges we have encountered in our constrained experimental setup with WIRC, we have demonstrated that our system is capable of measuring mass loss rates for most advantageous targets. Our technique occupies a unique niche in the current suite of approaches to metastable helium observations. First, the narrowband filter affords us better precision than space-based spectroscopy with *HST* WFC3, scaling from the precisions of Spake et al. (2018) and Mansfield et al. (2018). Second, while the *James Webb Space Telescope* will achieve much better precision (Allart, Bourrier, Lovis, D. Ehrenreich, Spake, et al., 2018), we can schedule and observe targets more readily on a ground-based 5 m telescope, allowing us to survey a wider range of planets. Third, the high efficiency of our technique lets us observe targets beyond the magnitude limits of high-resolution spectrographs on smaller telescopes. With future WIRC observations, we aim to characterize the fundamental relationships between mass loss, stellar activity, high-energy flux, and planetary age (Nortmann et al., 2018; Alonso-Floriano et al., 2019; Oklopčić, 2019; Owen, 2019).

3.6 Appendix: Posterior Probability Distributions

In this section, we show the posterior probability distributions for our light-curve fits to WASP-69b and WASP-52b.

References

Alam, Munazza K. et al. (Dec. 2018). “The HST PanCET Program: Hints of Na I and Evidence of a Cloudy Atmosphere for the Inflated Hot Jupiter WASP-52b”. In: *AJ* 156.6, 298, p. 298. doi: 10.3847/1538-3881/aaee89. arXiv: 1811.00935 [astro-ph.EP].

Allart, R., V. Bourrier, C. Lovis, D. Ehrenreich, J. Aceituno, et al. (Mar. 2019). “High-resolution confirmation of an extended helium atmosphere around WASP-107b”. In: *A&A* 623, A58, A58. doi: 10.1051/0004-6361/201834917. arXiv: 1901.08073 [astro-ph.EP].

Allart, R., V. Bourrier, C. Lovis, D. Ehrenreich, J. J. Spake, et al. (Dec. 2018). “Spectrally resolved helium absorption from the extended atmosphere of a warm Neptune-mass exoplanet”. In: *Science* 362.6421, pp. 1384–1387. doi: 10.1126/science.aat5879. arXiv: 1812.02189 [astro-ph.EP].

Alonso-Floriano, F. J. et al. (Sept. 2019). “He I λ 10 830 Å in the transmission spectrum of HD209458 b”. In: *A&A* 629, A110, A110. doi: 10.1051/0004-6361/201935979. arXiv: 1907.13425 [astro-ph.EP].

Anderson, D. R. et al. (Dec. 2014). “Three newly discovered sub-Jupiter-mass planets: WASP-69b and WASP-84b transit active K dwarfs and WASP-70Ab transits the evolved primary of a G4+K3 binary”. In: *MNRAS* 445.2, pp. 1114–1129. doi: 10.1093/mnras/stu1737. arXiv: 1310.5654 [astro-ph.EP].

Andretta, Vincenzo et al. (Apr. 2017). “Estimates of Active Region Area Coverage through Simultaneous Measurements of the He I $\lambda\lambda$ 5876 and 10830 Lines”. In:

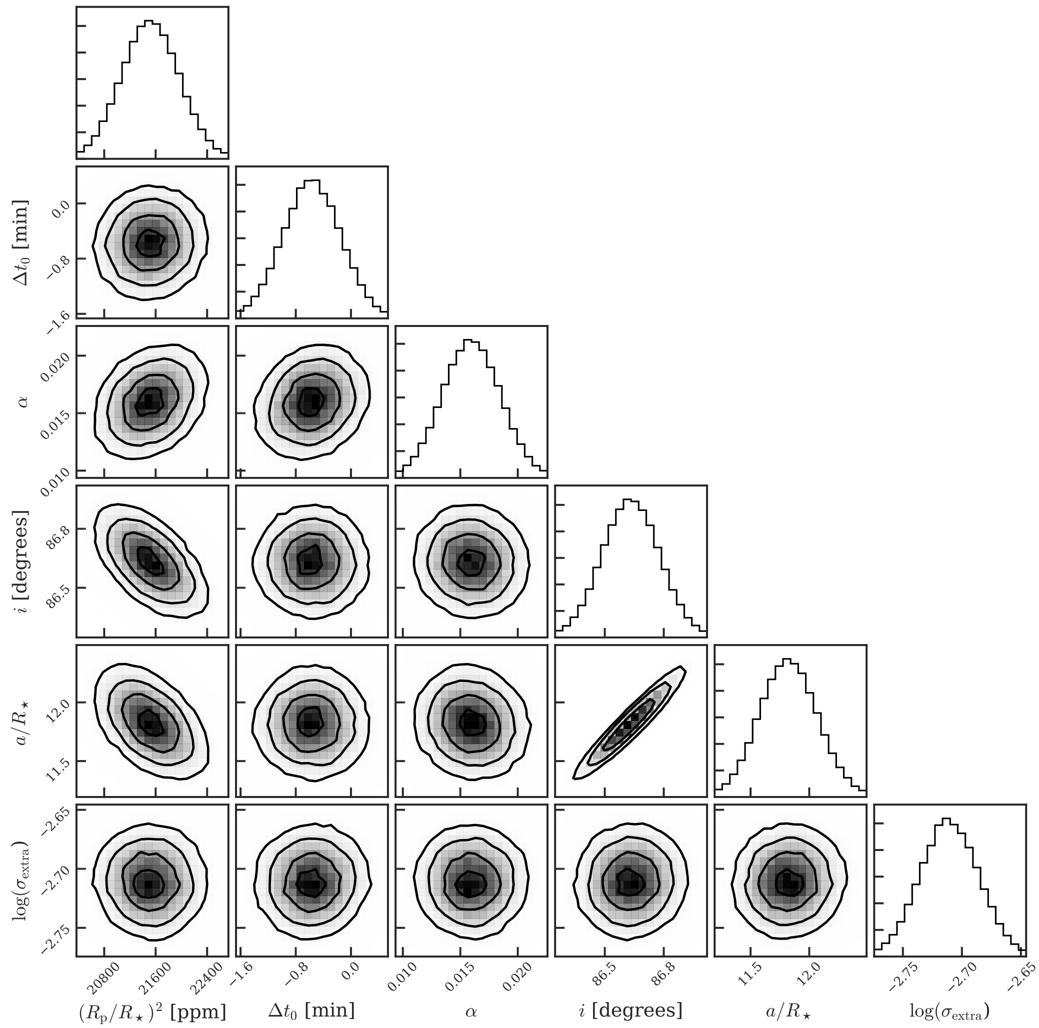

Figure 3.7: Corner plot of the posterior probability distributions for our fit to WASP-69b. The middle 99% of samples are shown with contours denoting 1, 2, and 3σ boundaries.

ApJ 839.2, 97, p. 97. DOI: 10.3847/1538-4357/aa6a14. arXiv: 1703.10060 [astro-ph.SR].

Baker, Ashley D., Cullen H. Blake, and Sam Halverson (June 2019). "The Oxyometer: A Novel Instrument Concept for Characterizing Exoplanet Atmospheres". In: *PASP* 131.1000, p. 064402. DOI: 10.1088/1538-3873/ab04b4. arXiv: 1901.02562 [astro-ph.IM].

Baluev, R. V. et al. (Nov. 2019). "Homogeneously derived transit timings for 17 exoplanets and reassessed TTV trends for WASP-12 and WASP-4". In: *MNRAS* 490.1, pp. 1294–1312. DOI: 10.1093/mnras/stz2620. arXiv: 1908.04505 [astro-ph.EP].

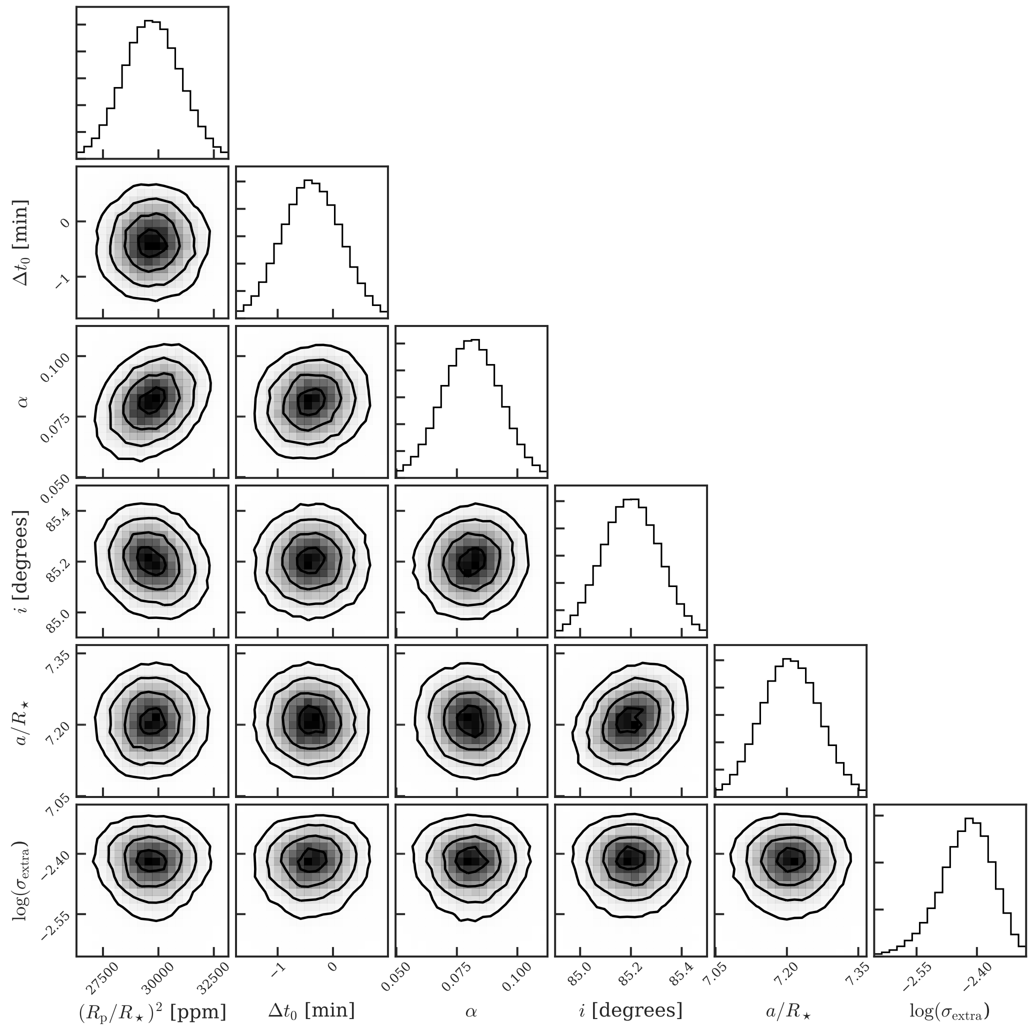

Figure 3.8: Same as Figure 3.7 but for WASP-52b.

Baştürk, Ö. et al. (Nov. 2019). “Transit timing variations of five transiting planets”. In: *Turkish Physical Society 35th International Physics Congress (TPS35)*. Vol. 2178. American Institute of Physics Conference Series, 030019, p. 030019. DOI: `10.1063/1.5135417`. arXiv: `1911.08331 [astro-ph.EP]`.

Bernath, Peter F. and Reginald Colin (Sept. 2009). “Revised molecular constants and term values for the X $^2\Pi$ and B$^2\Sigma^+$ states of OH”. In: *Journal of Molecular Spectroscopy* 257.1, pp. 20–23. DOI: `10.1016/j.jms.2009.06.003`.

Boch, T. and P. Fernique (May 2014). “Aladin Lite: Embed your Sky in the Browser”. In: *Astronomical Data Analysis Software and Systems XXIII*. Ed. by N. Manset and P. Forshay. Vol. 485. Astronomical Society of the Pacific Conference Series, p. 277.

Bonnarel, F. et al. (Apr. 2000). "The ALADIN interactive sky atlas. A reference tool for identification of astronomical sources". In: *A&AS* 143, pp. 33–40. DOI: 10.1051/aas:2000331.

Bourrier, V., D. Ehrenreich, R. Allart, et al. (June 2017). "Strong H I Lyman-α variations from an 11 Gyr-old host star: a planetary origin?" In: *A&A* 602, A106, A106. DOI: 10.1051/0004-6361/201730542. arXiv: 1703.00504 [astro-ph.EP].

Bourrier, V., D. Ehrenreich, G. King, et al. (Jan. 2017). "No hydrogen exosphere detected around the super-Earth HD 97658 b". In: *A&A* 597, A26, A26. DOI: 10.1051/0004-6361/201629253. arXiv: 1609.04416 [astro-ph.EP].

Bourrier, V., D. Ehrenreich, P. J. Wheatley, et al. (Mar. 2017). "Reconnaissance of the TRAPPIST-1 exoplanet system in the Lyman-α line". In: *A&A* 599, L3, p. L3. DOI: 10.1051/0004-6361/201630238. arXiv: 1702.07004 [astro-ph.EP].

Bourrier, V., A. Lecavelier des Etangs, et al. (Dec. 2018). "Hubble PanCET: an extended upper atmosphere of neutral hydrogen around the warm Neptune GJ 3470b". In: *A&A* 620, A147, A147. DOI: 10.1051/0004-6361/201833675. arXiv: 1812.05119 [astro-ph.EP].

Bradley, Larry et al. (Sept. 2016). *Photutils: Photometry tools*. ascl: 1609.011.

Bruno, Giovanni, Nikole K. Lewis, Munazza K. Alam, et al. (Feb. 2020). "WASP-52b. The effect of star-spot correction on atmospheric retrievals". In: *MNRAS* 491.4, pp. 5361–5375. DOI: 10.1093/mnras/stz3194. arXiv: 1911.05179 [astro-ph.EP].

Bruno, Giovanni, Nikole K. Lewis, Kevin B. Stevenson, et al. (Sept. 2018). "Starspot Occultations in Infrared Transit Spectroscopy: The Case of WASP-52b". In: *AJ* 156.3, 124, p. 124. DOI: 10.3847/1538-3881/aac6db. arXiv: 1808.09514 [astro-ph.EP].

Carter, Joshua A. and Joshua N. Winn (Oct. 2009). "Parameter Estimation from Time-series Data with Correlated Errors: A Wavelet-based Method and its Application to Transit Light Curves". In: *ApJ* 704.1, pp. 51–67. DOI: 10.1088/0004-637X/704/1/51. arXiv: 0909.0747 [astro-ph.EP].

Chen, G., N. Casasayas-Barris, et al. (Mar. 2020). "Detection of Na, K, and Hα absorption in the atmosphere of WASP-52b using ESPRESSO". In: *A&A* 635, A171, A171. DOI: 10.1051/0004-6361/201936986. arXiv: 2002.08379 [astro-ph.EP].

Chen, G., E. Pallé, et al. (Apr. 2017). "The GTC exoplanet transit spectroscopy survey. VI. Detection of sodium in WASP-52b's cloudy atmosphere". In: *A&A* 600, L11, p. L11. DOI: 10.1051/0004-6361/201730736. arXiv: 1703.06716 [astro-ph.EP].

Cloutier, Ryan and Kristen Menou (May 2020). "Evolution of the Radius Valley around Low-mass Stars from Kepler and K2". In: *AJ* 159.5, 211, p. 211. DOI: 10.3847/1538-3881/ab8237. arXiv: 1912.02170 [astro-ph.EP].

Crossfield, I. J. M. et al. (Jan. 2019). "An Upper Limit on He Absorption in GJ 1214b". In: *Research Notes of the American Astronomical Society* 3.1, 24, p. 24. DOI: 10.3847/2515-5172/ab01b8.

Dhillon, Vikram S. et al. (Aug. 2016). "HiPERCAM: a high-speed quintuple-beam CCD camera for the study of rapid variability in the universe". In: *Ground-based and Airborne Instrumentation for Astronomy VI*. Ed. by Christopher J. Evans, Luc Simard, and Hideki Takami. Vol. 9908. Society of Photo-Optical Instrumentation Engineers (SPIE) Conference Series, 99080Y, 99080Y. DOI: 10.1117/12.2229055. arXiv: 1606.09214 [astro-ph.IM].

dos Santos, Leonardo A. et al. (Feb. 2020). "The high-energy environment and atmospheric escape of the mini-Neptune K2-18 b". In: *A&A* 634, L4, p. L4. DOI: 10.1051/0004-6361/201937327. arXiv: 2001.04532 [astro-ph.EP].

Ehrenreich, D. et al. (Nov. 2012). "Hint of a transiting extended atmosphere on 55 Cancri b". In: *A&A* 547, A18, A18. DOI: 10.1051/0004-6361/201219981. arXiv: 1210.0531 [astro-ph.EP].

Ehrenreich, David et al. (June 2015). "A giant comet-like cloud of hydrogen escaping the warm Neptune-mass exoplanet GJ 436b". In: *Nature* 522.7557, pp. 459–461. DOI: 10.1038/nature14501. arXiv: 1506.07541 [astro-ph.EP].

Foreman-Mackey, Daniel et al. (Mar. 2013). "emcee: The MCMC Hammer". In: *PASP* 125.925, p. 306. DOI: 10.1086/670067. arXiv: 1202.3665 [astro-ph.IM].

France, Kevin et al. (Apr. 2016). "The MUSCLES Treasury Survey. I. Motivation and Overview". In: *ApJ* 820.2, 89, p. 89. DOI: 10.3847/0004-637X/820/2/89. arXiv: 1602.09142 [astro-ph.SR].

Fulton, Benjamin J. and Erik A. Petigura (Dec. 2018). "The California-Kepler Survey. VII. Precise Planet Radii Leveraging Gaia DR2 Reveal the Stellar Mass Dependence of the Planet Radius Gap". In: *AJ* 156.6, 264, p. 264. DOI: 10.3847/1538-3881/aae828. arXiv: 1805.01453 [astro-ph.EP].

Fulton, Benjamin J., Erik A. Petigura, et al. (Sept. 2017). "The California-Kepler Survey. III. A Gap in the Radius Distribution of Small Planets". In: *AJ* 154.3, 109, p. 109. DOI: 10.3847/1538-3881/aa80eb. arXiv: 1703.10375 [astro-ph.EP].

Gaidos, E. et al. (June 2020). "Zodiacal exoplanets in time - X. The orbit and atmosphere of the young 'neptune desert'-dwelling planet K2-100b". In: *MNRAS* 495.1, pp. 650–662. DOI: 10.1093/mnras/staa918. arXiv: 2003.12940 [astro-ph.EP].

García Muñoz, A. et al. (Jan. 2020). "Is π Men c's Atmosphere Hydrogen-dominated? Insights from a Non-detection of H I Lyα Absorption". In: *ApJL* 888.2, L21, p. L21. DOI: 10.3847/2041-8213/ab61ff. arXiv: 1912.06913 [astro-ph.EP].

Ghinassi, F. et al. (May 2002). "Transmission curves and effective refraction indices of MKO near infrared consortium filters at cryogenic temperatures". In: *A&A* 386, pp. 1157–1159. DOI: 10.1051/0004-6361:20020266. arXiv: astro-ph/0202483 [astro-ph].

Hardegree-Ullman, Kevin K. et al. (Mar. 2020). "Scaling K2. I. Revised Parameters for 222,088 K2 Stars and a K2 Planet Radius Valley at 1.9 $R_\oplus$". In: *ApJS* 247.1, 28, p. 28. DOI: 10.3847/1538-4365/ab7230. arXiv: 2001.11511 [astro-ph.SR].

Hébrard, G. et al. (Jan. 2013). "WASP-52b, WASP-58b, WASP-59b, and WASP-60b: Four new transiting close-in giant planets". In: *A&A* 549, A134, A134. DOI: 10.1051/0004-6361/201220363. arXiv: 1211.0810 [astro-ph.EP].

Husser, T. -O. et al. (May 2013). "A new extensive library of PHOENIX stellar atmospheres and synthetic spectra". In: *A&A* 553, A6, A6. DOI: 10.1051/0004-6361/201219058. arXiv: 1303.5632 [astro-ph.SR].

Indriolo, Nick et al. (Oct. 2009). "Interstellar Metastable Helium Absorption as a Probe of the Cosmic-ray Ionization Rate". In: *ApJ* 703.2, pp. 2131–2137. DOI: 10.1088/0004-637X/703/2/2131. arXiv: 0908.2816 [astro-ph.SR].

Kipping, David M. (Nov. 2013). "Efficient, uninformative sampling of limb darkening coefficients for two-parameter laws". In: *MNRAS* 435.3, pp. 2152–2160. DOI: 10.1093/mnras/stt1435. arXiv: 1308.0009 [astro-ph.SR].

Kirk, J. et al. (Dec. 2016). "Transmission spectroscopy of the inflated exoplanet WASP-52b, and evidence for a bright region on the stellar surface". In: *MNRAS* 463.3, pp. 2922–2931. DOI: 10.1093/mnras/stw2205. arXiv: 1608.08993 [astro-ph.EP].

Kirk, James et al. (Mar. 2020). "Confirmation of WASP-107b's Extended Helium Atmosphere with Keck II/NIRSPEC". In: *AJ* 159.3, 115, p. 115. DOI: 10.3847/1538-3881/ab6e66. arXiv: 2001.07667 [astro-ph.EP].

Kreidberg, Laura (Nov. 2015). "batman: BAsic Transit Model cAlculatioN in Python". In: *PASP* 127.957, p. 1161. DOI: 10.1086/683602. arXiv: 1507.08285 [astro-ph.EP].

Kreidberg, Laura and Antonija Oklopčić (June 2018). "Non-detection of a Helium Exosphere for the Hot Jupiter WASP-12b". In: *Research Notes of the American Astronomical Society* 2.2, 44, p. 44. DOI: 10.3847/2515-5172/aac887. arXiv: 1805.10671 [astro-ph.EP].

Kulow, Jennifer R. et al. (May 2014). "Lyα Transit Spectroscopy and the Neutral Hydrogen Tail of the Hot Neptune GJ 436b". In: *ApJ* 786.2, 132, p. 132. DOI: 10.1088/0004-637X/786/2/132. arXiv: 1403.6834 [astro-ph.EP].

Lavie, B. et al. (Sept. 2017). "The long egress of GJ 436b's giant exosphere". In: *A&A* 605, L7, p. L7. DOI: 10.1051/0004-6361/201731340. arXiv: 1709.04686 [astro-ph.EP].

Lecavelier Des Etangs, A. et al. (May 2010). "Evaporation of the planet HD 189733b observed in H I Lyman-α". In: *A&A* 514, A72, A72. DOI: 10.1051/0004-6361/200913347. arXiv: 1003.2206 [astro-ph.EP].

Lecavelier des Etangs, A. et al. (July 2012). "Temporal variations in the evaporating atmosphere of the exoplanet HD 189733b". In: *A&A* 543, L4, p. L4. DOI: 10.1051/0004-6361/201219363. arXiv: 1206.6274 [astro-ph.EP].

Lopez, Eric D. and Jonathan J. Fortney (Oct. 2013). "The Role of Core Mass in Controlling Evaporation: The Kepler Radius Distribution and the Kepler-36 Density Dichotomy". In: *ApJ* 776.1, 2, p. 2. DOI: 10.1088/0004-637X/776/1/2. arXiv: 1305.0269 [astro-ph.EP].

Louden, Tom et al. (Sept. 2017). "A precise optical transmission spectrum of the inflated exoplanet WASP-52b". In: *MNRAS* 470.1, pp. 742–754. DOI: 10.1093/mnras/stx984. arXiv: 1703.09285 [astro-ph.EP].

Mancini, L. et al. (Feb. 2017). "Orbital alignment and star-spot properties in the WASP-52 planetary system". In: *MNRAS* 465.1, pp. 843–857. DOI: 10.1093/mnras/stw1987. arXiv: 1608.02001 [astro-ph.EP].

Mansfield, Megan et al. (Dec. 2018). "Detection of Helium in the Atmosphere of the Exo-Neptune HAT-P-11b". In: *ApJL* 868.2, L34, p. L34. DOI: 10.3847/2041-8213/aaf166. arXiv: 1812.02214 [astro-ph.EP].

May, E. M. et al. (Sept. 2018). "MOPSS. I. Flat Optical Spectra for the Hot Jupiters WASP-4 b and WASP-52b". In: *AJ* 156.3, 122, p. 122. DOI: 10.3847/1538-3881/aad4a8. arXiv: 1807.06561 [astro-ph.EP].

Ninan, Joe P. et al. (May 2020). "Evidence for He I 10830 Å Absorption during the Transit of a Warm Neptune around the M-dwarf GJ 3470 with the Habitable-zone Planet Finder". In: *ApJ* 894.2, 97, p. 97. DOI: 10.3847/1538-4357/ab8559. arXiv: 1910.02070 [astro-ph.EP].

Nortmann, Lisa et al. (Dec. 2018). "Ground-based detection of an extended helium atmosphere in the Saturn-mass exoplanet WASP-69b". In: *Science* 362.6421, pp. 1388–1391. DOI: 10.1126/science.aat5348. arXiv: 1812.03119 [astro-ph.EP].

Oklopčić, Antonija (Aug. 2019). "Helium Absorption at 1083 nm from Extended Exoplanet Atmospheres: Dependence on Stellar Radiation". In: *ApJ* 881.2, 133, p. 133. DOI: 10.3847/1538-4357/ab2f7f. arXiv: 1903.02576 [astro-ph.EP].

Oklopčić, Antonija and Christopher M. Hirata (Mar. 2018). "A New Window into Escaping Exoplanet Atmospheres: 10830 Å Line of Helium". In: *ApJL* 855.1, L11, p. L11. DOI: 10.3847/2041-8213/aaada9. arXiv: 1711.05269 [astro-ph.EP].

Oliva, E. et al. (Sept. 2015). "Lines and continuum sky emission in the near infrared: observational constraints from deep high spectral resolution spectra with GIANO-TNG". In: *A&A* 581, A47, A47. DOI: 10.1051/0004-6361/201526291. arXiv: 1506.09004 [astro-ph.IM].

Owen, James E. (May 2019). “Atmospheric Escape and the Evolution of Close-In Exoplanets”. In: *Annual Review of Earth and Planetary Sciences* 47, pp. 67–90. DOI: 10.1146/annurev-earth-053018-060246. arXiv: 1807.07609 [astro-ph.EP].

Owen, James E. and Yanqin Wu (Oct. 2013). “Kepler Planets: A Tale of Evaporation”. In: *ApJ* 775.2, 105, p. 105. DOI: 10.1088/0004-637X/775/2/105. arXiv: 1303.3899 [astro-ph.EP].

– (Sept. 2017). “The Evaporation Valley in the Kepler Planets”. In: *ApJ* 847.1, 29, p. 29. DOI: 10.3847/1538-4357/aa890a. arXiv: 1705.10810 [astro-ph.EP].

Parviainen, H. and S. Aigrain (Nov. 2015). “LDTK: Limb Darkening Toolkit”. In: *MNRAS* 453.4, pp. 3821–3826. DOI: 10.1093/mnras/stv1857. arXiv: 1508.02634 [astro-ph.EP].

Salz, M., S. Czesla, P. C. Schneider, E. Nagel, et al. (Dec. 2018). “Detection of He I λ10830 Å absorption on HD 189733 b with CARMENES high-resolution transmission spectroscopy”. In: *A&A* 620, A97, A97. DOI: 10.1051/0004-6361/201833694. arXiv: 1812.02453 [astro-ph.EP].

Salz, M., S. Czesla, P. C. Schneider, and J. H. M. M. Schmitt (Feb. 2016). “Simulating the escaping atmospheres of hot gas planets in the solar neighborhood”. In: *A&A* 586, A75, A75. DOI: 10.1051/0004-6361/201526109. arXiv: 1511.09341 [astro-ph.EP].

Sanz-Forcada, J. and A. K. Dupree (Sept. 2008). “Active cool stars and He I 10 830 Å: the coronal connection”. In: *A&A* 488.2, pp. 715–721. DOI: 10.1051/0004-6361:20078501. arXiv: 0807.0175 [astro-ph].

Seager, S. and D. D. Sasselov (July 2000). “Theoretical Transmission Spectra during Extrasolar Giant Planet Transits”. In: *ApJ* 537.2, pp. 916–921. DOI: 10.1086/309088. arXiv: astro-ph/9912241 [astro-ph].

Sing, D. K. et al. (Mar. 2011). “Gran Telescopio Canarias OSIRIS transiting exoplanet atmospheric survey: detection of potassium in XO-2b from narrowband spectrophotometry”. In: *A&A* 527, A73, A73. DOI: 10.1051/0004-6361/201015579. arXiv: 1008.4795 [astro-ph.EP].

Spake, J. J. et al. (May 2018). “Helium in the eroding atmosphere of an exoplanet”. In: *Nature* 557.7703, pp. 68–70. DOI: 10.1038/s41586-018-0067-5. arXiv: 1805.01298 [astro-ph.EP].

Stefansson, Gudmundur et al. (Oct. 2017). “Toward Space-like Photometric Precision from the Ground with Beam-shaping Diffusers”. In: *ApJ* 848.1, 9, p. 9. DOI: 10.3847/1538-4357/aa88aa. arXiv: 1710.01790 [astro-ph.IM].

Tian, Feng (May 2015). “Atmospheric Escape from Solar System Terrestrial Planets and Exoplanets”. In: *Annual Review of Earth and Planetary Sciences* 43, pp. 459–476. DOI: 10.1146/annurev-earth-060313-054834.

Tinyanont, Samaporn et al. (Feb. 2019). "WIRC+Pol: A Low-resolution Near-infrared Spectropolarimeter". In: *PASP* 131.996, p. 025001. DOI: 10.1088/1538-3873/aaef0f. arXiv: 1811.03138 [astro-ph.IM].

Tsiaras, A. et al. (Apr. 2018). "A Population Study of Gaseous Exoplanets". In: *AJ* 155.4, 156, p. 156. DOI: 10.3847/1538-3881/aaaf75. arXiv: 1704.05413 [astro-ph.EP].

Van Eylen, V. et al. (Oct. 2018). "An asteroseismic view of the radius valley: stripped cores, not born rocky". In: *MNRAS* 479.4, pp. 4786–4795. DOI: 10.1093/mnras/sty1783. arXiv: 1710.05398 [astro-ph.EP].

Vidal-Madjar, A. et al. (Mar. 2003). "An extended upper atmosphere around the extrasolar planet HD209458b". In: *Nature* 422.6928, pp. 143–146. DOI: 10.1038/nature01448.

Virtanen, Pauli et al. (Feb. 2020). "SciPy 1.0: fundamental algorithms for scientific computing in Python". In: *Nature Methods* 17, pp. 261–272. DOI: 10.1038/s41592-019-0686-2. arXiv: 1907.10121 [cs.MS].

Vissapragada, Shreyas et al. (Mar. 2020). "Diffuser-assisted Infrared Transit Photometry for Four Dynamically Interacting Kepler Systems". In: *AJ* 159.3, 108, p. 108. DOI: 10.3847/1538-3881/ab65c8. arXiv: 1907.04445 [astro-ph.EP].

Waalkes, William C. et al. (July 2019). "Lyα in the GJ 1132 System: Stellar Emission and Planetary Atmospheric Evolution". In: *AJ* 158.1, 50, p. 50. DOI: 10.3847/1538-3881/ab24c2. arXiv: 1906.04274 [astro-ph.EP].

Wilson, John C. et al. (Mar. 2003). "A Wide-Field Infrared Camera for the Palomar 200-inch Telescope". In: *Instrument Design and Performance for Optical/Infrared Ground-based Telescopes*. Ed. by Masanori Iye and Alan F. M. Moorwood. Vol. 4841. Society of Photo-Optical Instrumentation Engineers (SPIE) Conference Series, pp. 451–458. DOI: 10.1117/12.460336.

Chapter 4

A SEARCH FOR PLANETARY METASTABLE HELIUM ABSORPTION IN THE V1298 TAU SYSTEM

Vissapragada, Shreyas et al. (Nov. 2021). "A Search for Planetary Metastable Helium Absorption in the V1298 Tau System". In: *AJ* 162.5, 222, p. 222. DOI: 10.3847/1538-3881/ac1bb0. arXiv: 2108.05358 [astro-ph.EP].

The atmospheres of close-in exoplanets evolve substantially over their lifetimes. As planets cool and contract after formation, their extended atmospheres are subject to intense high-energy radiation from their young, active host stars on timescales of up to a Gyr (Owen, 2019; King and Wheatley, 2021). This radiation heats the planetary thermosphere via photoionization, and can launch a hydrodynamic wind that carries mass away from the planet (Murray-Clay, Chiang, and Murray, 2009). Additionally, the planet's own cooling interior may itself power mass loss as the envelope opacity decreases (Ginzburg, Schlichting, and Sari, 2018; Gupta and Schlichting, 2019). Regardless of the mechanism, the impact of early atmospheric mass loss can be observed in population-level studies of older planets. Over the last decade, this phenomenon has been invoked to explain both the radius valley (Lopez and Fortney, 2013; Owen and Wu, 2013; Fulton, Petigura, et al., 2017; Owen and Wu, 2017; Fulton and Petigura, 2018; Van Eylen et al., 2018; Hardegree-Ullman et al., 2020) and the lower boundary of the hot Neptune desert (Lundkvist et al., 2016; Mazeh, Holczer, and Faigler, 2016; Owen and Lai, 2018).

In order to accurately interpret population-level trends, we must rely on models to predict the cumulative atmospheric mass loss from individual planets. Observations of present-day mass loss rates for close-in planets provide an invaluable test of these models. For nearby systems ($\lesssim$ 100 pc) that are not fully obscured by absorption from the interstellar medium, transmission spectroscopy in the wings of the Lyman-α line can reveal escaping high-velocity neutral hydrogen (e.g. Vidal-Madjar et al., 2003; Lecavelier Des Etangs et al., 2010; David Ehrenreich et al., 2015; Bourrier et al., 2018). Near-infrared observations of metastable helium absorption at 1083 nm provide a complementary probe of atmospheric escape (Antonija Oklopčić and Hirata, 2018; Spake, Sing, et al., 2018). The accessibility of the metastable helium triplet from the ground makes it well-suited to surveys using high-resolution spectroscopy (Allart, Bourrier, Lovis, D. Ehrenreich, Spake, et al., 2018; Nortmann et al., 2018; Salz, Czesla, Schneider, Nagel, et al., 2018; Allart, Bourrier, Lovis, D. Ehrenreich, Aceituno, et al., 2019; Alonso-Floriano et al., 2019; Kirk et al., 2020; Joe P. Ninan et al., 2020; Palle et al., 2020) as well as narrowband photometry (Vissapragada et al., 2020a; Paragas et al., 2021). Helium absorption has also been detected in two systems using high-precision $R \sim 100$ spectroscopy with the *Hubble Space Telescope* (Mansfield et al., 2018; Spake, Sing, et al., 2018), although the sensitivity of these measurements is limited by their relatively low spectral resolution.

Over the past few years, these observations have significantly expanded the sample of transiting planets with well-constrained present-day mass loss rates. However, all of the systems observed to date have estimated ages of a few Gyr. By that time, most of the major processes that sculpt these systems—including atmospheric erosion—have largely concluded. It would be preferable to observe atmospheric escape in young planetary systems, as this would allow us to test our understanding of mass loss physics during the epoch when most atmopsheric mass loss is predicted to occur. There are currently only seven confirmed young (< 100 Myr) transiting planet systems: K2-33 (David, Lynne A. Hillenbrand, et al., 2016; Mann et al., 2016), V1298 Tau (David, Cody, et al., 2019; David, Petigura, et al., 2019), DS Tuc A (Newton et al., 2019), TOI 837 (Bouma et al., 2020), AU Mic (Plavchan et al., 2020), TOI 942 (Carleo et al., 2021; Zhou et al., 2021), and HIP 67522 (Rizzuto et al., 2020). The expected magnitude of the outflows from these young planets depends on their gravitational potentials (e.g. Hirano et al., 2020), which can be calculated using their measured masses and radii. Unfortunately, it is difficult to obtain precise radial velocities (RVs) for young stars (e.g. Beichman et al., 2019; Plavchan et al., 2020; Klein et al., 2021), which severely limits our knowledge of the planetary masses.

Of the aforementioned young transiting systems, V1298 Tau is a uniquely favorable target for observations of atmospheric escape. First, it is one of only two K stars in the sample (David, Cody, et al., 2019). K-type stars are optimal for observations of metastable helium, as they have a favorable ratio of EUV to mid-UV flux, which sets the level population in the metastable state (Antonija Oklopčić, 2019). Although early M stars have a similarly favorable flux ratio, K stars output a larger total EUV flux than M stars, resulting in more helium ionization and subsequent recombination into the metastable state. We note that because V1298 Tau is a pre-main sequence star, the radiative physics may differ somewhat from the more mature K dwarfs considered in Antonija Oklopčić, 2019. The V1298 Tau system is also dynamically unique; although the orbital period of the outermost planet is poorly constrained, the orbital periods of the three interior planets are close to a 2:3:6 chain of mean-motion resonances, with planet c orbiting V1298 Tau every 8.2 days, planet d every 12.4 days, and planet b every 24.1 days (David, Petigura, et al., 2019). This should allow for strong constraints on the planetary masses using the transit-timing variation (TTV; Livingston et al. in prep.) technique, circumventing the difficulties of RV mass measurements for this young system.

In this work, we use the metastable helium triplet at 1083 nm to search for atmospheric outflows from the three innermost planets in the V1298 Tau system. In Section 4.1, we describe our narrowband helium transit observations with the Wide-field InfraRed Camera (WIRC; Wilson et al., 2003) on the Hale 200" telescope at Palomar Observatory, as well as complementary observations obtained with the Habitable-zone Planet Finder (HPF; Mahadevan, L. Ramsey, et al., 2012; Mahadevan, L. W. Ramsey, et al., 2014) near-infrared spectrograph on the 10m Hobby-Eberly Telescope (HET). In Section 4.2 we fit the resulting transit light curves, tentatively detecting an increased radius ratio in the helium bandpass for planet d. We discuss our results in Section 4.3, and we conclude in Section 4.4 by summarizing the implications of our results and detailing the highest-priority future observations needed for confirmation.

4.1 Observations

Palomar/WIRC

We observed two partial transits of V1298 Tau d, one full transit of V1298 Tau c, and one partial transit of V1298 Tau b between 2020 October and 2021 January. A summary of our observations is given in Table 4.1. We utilized a beam-shaping diffuser (Stefansson, Mahadevan, Hebb, et al., 2017; Vissapragada et al., 2020b) and a narrowband helium filter for these observations with an exposure time of 30 s. The diffuser molds the stellar PSFs into a top-hat shape with a FWHM of 3″, mitigating noise stemming from time-correlated variations in the stellar point spread function and improving our overall observing efficiency by allowing for longer integration times. Our custom narrowband helium filter is centered at 1083.3 nm with a FWHM of 0.635 nm. In Vissapragada et al., 2020a, we presented commissioning observations using this filter where we reproduced the helium absorption signal reported by Nortmann et al. (2018) for WASP-69b.

Table 4.1: Summary of V1298 Tau observations analyzed in this work

Instrument	Planet	Coverage	Date	Start Time	End Time	Exposures	Exposure Time	Start/Min/End Airmass
WIRC	d	Ingress	2020 Oct 8	06:09:49	13:17:25	669	30 s	2.10/1.03/1.24
WIRC	d	Egress	2020 Nov 27	03:46:32	11:48:57	759	30 s	1.57/1.03/1.93
WIRC	c	Full	2020 Dec 17	02:39:14	11:00:35	784	30 s	1.50/1.03/2.38
WIRC	b	Egress	2021 Jan 1	02:40:03	09:58:12	660	30 s	1.23/1.03/2.32
HPF	c	In-transit	2020 Oct 12	06:38:12	07:42:41	6	618 s	1.33/1.13/1.13
HPF	–	Out-of-transit	2020 Oct 13	11:33:20	12:05:18	3	618 s	1.14/1.14/1.23
HPF	–	Out-of-transit	2020 Oct 14	11:42:03	12:14:01	3	618 s	1.18/1.28/1.18
HPF	–	Out-of-transit	2020 Nov 14	09:33:42	10:32:51	6	565 s	1.16/1.16/1.37

All dates and times are UT.

As described in Vissapragada et al., 2020a, the filter bandpass shifts with angle of incidence (AOI). This means that only a small fraction of the $8.7' \times 8.7'$ field of view of our camera has an effective bandpass centered on the the metastable helium feature. We calibrated this effect at the start of each night by illuminating the detector with light from a helium arc lamp (which emits in the 1083 nm line) and placing V1298 Tau on the resultant bright semicircular region where the effective filter bandpass is aligned with the metastable helium feature. Before beginning the exposure sequence on each night, we also performed a seven-point dither to construct a sky background frame.

Conditions were clear for the first night of observations on 2020 October 8 UT, but on 2020 November 27 UT, the seeing was exceptionally poor for Palomar (sometimes exceeding 3″). On the night of 2020 December 17 UT, there were rapid transparency variations due to thin cirrus coverage for most of the observation. On the night of 2021 January 1 UT, conditions were mostly clear, with some thin cirrus coverage appearing in the final hour. Due to a software crash we lost about 15 minutes of data in the middle of this final night.

The data were dark-subtracted, flat-fielded, and corrected for bad pixels using the method detailed in Tinyanont et al. (2019). As in Vissapragada et al. (2020a), we also corrected the non-uniform background (which arises from telluric OH emission lines) by median-scaling the dithered background frame in 10 px radial steps beginning from the filter zero point at the top of the detector, where light has encountered the filter at normal incidence. After image calibration, we performed aperture photometry on the target star and two comparison stars of similar brightness (HD 284153 and HD 284154) using the `photutils` package (Bradley et al., 2019), trying apertures with radii ranging from 5 to 20 px in 1 px steps (the pixel scale for WIRC is 0.″25/px). We allowed the aperture centers to shift in each image in order to track variations in the telescope pointing, and found average pointing shifts of 2-3 px on all nights. We subtracted any residual local background using an annulus around each source with an inner radius of 25 px and an outer radius of 50 px.

We pre-processed the light curves for all aperture sizes by clipping 5σ outliers using a moving median filter with a window size of 11. We then selected the optimal aperture size for each night of data by minimizing the per-point rms of the median-filtered photometry. We preferred an 11 px aperture for the 2020 October 8 night, a 15 px aperture for the 2020 November 27 night, a 7 px aperture for the 2020 December 17 night, and a 10 px aperture for the 2021 January 1 night.

HPF/HET

We obtained high resolution spectra of V1298 Tau with the Habitable-zone Planet Finder (HPF) spectrograph (Mahadevan, L. Ramsey, et al., 2012; Mahadevan, L. W. Ramsey, et al., 2014), a high-resolution ($R \sim 55,000$) temperature-stabilized (Stefansson, Hearty, et al., 2016) fiber-fed (Kanodia et al., 2018) spectrograph on the 10m Hobby Eberly Telescope at McDonald Observatory. HPF operates in the near-infrared (NIR) covering the z, Y, and J bands from 810-1280 nm, and fully resolves the He 1083 nm line. We observed V1298 Tau with HPF on 2020 October 12-14 UT and 2020 November 14 UT. The October 12 observation coincided with a transit of V1298 Tau c. For the October observations, we used an exposure time of 617.7 s, and for the November observations we used an exposure time of 564.5 s. We collected 6 exposures on the first night, 3 exposures on the second night, 3 exposures on the third night, and 6 exposures on the fourth night, with a median S/N of 143 per 1D extracted pixel at 1 μm.

The HPF 1D spectra were processed using the procedures described in J. P. Ninan et al., 2018, Kaplan et al., 2019, Metcalf et al., 2019, and Stefansson, Cañas, et al., 2020. Following Joe P. Ninan et al., 2020, we elected to observe V1298 Tau without the simultaneous HPF Laser Frequency Comb (LFC) calibrator, to minimize any possible impact from scattered light in the target star fiber. We deblazed the spectra using a combination of a static flat HPF exposure and a simultaneous low-order polynomial fit to account for residual low-order spectral differences for the different HPF visits. To correct for OH-sky emission, we estimated the sky background using the simultaneous HPF sky fiber and subtracted this background from the target star spectrum following Joe P. Ninan et al., 2020.

We correct for telluric absorption by using `molecfit` (Smette et al., 2015; Kausch et al., 2015) to fit telluric features in the deblazed and continuum normalized HPF spectra. It is important to obtain an accurate correction for the time-varying telluric absorption, as there are two telluric water lines that partially overlap with the He 1083 nm feature. For the `molecfit` fit, we used a Gaussian kernel to describe the HPF PSF. Although in actuality the HPF PSF shape is more complex, we tried modeling the PSF as a combination of a Gaussian and a Lorentzian and found that this did not improve the quality of the telluric correction. We therefore opted to use the simpler Gaussian fit in our final analysis. We restricted the fit to water lines, and allowed for the time-varying shape of these telluric features by fitting each spectrum independently. We also inflated the uncertainties in the vicinity of the telluric region by a factor of 1.2 to match the uncertainty estimate with the as-observed additional scatter due to imperfections in the telluric correction.

Figure 4.1 shows the resulting spectra after the telluric correction is applied. After applying the telluric correction, we calculated the equivalent width of the line in a region from 1083.1–1083.48 nm (see grey region in Figure 4.1b), which spans the full extent of the observed variation in the He 1083 nm line. Also shown is a light curve of V1298 Tau c taken on 2020 October 12 from the ARCTIC (Astrophysical Research Consortium Telescope Imaging Camera; Huehnerhoff et al., 2016) imager on the Astrophysical Research Consortium (ARC) 3.5m Telescope at Apache Point Observatory. The light curve exhibits a clear stellar flare 19 min before the HPF spectroscopic observations started. These observations and their associated modeling are described in detail in Livingston et al. (in prep.) Briefly, data were taken with a beam-shaping diffuser and narrow-band (30 nm) filter with minimal telluric absorption lines centered around 857 nm (see e.g., Stefansson, Mahadevan, Hebb, et al., 2017; Stefansson, Mahadevan, Wisniewski, et al., 2018). The flare, transit, and correlated noise were modeled using the `allesfitter` package (Günther and Daylan, 2019; Günther and Daylan, 2021), using the Davenport et al. (2014) parameterization for the flare and a Matern-3/2 kernel from `celerite` (Daniel Foreman-Mackey et al., 2017) to describe the correlated noise.

4.2 Light-curve Modeling

Palomar/WIRC

We fit the aperture-optimized WIRC photometry using the `exoplanet` package (Dan Foreman-Mackey et al., 2020). The priors for our model parameters are listed in Table 4.2. For each WIRC dataset, we modeled the light curve with a limb-darkened transit model (normalized to one) from `starry` (Luger et al., 2019) multiplied by a systematics model and then added to a baseline model. We fixed the mean ephemerides to the best-fit solution from Livingston et al. (in prep.), and used `TTVOrbit` to allow for an offset in the transit timing for each data set. For planet c, we placed a restrictive prior $\mathcal{N}(0\text{ min}, 30\text{ min})$ on the offset $\Delta T_{\rm c}$ to avoid fitting correlated features at the edges of the light curve. For planet b, we used a wide uniform prior $\mathcal{U}(-120\text{ min}, 120\text{ min})$ on the offset $\Delta T_{\rm b}$. The transit timing for planet d was measured independently by the Las Cumbres Observatory Global Telecope (LCOGT Brown et al., 2013) 1 m Sinistro imager on 2020 October 8 UT (Livingston et al. in prep.), so we fit that transit time $t_{\rm ingress}$ with a normal prior centered on the LCOGT transit time, and allowed for a TTV offset between the

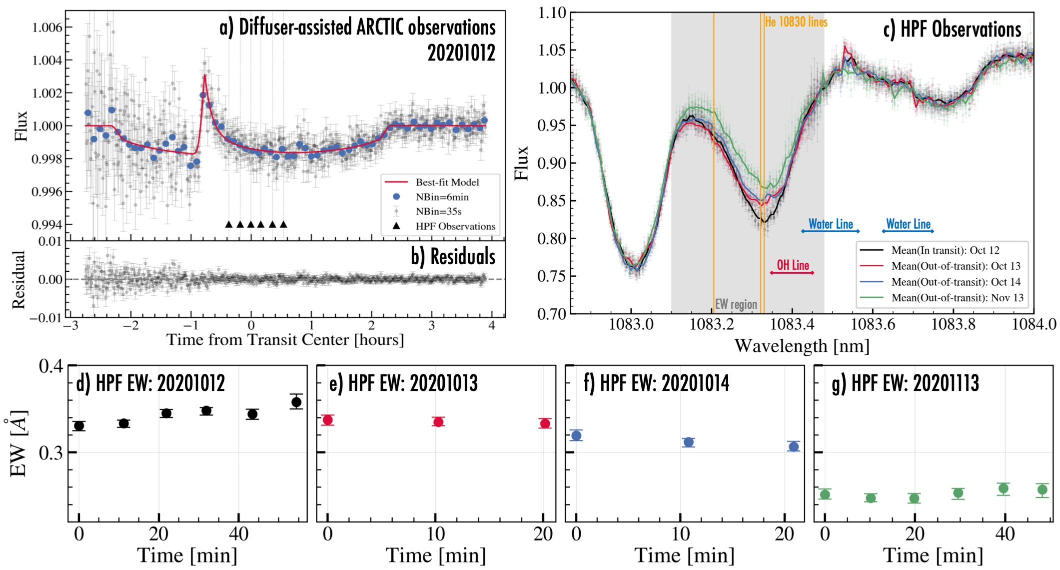

Figure 4.1: a) Diffuser-assisted transit observations of V1298 Tau c. Unbinned data are shown in black, and 6 min binned data are shown in blue. A large stellar flare is visible during the transit. The best-fit transit plus flare model is shown in red. The model and data are shown after removing the best-fit Gaussian Process correlated noise model. The black triangles denote the timing of the HPF observations obtained during the transit. b) Residuals from transit fit. c) Spectroscopic observations obtained with HPF of the He 1083 nm triplet (orange lines show the He 1083 nm triplet in the stellar rest frame). The averaged spectrum in black was obtained during the transit shown in the left panel, while averaged spectra from HPF visits on other nights are shown as colored points and lines. The locations of the OH and water lines are indicated in red and blue, respectively. d-g) Equivalent width (EW) measurements of the He 1083 nm line inside the grey region shown in panel c. We see a linear increase in the EWs during the transit (black points in d). The EWs remain stable over ~10 min timescales in the other visits, but change on timescales of days to months.

ingress and egress epochs with a uniform prior of $\mathcal{U}(-120\text{ min}, 120\text{ min})$.

We placed a uniform prior on the impact parameter b, which we sample using the algorithm from Espinoza, 2018. We fit this parameter jointly with detrended light curves from *K2* (David, Petigura, et al., 2019) in order to ensure that the final light curves have the correct transit duration, as we could only achieve partial phase coverage in most of our observations. We fit the the radius ratio in the WIRC bandpass with a wide uniform prior $\mathcal{U}(0, 0.3)$ for each planet. We use the difference between the WIRC radius ratio and the radius ratio in the $K2$ bandpass (David, Petigura, et al., 2019) as a measure of the excess absorption in the helium feature due to the presence of an extended atmosphere, which we label $\Delta R_\mathrm{p}/R_\star$.

We additionally included normal priors on the stellar mass and radius from David, Petigura, et al. (2019), and fit for the quadratic limb-darkening coefficients (u_1, u_2) using the Kipping (2013) prescription. Finally, we fit a photometric jitter term $\log(\sigma_{\rm extra})$ for each dataset to quantify the average scatter in excess of the photon noise.

For the baseline, we initially used a linear function $a_1 x' + a_0$ for each light curve, where a_i are free parameters with uniform priors $\mathcal{U}(-1, 1)$ for each dataset and $x' = x - \mathrm{med}(x)$ are the median-normalized BJD observation times. For planet c, where the observing conditions were relatively poor, we found that the results exhibited significant correlated noise, so we modeled the correlated component using an additional Gaussian Process (GP) term. We used a Matern-3/2 kernel as implemented in `celerite2` (Daniel Foreman-Mackey, 2018), with free parameters describing the timescale and amplitude, ρ and σ. We placed wide uniform priors of $\mathcal{U}(0, 0.3 \text{ days})$ and $\mathcal{U}(0, 0.1)$, respectively, on these two parameters.

For our systematic noise model we used a linear combination of detrending vectors, with each vector multiplied by a weight w_i and summed to generate the systematics model. We allowed each of these weights to vary as a free parameter in the fit with a uniform prior $\mathcal{U}(-1, 1)$. There were three detrending vectors for each night, including photometry for the two comparison stars and a proxy for the time-variable telluric water absorption. As discussed in the previous section, there are two telluric water lines that overlap with the metastable helium feature. In our photometric observations, we cannot fit for the telluric water spectrum and remove it from each individual image frame. Uncorrected time-varying absorption in these water lines can add correlated noise to the target star photometry and bias our estimate of the transit depth. We corrected this time-varying absorption using the method detailed in Paragas et al. (2021). In short, we used the integrated OH emission line intensities in our images to track the stability of the water feature using the ratio of water-contaminated to water-uncontaminated OH emission line intensities on the detector.

We used the No U-Turn Sampler (NUTS; Hoffman and Gelman, 2011) implemented in `PyMC3` (Salvatier, Wieckiâ, and Fonnesbeck, 2016) to sample the posterior distributions for our model parameters. We ran four chains, tuning each for 1,000 steps before taking 1,500 draws from the posterior (for a total of 6,000 draws). The Gelman-Rubin statistic (Gelman and Rubin, 1992) was less than 1.01 for all sampled parameters, indicating good convergence. We list the priors and posteriors for the

Table 4.2: Priors and posteriors for V1298 Tau fits for WIRC.

Parameter	Prior	Posterior	Units
$\Delta T_{0,\mathrm{c}}$	$\mathcal{N}(0,30)$	$-1.3^{+34.8}_{-29.2}$	min
b_c	Espinoza (2018)	$0.14^{+0.12}_{-0.09}$	–
$R_\mathrm{c}/R_\star$	$\mathcal{U}(0,0.3)$	$0.0128^{+0.0137}_{-0.0089}$	–
$\Delta R_\mathrm{c}/R_\star$	[derived]	$-0.025^{+0.014}_{-0.009}$	–
$\mathrm{t}_\mathrm{ingress}$	$\mathcal{N}(2459131.0943, 0.0077)$	$2459131.1088^{+0.0077}_{-0.0068}$	$\mathrm{BJD}_\mathrm{TDB}$
TTV_d	$\mathcal{U}(-120,120)$	-101^{+14}_{-12}	min
b_d	Espinoza (2018)	$0.124^{+0.124}_{-0.082}$	–
$R_\mathrm{d}/R_\star$	$\mathcal{U}(0,0.3)$	$0.0642^{+0.0047}_{-0.0048}$	–
$\Delta R_\mathrm{d}/R_\star$	[derived]	$0.0205^{+0.0055}_{-0.0053}$	–
$\Delta T_{0,\mathrm{b}}$	$\mathcal{U}(-120,120)$	$-56.5^{+14.4}_{-9.9}$	min
b_b	Espinoza (2018)	$0.439^{+0.041}_{-0.016}$	–
$R_\mathrm{b}/R_\star$	$\mathcal{U}(0,0.3)$	$0.0128^{+0.0137}_{-0.0089}$	–
$\Delta R_\mathrm{b}/R_\star$	[derived]	$0.0036^{+0.0095}_{-0.0107}$	–
$M_\star$	$\mathcal{N}(1.101, 0.050)$	$1.104^{+0.046}_{-0.045}$	$M_\odot$
$R_\star$	$\mathcal{N}(1.345, 0.056)$	$1.333^{+0.030}_{-0.024}$	$R_\odot$
u_1	Kipping (2013)	$1.80^{+0.11}_{-0.18}$	–
u_2	Kipping (2013)	$-0.851^{+0.160}_{-0.088}$	–

For brevity, we excluded the detrending vector weights, baseline coefficients, and jitter parameters from this table.

fits in Table 4.2, and plot the phased transit data along with the best-fit models and residuals in Figure 4.2.

4.3 Discussion

The Stellar Helium Line

The spectra in Figure 4.1 show a broad, deep helium feature for V1298 Tau, reaching equivalent widths of 0.35 Å. The line's equivalent width varies substantially on month-long timescales, decreasing to EW = 0.2 Å just one month after the first observation. We conclude that, for this 23 Myr-old pre-main sequence star, it is critical to acquire a reliable baseline measurement immediately before and after the transit. This stands in contrast to previous literature studies of older stars, which have successfully utilized baseline measurements collected across multiple epochs to measure the strength of the planetary helium absorption during the transit (Joe P. Ninan et al., 2020). The overall stellar line shape appears to remain consistent across all of our observations.

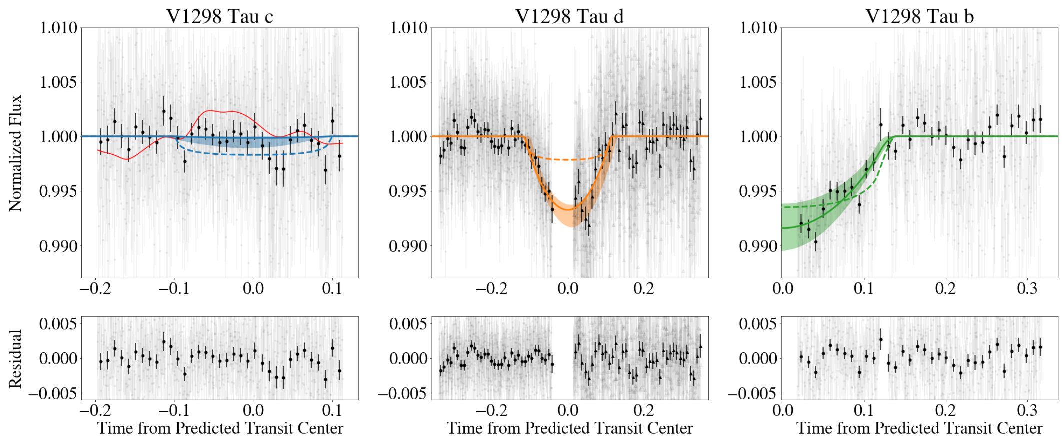

Figure 4.2: Detrended Palomar/WIRC helium light curves and residuals for V1298 Tau b, c, and d. For planet c (top left panel), we overplot the best-fit Gaussian Process model, which was subtracted from the light curve, as a solid red line. In all panels, unbinned data are shown in gray and data binned to 10 min cadence are shown in black. The circles and triangles for V1298 Tau d denote data from the first and second nights, respectively. In the top panels, the dashed colored line represents the best-fit *K2* optical light-curve model, the solid colored line indicates the best-fit WIRC light-curve model, and the shaded region represents the 68% confidence interval on the WIRC model.

Our helium transit light curves also require very strong limb-darkening in order to obtain a good fit. The Solar disk is known to exhibit strong limb-darkening in the helium line (e.g. Harvey and Sheeley, 1977), and this effect may be stronger for young, active stars. Additionally, there is a potential degeneracy between the model limb-darkening and the outflow geometry. Even for modest outflows, deviations from spherical symmetry in the extended metastable helium distribution can change the morphology of the light curve (Wang and Dai, 2021a; Wang and Dai, 2021b). Both of these factors may contribute to the "V-shaped" appearance of the light curves, especially for planet d.

A Stellar Flare Observed in Helium

Six HPF spectra were obtained during a white-light flare that overlapped with a transit of V1298 Tau c. As shown in Figure 4.1, the equivalent width (EW) of the He 1083 nm line appears to increase during the decay phase of the flare, whereas observations at other epochs exhibit stable EWs on similar timescales. We fit the EW increase in Figure 4.3 with a linear model (EW $= mt + b$) and find that $m = 0.66 \pm 0.19$ Å$\,\mathrm{day}^{-1}$. Integrating the resulting posteriors for the slope m suggests that $m > 0$ at 99.9% confidence.

Because the flare occurred during the transit of V1298 Tau c, it is difficult to definitively say whether the increase in helium EW during the transit is due to the star or the planet. CARMENES observations of the helium line in M dwarfs have shown evidence for enhanced helium absorption during flares (Fuhrmeister et al., 2020), consistent with our observations here. Recent work also suggests that stellar flares may lead to temporary enhancements in planetary mass loss rates and helium absorption; such enhancements are predicted to lag the peak of the flare by a few hours (the dynamical timescale; Wang and Dai, 2021a). Our observations were collected 0.5-1.5 hr from the flare peak, so we could also be observing enhanced helium absorption from planet c due to the flare.

However, as we will discuss in Section 4.3, our non-detection of helium absorption in planet c allows us to place an upper limit on the magnitude of helium absorption from the planet's atmosphere. This may indicate that helium in this planet's atmosphere is already mostly ionized, in which case any additional high-energy input from the flare would be unlikely to enhance the level population in the metastable state. We conclude that the simplest explanation is an enhancement in chromospheric helium absorption, but this can be tested with additional helium transit observations of planet c.

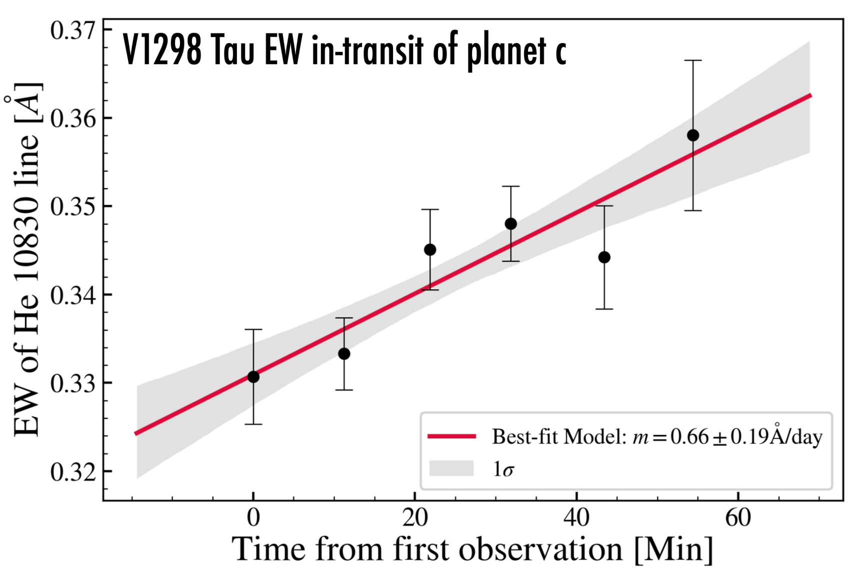

Figure 4.3: Linear fit to the metastable helium equivalent widths in the decay phase of the flare observed on 2020 October 12. The median model is plotted as a red line, and the grey shaded region represent the 1σ credible intervals.

Non-Detections for V1298 Tau b and c

We detected the egress of V1298 Tau b with a modest transit-timing offset of -57^{+14}_{-10} min. However, we did not require an extended planetary radius in the helium line to fit the data. Our upper limit of $\Delta R_b/R_\star < 0.019$ suggests that the planet does not exhibit strong helium absorption. This planet is relatively distant from its host star, so its atmosphere may not receive enough high-energy flux to drive a substantial outflow and/or create a substantial population of metastable helium. On the other hand, our data only cover half of the transit, which limits the sensitivity of our measurement. If planet b has an extended egress comparable to that of WASP-69 b (Nortmann et al., 2018) and WASP-107 b (Spake, A. Oklopčić, and L. A. Hillenbrand, 2021; Wang and Dai, 2021b), our data might still be consistent with a strong excess absorption signal during the transit. In this case the the transit-timing offset would need to be even larger, but we cannot exclude this possibility with the current partial phase coverage.

We were unable to detect the transit of V1298 Tau c at all. Our light curve exhibited strong correlated noise on the order of the broadband transit depth, likely stemming from the poor weather conditions during the observations. Our observations covered the full transit with approximately a transit duration's worth of additional baseline, so it would have required a TTV of $\gtrsim 3$ hr to shift the transit out of the observation window. We conclude that the non-detection is likely due to correlated noise in our light curve.

The non-detection of an escaping atmosphere is broadly consistent with recent work by Feinstein et al. (2021), who observed Hα variations with Gemini-N/GRACES during a transit of V1298 Tau c but concluded that these variations were most likely stellar in nature as they did not appear to originate in the planetary rest frame. Our result suggests that either this planet has a relatively low mass loss rate, or the helium in the observable region of its atmosphere is mostly ionized. Antonija Oklopčić (2019) modeled planets orbiting older (> Gyr) stars and found that planets on very close-in orbits should have helium ionization fronts at relatively low altitudes. Because ionization dominates over recombination through most of the upper atmospheres in these planets, the metastable state is not efficiently populated, and in-transit absorption in the 1083 nm line is suppressed. Although planet c's scaled semi-major axis is an order of magnitude larger than those of the planets with ionized atmospheres in Antonija Oklopčić (2019), the star also outputs 100× more high-energy radiation (Poppenhaeger, Ketzer, and Mallonn, 2021), so strong ionization is a plausible explanation for the non-detection. A thin ionization front at low altitudes would also place this planet in the recombination-limited mass loss regime (Murray-Clay, Chiang, and Murray, 2009; Owen and Alvarez, 2016; Lampón et al., 2021). Consequently, the mass-loss efficiency (in the energy-limited formalism) should be quite low.

A Tentative Signal for V1298 Tau d

For planet d, we find stronger evidence for an extended atmosphere with $\Delta R_{\mathrm{d}}/R_{\star} = 0.018 \pm 0.005$ (3.6σ). However, the posterior requires a rather large transit-timing offset between the ingress and egress epochs of V1298 Tau d of -100 ± 20 min. We note that the *K2* data, which spanned a period of two months, did not exhibit such large short-periodic TTVs. The data spanning ingress are well-behaved, with a scatter close to the photon noise limit and relatively little correlated noise. The transit time for this epoch was also independently measured with a broadband light curve (see §4.1), and the timing of ingress is tightly constrained by these data. On the other hand, the egress data have a larger variance relative to the photon noise limit and do not have any independent transit timing constraints. It is therefore possible that our constraints on the egress time are somehow biased by correlated noise in our data; if this is the case, it would also affect our estimate of the transit depth in the helium band. We therefore consider the measured excess absorption signal to be tentative at best.

We tested the robustness of our fit by adding the PSF widths and centroid offsets as covariates with their own weights in our systematics model. The former covariate is particularly relevant for the night of the egress observation (November 27), which had relatively poor and variable seeing. We found that the best-fit weights for these parameters were indistinguishable from zero, yielding parameter estimates within 1σ of those reported in Table 4.2. We conclude that our choice of systematics model has a negligible impact on the best-fit transit timing offset.

We next consider whether or not telluric effects might cause a spurious signal in our data. As discussed in §4.1, our helium bandpass overlaps with a strong telluric water feature, which can introduce a time-varying signal into our light curves (Paragas et al., 2021). While we correct for this effect by using a proxy for the time-varying water column as a detrending vector for all observations, the correction may be inadequate if the planetary helium absorption signal overlaps with the telluric water lines and both are variable. For typical line widths, the water line will encroach on the planetary helium feature for geocentric velocities of 50 km/s $\lesssim v \lesssim$ 85 km/s. The geocentric velocity of V1298 Tau on our WIRC nights ranges between -8 km/s (for the 2020 October observations) and 33 km/s (for the 2021 January observations). However, for strong planetary outflows the line may be broadened (Wang and Dai, 2021b), resulting in overlap with the telluric water features. Even at a modest 10 km/s geocentric velocity, the 2020 November HPF observations revealed that the strongly broadened stellar helium line was beginning to overlap with the telluric water lines. If the planetary helium line is similarly broad, then it is likely to overlap with the water line. Because the data for V1298 Tau d presented here are taken at small geocentric velocities, they should be less prone to this second-order effect.

Atmospheric Escape Modeling

If we assume that the excess absorption signal observed for V1298 Tau d is due to the extended atmosphere of the planet, we can translate this quantity into an inferred mass loss rate. We compare our measured $\Delta R_{\rm d}/R_\star$ value to predictions from the atmospheric escape model described in Antonija Oklopčić and Hirata (2018). This model treats the outflow as a 1D Parker wind with a fixed mass-loss rate $\dot{M}$ and thermosphere temperature T_0, and compute the level populations and resulting helium absorption signal during transit. We explored models spanning a wide range of thermosphere temperatures and mass loss rates, motivated by the broad range of values obtained in numerical simulations of atmospheric escape for a diverse sample of exoplanets presented in Salz, Czesla, Schneider, and Schmitt (2016). We mapped out the regions where the model predictions were consistent with our observations. For the photoionization and level population calculations we constructed an input stellar spectrum with an integrated XUV flux consistent with the estimate for V1298 Tau derived by Poppenhaeger, Ketzer, and Mallonn (2021), and a mid-UV flux consistent with spectra of T Tauri stars from Ingleby et al. (2013). We tested our sensitivity to the assumed high-energy stellar spectrum by re-running the intermediate mass model grid with a different input spectrum (also satisfying the integrated XUV flux estimate from Poppenhaeger, Ketzer, and Mallonn, 2021, but with different wavelength dependence), and found that it shifted our inferred mass loss rates upward by approximately a factor of three; we conclude that the stellar spectrum is a comparable or smaller source of uncertainty than the assumed planet mass (see discussion below).

In order to run these models, we must assume a value for the planet mass. Unfortunately, there are no published measurements of the mass of V1298 Tau d. We

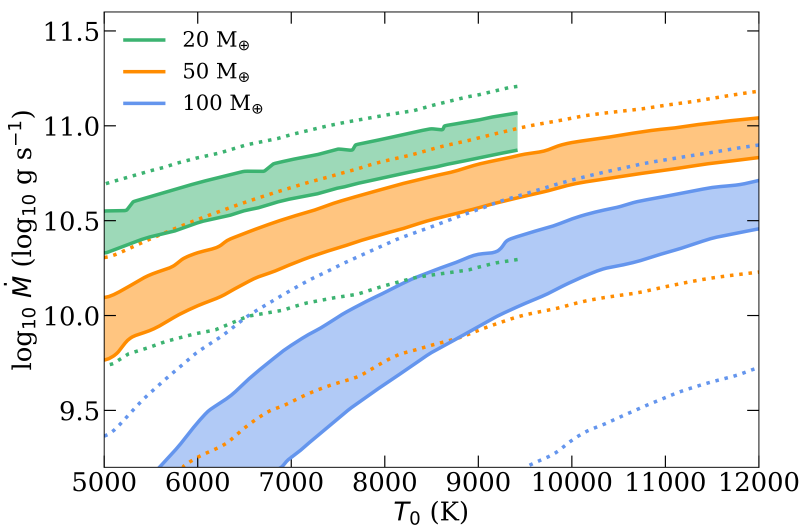

Figure 4.4: Combinations of mass-loss rate $\dot{M}$ and outflow temperature T_0 that generate helium absorption consistent with our V1298 Tau d light curve. Solutions are calculated assuming the planet is $20M_{\oplus}$ (green), $50M_{\oplus}$ (orange), and $100M_{\oplus}$ (blue). Shaded regions denote 1σ agreement with the observations and dotted lines denote 3σ agreement.

therefore ran three separate model grids for representative masses of 20 $M_{\oplus}$, 50 $M_{\oplus}$, and 100 $M_{\oplus}$. The latter mass is a rough empirical upper limit from Thorngren, Marley, and Fortney (2019), who studied an ensemble of older gas giant planets cooler than 1000 K. Planets in their sample with radii comparable to V1298 Tau d have $M \lesssim 100M_{\oplus}$, so we take this as a conservative upper limit on the mass of planet d. On the low-mass end, previous studies of the V1298 system (David, Cody, et al., 2019; David, Petigura, et al., 2019) have suggested that these planets may have masses closer to those of the sub-Neptune population observed by Kepler (i.e., 1-10 $M_{\oplus}$). This idea is supported by the current ensemble of TTV measurements for this system, which appear to favor $M_{\rm d} < 10M_{\oplus}$ (Livingston et al. in prep.). For masses below 10 $M_{\oplus}$, the radius at which isothermal Parker wind becomes supersonic (assuming our standard range of thermospheric temperatures and the high ionization state of the atmosphere caused by the strong XUV flux of the host star) falls below the nominal radius of the planet. Since we do not consider our model assumption to be applicable in the low-mass part of the parameter space, we restrict our analysis to planet masses above 20 $M_{\oplus}$. We therefore use a 20 $M_{\oplus}$ model as our lowest mass case, and present the results in Figure 4.4.

Perhaps unsurprisingly, we find that there are a wide range of mass-loss rates that are consistent with our observations. For the nominal input spectrum, we can place a lower limit of $M/\dot{M} \approx 24$ Gyr (3σ) on the atmospheric lifetime for the hottest 20 $M_\oplus$ model. At a fixed thermosphere temperature, as the assumed mass increases the maximum mass-loss rate consistent with the data decreases, leading to even longer atmospheric lifetimes. This suggests that the atmosphere of V1298 Tau d should be stable against catastrophic mass loss if the planetary mass is indeed 20 $M_\oplus$ or larger. We can also estimate the threshold for catastrophic mass loss, here defined as $M/\dot{M} \lesssim 1$ Gyr, by assuming the largest mass-loss rate consistent with our observations still holds for $M_\mathrm{d} < 20 M_\oplus$. This approach suggests that the envelope can be fully removed if $M_\mathrm{d} \lesssim (10^{11.2}\ \mathrm{g/s})(1\ \mathrm{Gyr}) \approx M_\oplus$. In reality, the crossover to catastrophic escape will happen at a larger mass as the mass-loss rate should be even larger for $M_\mathrm{d} < 20 M_\oplus$, but because we cannot model these cases with the 1D Parker wind methodology, we default to this conservative approximation.

4.4 Conclusions

In this work, we searched for metastable helium in the atmospheres of V1298 Tau b, c, and d. We first characterized the stellar helium line using high-resolution spectra from HET/HPF. We found that the helium line is relatively stable on hourly timescales in quiescent conditions, but can be highly variable timescales of days to months. We observed an appreciable increase in the helium equivalent width of spectra gathered during a transit of planet c, in the decay phase of a flare that was simultaneously observed photometrically with APO/ARCTIC. We concluded that this increase was most likely due to an increased population of metastable helium in the stellar chromosphere. We used diffuser-assisted narrowband photometry to measure light curves of V1298 Tau in a bandbass centered on the 1083 nm helium feature on four nights. We did not detect the transit of V1298 Tau c, and we modeled the transit of V1298 Tau b without needing an extended atmosphere. We found tentative evidence for planetary helium absorption in V1298 Tau d (3.6σ significance), but the best-fit model required a relatively large transit-timing offset between the two transit epochs.

V1298 Tau is the only known young transiting system near a resonant chain, making it an important target for young planet studies. Ongoing TTV studies should eventually allow us to obtain well-constrained mass measurements (Livingston et al. in prep), therefore circumventing the difficulties of obtaining precise radial velocity measurements for this young, active star. TESS will observe V1298 Tau from 2021 September to 2021 November, significantly expanding the TTV baseline and providing improved dynamical constraints on the planet masses. These new observations will also help to reduce the growing uncertainty in the planetary ephemerides, which will be crucial for scheduling future ground-based transit observations. We expect that in the coming years, additional helium transit observations will be able to clarify the planetary origin of the tentative signal we report here. Ideally these observations should be obtained with long baselines and at geocentric velocities where the stellar helium line and the telluric water features do not overlap. High resolution coverage of the metastable helium feature would also make it easier to disentangle the time-varying planetary, stellar, and telluric signals.

If the excess absorption signal from V1298 d can be confirmed at high signal-to-noise and combined with a well-constrained TTV mass measurement, our estimate of the planet's absolute mass loss rate will be limited by our knowledge of the star's high energy spectrum. Poppenhaeger, Ketzer, and Mallonn (2021) measured V1298 Tau's X-ray spectrum between 0.1 keV and 2 keV, but the photoionization physics for metastable helium is governed primarily by mid-UV and EUV flux near the ionization thresholds of the metastable and ground states, respectively (Antonija Oklopčić and Hirata, 2018; Antonija Oklopčić, 2019). One way of reconstructing the EUV spectrum is the differential emission measure technique, which relies on measurements of stellar emission lines in the FUV (Duvvuri et al., 2021). Although it would be challenging to detect these lines in V1298 Tau's spectrum, as this star is located at a distance of 108.5 pc, they may be observable with the *Hubble Space Telescope*.

Constraining mass-loss rates in a young, well-characterized multi-planet system remains an important goal. These measurements can help differentiate between the recombination-limited, energy-limited, and photon-limited regimes for mass loss at early times, which would have crucial implications for the outflow efficiencies (Lampón et al., 2021). In turn, this would allow us to benchmark population-level mass-loss models, like those used to infer core masses and compositions of the *Kepler* planets (Rogers and Owen, 2021). As the precision of mass-loss measurements improve for younger planets, V1298 Tau will be a keystone system for understanding and characterizing this crucial process when it is most important for planetary evolution.

References

Allart, R., V. Bourrier, C. Lovis, D. Ehrenreich, J. Aceituno, et al. (Mar. 2019). "High-resolution confirmation of an extended helium atmosphere around WASP-107b". In: *A&A* 623, A58, A58. DOI: 10.1051/0004-6361/201834917. arXiv: 1901.08073 [astro-ph.EP].

Allart, R., V. Bourrier, C. Lovis, D. Ehrenreich, J. J. Spake, et al. (Dec. 2018). "Spectrally resolved helium absorption from the extended atmosphere of a warm Neptune-mass exoplanet". In: *Science* 362.6421, pp. 1384–1387. DOI: 10.1126/science.aat5879. arXiv: 1812.02189 [astro-ph.EP].

Alonso-Floriano, F. J. et al. (Sept. 2019). "He I λ 10 830 Å in the transmission spectrum of HD209458 b". In: *A&A* 629, A110, A110. DOI: 10.1051/0004-6361/201935979. arXiv: 1907.13425 [astro-ph.EP].

Beichman, Charles et al. (June 2019). "A Mass Limit for the Young Transiting Planet V1298 Tau b". In: *Research Notes of the American Astronomical Society* 3.6, 89, p. 89. DOI: 10.3847/2515-5172/ab2c9d.

Bouma, L. G. et al. (Nov. 2020). "Cluster Difference Imaging Photometric Survey. II. TOI 837: A Young Validated Planet in IC 2602". In: *AJ* 160.5, 239, p. 239. DOI: 10.3847/1538-3881/abb9ab. arXiv: 2009.07845 [astro-ph.EP].

Bourrier, V. et al. (Dec. 2018). "Hubble PanCET: an extended upper atmosphere of neutral hydrogen around the warm Neptune GJ 3470b". In: *A&A* 620, A147, A147. DOI: 10.1051/0004-6361/201833675. arXiv: 1812.05119 [astro-ph.EP].

Bradley, Larry et al. (Oct. 2019). *astropy/photutils: v0.7.1*. Version v0.7.1. DOI: 10.5281/zenodo.3478575.

Brown, T. M. et al. (Sept. 2013). "Las Cumbres Observatory Global Telescope Network". In: *PASP* 125.931, p. 1031. DOI: 10.1086/673168. arXiv: 1305.2437 [astro-ph.IM].

Carleo, I. et al. (Jan. 2021). "The GAPS Programme at TNG. XXVIII. A pair of hot-Neptunes orbiting the young star TOI-942". In: *A&A* 645, A71, A71. DOI: 10.1051/0004-6361/202039042. arXiv: 2011.13795 [astro-ph.EP].

Davenport, James R. A. et al. (Dec. 2014). "Kepler Flares. II. The Temporal Morphology of White-light Flares on GJ 1243". In: *ApJ* 797.2, 122, p. 122. DOI: 10.1088/0004-637X/797/2/122. arXiv: 1411.3723 [astro-ph.SR].

David, Trevor J., Ann Marie Cody, et al. (Aug. 2019). "A Warm Jupiter-sized Planet Transiting the Pre-main-sequence Star V1298 Tau". In: *AJ* 158.2, 79, p. 79. DOI: 10.3847/1538-3881/ab290f. arXiv: 1902.09670 [astro-ph.EP].

David, Trevor J., Lynne A. Hillenbrand, et al. (June 2016). "A Neptune-sized transiting planet closely orbiting a 5-10-million-year-old star". In: *Nature* 534.7609, pp. 658–661. DOI: 10.1038/nature18293. arXiv: 1606.06729 [astro-ph.EP].

David, Trevor J., Erik A. Petigura, et al. (Nov. 2019). "Four Newborn Planets Transiting the Young Solar Analog V1298 Tau". In: *ApJL* 885.1, L12, p. L12. DOI: 10.3847/2041-8213/ab4c99. arXiv: 1910.04563 [astro-ph.EP].

Duvvuri, Girish M. et al. (May 2021). "Reconstructing the Extreme Ultraviolet Emission of Cool Dwarfs Using Differential Emission Measure Polynomials". In: *ApJ* 913.1, 40, p. 40. DOI: 10.3847/1538-4357/abeaaf. arXiv: 2102.08493 [astro-ph.SR].

Ehrenreich, David et al. (June 2015). "A giant comet-like cloud of hydrogen escaping the warm Neptune-mass exoplanet GJ 436b". In: *Nature* 522.7557, pp. 459–461. DOI: 10.1038/nature14501. arXiv: 1506.07541 [astro-ph.EP].

Espinoza, Néstor (Nov. 2018). "Efficient Joint Sampling of Impact Parameters and Transit Depths in Transiting Exoplanet Light Curves". In: *Research Notes of the American Astronomical Society* 2.4, 209, p. 209. DOI: 10.3847/2515-5172/aaef38. arXiv: 1811.04859 [astro-ph.EP].

Feinstein, Adina et al. (July 2021). "H-alpha and Ca II Infrared Triplet Variations During a Transit of the 23 Myr Planet V1298 Tau c". In: *Posters from the TESS Science Conference II (TSC2)*, 40, p. 40. DOI: 10.5281/zenodo.5122821.

Foreman-Mackey, Dan et al. (May 2020). *exoplanet-dev/exoplanet: exoplanet v0.3.2*. Version v0.3.2. DOI: 10.5281/zenodo.3785072.

Foreman-Mackey, Daniel (Feb. 2018). "Scalable Backpropagation for Gaussian Processes using Celerite". In: *Research Notes of the American Astronomical Society* 2.1, 31, p. 31. DOI: 10.3847/2515-5172/aaaf6c. arXiv: 1801.10156 [astro-ph.IM].

Foreman-Mackey, Daniel et al. (Dec. 2017). "Fast and Scalable Gaussian Process Modeling with Applications to Astronomical Time Series". In: *AJ* 154.6, 220, p. 220. DOI: 10.3847/1538-3881/aa9332. arXiv: 1703.09710 [astro-ph.IM].

Fuhrmeister, B. et al. (Aug. 2020). "The CARMENES search for exoplanets around M dwarfs. Variability of the He I line at 10 830 Å". In: *A&A* 640, A52, A52. DOI: 10.1051/0004-6361/202038279. arXiv: 2006.09372 [astro-ph.SR].

Fulton, Benjamin J. and Erik A. Petigura (Dec. 2018). "The California-Kepler Survey. VII. Precise Planet Radii Leveraging Gaia DR2 Reveal the Stellar Mass Dependence of the Planet Radius Gap". In: *AJ* 156.6, 264, p. 264. DOI: 10.3847/1538-3881/aae828. arXiv: 1805.01453 [astro-ph.EP].

Fulton, Benjamin J., Erik A. Petigura, et al. (Sept. 2017). "The California-Kepler Survey. III. A Gap in the Radius Distribution of Small Planets". In: *AJ* 154.3, 109, p. 109. DOI: 10.3847/1538-3881/aa80eb. arXiv: 1703.10375 [astro-ph.EP].

Gelman, Andrew and Donald B. Rubin (Jan. 1992). "Inference from Iterative Simulation Using Multiple Sequences". In: *Statistical Science* 7, pp. 457–472. DOI: 10.1214/ss/1177011136.

Ginzburg, Sivan, Hilke E. Schlichting, and Re'em Sari (May 2018). "Core-powered mass-loss and the radius distribution of small exoplanets". In: *MNRAS* 476.1, pp. 759–765. DOI: 10.1093/mnras/sty290. arXiv: 1708.01621 [astro-ph.EP].

Günther, Maximilian N. and Tansu Daylan (Mar. 2019). *allesfitter: Flexible star and exoplanet inference from photometry and radial velocity*. ascl: 1903.003.

– (May 2021). "Allesfitter: Flexible Star and Exoplanet Inference from Photometry and Radial Velocity". In: *ApJS* 254.1, 13, p. 13. DOI: 10.3847/1538-4365/abe70e. arXiv: 2003.14371 [astro-ph.EP].

Gupta, Akash and Hilke E. Schlichting (July 2019). "Sculpting the valley in the radius distribution of small exoplanets as a by-product of planet formation: the core-powered mass-loss mechanism". In: *MNRAS* 487.1, pp. 24–33. DOI: 10.1093/mnras/stz1230. arXiv: 1811.03202 [astro-ph.EP].

Hardegree-Ullman, Kevin K. et al. (Mar. 2020). "Scaling K2. I. Revised Parameters for 222,088 K2 Stars and a K2 Planet Radius Valley at 1.9 $R_\oplus$". In: *ApJS* 247.1, 28, p. 28. DOI: 10.3847/1538-4365/ab7230. arXiv: 2001.11511 [astro-ph.SR].

Harvey, J. W. and Jr. Sheeley N. R. (Oct. 1977). "A comparison of He ii 304 Å and He i 10 830 Å spectroheliograms". In: *SoPh* 54.2, pp. 343–351. DOI: 10.1007/BF00159924.

Hirano, Teruyuki et al. (Aug. 2020). "Limits on the Spin-Orbit Angle and Atmospheric Escape for the 22 Myr Old Planet AU Mic b". In: *ApJL* 899.1, L13, p. L13. DOI: 10.3847/2041-8213/aba6eb. arXiv: 2006.13243 [astro-ph.EP].

Hoffman, Matthew D. and Andrew Gelman (Nov. 2011). "The No-U-Turn Sampler: Adaptively Setting Path Lengths in Hamiltonian Monte Carlo". In: *arXiv e-prints*, arXiv:1111.4246, arXiv:1111.4246. arXiv: 1111.4246 [stat.CO].

Huehnerhoff, Joseph et al. (Aug. 2016). "Astrophysical Research Consortium Telescope Imaging Camera (ARCTIC) facility optical imager for the Apache Point Observatory 3.5m telescope". In: *Ground-based and Airborne Instrumentation for Astronomy VI*. Ed. by Christopher J. Evans, Luc Simard, and Hideki Takami. Vol. 9908. Society of Photo-Optical Instrumentation Engineers (SPIE) Conference Series, 99085H, 99085H. DOI: 10.1117/12.2234214.

Ingleby, Laura et al. (Apr. 2013). "Accretion Rates for T Tauri Stars Using Nearly Simultaneous Ultraviolet and Optical Spectra". In: *ApJ* 767.2, 112, p. 112. DOI: 10.1088/0004-637X/767/2/112. arXiv: 1303.0769 [astro-ph.SR].

Kanodia, Shubham et al. (Aug. 2018). "Overview of the spectrometer optical fiber feed for the habitable-zone planet finder". In: *Ground-based and Airborne Instrumentation for Astronomy VII*. Ed. by Christopher J. Evans, Luc Simard, and Hideki Takami. Vol. 10702. Society of Photo-Optical Instrumentation Engineers (SPIE) Conference Series, 107026Q, 107026Q. DOI: 10.1117/12.2313491. arXiv: 1808.00557 [astro-ph.IM].

Kaplan, Kyle F. et al. (Oct. 2019). "The Algorithms Behind the HPF and NEID Pipeline". In: *Astronomical Data Analysis Software and Systems XXVII*. Ed. by Peter J. Teuben et al. Vol. 523. Astronomical Society of the Pacific Conference Series, p. 567.

Kausch, W. et al. (Apr. 2015). "Molecfit: A general tool for telluric absorption correction. II. Quantitative evaluation on ESO-VLT/X-Shooterspectra". In: *A&A* 576, A78, A78. DOI: 10.1051/0004-6361/201423909. arXiv: 1501.07265 [astro-ph.IM].

King, George W. and Peter J. Wheatley (Jan. 2021). "EUV irradiation of exoplanet atmospheres occurs on Gyr time-scales". In: *MNRAS* 501.1, pp. L28–L32. DOI: 10.1093/mnrasl/slaa186. arXiv: 2007.13731 [astro-ph.EP].

Kipping, David M. (Nov. 2013). "Efficient, uninformative sampling of limb darkening coefficients for two-parameter laws". In: *MNRAS* 435.3, pp. 2152–2160. DOI: 10.1093/mnras/stt1435. arXiv: 1308.0009 [astro-ph.SR].

Kirk, James et al. (Mar. 2020). "Confirmation of WASP-107b's Extended Helium Atmosphere with Keck II/NIRSPEC". In: *AJ* 159.3, 115, p. 115. DOI: 10.3847/1538-3881/ab6e66. arXiv: 2001.07667 [astro-ph.EP].

Klein, Baptiste et al. (Mar. 2021). "Investigating the young AU Mic system with SPIRou: large-scale stellar magnetic field and close-in planet mass". In: *MNRAS* 502.1, pp. 188–205. DOI: 10.1093/mnras/staa3702. arXiv: 2011.13357 [astro-ph.EP].

Lampón, M. et al. (Apr. 2021). "Evidence of energy-, recombination-, and photon-limited escape regimes in giant planet H/He atmospheres". In: *A&A* 648, L7, p. L7. DOI: 10.1051/0004-6361/202140423. arXiv: 2104.08832 [astro-ph.EP].

Lecavelier Des Etangs, A. et al. (May 2010). "Evaporation of the planet HD 189733b observed in H I Lyman-α". In: *A&A* 514, A72, A72. DOI: 10.1051/0004-6361/200913347. arXiv: 1003.2206 [astro-ph.EP].

Lopez, Eric D. and Jonathan J. Fortney (Oct. 2013). "The Role of Core Mass in Controlling Evaporation: The Kepler Radius Distribution and the Kepler-36 Density Dichotomy". In: *ApJ* 776.1, 2, p. 2. DOI: 10.1088/0004-637X/776/1/2. arXiv: 1305.0269 [astro-ph.EP].

Luger, Rodrigo et al. (Feb. 2019). "starry: Analytic Occultation Light Curves". In: *AJ* 157.2, 64, p. 64. DOI: 10.3847/1538-3881/aae8e5. arXiv: 1810.06559 [astro-ph.IM].

Lundkvist, M. S. et al. (Apr. 2016). "Hot super-Earths stripped by their host stars". In: *Nature Communications* 7, 11201, p. 11201. DOI: 10.1038/ncomms11201. arXiv: 1604.05220 [astro-ph.EP].

Mahadevan, Suvrath, Lawrence Ramsey, et al. (Sept. 2012). "The habitable-zone planet finder: a stabilized fiber-fed NIR spectrograph for the Hobby-Eberly Telescope". In: *Ground-based and Airborne Instrumentation for Astronomy IV*. Ed. by Ian S. McLean, Suzanne K. Ramsay, and Hideki Takami. Vol. 8446. Society of Photo-Optical Instrumentation Engineers (SPIE) Conference Series, 84461S, 84461S. DOI: 10.1117/12.926102. arXiv: 1209.1686 [astro-ph.EP].

Mahadevan, Suvrath, Lawrence W. Ramsey, et al. (July 2014). "The Habitable-zone Planet Finder: A status update on the development of a stabilized fiber-fed near-infrared spectrograph for the for the Hobby-Eberly telescope". In: *Ground-based and Airborne Instrumentation for Astronomy V*. Ed. by Suzanne K. Ramsay, Ian S. McLean, and Hideki Takami. Vol. 9147. Society of Photo-Optical Instrumentation Engineers (SPIE) Conference Series, 91471G, 91471G. DOI: 10.1117/12.2056417.

Mann, Andrew W. et al. (Sept. 2016). "Zodiacal Exoplanets in Time (ZEIT). III. A Short-period Planet Orbiting a Pre-main-sequence Star in the Upper Scorpius OB Association". In: *AJ* 152.3, 61, p. 61. DOI: 10.3847/0004-6256/152/3/61. arXiv: 1604.06165 [astro-ph.EP].

Mansfield, Megan et al. (Dec. 2018). "Detection of Helium in the Atmosphere of the Exo-Neptune HAT-P-11b". In: *ApJL* 868.2, L34, p. L34. DOI: 10.3847/2041-8213/aaf166. arXiv: 1812.02214 [astro-ph.EP].

Mazeh, T., T. Holczer, and S. Faigler (May 2016). "Dearth of short-period Neptunian exoplanets: A desert in period-mass and period-radius planes". In: *A&A* 589, A75, A75. DOI: 10.1051/0004-6361/201528065. arXiv: 1602.07843 [astro-ph.EP].

Metcalf, Andrew J. et al. (Feb. 2019). "Stellar spectroscopy in the near-infrared with a laser frequency comb". In: *Optica* 6.2, p. 233. DOI: 10.1364/OPTICA.6.000233. arXiv: 1902.00500 [astro-ph.EP].

Murray-Clay, Ruth A., Eugene I. Chiang, and Norman Murray (Mar. 2009). "Atmospheric Escape From Hot Jupiters". In: *ApJ* 693.1, pp. 23–42. DOI: 10.1088/0004-637X/693/1/23. arXiv: 0811.0006 [astro-ph].

Newton, Elisabeth R. et al. (July 2019). "TESS Hunt for Young and Maturing Exoplanets (THYME): A Planet in the 45 Myr Tucana-Horologium Association". In: *ApJL* 880.1, L17, p. L17. DOI: 10.3847/2041-8213/ab2988. arXiv: 1906.10703 [astro-ph.EP].

Ninan, J. P. et al. (Aug. 2018). "The Habitable-Zone Planet Finder: improved flux image generation algorithms for H2RG up-the-ramp data". In: *High Energy, Optical, and Infrared Detectors for Astronomy VIII*. Ed. by Andrew D. Holland and James Beletic. Vol. 10709. Society of Photo-Optical Instrumentation Engineers (SPIE) Conference Series, 107092U, 107092U. DOI: 10.1117/12.2312787.

Ninan, Joe P. et al. (May 2020). “Evidence for He I 10830 Å Absorption during the Transit of a Warm Neptune around the M-dwarf GJ 3470 with the Habitable-zone Planet Finder”. In: *ApJ* 894.2, 97, p. 97. doi: 10.3847/1538-4357/ab8559. arXiv: 1910.02070 [astro-ph.EP].

Nortmann, Lisa et al. (Dec. 2018). “Ground-based detection of an extended helium atmosphere in the Saturn-mass exoplanet WASP-69b”. In: *Science* 362.6421, pp. 1388–1391. doi: 10.1126/science.aat5348. arXiv: 1812.03119 [astro-ph.EP].

Oklopčić, Antonija (Aug. 2019). “Helium Absorption at 1083 nm from Extended Exoplanet Atmospheres: Dependence on Stellar Radiation”. In: *ApJ* 881.2, 133, p. 133. doi: 10.3847/1538-4357/ab2f7f. arXiv: 1903.02576 [astro-ph.EP].

Oklopčić, Antonija and Christopher M. Hirata (Mar. 2018). “A New Window into Escaping Exoplanet Atmospheres: 10830 Å Line of Helium”. In: *ApJL* 855.1, L11, p. L11. doi: 10.3847/2041-8213/aaada9. arXiv: 1711.05269 [astro-ph.EP].

Owen, James E. (May 2019). “Atmospheric Escape and the Evolution of Close-In Exoplanets”. In: *Annual Review of Earth and Planetary Sciences* 47, pp. 67–90. doi: 10.1146/annurev-earth-053018-060246. arXiv: 1807.07609 [astro-ph.EP].

Owen, James E. and Marcelo A. Alvarez (Jan. 2016). “UV Driven Evaporation of Close-in Planets: Energy-limited, Recombination-limited, and Photon-limited Flows”. In: *ApJ* 816.1, 34, p. 34. doi: 10.3847/0004-637X/816/1/34. arXiv: 1504.07170 [astro-ph.EP].

Owen, James E. and Dong Lai (Oct. 2018). “Photoevaporation and high-eccentricity migration created the sub-Jovian desert”. In: *MNRAS* 479.4, pp. 5012–5021. doi: 10.1093/mnras/sty1760. arXiv: 1807.00012 [astro-ph.EP].

Owen, James E. and Yanqin Wu (Oct. 2013). “Kepler Planets: A Tale of Evaporation”. In: *ApJ* 775.2, 105, p. 105. doi: 10.1088/0004-637X/775/2/105. arXiv: 1303.3899 [astro-ph.EP].

– (Sept. 2017). “The Evaporation Valley in the Kepler Planets”. In: *ApJ* 847.1, 29, p. 29. doi: 10.3847/1538-4357/aa890a. arXiv: 1705.10810 [astro-ph.EP].

Palle, E. et al. (June 2020). “A He I upper atmosphere around the warm Neptune GJ 3470 b”. In: *A&A* 638, A61, A61. doi: 10.1051/0004-6361/202037719. arXiv: 2004.12812 [astro-ph.EP].

Paragas, Kimberly et al. (Mar. 2021). “Metastable Helium Reveals an Extended Atmosphere for the Gas Giant HAT-P-18b”. In: *ApJL* 909.1, L10, p. L10. doi: 10.3847/2041-8213/abe706. arXiv: 2102.08392 [astro-ph.EP].

Plavchan, Peter et al. (June 2020). “A planet within the debris disk around the pre-main-sequence star AU Microscopii”. In: *Nature* 582.7813, pp. 497–500. doi: 10.1038/s41586-020-2400-z. arXiv: 2006.13248 [astro-ph.EP].

Poppenhaeger, K., L. Ketzer, and M. Mallonn (Jan. 2021). "X-ray irradiation and evaporation of the four young planets around V1298 Tau". In: *MNRAS* 500.4, pp. 4560–4572. DOI: 10.1093/mnras/staa1462. arXiv: 2005.10240 [astro-ph.EP].

Rizzuto, Aaron C. et al. (July 2020). "TESS Hunt for Young and Maturing Exoplanets (THYME). II. A 17 Myr Old Transiting Hot Jupiter in the Sco-Cen Association". In: *AJ* 160.1, 33, p. 33. DOI: 10.3847/1538-3881/ab94b7. arXiv: 2005.00013 [astro-ph.EP].

Rogers, James G. and James E. Owen (May 2021). "Unveiling the planet population at birth". In: *MNRAS* 503.1, pp. 1526–1542. DOI: 10.1093/mnras/stab529. arXiv: 2007.11006 [astro-ph.EP].

Salvatier, John, Thomas V. Wieckiâ, and Christopher Fonnesbeck (Oct. 2016). *PyMC3: Python probabilistic programming framework*. ascl: 1610.016.

Salz, M., S. Czesla, P. C. Schneider, E. Nagel, et al. (Dec. 2018). "Detection of He I λ10830 Å absorption on HD 189733 b with CARMENES high-resolution transmission spectroscopy". In: *A&A* 620, A97, A97. DOI: 10.1051/0004-6361/201833694. arXiv: 1812.02453 [astro-ph.EP].

Salz, M., S. Czesla, P. C. Schneider, and J. H. M. M. Schmitt (Feb. 2016). "Simulating the escaping atmospheres of hot gas planets in the solar neighborhood". In: *A&A* 586, A75, A75. DOI: 10.1051/0004-6361/201526109. arXiv: 1511.09341 [astro-ph.EP].

Smette, A. et al. (Apr. 2015). "Molecfit: A general tool for telluric absorption correction. I. Method and application to ESO instruments". In: *A&A* 576, A77, A77. DOI: 10.1051/0004-6361/201423932. arXiv: 1501.07239 [astro-ph.IM].

Spake, J. J., A. Oklopčić, and L. A. Hillenbrand (Dec. 2021). "The Posttransit Tail of WASP-107b Observed at 10830 Å". In: *AJ* 162.6, 284, p. 284. DOI: 10.3847/1538-3881/ac178a. arXiv: 2107.08999 [astro-ph.EP].

Spake, J. J., D. K. Sing, et al. (May 2018). "Helium in the eroding atmosphere of an exoplanet". In: *Nature* 557.7703, pp. 68–70. DOI: 10.1038/s41586-018-0067-5. arXiv: 1805.01298 [astro-ph.EP].

Stefansson, Gudmundur, Caleb Cañas, et al. (Mar. 2020). "A Sub-Neptune-sized Planet Transiting the M2.5 Dwarf G 9-40: Validation with the Habitable-zone Planet Finder". In: *AJ* 159.3, 100, p. 100. DOI: 10.3847/1538-3881/ab5f15. arXiv: 1912.00291 [astro-ph.EP].

Stefansson, Gudmundur, Frederick Hearty, et al. (Dec. 2016). "A Versatile Technique to Enable Sub-milli-Kelvin Instrument Stability for Precise Radial Velocity Measurements: Tests with the Habitable-zone Planet Finder". In: *ApJ* 833.2, 175, p. 175. DOI: 10.3847/1538-4357/833/2/175. arXiv: 1610.06216 [astro-ph.IM].

Stefansson, Gudmundur, Suvrath Mahadevan, Leslie Hebb, et al. (Oct. 2017). “Toward Space-like Photometric Precision from the Ground with Beam-shaping Diffusers”. In: *ApJ* 848.1, 9, p. 9. DOI: 10.3847/1538-4357/aa88aa. arXiv: 1710.01790 [astro-ph.IM].

Stefansson, Gudmundur, Suvrath Mahadevan, John Wisniewski, et al. (Aug. 2018). “Extreme precision photometry from the ground with beam-shaping diffusers for K2, TESS, and beyond”. In: *Ground-based and Airborne Instrumentation for Astronomy VII*. Ed. by Christopher J. Evans, Luc Simard, and Hideki Takami. Vol. 10702. Society of Photo-Optical Instrumentation Engineers (SPIE) Conference Series, 1070250, p. 1070250. DOI: 10.1117/12.2312833. arXiv: 1808.02187 [astro-ph.IM].

Thorngren, Daniel P., Mark S. Marley, and Jonathan J. Fortney (Sept. 2019). “An Empirical Mass-Radius Relation for Cool Giant Planets”. In: *Research Notes of the American Astronomical Society* 3.9, 128, p. 128. DOI: 10.3847/2515-5172/ab4353.

Tinyanont, Samaporn et al. (Feb. 2019). “WIRC+Pol: A Low-resolution Near-infrared Spectropolarimeter”. In: *PASP* 131.996, p. 025001. DOI: 10.1088/1538-3873/aaef0f. arXiv: 1811.03138 [astro-ph.IM].

Van Eylen, V. et al. (Oct. 2018). “An asteroseismic view of the radius valley: stripped cores, not born rocky”. In: *MNRAS* 479.4, pp. 4786–4795. DOI: 10.1093/mnras/sty1783. arXiv: 1710.05398 [astro-ph.EP].

Vidal-Madjar, A. et al. (Mar. 2003). “An extended upper atmosphere around the extrasolar planet HD209458b”. In: *Nature* 422.6928, pp. 143–146. DOI: 10.1038/nature01448.

Vissapragada, Shreyas et al. (Mar. 2020a). “Diffuser-assisted Infrared Transit Photometry for Four Dynamically Interacting Kepler Systems”. In: *AJ* 159.3, 108, p. 108. DOI: 10.3847/1538-3881/ab65c8. arXiv: 1907.04445 [astro-ph.EP].

– (Mar. 2020b). “Diffuser-assisted Infrared Transit Photometry for Four Dynamically Interacting Kepler Systems”. In: *AJ* 159.3, 108, p. 108. DOI: 10.3847/1538-3881/ab65c8. arXiv: 1907.04445 [astro-ph.EP].

Wang, Lile and Fei Dai (June 2021a). “Metastable Helium Absorptions with 3D Hydrodynamics and Self-consistent Photochemistry. I. WASP-69b, Dimensionality, X-Ray and UV Flux Level, Spectral Types, and Flares”. In: *ApJ* 914.2, 98, p. 98. DOI: 10.3847/1538-4357/abf1ee. arXiv: 2101.00042 [astro-ph.EP].

– (June 2021b). “Metastable Helium Absorptions with 3D Hydrodynamics and Self-consistent Photochemistry. II. WASP-107b, Stellar Wind, Radiation Pressure, and Shear Instability”. In: *ApJ* 914.2, 99, p. 99. DOI: 10.3847/1538-4357/abf1ed. arXiv: 2101.00045 [astro-ph.EP].

Wilson, John C. et al. (Mar. 2003). “A Wide-Field Infrared Camera for the Palomar 200-inch Telescope”. In: *Instrument Design and Performance for Optical/Infrared Ground-based Telescopes*. Ed. by Masanori Iye and Alan F. M. Moorwood. Vol. 4841. Society of Photo-Optical Instrumentation Engineers (SPIE) Conference Series, pp. 451–458. DOI: 10.1117/12.460336.

Zhou, George et al. (Jan. 2021). “Two Young Planetary Systems around Field Stars with Ages between 20 and 320 Myr from TESS”. In: *AJ* 161.1, 2, p. 2. DOI: 10.3847/1538-3881/abba22. arXiv: 2011.13349 [astro-ph.EP].

Chapter 5

THE MAXIMUM MASS-LOSS EFFICIENCY FOR A PHOTOIONIZATION-DRIVEN ISOTHERMAL PARKER WIND

Vissapragada, Shreyas et al. (Mar. 2022). "The Maximum Mass-loss Efficiency for a Photoionization-driven Isothermal Parker Wind". In: *ApJ* 927.1, 96, p. 96. DOI: 10.3847/1538-4357/ac4e8a. arXiv: 2201.09889 [astro-ph.EP].

5.1 Introduction

A majority of the extrasolar planets discovered by transit surveys orbit close to their host stars and are subjected to intense irradiation. The incident flux received by these planets can remove their atmospheres if the heating is large compared to the planet's gravitational potential. Indeed, we see evidence for atmospheric escape in the radius-period distribution of close-in planets (the 'evaporation valley') observed by *Kepler* and *K2* (Fulton, Petigura, et al., 2017; Fulton and Petigura, 2018; Van Eylen et al., 2018; Hardegree-Ullman et al., 2020). We can quantify the present-day mass loss rates of the most favorable transiting planets by measuring the amount of absorption during the transit in spectral lines where outflowing material becomes opaque. To date, atmospheric outflows have been detected using Lyman-α (e.g. Vidal-Madjar, Lecavelier des Etangs, et al., 2003), Hα (e.g. F. Yan and Henning, 2018), metal lines (e.g. Vidal-Madjar, Désert, et al., 2004), and metastable helium (e.g. Spake, Sing, et al., 2018).

The upper atmospheres of planets are engines that turn light into heat. This heating drives hydrodynamic escape by lifting material out of the planet's gravitational potential well. We can use this concept to calculate an "energy-limited" mass loss rate, as first done (albeit in the context of highly conductive atmospheres) by Watson, Donahue, and Walker (1981):

$$\dot{M} = \frac{\varepsilon \pi R_{\mathrm{XUV}}^2 F_{\mathrm{XUV}}}{K G M_{\mathrm{p}}/R_{\mathrm{p}}}. \tag{5.1}$$

The numerator of this equation is an estimate for the heating rate of the planet (in erg s^{-1}), where the stellar high-energy flux F_{XUV} (in erg s^{-1} cm^{-2}) impinges on a cross-sectional area πR_{XUV}^2 of the planet, heating it with efficiency ε. The denominator is the gravitational potential (in erg g^{-1}), with a correction factor K to account for the fact that atoms need only be lifted past the Roche lobe to escape the planet (Erkaev et al., 2007):

$$K = 1 - \frac{3}{2}\left(\frac{R_p}{R_{Roche}}\right) + \frac{1}{2}\left(\frac{R_p}{R_{Roche}}\right)^3. \tag{5.2}$$

For small planet-to-star mass ratios, the Roche radius can be written as:

$$R_{roche} \approx a\left(\frac{M_p}{3M_\star}\right)^{1/3}. \tag{5.3}$$

The limitations of this formalism are well-documented (e.g. Murray-Clay, Chiang, and Murray, 2009; Salz, Schneider, et al., 2016; Salz, Czesla, Schneider, and Schmitt, 2016; Kubyshkina et al., 2018; Owen, 2019; Krenn et al., 2021). Detailed hydrodynamical models show that the efficiency ε depends strongly on a number of factors, including the planetary mass, radius, atmospheric composition, assumed heating processes, and stellar spectrum (Owen and Jackson, 2012; Shematovich, Ionov, and Lammer, 2014). Despite these drawbacks, this equation offers a convenient way to predict mass loss without expensive computational modeling, and it has been used extensively to model the *Kepler* evaporation valley (Lopez and Fortney, 2013; Owen and Wu, 2013; Owen and Wu, 2017).

The energy-limited framework has also recently been used to interpret measurements of metastable helium absorption from close-in transiting gas giant planets (Lampón, López-Puertas, Sanz-Forcada, et al., 2021; Lampón, López-Puertas, Czesla, et al., 2021). Helium observations are typically modeled using an isothermal Parker wind (parameterized by an assumed outflow temperature T_0 and mass-loss rate $\dot{M}$) coupled to a set of photoionization equations that can be solved for the He level populations as a function of altitude (Antonija Oklopčić and Hirata, 2018). The photoionized Parker wind model is faster to compute than expensive self-consistent 3D simulations (Wang and Dai, 2021a; Wang and Dai, 2021b), making it easier to map out the parameter spaces that fit measurements (and non-detections) of absorption in the metastable helium triplet (Mansfield et al., 2018; Gaidos, T. Hirano, Mann, et al., 2020; Gaidos, T. Hirano, Wilson, et al., 2020; Teruyuki Hirano et al., 2020; Ninan et al., 2020; Vissapragada, Knutson, et al., 2020; Krishnamurthy et al., 2021; Paragas et al., 2021). However, there is a degeneracy between $\dot{M}$ and T_0 in the Parker wind model, which can lead to uncertainties in $\dot{M}$ that span multiple orders of magnitude. This is particularly problematic for lower signal-to-noise and/or spectroscopically unresolved observations of helium absorption where the temperature of the outflow is unconstrained by the data.

In this work, we show that the $\dot{M} - T_0$ degeneracy in helium observations can be partially resolved because there is an upper limit to the efficiency of an energy-limited H/He outflow corresponding to the maximal amount of heating from photoionization. In §5.2, we derive an expression for $\varepsilon_{\rm max}$ in a lossless isothermal wind, i.e. a wind in which radiative cooling is negligible. We show that this expression can be used to define a bounded region in the $\dot{M} - T_0$ plane, beyond which there is not enough heat to power the outflow. In §5.3 we use this framework to resolve the $\dot{M} - T_0$ degeneracy in previous modeling of metastable helium absorption from HAT-P-11b, WASP-69b, and HAT-P-18b. Finally, we offer some concluding thoughts in §5.4.

5.2 The Maximum Mass-Loss Efficiency

We first calculate the maximal outflow efficiency ε for a lossless isothermal wind, assuming that the heat source is photoionization of H and He. Then, we use the maximum efficiency to trace out a critical region on the $\dot{M} - T_0$ plane, which can be used to assess energetic self-consistency. Because constants can always be absorbed into the efficiency ε, we will make the common arbitrary definition $R_{\rm XUV} \equiv R_{\rm p}$ in Equation (5.1) and absorb the constant $(R_{\rm XUV}/R_{\rm p})^2$ into ε, admitting the somewhat awkward possibility that $\varepsilon > 1$ if $R_{\rm XUV} \gg R_{\rm p}$. We note that other authors have proceeded by fixing ε and calculating $R_{\rm XUV}$ instead (e.g. Erkaev et al., 2007; Salz, Czesla, Schneider, and Schmitt, 2016; Kubyshkina et al., 2018). This calculation could be restructured for $R_{\rm XUV}$ or the product $\varepsilon R_{\rm XUV}^2$, but we choose to work with the efficiency term because this is typically the free parameter assumed in planetary population studies. We also note that varying authors have different definitions of the "efficiency" term in the context of planetary wind. For example, Shematovich, Ionov, and Lammer (2014) defines it as the ratio of the local heating rate to the radiative input (treating the cooling processes separately), which is adopted by Erkaev et al. (2007) and Kubyshkina et al. (2018), whereas Salz, Schneider, et al. (2016) includes the cooling rate explicitly. Throughout this work, when we refer to the "efficiency," we are referring explicitly to the ε term in Equation (5.1).

An Upper Limit to the Mass-Loss Efficiency

To compute ε, we begin by writing down the equation for energy balance in the wind (Lamers and Cassinelli, 1999; Erkaev et al., 2007):

$$\dot{M}\left(\frac{KGM_{\rm p}}{R_{\rm p}} + \frac{\Delta v^2}{2} + \frac{5}{2}\frac{k\Delta T}{\mu m_{\rm H}}\right) = \iiint \Gamma_{\rm net} dV, \tag{5.4}$$

where $\dot{M}$ is the mass-loss rate of the planet, K is as defined in Equation (5.2), Δv is the difference in outflow velocity between $R_{\rm p}$ and $R_{\rm Roche}$, ΔT is the difference in temperature between $R_{\rm p}$ and $R_{\rm Roche}$, and μ is the mean particle mass of the outflow. The terms on the left-hand side correspond to the difference in gravitational potential energy, kinetic energy, and enthalpy (for a monatomic outflow) between the planetary radius and the Roche lobe. On the right-hand side is the integrated net heating rate per unit volume, with $\Gamma_{\rm net} = \Gamma - \Lambda$ (where Γ and Λ are the heating and cooling rates, respectively) in erg s^{-1} cm^{-3}.

In this work we only consider isothermal winds where $\Delta T = 0$ and assume that the kinetic energy term is small. In the Parker wind model, material is accelerated to velocities on the order of the sound speed at the Roche lobe. This means that $\Delta v \sim 10^6$ cm s^{-1} (e.g. Murray-Clay, Chiang, and Murray, 2009; Antonija Oklopčić and Hirata, 2018) and $(\Delta v)^2/2 \sim 5 \times 10^{11}$ erg/g, whereas the gravitational potential term is $\gtrsim 10^{12}$ erg/g for all of the planets considered in this work. These are the same assumptions made by Erkaev et al. (2007) to reproduce the energy-limited mass loss expression from Watson, Donahue, and Walker (1981) in Equation (5.1).

With these assumptions, and using Equation (5.1) to substitute for the gravitational potential term, we have:

$$\varepsilon \pi R_{\rm p}^2 F_{\rm XUV} = \iiint (\Gamma - \Lambda) dV, \tag{5.5}$$

This simply reflects our assumption that the numerator of Equation (5.1) is a proxy for the total heating experienced by the planet. We then calculate ε for an atmosphere where radiative losses are negligible; that is, one where all heating goes into driving the outflow and $\Lambda \ll \Gamma$. This corresponds to:

$$\varepsilon_{\rm max} \pi R_{\rm p}^2 F_{\rm XUV} = \iiint_H \Gamma dV, \tag{5.6}$$

where $\varepsilon_{\rm max}$ is the maximum mass-loss efficiency and H denotes the dayside hemisphere where the heating occurs. If we assume that all heating comes from photoionization, we can write the total heating rate as a sum of heating rates for each photoprocess of interest (e.g. Osterbrock and Ferland, 2006):

$$\Gamma = \sum_i \Gamma_i \tag{5.7}$$

$$= \sum_i n_{i,r} \int_{\min(\nu_i)}^{\infty} (h\nu - h\nu_i) \times \frac{F_\nu \cos(\theta) \exp(-\tau_{\nu,r})}{h\nu} \sigma_{\nu,i} d\nu. \tag{5.8}$$

In this equation, $h\nu$ denotes the photon energy. The subscript i denotes different photoproceses (for instance, hydrogen photoionization), the subscript ν denotes a quantity that varies with frequency, and the subscript r denotes one that varies with radius. The number density profile of the species being photoionized is $n_{i,r}$, the ionization threshold for the process is $h\nu_i$, and $h\nu - h\nu_i$ is the maximum yield per photoprocess. For example, a photon with energy $h\nu = 20$ eV yields 6.4 eV when ionizing a hydrogen atom out of its ground state ($h\nu_{\mathrm{H}} = 13.6$ eV). $F_\nu \cos(\theta) \exp(-\tau_{\nu,r})$ is the spectrum of radiation reaching radius r from the center of the planet and latitude θ with respect to the substellar point in erg s^{-1} cm^{-2} Hz^{-1}. Finally, $\sigma_{\nu,i}$ is the frequency-dependent cross-section for photoprocess i. The frequency integral is taken from the minimum photoionization threshold over all relevant photoprocesses $\min(\nu_i)$ to allow for a consistent definition of F_{XUV}.

The optical depth term is defined as:

$$\tau_{\nu,r} = \sum_i \sigma_{i,\nu} \int_r^{\infty} n_{i,r} dr. \tag{5.9}$$

This definition implictly assumes that the optical depth reaches a large value at R_{p}. For high-energy photons where the photoionization cross-sections are small this condition may not always be satisfied, implying that photons can freely reach this depth. However, these photons cannot pass through the planet, and their energy must be deposited somewhere. We assume that they participate in the energy balance of the lower atmosphere at $R \sim R_{\mathrm{p}}$, and that they do not heat the outflow.

We collect the photon energy terms into a normalized yield term η_ν:

$$\eta_\nu = \frac{h\nu - h\nu_i}{h\nu} = 1 - \frac{\nu_i}{\nu}. \tag{5.10}$$

In reality, this is an upper limit on the yield. We have assumed that the photoelectrons resulting from ionization transform all of their energy into heat, but they can also excite or ionize other atoms (Murray-Clay, Chiang, and Murray, 2009; Shematovich, Ionov, and Lammer, 2014). By neglecting these minor energy deposition channels, we obtain a slightly more generous upper limit than we would otherwise. With the yield term now defined, we can write the total heating rate as:

$$\Gamma = \sum_i n_{i,r} \int_{\min(\nu_i)}^{\infty} \eta_\nu F_\nu \cos(\theta) \exp(-\tau_{\nu,r}) \sigma_{\nu,i} d\nu. \tag{5.11}$$

We integrate this equation over the dayside hemisphere (for the geometry of the integral see e.g. Chapter 2 of Seager, 2010):

$$\iiint_H \Gamma dV = \int_0^{2\pi} \int_0^{\pi/2} \int_{R_\mathrm{p}}^{R_\mathrm{Roche}} \Gamma r^2 \sin\theta dr d\theta d\phi \tag{5.12}$$

$$= \pi \int_{R_\mathrm{p}}^{R_\mathrm{Roche}} r^2 \sum_i n_{i,r} \times \int_{\min(\nu_i)}^{\infty} \eta_\nu F_\nu \exp(-\tau_{\nu,r}) \sigma_{\nu,i} d\nu dr. \tag{5.13}$$

We then substitute Equation (5.13) into Equation (5.6), where the factors of π cancel. Noting that F_XUV can be written as:

$$F_\mathrm{XUV} = \int_{\min(\nu_i)}^{\infty} F_\nu d\nu, \tag{5.14}$$

we arrive at:

$$\varepsilon_\mathrm{max} = \frac{1}{R_\mathrm{p}^2} \int_{R_\mathrm{p}}^{R_\mathrm{Roche}} r^2 \times \sum_i n_{i,r} \frac{\int_{\min(\nu_i)}^{\infty} \eta_\nu F_\nu \exp(-\tau_{\nu,r}) \sigma_{\nu,i} d\nu}{\int_{\min(\nu_i)}^{\infty} F_\nu d\nu} dr. \tag{5.15}$$

Heating Cross-Sections

We can define the ratio of frequency integrals in Equation (5.15) as a cross section weighted by the stellar spectrum and heating efficiency for photoprocess i. We call this the "heating cross-section", and note that the optical depth dependence causes it to vary with radius:

$$\bar{\sigma}_{i,r} = \frac{\int_{\min(\nu_i)}^{\infty} \eta_\nu F_\nu \exp{(-\tau_{\nu,r})} \sigma_{\nu,i} d\nu}{\int_{\min(\nu_i)}^{\infty} F_\nu d\nu} \tag{5.16}$$

To calculate this heating cross-section, we require a stellar spectrum and a frequency-dependent cross-section for each photoprocess. For the spectrum, we use the v2.2 panchromatic SEDs at 1 Å binning from the MUSCLES survey (France et al., 2016; Loyd et al., 2016; Youngblood et al., 2016). For the hydrogen photoionization cross-section, we use (e.g. Osterbrock and Ferland, 2006):

$$\begin{aligned} \sigma_i(\nu) &= \sigma_{\nu_i} \frac{\exp\left(4 - 4\frac{\tan^{-1}\epsilon}{\epsilon}\right)}{1 - \exp{(-2\pi/\epsilon)}} \left(\frac{\nu_i}{\nu}\right)^4, \\ &\nu > \nu_i, \end{aligned} \tag{5.17}$$

where $\epsilon = \nu/\nu_{\mathrm{i}} - 1$. The threshold energy for neutral hydrogen photoionization is $h\nu_{\mathrm{H}} = 13.6$ eV, and the cross-section at this threshold is $\sigma_{\nu_{\mathrm{H}}} = 6.3 \times 10^{-18}$ cm^{-2}. We also consider heat generated by the photoionization of ionized helium, a relatively minor process. The cross section for this hydrogen-like species is also given by Equation (5.17), but the threshold energy is $h\nu_{\mathrm{He}^+} = Z^2 h\nu_{\mathrm{H}} = 54.4$ eV, and the cross-section at this threshold is $\sigma_{\nu_{\mathrm{He}^+}} = \sigma_{\nu_{\mathrm{H}}}/Z^2 = 1.6 \times 10^{-18}$ cm^{-2}. For the neutral helium photoionization cross-section, we use (M. Yan, Sadeghpour, and Dalgarno, 1998):

$$\begin{aligned} \sigma_{\mathrm{He}}(\nu) &= \frac{\sigma_{\mathrm{a}}}{(h\nu/1\ \mathrm{keV})^{7/2}} \left(1 + \sum_{n=1}^{6} \frac{a_n}{(\nu/\nu_{\mathrm{He}})^{n/2}}\right), \\ &\nu > \nu_{\mathrm{He}} \end{aligned} \tag{5.18}$$

where the threshold photon energy $h\nu_{\mathrm{He}} = 24.6$ eV, $\sigma_{\mathrm{a}} = 7.33 \times 10^{-22}$cm^2, and the constants a_n are from Table 4 of M. Yan, Sadeghpour, and Dalgarno (1998).

With the heating cross-section defined, we can now write the expression for $\varepsilon_{\max}$ in a more illustrative form:

$$\varepsilon_{\max} = \frac{1}{R_{\mathrm{p}}^2} \int_{R_p}^{R_{\mathrm{Roche}}} r^2 \sum_i n_{i,r} \bar{\sigma}_{i,r} dr. \tag{5.19}$$

The $n\sigma$ terms in the summation, which we will refer to as "heating coefficients", can be thought of analogously to absorption coefficients (e.g. Seager, 2010). Thus, the efficiency of an isothermal wind cannot be greater than the normalized second moment of its total heating coefficient.

We note that Equation (5.19) gives us a simple way to compare the relative heating efficiencies of neutral hydrogen and helium. These processes will be similarly important for heating the atmosphere when the heating coefficients are comparable: $n_{\mathrm{H}}\bar{\sigma}_{\mathrm{H}} \sim n_{\mathrm{He}}\bar{\sigma}_{\mathrm{He}}$. In the high-energy limit, the cross-section for neutral helium photoionization is an order of magnitude larger than that for hydrogen photoionization, but there are also fewer helium atoms to ionize. We consider a 90-10 hydrogen-helium atmosphere that is optically thin, i.e. where $\exp(-\tau_{\nu,r}) \sim 1$ in Equation (5.16). In this case, the heating coefficients depend only on the assumed stellar spectrum. Stepping through the ensemble of stellar spectra collected by MUSCLES, we find that the optically-thin heating coefficient for helium ranges from 20% (for ϵ Eri) to 67% (for GJ 1214) that of hydrogen. For a stellar spectrum similar to the M stars in the MUSCLES sample, helium photoionization can be a large (though still sub-dominant) heat source; pure-hydrogen escape models that have been developed for planets orbiting earlier stars may therefore underestimate the total thermospheric energy budget for planets orbiting M stars. K stars in this sample output relatively more flux near the hydrogen photoionzation threshold, so helium photoionization is a smaller heat source for planets orbiting K stars. These relative efficiencies are similar to those obtained from more detailed computational modeling (Salz, Czesla, Schneider, and Schmitt, 2016). These calculations are only meant to be illustrative; in general, the optical depth term $\exp(-\tau_{\nu,r})$ can be important, and the heating coefficients change substantially with radius.

Energetic Self-Consistency

We next consider the implications of this upper limit on the mass loss efficiency for a photoionized isothermal Parker wind model, which parameterizes the density structure at the substellar point $n_{i,r}$ in terms of a mass-loss rate $\dot{M}$ and the outflow temperature T_0. For helium studies, the Parker wind is typically taken to be one-dimensional, but this greatly overestimates the work done. The wind is strongest at the substellar point because the irradiation is strongest there, but decreases in strength towards the terminator due to the diminished incident flux, and no wind is launched on the planetary nightside as the atmosphere is not irradiated there. This can be accounted for as follows: the planet is heated over only π steradians (Equation 5.13), so the outflow is driven only over π steradians on the planetary dayside and the work done is decreased by a factor of 1/4 compared to a 1D isotropically-irradiated outflow (Stone and Proga, 2009; Salz, Schneider, et al., 2016).

Because the density distributions are functions of $\dot{M}$ and T_0 in this model, the energy-limited efficiency is itself a function of these parameters, and the mass-loss rate must satisfy:

$$\frac{\dot{M}}{4} \leq \frac{\varepsilon_{\max}(\dot{M}, T_0)\pi R_p^3 F_{\rm XUV}}{KGM_p}, \tag{5.20}$$

where the factor of 1/4 comes from the aforementioned 3D outflow geometry. Had we derived $\varepsilon_{\max}$ assuming an isotropically-irradiated 1D outflow without this geometric factor, then we would be integrating over the entire planet in Equation (5.12), picking up a factor of 4 (the angular part of the integral would evaluate to 4π rather than π). Thus, the constraint on $\dot{M}$ would remain the same.

This inequality defines an allowed region on the $\dot{M} - T_0$ plane. The problem is fundamentally one of energetic self-consistency: if we assume a mass-loss rate and thermosphere temperature, do the resulting density profiles allow enough heating to power the assumed mass-loss rate? For solutions outside the allowed region, the answer is no: they are not permitted unless there is some additional source of heat. Solutions on the boundary are exactly energy-limited; that is, they generate exactly enough heat to power their outflow. Solutions inside the boundary generate excess heat, which can always be balanced by additional cooling. If the cooling rate is known precisely, Equation (5.20) traces out a curve rather than an allowed region. We briefly consider this case in Appendix 5.5.

Regime of Validity

We note that our calculation is valid only for gas giant planets with H/He-rich envelopes and lower gravitational potentials experiencing (approximately) radially symmetric outflows. Detailed numerical simulations indicate that planets with gravitational potentials $\Phi_p \gtrsim 10^{13.1}$ erg g^{-1} exhibit strong temperature gradients, and cooling through Lyman-α and free-free emission becomes important (Salz, Schneider, et al., 2016; Salz, Czesla, Schneider, and Schmitt, 2016). We have focused on isothermal, lossless outflows, so our model is therefore better suited to modeling lower gravity planets. High-gravity planets will still be governed by energy balance, but the isothermal Parker wind will not correctly describe the density distributions. We also note that H/He-rich Parker winds have been inadequate in predicting metastable helium signatures for sub-Neptunes thus far, which may indicate these planets differ substantially in composition from the pure H/He atmosphere assumed here (Kasper et al., 2020; Krishnamurthy et al., 2021). Therefore, we do not recommend using this methodology for planets with $R_\mathrm{p} \lesssim 4R_\oplus$. These criteria are satisfied for $\sim$ 30% of the $\sim$1000 transiting exoplanets with measured masses and radii on the NASA Exoplanet Archive.

Our model additionally assumes an idealized geometry for the wind, and will be less accurate for outflows deviating from the assumed geometry. There are several factors that contribute to such deviations. Interactions between the planetary and stellar winds can sculpt the outflow into a comet-like tail (McCann et al., 2019; Wang and Dai, 2021b; MacLeod and Antonija Oklopčić, 2021), and we therefore expect the model to perform worse for planets orbiting young and/or exceptionally active stars. WASP-107 b orbits a relatively active star and has a strongly blueshifted helium line profile and strong post-egress absorption (Allart, Bourrier, Lovis, Ehrenreich, Aceituno, et al., 2019; Kirk et al., 2020; Spake, A. Oklopčić, and Hillenbrand, 2021), both signs of an asymmetric outflow. There were initially hints of a similar tail for WASP-69b (Nortmann et al., 2018). However, subsequent observations and modeling both indicate that this planet's outflow is relatively symmetric (Vissapragada, Jontof-Hutter, et al., 2020; Wang and Dai, 2021a). Simulations and observations of the transiting planet HD 63433c, which orbits a 440 Myr old star, indicate that it also has a comet-like tail (Zhang et al., 2021), and simulations of the young planet AU Mic b suggest the strong stellar wind should shape its outflow as well (Carolan et al., 2020), though helium has not yet been conclusively detected in its atmosphere (Teruyuki Hirano et al., 2020).

Magnetically-controlled outflows are also expected to deviate from the idealized geometry in this work. Outflowing material near equatorial latitudes follow closed magnetic field lines falling back onto the planet, whereas material near the poles may escape (Adams, 2011; Trammell, Arras, and Li, 2011; Owen and Adams, 2014; Trammell, Li, and Arras, 2014). However, it is presently unclear to what extent magnetic fields may affect metastable helium observations, which have thus far been well-fit by models without magnetic fields. This may be because the planetary outflows are dominated by ram pressure rather than magnetic pressure within the metastable helium photosphere (Zhang et al., 2021).

5.3 Application to Metastable Helium Observations

To show how the constraints from our energy-limited model may be used in practice, we consider published observations of metastable helium absorption from HAT-P-11b, WASP-69b, and HAT-P-18b. These three planets have all been observed using narrowband photometry or low-resolution spectroscopy, which provide minimal information about the line shape. This means that when an isothermal Parker wind model is used to fit the measured absorption signal, there is a large degeneracy between the mass-loss rate and the assumed outflow temperature. This degeneracy can be broken with line-shape measurements of sufficiently high precision, which independently constrain the outflow temperature (e.g. Dos Santos et al., 2021). However, the line shape can also vary when the absorbing region is not optically thin (Salz, Czesla, Schneider, Nagel, et al., 2018), and when the outflow itself kinematically broadens the line (Allart, Bourrier, Lovis, Ehrenreich, Aceituno, et al., 2019; Wang and Dai, 2021b; Seidel et al., 2021). This means that line shape alone is an imperfect proxy for outflow temperature. Even if this was not the case, the signal-to-noise ratio of the measured line profile is often too low to provide a useful constraint on the outflow temperature (Lampón, López-Puertas, Lara, et al., 2020; Lampón, López-Puertas, Sanz-Forcada, et al., 2021).

In this section, we show that we can use the energy-limited framework to place an upper bound on the temperatures of these outflows, resulting in tighter constraints on the retrieved mass-loss rates from the Parker wind model. For each of the three planets considered here, we used the `p-winds` code (e.g. Dos Santos et al., 2021) to calculate isothermal Parker wind models and compared those models to the observed metastable helium signal. `p-winds` is an open-source implementation of the model described by Antonija Oklopčić and Hirata (2018) and Lampón, López-Puertas, Lara, et al. (2020). We evaluated these models over a grid defined by $\dot{M} = 10^9 - 10^{12}$ g s^{-1} and $T_0 = 5000 - 15000$ K. The temperature grid roughly corresponds to the range of temperatures seen in self-consistent simulations (Salz, Schneider, et al., 2016; Wang and Dai, 2021a; Wang and Dai, 2021b). At each point on our grid, we computed the outflow density structure (for a 90/10 H/He composition) and calculated the corresponding ionization structure and level populations with `p-winds`. In these calculations, we noticed that the approximation for the hydrogen photoionization rate in Equation (9) of Antonija Oklopčić and Hirata (2018) tended to over-predict the rate close to the ionization front, which is consequential for the modeled mass-loss efficiency. We therefore updated the calculation in `p-winds` to avoid the approximation. We also note that our number density of ionized helium is overestimated because some of the ionized helium will end up populating He^{2+} in steady-state, which `p-winds` does not account for. By ignoring this minor (e.g. Salz, Schneider, et al., 2016) sink, we obtain a slightly larger $\varepsilon_{\rm max}$ than we otherwise would.

We then used the framework from §5.2 to calculate the self-consistent $\dot{M} - T_0$ region for each planet. At each $(\dot{M}, T_0)$ wind on the grid, we integrated the density distributions of H and He to obtain column densities, from which we computed the total optical depth as a function of frequency and radius $\tau_{\nu,r}$. Using this optical depth, the cross sections in Equations (5.17) and (5.18), the yield term in Equation (5.10), and the assumed stellar spectrum, we then calculated the heating cross-sections using Equation (5.16). Finally, we multiplied by the density distributions to get the heating coefficients, summed to get the total heating coefficient, and took the second moment to get the upper limit on the mass-loss efficiency per Equation (5.19). To assess whether or not a given outflow was self-consistent, we used this $\varepsilon_{\rm max}$ to calculate the maximum mass-loss rate via Equation (5.20). If we found a maximum mass-loss rate lower than the assumed mass-loss rate, the solution was energetically inconsistent; otherwise, it was admissible. This procedure has been added in v1.2.4 of the `p-winds` code.

HAT-P-11b

HAT-P-11b is slightly larger in mass and radius than Neptune ($\Phi_{\rm p} \approx 3{\times}10^{12}$ erg g^{-1}), and orbits its K4 host star with a period of 5 days (Bakos et al., 2010). Mansfield et al. (2018) detected helium absorption in the atmosphere of this planet at low resolving power with *HST* WFC3/G102, and Allart, Bourrier, Lovis, Ehrenreich, Spake, et al. (2018) detected a comparable absorption signal at high resolving power with CARMENES. For this planet, the high signal-to-noise of the line shape measured by Allart, Bourrier, Lovis, Ehrenreich, Spake, et al. (2018) provides us with an independent measurement of the outflow temperature. Dos Santos et al. (2021) fitted the line absorption profile from Allart, Bourrier, Lovis, Ehrenreich, Spake, et al. (2018) with a Parker wind model using the `p-winds` code and found that it was best matched by an outflow with $T_0 = 7200 \pm 700$ K and $\dot{M} = 2.5^{+0.8}_{-0.6} \times 10^{10}$ g s^{-1}. In this study we instead fitted the unresolved measurements from Mansfield et al. (2018), and used our energy-limited framework to help resolve the $\dot{M} - T_0$ degeneracy. We use the stellar spectrum of HD 40307 for this calculation, which is the same choice made by Dos Santos et al. (2021).

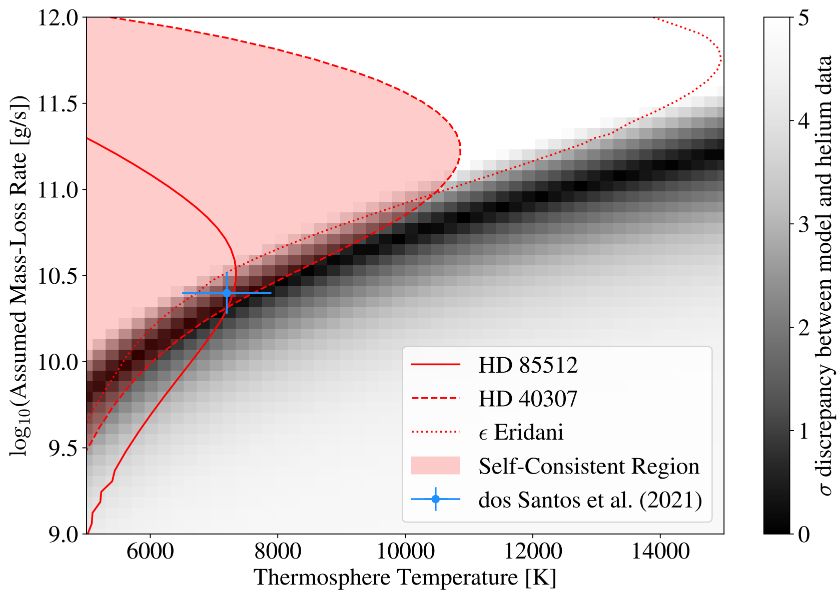

Figure 5.1: Mass-loss modeling for the HAT-P-11b observations presented in Mansfield et al. (2018). The black shading indicates the σ discrepancy between the mass-loss model in each grid cell and the metastable helium observation. The red shading indicates the self-consistent region from Equation (5.20) using the scaled spectrum of HD 40307, and the boundary for a perfectly energy-limited outflow assuming this spectrum is given with the dashed red line. The solid and dotted red lines give the boundary of the self-consistent regions for HD 85512 and ϵ Eridani, respectively. The blue point additionally indicates the 1σ range from the Dos Santos et al. (2021) retrieval on the Allart, Bourrier, Lovis, Ehrenreich, Spake, et al. (2018) high-resolution spectrum.

We show the resulting constraints on the outflow rate and temperature in Figure 5.1, and compare these constraints to the result from Dos Santos et al. (2021). We find that some of the previously reported Parker wind solutions with high temperatures and high mass-loss rates are in fact energetically inconsistent; i.e. they do not have enough H and He to power the outflow by photoionization. This allows us to partially resolve the degeneracy between mass-loss rate and thermosphere temperature: the outflow must be cooler than $\sim 10,000$ K and relatively weak ($\dot{M} \lesssim 10^{11}$ g s^{-1}). Our results are in good agreement with Dos Santos et al. (2021), and their retrieved value matches our energy-limited contour within the 1σ level. We therefore conclude that this outflow is energy-limited. This is also consistent with the simulations of Salz, Schneider, et al. (2016), who explicitly modeled radiative cooling in HAT-P-11b's outflowing atmosphere and found it to be negligible.

We also quantify our sensitivity to the choice of high-energy stellar spectrum by overplotting the boundary of the self-consistent region calculated using scaled spectra for HD 85512, which is less energetic in the XUV than the HD 40307 spectrum, and ϵ Eridani which is more energetic in the XUV (see Figure 5.2). To be fully consistent, we also re-calculated the constraints from the Parker wind models with the same stellar spectrum. However, we found that this does not substantially change the range of mass-loss rates and temperatures that are consistent with the metastable helium data, as the stellar spectra have similar shapes at wavelengths longward of 100 Å. In Figure 5.1, we show that the range of self-consistent solutions is somewhat larger when we use ϵ Eridani as a proxy for the star's high energy spectrum, and smaller when we use HD 85512, reflecting the differences in XUV luminosities for these stars. A larger XUV intensity tends to increase ionization throughout the outflow (though this is also somewhat dependent on the spectral shape, see e.g. Guo and Ben-Jaffel, 2016), leading to lower neutral densities, and thus smaller values of $\varepsilon_{\mathrm{max}}$ per Equation (5.19). However, this effect is sub-linear and does not compensate for the linear dependence on F_{XUV} in the expression for the maximum mass-loss rate in Equation (5.20), so larger XUV luminosities lead to larger self-consistent regions.

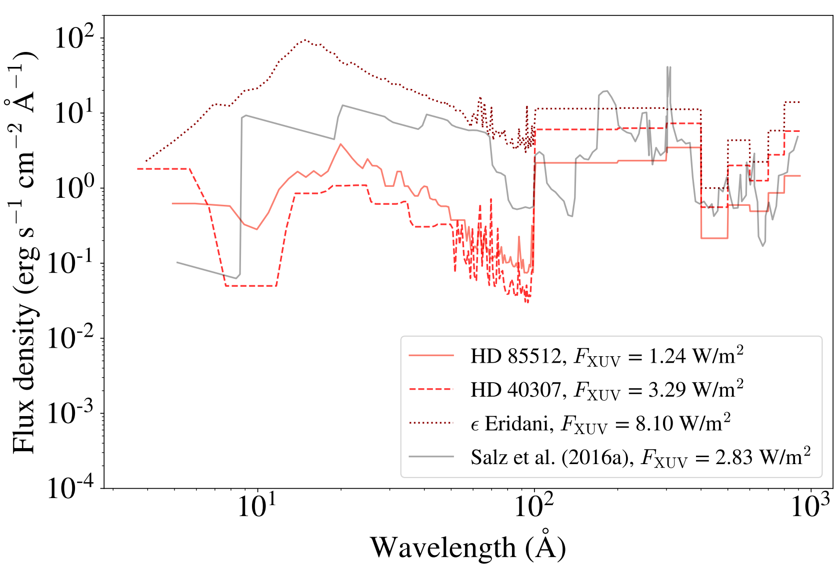

Figure 5.2: High-energy stellar spectra considered for HAT-P-11. All spectra have been scaled to the location of HAT-P-11b. Note that the Salz, Schneider, et al. (2016) spectrum is binned differently than the three MUSCLES spectra.

We can use the Salz, Schneider, et al. (2016) simulation to explore the validity of the Parker wind model for this planet, as their model self-consistently predicts the temperature and density profiles at the substellar point. Their model suggests a mass-loss rate at the sub-stellar point of $10^{10.89}$ g s^{-1}, which they divide by 4 to correct for the non-uniform radiation (as we do in Equation 5.20) for a final mass-loss rate of $\dot{M}_{\rm sim} = 10^{10.29}$ g s^{-1}. As we are comparing density profiles at the substellar point we selected isothermal Parker wind models with $\dot{M} = 10^{10.89}$ g s^{-1} and T_0 ranging from 5000 K to 10000 K in 1000 K steps. For the photoionization calculation we used the spectrum of HD 40307, which is closest to the spectrum used by Salz, Schneider, et al. (2016). In Figure 5.3, we plot the total number density of hydrogen and the number density of neutral hydrogen from our models and compare it to the self-consistent simulations.

Throughout most of the outflow, the total hydrogen number densities agree quite well between the two models. They differ by orders of magnitude in total density near $R = R_{\rm p}$, but this is expected. The Parker wind model is a poor approximation for the lower atmosphere, but this region has a negligible effect on the predicted outflow. The high number density of hydrogen close to the planet leads to a very large optical depth near $R_{\rm p}$ so it does not contribute much to the heating budget in either model. Our model appears to give somewhat smaller number densities for neutral hydrogen near the Roche radius. This likely arises from our use of a K star spectrum from MUSCLES, whereas Salz, Schneider, et al. (2016) used an inactive solar spectrum to reconstruct the shape of the spectrum in the EUV (see Figure 5.2). The discrepancy grows to about a factor of 2 at the Roche radius, but the densities here are small. Overall, the agreement between the two models is reasonable given the difference in methodology, and both models agree with the retrieval from Dos Santos et al. (2021) for HAT-P-11b.

WASP-69b

WASP-69b is a Neptune-mass, Jupiter-sized planet ($\Phi_{\rm p} \approx 4 \times 10^{12}$ erg g^{-1}) in a 4 day orbit around a K5 host star (Anderson et al., 2014). The low density and large scale height of this planet, combined with the host star's favorable ratio of EUV to XUV flux (Antonija Oklopčić, 2019), made it an ideal target for initial studies of mass loss with the metastable helium line. The helium absorption signal for this planet has been measured both spectroscopically (Nortmann et al., 2018) and photometrically (Vissapragada, Jontof-Hutter, et al., 2020). In the latter work, we attempted to infer the mass-loss rate of WASP-69b using the Parker wind model from Antonija Oklopčić and Hirata (2018), and were able to place joint constraints on its mass-loss rate and thermosphere temperature.

In Figure 5.4, we show the energetically self-consistency region and compare it to

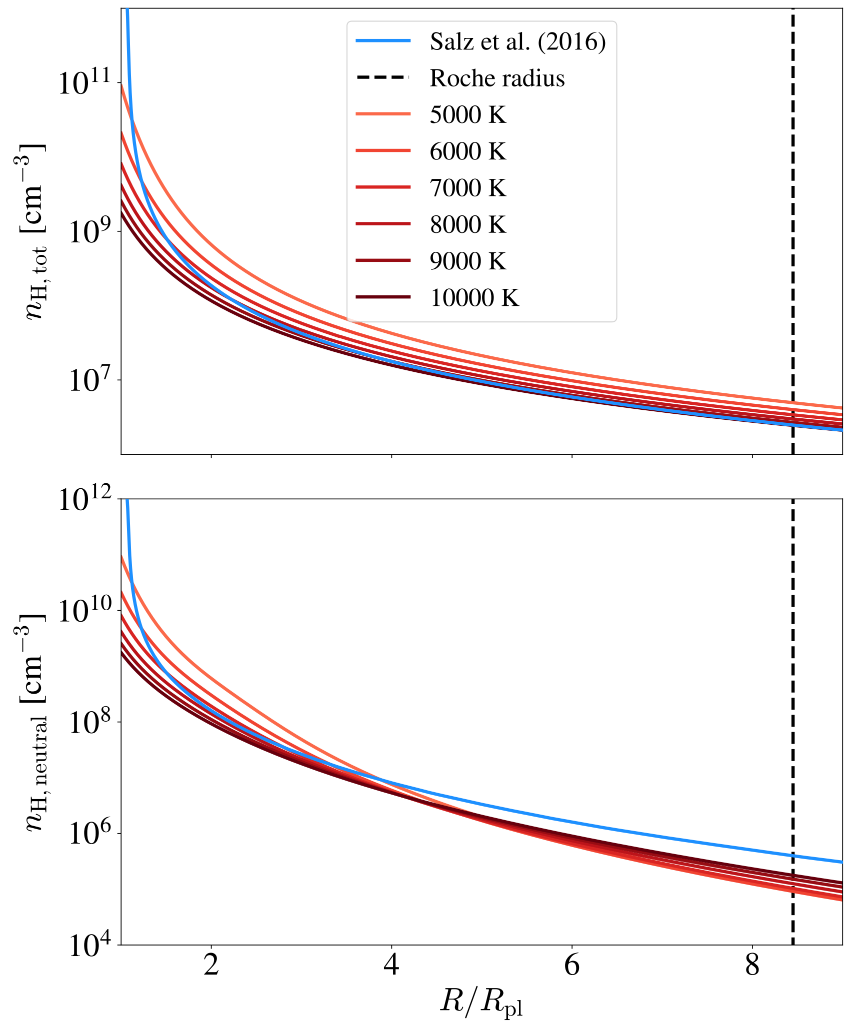

Figure 5.3: Total number density of hydrogen (top) and number density of neutral hydrogen (bottom) for HAT-P-11b at the substellar point. Profiles from the Salz, Schneider, et al. (2016) simulation are shown in blue, and our photoionized Parker wind model in red, with darker colors corresponding to higher temperatures.

the set of Parker wind models that match the metastable helium absorption reported in Vissapragada, Jontof-Hutter, et al. (2020), using the stellar spectrum of HD 85512 as we did in that work. We find that the outflow must be cooler than 14,000 K and relatively weak ($\dot{M} \lesssim 10^{11.5}$ g s^{-1}). WASP-69b was also modeled self-consistently by Wang and Dai (2021a), who used a more sophisticated 3D approach coupling hydrodynamics and thermochemistry. These authors found that the data were best-matched by models with $\dot{M} \sim 10^{11}$ g s^{-1}, in agreement with our upper limit. The Wang and Dai (2021a) model also achieves a maximum temperature in the substellar direction of $\sim 10^4$ K, so (similarly to Lampón, López-Puertas, Lara, et al., 2020) we find that the isothermal Parker wind model agrees best with non-isothermal models

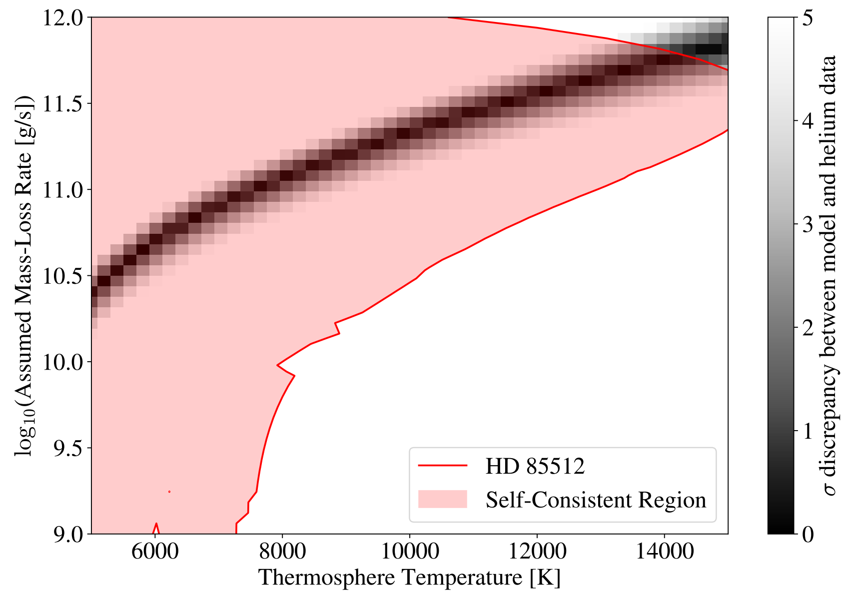

Figure 5.4: Same as Figure 5.1, but for the WASP-69b observations presented in Vissapragada, Jontof-Hutter, et al. (2020).

near the maximum temperature.

HAT-P-18b

HAT-P-18b is a Jupiter-sized, Saturn-mass planet ($\Phi_p \approx 4 \times 10^{12}$ erg g^{-1}) orbiting a K2 dwarf with a period of 5.5 days (Hartman et al., 2011). In Paragas et al., 2021, we used narrowband photometry to detect helium absorption from an outflowing atmosphere with a significance of 4σ. In Figure 5.5, we fit the measurement from that work using our Parker wind model and compare the resulting contour to the energetically self-consistent region. For the XUV spectrum, we used the MUSCLES spectrum of the young K2 dwarf ϵ Eridani. Though HAT-P-18b is rather old $12.4^{+4.4}_{-6.4}$ Gyr (Hartman et al., 2011), it is quite active ($\log(R'_{\mathrm{HK}}) = -4.73$; H. Isaacson priv. comm.), so ϵ Eridani ($\log(R'_{\mathrm{HK}}) = -4.51$; Wright et al., 2004) is a reasonable choice of XUV proxy from the MUSCLES catalog.

For this planet, we could not limit the allowed mass-loss rate using energetics alone. The majority of models consistent with the helium data are also self-consistent. This is because the host star outputs a large XUV flux; as we discussed in Section 5.3, this tends to increase the number of self-consistent solutions with large mass-loss rates. More precise constraints on the mass-loss rate in this system will require precise line shape constraints from spectroscopic follow-up. The faintness (J = 10.8) of this system makes spectroscopic follow-up with CARMENES difficult, as its J

magnitude is larger than the recommended magnitude limit for this instrument[1], so line-shape measurements will require time on larger facilities like Keck-II/NIRSPEC (e.g. Kirk et al., 2020; Spake, A. Oklopčić, and Hillenbrand, 2021).

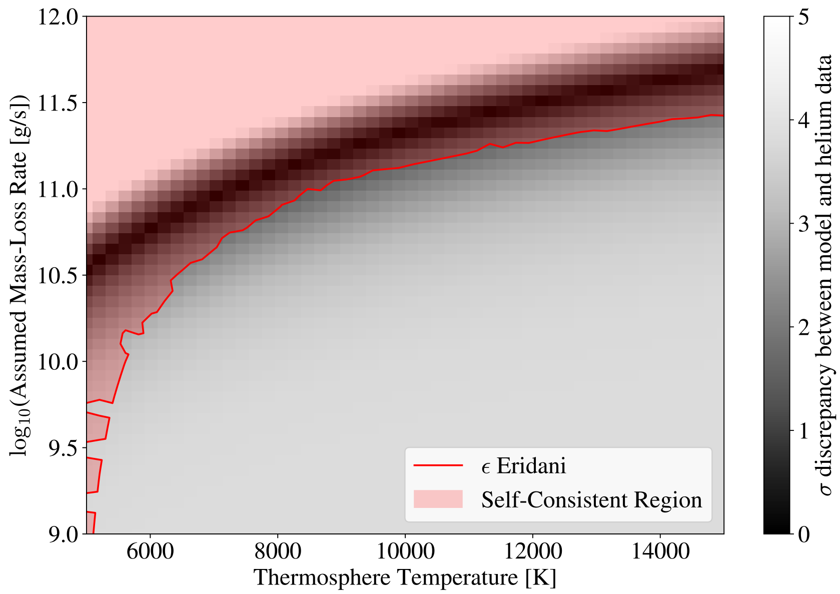

Figure 5.5: Same as Figure 5.1, but for the HAT-P-18b observations presented in Paragas et al. (2021).

5.4 Discussion and Conclusions

The isothermal Parker wind model is commonly used to interpret observations of metastable helium, with the ultimate goal of obtaining precise mass-loss rates for planets with observed helium absorption. However, there is a degeneracy between the outflow temperature and mass-loss rate in these models. The temperature can be constrained with spectroscopically-resolved observations at high SNR, but remains a large source of uncertainty when fitting unresolved measurements and/or those at a lower SNR. We partially resolved this degeneracy by determining the maximum mass-loss efficiency of an isothermal wind driven by photoionization. We found that the efficiency is limited by a quantity we call the heating coefficient, which is the product of the number density and a weighted photoionization cross section, as described by Equation (5.19). We leveraged this constraint to show that a subset of the isothermal Parker wind models that agree with observations do not generate enough heat to remain energetically self-consistent. Outflows that generate just enough heat to remain self-consistent are exactly energy-limited, with the numerical

[1]https://carmenes.caha.es/ext/instrument/index.html

value of the efficiency term depending on the assumed mass-loss rate, and outflows that generate excess heat must re-radiate some of their energy.

We re-examined published photometric and low-resolution spectroscopic observations of mass loss from HAT-P-11b, WASP-69b, and HAT-P-18b, which were originally fitted with a Parker wind model that allowed for a wide range of outflow temperatures and mass loss rates. We showed that the outflows from the former two planets must be relatively weak ($\dot{M} \lesssim 10^{11.5}$ g s^{-1}), but found that energetics could not further constrain the mass-loss rate for HAT-P-18b. Our results are in good agreement with more detailed numerical simulations of WASP-69b (Wang and Dai, 2021a) and HAT-P-11b (Salz, Schneider, et al., 2016), and additionally agree with complementary constraints on the outflow temperature of HAT-P-11b from line shape measurements (Allart, Bourrier, Lovis, Ehrenreich, Spake, et al., 2018; Dos Santos et al., 2021). Furthermore, when line shape information is available (as it is for seven planets in the literature: HAT-P-11b, HAT-P-32b, WASP-69b, WASP-107b, HD 189733b, HD 209458b, and GJ 3470b) we can use our methodology to assess how close an outflow is to the energy limit. In this study, we showed that HAT-P-11b is experiencing an energy-limited outflow.

Our investigation revealed that the location of the self-consistent region on the $\dot{M} - T_0$ plane can shift in response to changing assumptions. First, as we showed in Figure 5.1, the extent of this region is sensitive to the assumed stellar spectrum; whenever possible, the spectra used in this model should be observationally calibrated. The models are also sensitive to the details of the photoionization calculation; any over- or under-estimation of the ionization fraction changes the self-consistent region. The assumed ratio of hydrogen to helium also matters, because the heating cross-section for neutral helium can be an order of magnitude larger than that for hydrogen for the late-type stars we considered in this work. Finally, the self-consistent region can move to higher temperatures if there are additional heat sources that are not included in the model. For instance, core-powered mass-loss (Ginzburg, Schlichting, and Sari, 2016; Gupta and Schlichting, 2019; Gupta and Schlichting, 2020; Gupta and Schlichting, 2021) could provide additional luminosity on the right-hand side of Equation (5.6).

In addition to refining the inferred mass-loss rates from metastable helium observations, our energetics framework also allows us to more generally elucidate the connection between the mass-loss efficiency in the energy limit and the outflow photophysics. This can be important when considering other potential heat sources.

For example, Howe, Adams, and Meyer (2020) studied the potential heating from photodissociation of molecular hydrogen and found that it was a sub-dominant outflow driver when ε was fixed to 0.1. Although our framework is imperfect for considering molecular winds, as there are more sources of heating and cooling to consider (Glassgold and Najita, 2015; Salz, Schneider, et al., 2016), we can nonetheless use it to explore what happens when we relax the assumption of fixed efficiency. The cross-section for molecular hydrogen photodissociation is resonant at the frequencies of Lyman-Werner transitions (e.g. Heays, Bosman, and van Dishoeck, 2017), causing the gas to self-shield. This means that the optical depth to dissociating photons will quickly exceed unity in the outer region of the outflow, greatly reducing the heating rate per Equation 5.15 inside a thin photodissociated region (Draine and Bertoldi, 1996). We conclude that self-shielding may cause ε to be even lower than assumed by Howe, Adams, and Meyer (2020).

Population-level surveys of present-day mass loss are increasingly within reach. As the body of published helium absorption signals continues to grow, it is important to develop models that allow us to quickly and uniformly infer mass-loss rates from a large sample of observations. Our new outflow energetics framework can be used to enhance the scientific output of these surveys by providing more precise constraints on the retrieved mass-loss rates without significant computational expense. Although this method is currently limited to lower gravity planets, it could be extended to higher gravities in future studies by using simple prescriptions for the density structures and cooling rates of non-isothermal outflows. Despite this limitation, our framework can already be used to model helium signals from low-gravity, H/He-rich planets, like those in and near the Neptune desert. Helium observations have the potential to provide the first population-level constraints on the predicted mass-loss rates for these enigmatic planets.

5.5 Appendix: Non-Negligible Cooling

In the recombination limit, cooling becomes important (Murray-Clay, Chiang, and Murray, 2009; Owen and Alvarez, 2016; Lampón, López-Puertas, Czesla, et al., 2021), and the approximation we made in Equation (5.6) greatly overpredicts the efficiency. We can repeat the calculation without making that assumption. When the cooling rate Λ can be written exactly, the efficiency is:

$$\varepsilon_{\rm RL} = \frac{1}{R_{\rm p}^2}\int_{R_p}^{R_{\rm Roche}} r^2 \sum_i n_{i,r}\bar{\sigma}_{i,r} dr - \frac{4}{R_{\rm p}^2}\frac{1}{F_{\rm XUV}}\int_{R_{\rm p}}^{R_{\rm Roche}} \Lambda r^2 dr, \tag{5.21}$$

where the factor of four in the numerator of the cooling term reflects the fact that the planet can cool through all 4π steradians. Typically, Lyman-α is taken to be the dominant coolant for the outflow, in which case the cooling rate can be written:

$$\Lambda = C\left(\frac{n_{\rm H^+,r}}{\rm cm^{-3}}\right)\left(\frac{n_{\rm H,r}}{\rm cm^{-3}}\right)\exp\left(-T_{\rm c}/T_0\right), \tag{5.22}$$

where $n_{\rm H^+,r}$ is the number density profile of ionized hydrogen, $n_{\rm H,r}$ is that of neutral hydrogen, $C = 7.5 \times 10^{-19}$ erg s^{-1}/cm^3, and $T_c = 118348$ K (Black, 1981; Murray-Clay, Chiang, and Murray, 2009; Owen and Alvarez, 2016). Rather than tracing out a permitted region on the $\dot{M} - T_0$ plane as in Equation (5.19), Equation (5.21) traces out a single curve of allowed solutions because the cooling is specified exactly. There are, however, many other cooling processes to consider even in a H/He gas including helium line emission, hydrogen and helium recombination cooling, and free-free emission (Black, 1981; Salz, Schneider, et al., 2016). Additionally, our fundamental assumption of an isothermal wind is more readily violated for planets in the recombination limit when wind-launching is treated self-consistently (Salz, Schneider, et al., 2016). For these reasons, our framework is ill-suited to exactly treat planets with strong cooling, and we default to the upper-limit formulation in Equation (5.20).

References

Adams, Fred C. (Mar. 2011). "Magnetically Controlled Outflows from Hot Jupiters". In: *ApJ* 730.1, 27, p. 27. DOI: `10.1088/0004-637X/730/1/27`. arXiv: `1101.4234 [astro-ph.EP]`.

Allart, R., V. Bourrier, C. Lovis, D. Ehrenreich, J. Aceituno, et al. (Mar. 2019). "High-resolution confirmation of an extended helium atmosphere around WASP-107b". In: *A&A* 623, A58, A58. DOI: `10.1051/0004-6361/201834917`. arXiv: `1901.08073 [astro-ph.EP]`.

Allart, R., V. Bourrier, C. Lovis, D. Ehrenreich, J. J. Spake, et al. (Dec. 2018). "Spectrally resolved helium absorption from the extended atmosphere of a warm Neptune-mass exoplanet". In: *Science* 362.6421, pp. 1384–1387. DOI: `10.1126/science.aat5879`. arXiv: `1812.02189 [astro-ph.EP]`.

Anderson, D. R. et al. (Dec. 2014). “Three newly discovered sub-Jupiter-mass planets: WASP-69b and WASP-84b transit active K dwarfs and WASP-70Ab transits the evolved primary of a G4+K3 binary”. In: *MNRAS* 445.2, pp. 1114–1129. DOI: 10.1093/mnras/stu1737. arXiv: 1310.5654 [astro-ph.EP].

Bakos, G. Á. et al. (Feb. 2010). “HAT-P-11b: A Super-Neptune Planet Transiting a Bright K Star in the Kepler Field”. In: *ApJ* 710.2, pp. 1724–1745. DOI: 10.1088/0004-637X/710/2/1724. arXiv: 0901.0282 [astro-ph.EP].

Black, J. H. (Nov. 1981). “The physical state of primordial intergalactic clouds”. In: *MNRAS* 197, pp. 553–563. DOI: 10.1093/mnras/197.3.553.

Carolan, S. et al. (Nov. 2020). “The dichotomy of atmospheric escape in AU Mic b”. In: *MNRAS* 498.1, pp. L53–L57. DOI: 10.1093/mnrasl/slaa127. arXiv: 2006.13606 [astro-ph.EP].

Dos Santos, Leonardo A. et al. (Nov. 2021). “p-winds: an open-source Python code to model planetary outflows and upper atmospheres”. In: *arXiv e-prints*, arXiv:2111.11370, arXiv:2111.11370. arXiv: 2111.11370 [astro-ph.EP].

Draine, B. T. and Frank Bertoldi (Sept. 1996). “Structure of Stationary Photodissociation Fronts”. In: *ApJ* 468, p. 269. DOI: 10.1086/177689. arXiv: astro-ph/9603032 [astro-ph].

Erkaev, N. V. et al. (Sept. 2007). “Roche lobe effects on the atmospheric loss from “Hot Jupiters””. In: *A&A* 472.1, pp. 329–334. DOI: 10.1051/0004-6361:20066929. arXiv: astro-ph/0612729 [astro-ph].

France, Kevin et al. (Apr. 2016). “The MUSCLES Treasury Survey. I. Motivation and Overview”. In: *ApJ* 820.2, 89, p. 89. DOI: 10.3847/0004-637X/820/2/89. arXiv: 1602.09142 [astro-ph.SR].

Fulton, Benjamin J. and Erik A. Petigura (Dec. 2018). “The California-Kepler Survey. VII. Precise Planet Radii Leveraging Gaia DR2 Reveal the Stellar Mass Dependence of the Planet Radius Gap”. In: *AJ* 156.6, 264, p. 264. DOI: 10.3847/1538-3881/aae828. arXiv: 1805.01453 [astro-ph.EP].

Fulton, Benjamin J., Erik A. Petigura, et al. (Sept. 2017). “The California-Kepler Survey. III. A Gap in the Radius Distribution of Small Planets”. In: *AJ* 154.3, 109, p. 109. DOI: 10.3847/1538-3881/aa80eb. arXiv: 1703.10375 [astro-ph.EP].

Gaidos, E., T. Hirano, A. W. Mann, et al. (June 2020). “Zodiacal exoplanets in time - X. The orbit and atmosphere of the young ’neptune desert’-dwelling planet K2-100b”. In: *MNRAS* 495.1, pp. 650–662. DOI: 10.1093/mnras/staa918. arXiv: 2003.12940 [astro-ph.EP].

Gaidos, E., T. Hirano, D. J. Wilson, et al. (Oct. 2020). “Zodiacal exoplanets in time - XI. The orbit and radiation environment of the young M dwarf-hosted planet K2-25b”. In: *MNRAS* 498.1, pp. L119–L124. DOI: 10.1093/mnrasl/slaa136. arXiv: 2007.12701 [astro-ph.EP].

Ginzburg, Sivan, Hilke E. Schlichting, and Re'em Sari (July 2016). "Super-Earth Atmospheres: Self-consistent Gas Accretion and Retention". In: *ApJ* 825.1, 29, p. 29. DOI: 10.3847/0004-637X/825/1/29. arXiv: 1512.07925 [astro-ph.EP].

Glassgold, A. E. and J. R. Najita (Sept. 2015). "Photochemical Heating of Dense Molecular Gas". In: *ApJ* 810.2, 125, p. 125. DOI: 10.1088/0004-637X/810/2/125. arXiv: 1506.04167 [astro-ph.SR].

Guo, J. H. and Lotfi Ben-Jaffel (Feb. 2016). "The Influence of the Extreme Ultraviolet Spectral Energy Distribution on the Structure and Composition of the Upper Atmosphere of Exoplanets". In: *ApJ* 818.2, 107, p. 107. DOI: 10.3847/0004-637X/818/2/107. arXiv: 1512.06470 [astro-ph.EP].

Gupta, Akash and Hilke E. Schlichting (July 2019). "Sculpting the valley in the radius distribution of small exoplanets as a by-product of planet formation: the core-powered mass-loss mechanism". In: *MNRAS* 487.1, pp. 24–33. DOI: 10.1093/mnras/stz1230. arXiv: 1811.03202 [astro-ph.EP].

– (Mar. 2020). "Signatures of the core-powered mass-loss mechanism in the exoplanet population: dependence on stellar properties and observational predictions". In: *MNRAS* 493.1, pp. 792–806. DOI: 10.1093/mnras/staa315. arXiv: 1907.03732 [astro-ph.EP].

– (July 2021). "Caught in the act: core-powered mass-loss predictions for observing atmospheric escape". In: *MNRAS* 504.3, pp. 4634–4648. DOI: 10.1093/mnras/stab1128. arXiv: 2103.08785 [astro-ph.EP].

Hardegree-Ullman, Kevin K. et al. (Mar. 2020). "Scaling K2. I. Revised Parameters for 222,088 K2 Stars and a K2 Planet Radius Valley at 1.9 $R_\oplus$". In: *ApJS* 247.1, 28, p. 28. DOI: 10.3847/1538-4365/ab7230. arXiv: 2001.11511 [astro-ph.SR].

Hartman, J. D. et al. (Jan. 2011). "HAT-P-18b and HAT-P-19b: Two Low-density Saturn-mass Planets Transiting Metal-rich K Stars". In: *ApJ* 726.1, 52, p. 52. DOI: 10.1088/0004-637X/726/1/52. arXiv: 1007.4850 [astro-ph.EP].

Heays, A. N., A. D. Bosman, and E. F. van Dishoeck (June 2017). "Photodissociation and photoionisation of atoms and molecules of astrophysical interest". In: *A&A* 602, A105, A105. DOI: 10.1051/0004-6361/201628742. arXiv: 1701.04459 [astro-ph.SR].

Hirano, Teruyuki et al. (Aug. 2020). "Limits on the Spin-Orbit Angle and Atmospheric Escape for the 22 Myr Old Planet AU Mic b". In: *ApJL* 899.1, L13, p. L13. DOI: 10.3847/2041-8213/aba6eb. arXiv: 2006.13243 [astro-ph.EP].

Howe, Alex R., Fred C. Adams, and Michael R. Meyer (May 2020). "Survival of Primordial Planetary Atmospheres: Photodissociation-driven Mass Loss". In: *ApJ* 894.2, 130, p. 130. DOI: 10.3847/1538-4357/ab620c. arXiv: 1912.08820 [astro-ph.EP].

Kasper, David et al. (Dec. 2020). “Nondetection of Helium in the Upper Atmospheres of Three Sub-Neptune Exoplanets”. In: *AJ* 160.6, 258, p. 258. DOI: 10.3847/1538-3881/abbee6. arXiv: 2007.12968 [astro-ph.EP].

Kirk, James et al. (Mar. 2020). “Confirmation of WASP-107b’s Extended Helium Atmosphere with Keck II/NIRSPEC”. In: *AJ* 159.3, 115, p. 115. DOI: 10.3847/1538-3881/ab6e66. arXiv: 2001.07667 [astro-ph.EP].

Krenn, A. F. et al. (June 2021). “A critical assessment of the applicability of the energy-limited approximation for estimating exoplanetary mass-loss rates”. In: *A&A* 650, A94, A94. DOI: 10.1051/0004-6361/202140437. arXiv: 2105.05858 [astro-ph.EP].

Krishnamurthy, Vigneshwaran et al. (Sept. 2021). “Nondetection of Helium in the Upper Atmospheres of TRAPPIST-1b, e, and f”. In: *AJ* 162.3, 82, p. 82. DOI: 10.3847/1538-3881/ac0d57. arXiv: 2106.11444 [astro-ph.EP].

Kubyshkina, D. et al. (Oct. 2018). “Overcoming the Limitations of the Energy-limited Approximation for Planet Atmospheric Escape”. In: *ApJL* 866.2, L18, p. L18. DOI: 10.3847/2041-8213/aae586. arXiv: 1810.06920 [astro-ph.EP].

Lamers, Henny J. G. L. M. and Joseph P. Cassinelli (1999). *Introduction to Stellar Winds*.

Lampón, M., M. López-Puertas, S. Czesla, et al. (Apr. 2021). “Evidence of energy-, recombination-, and photon-limited escape regimes in giant planet H/He atmospheres”. In: *A&A* 648, L7, p. L7. DOI: 10.1051/0004-6361/202140423. arXiv: 2104.08832 [astro-ph.EP].

Lampón, M., M. López-Puertas, L. M. Lara, et al. (Apr. 2020). “Modelling the He I triplet absorption at 10 830 Å in the atmosphere of HD 209458 b”. In: *A&A* 636, A13, A13. DOI: 10.1051/0004-6361/201937175. arXiv: 2003.04872 [astro-ph.EP].

Lampón, M., M. López-Puertas, J. Sanz-Forcada, et al. (Mar. 2021). “Modelling the He I triplet absorption at 10 830 Å in the atmospheres of HD 189733 b and GJ 3470 b”. In: *A&A* 647, A129, A129. DOI: 10.1051/0004-6361/202039417. arXiv: 2101.09393 [astro-ph.EP].

Lopez, Eric D. and Jonathan J. Fortney (Oct. 2013). “The Role of Core Mass in Controlling Evaporation: The Kepler Radius Distribution and the Kepler-36 Density Dichotomy”. In: *ApJ* 776.1, 2, p. 2. DOI: 10.1088/0004-637X/776/1/2. arXiv: 1305.0269 [astro-ph.EP].

Loyd, R. O. P. et al. (June 2016). “The MUSCLES Treasury Survey. III. X-Ray to Infrared Spectra of 11 M and K Stars Hosting Planets”. In: *ApJ* 824.2, 102, p. 102. DOI: 10.3847/0004-637X/824/2/102. arXiv: 1604.04776 [astro-ph.SR].

MacLeod, Morgan and Antonija Oklopčić (July 2021). "Stellar Wind Confinement of Evaporating Exoplanet Atmospheres and its Signatures in 1083 nm Observations". In: *arXiv e-prints*, arXiv:2107.07534, arXiv:2107.07534. arXiv: 2107.07534 [astro-ph.EP].

Mansfield, Megan et al. (Dec. 2018). "Detection of Helium in the Atmosphere of the Exo-Neptune HAT-P-11b". In: *ApJL* 868.2, L34, p. L34. DOI: 10.3847/2041-8213/aaf166. arXiv: 1812.02214 [astro-ph.EP].

McCann, John et al. (Mar. 2019). "Morphology of Hydrodynamic Winds: A Study of Planetary Winds in Stellar Environments". In: *ApJ* 873.1, 89, p. 89. DOI: 10.3847/1538-4357/ab05b8. arXiv: 1811.09276 [astro-ph.EP].

Murray-Clay, Ruth A., Eugene I. Chiang, and Norman Murray (Mar. 2009). "Atmospheric Escape From Hot Jupiters". In: *ApJ* 693.1, pp. 23–42. DOI: 10.1088/0004-637X/693/1/23. arXiv: 0811.0006 [astro-ph].

Ninan, Joe P. et al. (May 2020). "Evidence for He I 10830 Å Absorption during the Transit of a Warm Neptune around the M-dwarf GJ 3470 with the Habitable-zone Planet Finder". In: *ApJ* 894.2, 97, p. 97. DOI: 10.3847/1538-4357/ab8559. arXiv: 1910.02070 [astro-ph.EP].

Nortmann, Lisa et al. (Dec. 2018). "Ground-based detection of an extended helium atmosphere in the Saturn-mass exoplanet WASP-69b". In: *Science* 362.6421, pp. 1388–1391. DOI: 10.1126/science.aat5348. arXiv: 1812.03119 [astro-ph.EP].

Oklopčić, Antonija (Aug. 2019). "Helium Absorption at 1083 nm from Extended Exoplanet Atmospheres: Dependence on Stellar Radiation". In: *ApJ* 881.2, 133, p. 133. DOI: 10.3847/1538-4357/ab2f7f. arXiv: 1903.02576 [astro-ph.EP].

Oklopčić, Antonija and Christopher M. Hirata (Mar. 2018). "A New Window into Escaping Exoplanet Atmospheres: 10830 Å Line of Helium". In: *ApJL* 855.1, L11, p. L11. DOI: 10.3847/2041-8213/aaada9. arXiv: 1711.05269 [astro-ph.EP].

Osterbrock, Donald E. and Gary J. Ferland (2006). *Astrophysics of gaseous nebulae and active galactic nuclei*.

Owen, James E. (May 2019). "Atmospheric Escape and the Evolution of Close-In Exoplanets". In: *Annual Review of Earth and Planetary Sciences* 47, pp. 67–90. DOI: 10.1146/annurev-earth-053018-060246. arXiv: 1807.07609 [astro-ph.EP].

Owen, James E. and Fred C. Adams (Nov. 2014). "Magnetically controlled mass-loss from extrasolar planets in close orbits". In: *MNRAS* 444.4, pp. 3761–3779. DOI: 10.1093/mnras/stu1684. arXiv: 1408.3636 [astro-ph.EP].

Owen, James E. and Marcelo A. Alvarez (Jan. 2016). "UV Driven Evaporation of Close-in Planets: Energy-limited, Recombination-limited, and Photon-limited Flows". In: *ApJ* 816.1, 34, p. 34. DOI: 10.3847/0004-637X/816/1/34. arXiv: 1504.07170 [astro-ph.EP].

Owen, James E. and Alan P. Jackson (Oct. 2012). "Planetary evaporation by UV & X-ray radiation: basic hydrodynamics". In: *MNRAS* 425.4, pp. 2931–2947. DOI: 10.1111/j.1365-2966.2012.21481.x. arXiv: 1206.2367 [astro-ph.EP].

Owen, James E. and Yanqin Wu (Oct. 2013). "Kepler Planets: A Tale of Evaporation". In: *ApJ* 775.2, 105, p. 105. DOI: 10.1088/0004-637X/775/2/105. arXiv: 1303.3899 [astro-ph.EP].

– (Sept. 2017). "The Evaporation Valley in the Kepler Planets". In: *ApJ* 847.1, 29, p. 29. DOI: 10.3847/1538-4357/aa890a. arXiv: 1705.10810 [astro-ph.EP].

Paragas, Kimberly et al. (Mar. 2021). "Metastable Helium Reveals an Extended Atmosphere for the Gas Giant HAT-P-18b". In: *ApJL* 909.1, L10, p. L10. DOI: 10.3847/2041-8213/abe706. arXiv: 2102.08392 [astro-ph.EP].

Salz, M., S. Czesla, P. C. Schneider, E. Nagel, et al. (Dec. 2018). "Detection of He I λ10830 Å absorption on HD 189733 b with CARMENES high-resolution transmission spectroscopy". In: *A&A* 620, A97, A97. DOI: 10.1051/0004-6361/201833694. arXiv: 1812.02453 [astro-ph.EP].

Salz, M., S. Czesla, P. C. Schneider, and J. H. M. M. Schmitt (Feb. 2016). "Simulating the escaping atmospheres of hot gas planets in the solar neighborhood". In: *A&A* 586, A75, A75. DOI: 10.1051/0004-6361/201526109. arXiv: 1511.09341 [astro-ph.EP].

Salz, M., P. C. Schneider, et al. (Jan. 2016). "Energy-limited escape revised. The transition from strong planetary winds to stable thermospheres". In: *A&A* 585, L2, p. L2. DOI: 10.1051/0004-6361/201527042. arXiv: 1511.09348 [astro-ph.EP].

Seager, Sara (2010). *Exoplanet Atmospheres: Physical Processes*.

Seidel, J. V. et al. (Sept. 2021). "Into the storm: diving into the winds of the ultra-hot Jupiter WASP-76 b with HARPS and ESPRESSO". In: *A&A* 653, A73, A73. DOI: 10.1051/0004-6361/202140569. arXiv: 2107.09530 [astro-ph.EP].

Shematovich, V. I., D. E. Ionov, and H. Lammer (Nov. 2014). "Heating efficiency in hydrogen-dominated upper atmospheres". In: *A&A* 571, A94, A94. DOI: 10.1051/0004-6361/201423573. arXiv: 1409.0730 [astro-ph.EP].

Spake, J. J., A. Oklopčić, and L. A. Hillenbrand (Dec. 2021). "The Posttransit Tail of WASP-107b Observed at 10830 Å". In: *AJ* 162.6, 284, p. 284. DOI: 10.3847/1538-3881/ac178a. arXiv: 2107.08999 [astro-ph.EP].

Spake, J. J., D. K. Sing, et al. (May 2018). "Helium in the eroding atmosphere of an exoplanet". In: *Nature* 557.7703, pp. 68–70. DOI: 10.1038/s41586-018-0067-5. arXiv: 1805.01298 [astro-ph.EP].

Stone, James M. and Daniel Proga (Mar. 2009). "Anisotropic Winds from Close-In Extrasolar Planets". In: *ApJ* 694.1, pp. 205–213. DOI: 10.1088/0004-637X/694/1/205. arXiv: 0812.2568 [astro-ph].

Trammell, George B., Phil Arras, and Zhi-Yun Li (Feb. 2011). “Hot Jupiter Magnetospheres”. In: *ApJ* 728.2, 152, p. 152. DOI: 10.1088/0004-637X/728/2/152. arXiv: 1011.0017 [astro-ph.EP].

Trammell, George B., Zhi-Yun Li, and Phil Arras (June 2014). “Magnetohydrodynamic Simulations of Hot Jupiter Upper Atmospheres”. In: *ApJ* 788.2, 161, p. 161. DOI: 10.1088/0004-637X/788/2/161. arXiv: 1404.5817 [astro-ph.EP].

Van Eylen, V. et al. (Oct. 2018). “An asteroseismic view of the radius valley: stripped cores, not born rocky”. In: *MNRAS* 479.4, pp. 4786–4795. DOI: 10.1093/mnras/sty1783. arXiv: 1710.05398 [astro-ph.EP].

Vidal-Madjar, A., J. -M. Désert, et al. (Mar. 2004). “Detection of Oxygen and Carbon in the Hydrodynamically Escaping Atmosphere of the Extrasolar Planet HD 209458b”. In: *ApJL* 604.1, pp. L69–L72. DOI: 10.1086/383347. arXiv: astro-ph/0401457 [astro-ph].

Vidal-Madjar, A., A. Lecavelier des Etangs, et al. (Mar. 2003). “An extended upper atmosphere around the extrasolar planet HD209458b”. In: *Nature* 422.6928, pp. 143–146. DOI: 10.1038/nature01448.

Vissapragada, Shreyas, Daniel Jontof-Hutter, et al. (Mar. 2020). “Diffuser-assisted Infrared Transit Photometry for Four Dynamically Interacting Kepler Systems”. In: *AJ* 159.3, 108, p. 108. DOI: 10.3847/1538-3881/ab65c8. arXiv: 1907.04445 [astro-ph.EP].

Vissapragada, Shreyas, Heather A. Knutson, et al. (June 2020). “Constraints on Metastable Helium in the Atmospheres of WASP-69b and WASP-52b with Ultranarrowband Photometry”. In: *AJ* 159.6, 278, p. 278. DOI: 10.3847/1538-3881/ab8e34. arXiv: 2004.13728 [astro-ph.EP].

Wang, Lile and Fei Dai (June 2021a). “Metastable Helium Absorptions with 3D Hydrodynamics and Self-consistent Photochemistry. I. WASP-69b, Dimensionality, X-Ray and UV Flux Level, Spectral Types, and Flares”. In: *ApJ* 914.2, 98, p. 98. DOI: 10.3847/1538-4357/abf1ee. arXiv: 2101.00042 [astro-ph.EP].

– (June 2021b). “Metastable Helium Absorptions with 3D Hydrodynamics and Self-consistent Photochemistry. II. WASP-107b, Stellar Wind, Radiation Pressure, and Shear Instability”. In: *ApJ* 914.2, 99, p. 99. DOI: 10.3847/1538-4357/abf1ed. arXiv: 2101.00045 [astro-ph.EP].

Watson, A. J., T. M. Donahue, and J. C. G. Walker (Nov. 1981). “The dynamics of a rapidly escaping atmosphere: Applications to the evolution of Earth and Venus”. In: *Icarus* 48.2, pp. 150–166. DOI: 10.1016/0019-1035(81)90101-9.

Wright, J. T. et al. (June 2004). “Chromospheric Ca II Emission in Nearby F, G, K, and M Stars”. In: *ApJS* 152.2, pp. 261–295. DOI: 10.1086/386283. arXiv: astro-ph/0402582 [astro-ph].

Yan, Fei and Thomas Henning (July 2018). “An extended hydrogen envelope of the extremely hot giant exoplanet KELT-9b”. In: *Nature Astronomy* 2, pp. 714–718. DOI: 10.1038/s41550-018-0503-3. arXiv: 1807.00869 [astro-ph.EP].

Yan, M., H. R. Sadeghpour, and A. Dalgarno (Mar. 1998). “Photoionization Cross Sections of He and H_2”. In: *ApJ* 496.2, pp. 1044–1050. DOI: 10.1086/305420.

Youngblood, Allison et al. (June 2016). “The MUSCLES Treasury Survey. II. Intrinsic LYα and Extreme Ultraviolet Spectra of K and M Dwarfs with Exoplanets*”. In: *ApJ* 824.2, 101, p. 101. DOI: 10.3847/0004-637X/824/2/101. arXiv: 1604.01032 [astro-ph.SR].

Zhang, Michael et al. (Apr. 2021). “No Escaping Helium from 55 Cnc e”. In: *AJ* 161.4, 181, p. 181. DOI: 10.3847/1538-3881/abe382. arXiv: 2012.02198 [astro-ph.EP].

Chapter 6

THE UPPER EDGE OF THE NEPTUNE DESERT IS STABLE AGAINST PHOTOEVAPORATION

6.1 Introduction

The transit and radial velocity techniques have revealed masses and radii for thousands of planets spanning a wide range of orbital periods. These surveys indicate that relatively few sub-Jovian planets reside on close-in orbits. This "Neptune desert" is a robust feature of the planetary census, which is relatively complete in this regime (Szabó and Kiss, 2011; Beaugé and Nesvorný, 2013; Lundkvist et al., 2016). Mazeh, Holczer, and Faigler (2016) defined boundaries for the Neptune desert by searching for curves that maximize the contrast between regions of the mass-period plane with and without planets. We plot their definition for the Neptune desert in Figure 6.1 along with the planetary population observed to date.

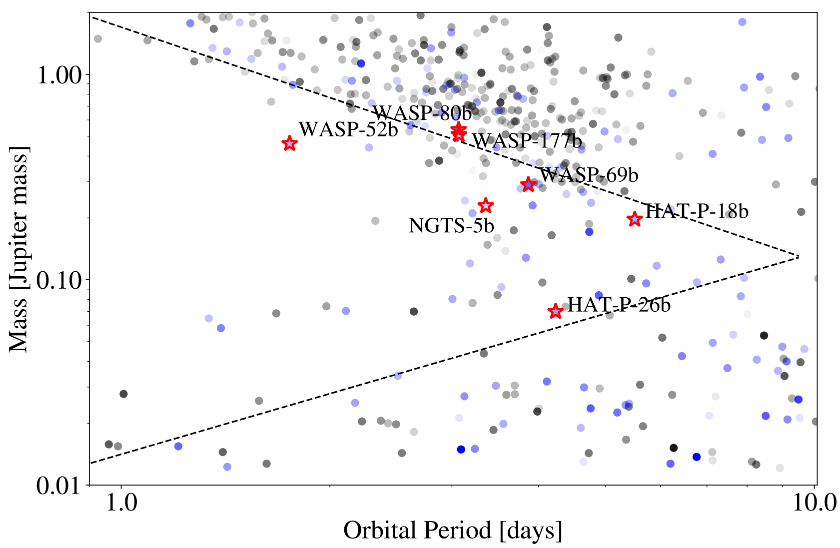

Figure 6.1: Transiting exoplanets with fractional mass uncertainties of less than 30%, with the dashed lines indicating the Neptune desert boundaries from Mazeh, Holczer, and Faigler (2016). Planets orbiting stars with 4000 K< $T_{\rm eff}$ < 5400 K are colored blue, and the seven targets constituting our sample are outlined with red stars. The point opacity scales inversely with the stellar J magnitude.

Given its close-in location, it is natural to wonder whether the desert might have been created by atmospheric mass loss (e.g. Youdin, 2011; Beaugé and Nesvorný, 2013; Kurokawa and Nakamoto, 2014; Ionov, Pavlyuchenkov, and Shematovich, 2018; Owen and Lai, 2018). Planets with short orbital periods are subjected to intense amounts of high-energy radiation that can drive atmospheric outflows (Owen, 2019). The resulting atmospheric mass-loss rates can be large, especially for planets orbiting young stars, which emit proportionally more of their energy in high-energy photons. If close-in gas-giant planets formed *in situ* (e.g. Batygin, Bodenheimer, and G. P. Laughlin, 2016) or arrived at their present-day locations relatively early ($\sim$10 Myr) via disk migration (e.g. Ida and D. N. C. Lin, 2008), they might have experienced a period of strong photoevaporation (e.g. Murray-Clay, Chiang, and Murray, 2009). Hot Neptunes typically have lower gravitational potentials than their Jovian counterparts, making them more susceptible to photoevaporation and/or Roche lobe overflow (Kurokawa and Nakamoto, 2014; Valsecchi et al., 2015; Koskinen et al., 2022). This means that Jupiters could survive at orbital separations where most Neptunes would be destroyed.

If this population of close-in giant planets instead arrived at their present locations relatively late ($\sim$Gyr) via dynamical interactions with other bodies in their systems (Rasio and Ford, 1996), we would expect photoevaporation to play a relatively minor role in their long-term evolution. In this scenario, planets undergoing high-eccentricity migration circularized onto orbits with final semimajor axes of $a \approx 2r_{\rm peri}$, where $r_{\rm peri}$ is the pericenter distance when the eccentricity $e \sim 1$. Neptune-mass planets with small present-day semimajor axes would have had pericenter passages inside the stellar tidal disruption radius, whereas Jupiter-mass planets would survive at comparable separations (Ford and Rasio, 2006; Guillochon, Ramirez-Ruiz, and D. Lin, 2011; Matsakos and Königl, 2016; Owen and Lai, 2018).

Our ability to explain the Neptune desert is thus intimately linked to our understanding of the origins of close-in giant planets (Dawson and Johnson, 2018). Unfortunately, previous studies have found it difficult to differentiate between atmospheric escape and high-eccentricity migration as explanations for this feature. Depending on their assumptions about the energy-limited mass-loss efficiency, stellar X-ray and ultraviolet (XUV) flux, initial star-planet separation, and pressure at the XUV photobase, some published studies suggest that sub-Jovian planets near the upper edge of the desert are stable against evaporation, while other suggest that they experience runaway envelope escape (Kurokawa and Nakamoto, 2014; Ionov, Pavlyuchenkov, and Shematovich, 2018; Owen and Lai, 2018; Rao et al., 2021). High-eccentricity migration models also have their own uncertainties, most notably the assumed tidal quality factor, the initial star-planet separation, and the eccentricity excitation mechanism (Matsakos and Königl, 2016; Owen and Lai, 2018). Previous observational studies have used the orbital properties and multiplicity of hot Jupiter systems to constrain the fraction of hot Jupiters that might have formed via high-eccentricity migration (e.g. Winn et al., 2010; Knutson, Fulton, et al., 2014; Dawson, Murray-Clay, and Johnson, 2015; Ngo et al., 2016; Rice, S. Wang, and G. Laughlin, 2022). Although it appears unlikely that all hot Jupiters formed this way, such planets almost certainly comprise a subset of the hot Jupiter population (see the review by Dawson and Johnson, 2018).

Observations of atmospheric escape can provide a complementary basis to differentiate between these scenarios for the origin of the Neptune desert. If atmospheric escape is indeed the mechanism that clears the Neptune desert, planets at its edge would have been marginally stable against photoevaporation. These planets would therefore be expected to exhibit relatively strong outflow signatures, even given the reduced XUV fluxes of their middle-aged host stars. Recent studies have demonstrated that the metastable helium triplet can be used to detect and characterize planetary outflows for close-in transiting planets (Spake, Sing, et al., 2018; Antonija Oklopčić and Hirata, 2018). Unlike the Lyman-α transit depth – which is controlled not by the planetary mass-loss rate, but by the distance neutral hydrogen atoms can travel before they are photoionized (Owen, Murray-Clay, et al., 2021) – the metastable helium absorption amplitude probes low-velocity thermospheric gas near the wind-launching radius. This means that it can be readily modeled using a one-dimensional isothermal Parker wind to infer a mass-loss rate (Antonija Oklopčić and Hirata, 2018; Lampón, López-Puertas, Lara, et al., 2020). Although uncertainties in the assumed incident XUV spectrum, outflow temperature, and outflow composition limit our ability to predict the metastable helium population in the Parker wind model, we can still constrain present-day mass-loss rates well enough for planetary evolution studies. This is especially true when we incorporate additional information like line shapes and energetics (dos Santos et al., 2022; Vissapragada, Knutson, dos Santos, et al., 2022).

We recently installed a narrowband filter centered on the metastable helium line (Vissapragada, Knutson, Jovanovic, et al., 2020) in the Wide-field InfraRed Camera (WIRC; Wilson et al., 2003) at the Hale 200-inch Telescope at Palomar Observatory. We commissioned this new observing mode by confirming the outflow of WASP-69b, finding an absorption signal commensurate with spectroscopically resolved observations by Nortmann et al. (2018). As part of this same study we also observed a transit of WASP-52b but did not detect a strong signal. We have since used this same observing mode to detect an atmopsheric outflow from HAT-P-18b (Paragas et al., 2021) and found a tentative evidence for an outflow from the young planet V1298 Tau d (Vissapragada, Stefánsson, et al., 2021).

From 2019-2021, we used our narrowband helium photometer to survey the metastable helium line in a seven-planet sample near the upper edge of the Neptune desert. There are currently ten published helium detections in the literature: WASP-107b (Spake, Sing, et al., 2018; Allart, Bourrier, Lovis, Ehrenreich, Aceituno, et al., 2019; James Kirk et al., 2020; Spake, A. Oklopčić, and L. A. Hillenbrand, 2021), HAT-P-11b (Allart, Bourrier, Lovis, Ehrenreich, Spake, et al., 2018; Mansfield et al., 2018), WASP-69b (Nortmann et al., 2018; Vissapragada, Knutson, Jovanovic, et al., 2020), HD 209458b (Alonso-Floriano et al., 2019), HD 189733b (Salz, Czesla, Schneider, Nagel, et al., 2018; Guilluy et al., 2020), GJ 3470b (Palle et al., 2020; Ninan et al., 2020), HAT-P-18b (Paragas et al., 2021), HAT-P-32b (Czesla et al., 2022), TOI-560.01 (Zhang et al., 2022), and GJ 1214b (Orell-Miquel et al., 2022). These observations, along with many non-detections and tentative detections in the literature, span wide ranges in planetary mass and radius, stellar spectral type and activity level, system age, observing methodology, and data reduction technique. This heterogeneity can obfuscate underlying trends in the data, because the measured helium absorption signal depends on a variety of factors that all vary across the sample. We therefore focus on a uniformly selected sample of helium observations obtained with Palomar to search for trends in measured mass-loss rates for planets at the upper edge of the Neptune desert.

In this work we present the results of our survey, including a re-analysis of the published transit observations from Vissapragada, Knutson, Jovanovic, et al., 2020 and Paragas et al., 2021. We also present new observations of an additional eight transits for five planets: WASP-52b, WASP-80b, WASP-177b, HAT-P-26b, and NGTS-5b. In Section 6.2, we describe our sample selection methodology as well as our observation and data reduction procedures. In Section 6.3, we summarize our observations and present helium-band light curves for each of our seven targets. In Section 6.4, we model each of our light curves using a one-dimensional isothermal Parker wind model to constrain the planetary mass-loss rates. We discuss the implications of our results for the population-level picture of atmospheric escape in Section 6.5, and summarize our conclusions in Section 6.6.

6.2 Observations

Sample Selection

Table 6.1: Stellar and planetary parameters for sample selected in this work

Star	J mag	$T_\star$ (K)	$R_\star$ ($R_\odot$)	$M_\star$ ($M_\odot$)	$\log(R'_{\rm HK})$	$M_{\rm p}$ ($M_{\rm J}$)	$R_{\rm p}$ ($R_{\rm J}$)	$\rho_{\rm p}$ (g cm^{-3})	P (d)	a (au)	Reference
WASP-69	8.0	4715^{+50}_{-50}	$0.813^{+0.028}_{-0.028}$	$0.826^{+0.029}_{-0.029}$	-4.54	$0.260^{+0.017}_{-0.017}$	$1.057^{+0.047}_{-0.047}$	$0.291^{+0.041}_{-0.041}$	3.87	0.045	A14
WASP-52	10.6	5000^{+100}_{-100}	$0.79^{+0.02}_{-0.02}$	$0.87^{+0.03}_{-0.03}$	-4.4	$0.459^{+0.022}_{-0.021}$	$1.27^{+0.03}_{-0.03}$	$0.29^{+0.03}_{-0.03}$	1.75	0.027	H13
HAT-P-18	10.8	4803^{+80}_{-80}	$0.749^{+0.037}_{-0.037}$	$0.770^{+0.031}_{-0.031}$	-4.73	$0.197^{+0.013}_{-0.013}$	$0.995^{+0.052}_{-0.052}$	$0.25^{+0.04}_{-0.04}$	5.51	0.056	H11a, V22
WASP-80	9.2	4143^{+92}_{-94}	$0.586^{+0.017}_{-0.018}$	$0.577^{+0.051}_{-0.054}$	-4.04	$0.538^{+0.035}_{-0.036}$	$0.999^{+0.030}_{-0.031}$	$0.717^{+0.039}_{-0.032}$	3.07	0.034	T15, F21
WASP-177	10.7	5017^{+70}_{-70}	$0.885^{+0.046}_{-0.046}$	$0.876^{+0.038}_{-0.038}$	–	$0.508^{+0.038}_{-0.038}$	$1.58^{+0.66}_{-0.36}$	$0.172^{+0.203}_{-0.110}$	3.07	0.040	T19
HAT-P-26	10.1	5079^{+88}_{-88}	$0.788^{+0.098}_{-0.043}$	$0.816^{+0.033}_{-0.033}$	-4.99	$0.059^{+0.007}_{-0.007}$	$0.565^{+0.072}_{-0.032}$	$0.40^{+0.10}_{-0.10}$	4.23	0.048	H11b
NGTS-5	12.1	4987^{+41}_{-41}	$0.739^{+0.014}_{-0.012}$	$0.661^{+0.068}_{-0.061}$	-4.63	$0.229^{+0.037}_{-0.037}$	$1.136^{+0.023}_{-0.023}$	$0.193^{+0.032}_{-0.034}$	3.36	0.038	E19

J magnitudes are taken from 2MASS (Cutri et al., 2003). Orbital periods and semimajor axes are truncated with errors omitted for clarity. In the references column, A14 is Anderson et al. (2014), H13 is Hébrard et al. (2013), H11a is Hartman, Bakos, Sato, et al. (2011), V22 is Vissapragada, Knutson, dos Santos, et al. (2022), T15 is Amaury H. M. J. Triaud et al. (2015), F21 is Fossati et al. (2021), T19 is O. D. Turner et al. (2019), H11b is Hartman, Bakos, D. M. Kipping, et al. (2011), and E19 is Eigmüller et al. (2019). The $\log(R'_{\rm HK})$ value for NGTS-5b was calculated using an S-value from P. Eigmüller (private communication).

To construct our survey sample, we searched the NASA Exoplanet Archive (Akeson et al., 2013) for transiting giant ($R > 4R_\oplus$) planets with measured masses orbiting K-type host stars ($T_\star = 4000 - 5400$ K). Planets orbiting K-type stars are predicted to have the largest fractional metastable helium populations, and therefore to exhibit the strongest helium absorption signatures during transit (Antonija Oklopčić, 2019; L. Wang and Dai, 2021a). This is because K stars have relatively high EUV fluxes, which populate the metastable state via ground-state ionization and subsequent recombination, and relatively low mid-UV fluxes, which ionize and depopulate the metastable state. A large fraction of the EUV flux also comes from coronal iron lines, and Poppenhaeger (2022) highlighted that this consideration also favors K stars for helium studies. The stellar spectral type gives only an approximate expectation for the high-energy spectrum of the star however, and the discovery of a strong helium signature for HAT-P-32b (a gas-giant planet orbiting an F star) is a reminder that other stars with favorable spectral energy distributions (SEDs) can also exhibit strong signals regardless of their spectral type (Czesla et al., 2022). Nevertheless, the bulk of planets with detected outflows in the literature orbit K stars.

We used this initial sample to create a rank-ordered list based on predicted signal-to-noise ratio (SNR). We estimated the SNR by first calculating lower atmospheric planetary scale heights using masses, radii, and equilibrium temperatures from the NASA Exoplanet Archive with a mean molecular weight of 2.3 amu. We then assumed that a typical helium absorption extends 85.5 lower atmospheric scale heights at the core of the helium feature, corresponding to the magnitude of the measured excess absorption signal for WASP-69b (Nortmann et al., 2018). We selected this planet as a benchmark simply because it was among the first published measurements of a planetary helium line at high resolving power, but a different choice for the signal amplitude would not have affected the relative rankings. Assuming a line shape similar to that observed by Nortmann et al. (2018), we convolved the expected absorption features with our measured filter transmission profile to get a Palomar/WIRC signal estimate. We calculated the expected photometric noise for each observation by scaling on-sky noise statistics from previous observations (Vissapragada, Jontof-Hutter, et al., 2020; Vissapragada, Knutson, Jovanovic, et al., 2020) to the 2MASS J magnitudes for each host star. From the resulting rank-ordered list, we removed two targets with extensive previous observations (WASP-107b and HD 189733b; Salz, Czesla, Schneider, Nagel, et al., 2018; Spake, Sing, et al., 2018; Allart, Bourrier, Lovis, Ehrenreich, Aceituno, et al., 2019; Guilluy et al., 2020; James Kirk et al., 2020; Spake, A. Oklopčić, and L. A.

Hillenbrand, 2021) and one target that lacked nearby comparison stars, which are required for our photometric observation technique, and had an exceptionally long transit duration (KELT-11b).

We were able to obtain observing time for eight of the highest-priority targets, one of which (HAT-P-12b) we did not ultimately observe due to telescope closures and poor weather conditions. In Table 6.1, we present the stellar and planetary parameters for the remaining seven targets constituting our sample. All of the new targets in our sample except for NGTS-5b (a relatively recent discovery) were independently identified by James Kirk et al. (2020) as good candidates for metastable helium observations. These seven planets lie near the edge of the Neptune desert, visualized in Figure 6.1. HAT-P-26b is close to the lower edge of the desert, and the other six planets trace the upper edge.

Palomar/WIRC Observations

Table 6.2: Summary of Palomar/WIRC observations analyzed in this work.

Planet	Date	Start Time	End Time	n_{exp}	t_{exp} (s)	Start/Min/End Airmass	n_{comp}	n_{dither}	r_{phot} (px)	σ [%]	σ/σ_{phot}
WASP-69b	2019 Aug 16	04:26:06	11:01:00	345	60	1.73/1.28/2.52	4	4	10	0.24	2.2
WASP-52b	2019 Sep 17	03:16:57	11:14:49	291	90	2.04/1.10/1.97	4	4	7	0.70	1.4
HAT-P-18b	2020 Jun 05	05:03:30	10:41:41	207	90	1.24/1.00/1.21	4	4	7	1.15	1.9
HAT-P-18b	2020 Jul 08	05:06:57	11:03:26	217	90	1.01/1.00/2.33	6	4	11	0.82	1.2
WASP-80b	2020 Jul 09	05:20:35	11:28:27	311	60	2.05/1.23/1.61	5	26	8	0.56/0.54	2.3/2.1
WASP-52b	2020 Aug 04	05:48:11	11:03:11	192	90	2.33/1.10/1.13	3	6	11	0.87	1.4
WASP-177b	2020 Oct 02	03:01:32	08:53:57	215	90	1.50/1.22/2.06	2	4	9	0.73	1.2
HAT-P-26b	2021 Feb 18	08:19:21	12:48:06	165	90	2.03/1.15/1.17	1	4	12	1.80	2.8
NGTS-5b	2021 Apr 30	05:56:31	11:31:18	204	90	1.30/1.13/1.82	1	7	8	3.80	1.7
HAT-P-26b	2021 May 01	04:34:13	11:40:54	260	90	1.53/1.15/2.53	2	5	12	0.81	1.6
HAT-P-26b	2021 May 18	04:20:36	10:29:36	225	90	1.30/1.15/2.44	2	7	9	0.61	1.4
NGTS-5b	2021 May 27	04:25:11	10:20:52	217	90	1.26/1.13/2.27	1	7	8	2.5	1.5

In the column headers, n_{exp} refers to the total number of exposures, t_{exp} is the exposure time, n_{comp} is the number of comparison stars, n_{dither} is the total number of dither frames used in constructing the background, r_{phot} is the radius of the circular aperture used in the photometric extraction, σ is the rms scatter of the residuals to our final light-curve fit, and σ/σ_{phot} is the ratio of the rms scatter to the photon noise limit. The two σ and σ/σ_{phot} values for the WASP-80b observation indicate the noise before and after the instrument was reset. All dates and times are UT.

From 2019–2021, we observed transits for the seven targets in our sample over 12 nights. We summarize these observations in Table 6.2. All transits were observed in a custom metastable helium filter centered at 1083.3 nm with a full-width at half-maximum (FWHM) of 0.635 nm, previously introduced in Vissapragada, Knutson, Jovanovic, et al. (2020). Each observation followed a similar sequence to that described in our previous papers (Vissapragada, Knutson, Jovanovic, et al., 2020; Paragas et al., 2021; Vissapragada, Stefánsson, et al., 2021). We began each night by observing a helium arc lamp through the helium filter, allowing us to position the target star where the effective transmission function of the filter was centered on the helium feature. The exact positioning within this region was selected to maximize the number of suitable comparison stars; the number of comparison stars for each night is noted in Table 6.2. On most nights, after acquiring and positioning the target star we used a custom NIR beam-shaping diffuser to mold the PSF into a top-hat 3″ in diameter, allowing for precise control of time-correlated systematics (Stefansson et al., 2017; Vissapragada, Jontof-Hutter, et al., 2020). The only exception was our observation of HAT-P-18b on UT 2020 Jun 05. Weather conditions were poor that night, and we chose to slightly defocus the telescope to 1.″2 instead of using the diffuser in order to minimize the sky background flux in our photometric aperture. As described in Vissapragada, Knutson, Jovanovic, et al., 2020, the center wavelength of the filter shifts across the field of view, and the resulting sky background is highly structured with bright rings corresponding to OH emission features. To correct for the structured background, we obtained a number of dithered background frames on each night (noted in Table 6.2).

Data Reduction

We dark-corrected and flat-fielded each image, and then corrected detector cosmetics including bad pixels and residual striping (for a more detailed description, see Vissapragada, Jontof-Hutter, et al., 2020). To subtract the sky background from each science frame, we first constructed a background frame from the aforementioned dither sequence. Then, we sigma-clipped the science frame to remove sources, and finally we median-scaled the dither frame to match the science frame in 10 px radial steps from the "zero-point", which is where light encounters the filter at normal incidence (Vissapragada, Knutson, Jovanovic, et al., 2020). We demonstrated in Paragas et al. (2021) that these scaling factors can also be used to decorrelate the time-varying water absorption, which can otherwise contaminate the transit signal. The OH line at 1083.4 nm overlaps with nearby water features at the resolution of our filter, and its flux evolves differently over the night relative to the uncontaminated OH lines. By taking the ratio of scaling factors in the contaminated and uncontaminated OH lines, we can construct a proxy for the time-varying water absorption. This proxy is included as a covariate in our light-curve fits.

We performed aperture photometry on each source using the `photutils` package, following the procedure detailed in Vissapragada, Knutson, Jovanovic, et al. (2020). We tested apertures from 3 to 15 pixels ($0\farcs75$–$3\farcs75$) in radius for each transit observation. We allowed the locations of the apertures to shift (separately for each star) from image to image to account for variations in telescope pointing. We found that the pointing variations were smaller than $1''$ across all datasets except for our observation of WASP-80b on UT 2020 Jul 09, where the instrument crashed during the observation and had to be reset. We included the centroid offsets as covariates in our light-curve fits along with the airmass curves. To select the optimal aperture for use in light-curve modeling, we first normalized the target star's light curve by an average of the comparison star light curves, and subsequently removed 4σ outliers using a moving median filter. We then selected the aperture size that minimized the per-point rms scatter in the averaged and moving-median-corrected target star photometry. The optimized aperture sizes are noted in Table 6.2.

Light-curve Modeling

After calculating the optimized photometry for each transit observation along with the corresponding decorrelation vectors (airmass, centroid offset, and absorption proxy), we proceeded to fit the transit light curves using `exoplanet` (Foreman-Mackey, Luger, Agol, Barclay, L. Bouma, et al., 2021; Foreman-Mackey, Luger, Agol, Barclay, L. G. Bouma, et al., 2021). Our procedure is similar to that described in Paragas et al. (2021) and Vissapragada, Stefánsson, et al. (2021). Briefly, each target light curve is modeled with a limb-darkened `starry` transit light curve (Luger et al., 2019), which is multiplied by a systematics model. The transit light curve is parameterized by the radius ratio $R_\mathrm{p}/R_\star$, the orbital period P, the epoch T_0, the scaled semi-major axis $a/R_\star$, the impact parameter b, and the quadratic limb darkening coefficients (u_1, u_2).

We experiment with leaving the limb darkening coefficients free (sampling them using the approach from David M. Kipping, 2013) and fixing them to values computed from `ldtk` (Husser et al., 2013; Parviainen and Aigrain, 2015). Both approaches have advantages and drawbacks. Using the computed values can be advantageous for faint stars, where the precision on the transit shape is too low for our data to constrain the limb darkening themselves. On the other hand, the `PHOENIX` models (Husser et al., 2013) underlying `ldtk` may not accurately describe the stellar brightness profile in the helium line because the line is formed in the chromosphere. For some stars in our sample, we observe mismatches between the `ldtk` calculations and the retrieved limb darkening parameters; this could either be due to strong stellar limb darkening or an optically-thin component of the outflow altering the transit shape and biasing the inference for the observed limb darkening parameters (e.g. MacLeod and Antonija Oklopčić, 2022; L. Wang and Dai, 2021a; L. Wang and Dai, 2021b). Therefore, we repeat the fits for each planet leaving the limb darkening coefficients free and holding them fixed to the calculated values, and adopt the fixed solution when it agrees with the free retrieval or when the free retrieval is otherwise uninformative on the limb darkening coefficients. We show how the posteriors on the limb darkening coefficients compare to the calculated values in Appendix 6.7.

We fix the eccentricities to zero in our fits; none of the planets in our sample are known to have eccentric orbits, although we note that there is tentative evidence (1-2σ) that HAT-P-18b and HAT-P-26b may have small but non-zero orbital eccentricities (Hartman, Bakos, Sato, et al., 2011; Hartman, Bakos, D. M. Kipping, et al., 2011; Wallack et al., 2019). We modeled the systematics as a linear combination of comparison star light curves and decorrelation vectors, with the weights left as free parameters in each fit. We also included the mean-subtracted BJD times as a decorrelation vector, which functions as a linear baseline. Each weight was assigned a uniform prior of $\mathcal{U}(-2, 2)$. We list the rest of the priors for the transit light-curve modeling in Table 6.3.

Table 6.3: Priors for the light-curve fits.

Planet	P (days)	T_0 (BJD - 2450000)	b	$a/R_\star$	WIRC $R_\mathrm{p}/R_\star$	References
WASP-69b	$\mathcal{N}(3.8681390, 0.0000006)$	$\mathcal{N}(7176.17789, 0.00017)$	$\mathcal{N}(0.686, 0.023)$	$\mathcal{N}(12.00, 0.46)$	$\mathcal{U}(0., 0.25)$	A14, K22
WASP-52b	$\mathcal{N}(1.74978119, 0.00000010)$	$\mathcal{N}(6770.05972, 0.00004)$	$\mathcal{N}(0.60, 0.02)$	$\mathcal{N}(7.38, 0.11)$	$\mathcal{U}(0., 0.25)$	H13, K22
HAT-P-18b	$\mathcal{N}(5.5080300, 0.0000008)$	$\mathcal{N}(7276.25646, 0.00010)$	$\mathcal{N}(0.352, 0.057)$	$\mathcal{N}(16.39, 0.24)$	$\mathcal{U}(0., 0.25)$	K17, K22
WASP-80b	$\mathcal{N}(3.06785271, 0.00000019)$	$\mathcal{N}(6671.49615, 0.00004)$	$\mathcal{N}(0.215, 0.022)$	$\mathcal{N}(12.63, 0.13)$	$\mathcal{U}(0., 0.25)$	T15, K22
WASP-177b	$\mathcal{N}(3.071722, 0.000001)$	$\mathcal{N}(7994.37140, 0.00028)$	$\mathcal{N}(0.980, 0.092)$	$\mathcal{N}(9.610, 0.530)$	$\mathcal{U}(0., 0.4)$	T19
HAT-P-26b	$\mathcal{N}(4.2345002, 0.0000007)$	$\mathcal{N}(6892.59046, 0.00010)$	$\mathcal{N}(0.303, 0.122)$	$\mathcal{N}(13.06, 0.83)$	$\mathcal{U}(0., 0.25)$	H11, K22
NGTS-5b	$\mathcal{N}(3.3569866, 0.0000026)$	$\mathcal{N}(7740.35262, 0.00026)$	$\mathcal{N}(0.653, 0.048)$	$\mathcal{N}(11.111, 0.32)$	$\mathcal{U}(0., 0.4)$	E19

$\mathcal{U}(a, b)$ indicates a uniform prior between a and b and $\mathcal{N}(a, b)$ indicates a normal prior with mean a and standard deviation b. In the References column, A14 is Anderson et al. (2014), K22 is Kokori et al. (2022), H13 is Hébrard et al. (2013), K17 is J. Kirk, P. J. Wheatley, T. Louden, Doyle, et al. (2017), T15 is Amaury H. M. J. Triaud et al. (2015), T19 is O. D. Turner et al. (2019), H11 is Hartman, Bakos, D. M. Kipping, et al. (2011), and E19 is Eigmüller et al. (2019).

After defining the model, we sampled the posterior distributions for each model parameter using the No U-Turn Sampler (NUTS Hoffman and Gelman, 2011) implemented in `pymc3` (Salvatier, Wieckiâ, and Fonnesbeck, 2016). In each light-curve fit, we ran four chains for 1,500 tuning steps each before taking 2,500 draws. This resulted in a total of 10,000 draws, which we used to derive the final results. When performing joint fits across multiple nights of WIRC data, we doubled the number of tuning steps and draws. We verified the convergence of each fit by visually inspecting the trace plots to ensure that the chains were well-mixed, and also by checking that the Gelman-Rubin statistic (Gelman and Rubin, 1992) was $\hat{R} \ll 1.01$ for every sampled parameter.

In addition to the comparison star photometry, each night of data has three additional covariates as described in Section 6.2: the airmass curve, the water absorption proxy, and the centroid offsets. We determined which of these covariates to include in the final model by repeating the fit with every combination of these three parameters and calculated the Bayesian Information Criterion (BIC; Schwarz, 1978) for each fit:

$$\mathrm{BIC} = k \ln n - 2 \ln \hat{\mathcal{L}}, \tag{6.1}$$

where k is the number of fit parameters, n is the number of data points, and $\hat{\mathcal{L}}$ is the maximum likelihood estimate, or MLE. We report the differences in BIC (ΔBIC) between each fit and a fit with no additional covariates in Appendix 6.8, and select the model with the minimal BIC. Because `pymc3` takes a fully Bayesian approach, we actually obtain an estimate of the maximum a posteriori (MAP) solution, and the likelihood at this point can differ from the MLE when the priors are informative. To ensure that our model selection is not strongly impacted by this difference, we also consider the two Bayesian model selection methodologies provided by the `arviz` package: the Pareto-smoothed importance sampling leave-one-out statistic (PSIS-LOO; Vehtari, Gelman, and Gabry, 2017) and the Watanabe-Akaike Information Criterion, sometimes referred to as the Widely Applicable Information Criterion (WAIC; Watanabe, 2010). Both are methods for evaluating the out-of-sample predictive accuracy of a model, and more detailed comparisons between these statistics and the BIC can be found in e.g. Gelman, Hwang, and Vehtari (2014). For each dataset, we verified that the detrending model with the lowest BIC also had the highest PSIS-LOO and WAIC values (within the uncertainties reported by `arviz`), indicating the highest predictive accuracy.

After selecting optimized detrending models for each night of data, we obtained final fits for each planet, in some cases jointly fitting multiple nights of data. In the final version of the fits we also included a jitter term on each night $\log(\sigma_{\rm extra})$, which quantifies the discrepancy between the photon noise and the true variance in the data (i.e. $\sigma^2 = \sigma^2_{\rm photon} + \sigma^2_{\rm extra}$). Final σ values for each light curve are provided in Table 6.2, as well as the ratio $\sigma/\sigma_{\rm phot}$ between the achieved rms and the photon noise in the unbinned residuals. Allan deviation plots for each light curve are presented in Appendix 6.9.

We summarize the resulting posteriors for our light-curve fits in Table 6.4. In this table, we also report the excess absorption at mid-transit, $\delta_{\rm mid}$. To derive this parameter, we first construct a comparison light curve at each step in the fit using the radius ratio measured in a nearby bandpass along with our transit shape and limb darkening parameters. We then subtract the minimum value of the comparison light curve from the minimum value of our helium light curve at each step in the fit to obtain a distribution of $\delta_{\rm mid}$ values, which is summarized in Table 6.4. To construct the comparison light curves for WASP-69b, WASP-52b, HAT-P-18b, WASP-80b, and HAT-P-26b, we used the radius ratios from *HST*/WFC3 G141 between 1110.8 nm and 1141.6 nm obtained by (Tsiaras et al., 2018). WASP-177b and NGTS-5b are relatively recent discoveries and have not been observed by *HST*; for the former planet, we fit jointly with existing *TESS* (bandpass between 600 nm–1000 nm) observations of this system, and for the latter planet we use the reported radius ratio from NGTS (an average across optical and NIR wavelengths; Eigmüller et al., 2019) since *TESS* has not yet observed the system.

Table 6.4: Posteriors for the light-curve fits.

Planet	LDC	P (days)	T_0 (BJD − 2450000)	b	$a/R_\star$	WIRC $R_p/R_\star$	u_1	u_2	δ_{mid} (%)
WASP-69b	free	$3.86813899^{+0.00000053}_{-0.00000054}$	$7176.17789^{+0.00017}_{-0.00016}$	$0.679^{+0.019}_{-0.019}$	$11.64^{+0.28}_{-0.28}$	$0.1462^{+0.0026}_{-0.0025}$	$0.47^{+0.33}_{-0.30}$	$0.20^{+0.40}_{-0.42}$	$0.506^{+0.068}_{-0.066}$
	fixed	$3.86813940^{+0.00000051}_{-0.00000052}$	$7176.17797^{+0.00016}_{-0.00016}$	$0.691^{+0.017}_{-0.017}$	$11.79^{+0.27}_{-0.28}$	$0.1467^{+0.0017}_{-0.0017}$	0.38	0.12	$0.512^{+0.049}_{-0.048}$
WASP-52b	free	$1.749781181^{+0.000000099}_{-0.000000099}$	$6770.05972^{+0.000040}_{-0.000040}$	$0.596^{+0.018}_{-0.018}$	$7.40^{+0.10}_{-0.10}$	$0.1728^{+0.0038}_{-0.0039}$	$0.26^{+0.28}_{-0.19}$	$0.12^{+0.31}_{-0.25}$	$0.28^{+0.14}_{-0.14}$
	fixed	$1.749781183^{+0.000000099}_{-0.000000099}$	$6770.059719^{+0.000039}_{-0.000040}$	$0.594^{+0.017}_{-0.016}$	$7.373^{+0.096}_{-0.096}$	$0.1729^{+0.0035}_{-0.0036}$	0.35	0.12	$0.29^{+0.13}_{-0.13}$
HAT-P-18b	**free**	$5.50802974^{+0.00000078}_{-0.00000077}$	$7276.256448^{+0.000099}_{-0.000098}$	$0.365^{+0.047}_{-0.049}$	$16.44^{+0.23}_{-0.23}$	$0.1567^{+0.0046}_{-0.0047}$	$0.67^{+0.29}_{-0.32}$	$0.08^{+0.41}_{-0.37}$	$0.70^{+0.16}_{-0.16}$
	fixed	$5.50802973^{+0.00000077}_{-0.00000077}$	$7276.256446^{+0.000099}_{-0.000097}$	$0.412^{+0.040}_{-0.041}$	$16.54^{+0.23}_{-0.23}$	$0.1624^{+0.0035}_{-0.0036}$	0.38	0.12	$0.84^{+0.13}_{-0.13}$
WASP-80b	free	$3.06785259^{+0.00000019}_{-0.00000018}$	$6671.49614^{+0.00004}_{-0.00004}$	$0.216^{+0.022}_{-0.022}$	$12.66^{+0.12}_{-0.12}$	$0.1708^{+0.0055}_{-0.0055}$	$0.40^{+0.36}_{-0.27}$	$0.21^{+0.38}_{-0.40}$	$-0.01^{+0.23}_{-0.22}$
	fixed	$3.06785259^{+0.00000019}_{-0.00000018}$	$56671.496140^{+0.000040}_{-0.000040}$	$0.219^{+0.021}_{-0.022}$	$12.68^{+0.11}_{-0.11}$	$0.1716^{+0.0051}_{-0.0051}$	0.31	0.15	$0.02^{+0.20}_{-0.20}$
WASP-177b	free	$3.07172220^{+0.00000068}_{-0.00000068}$	$7994.37141^{+0.00025}_{-0.00024}$	$0.980^{+0.071}_{-0.057}$	$9.51^{+0.37}_{-0.30}$	$0.230^{+0.056}_{-0.043}$	$0.62^{+0.59}_{-0.45}$	$-0.03^{+0.43}_{-0.42}$	$0.70^{+0.35}_{-0.35}$
	fixed	$3.07172221^{+0.00000068}_{-0.00000069}$	$7994.37142^{+0.00025}_{-0.00024}$	$0.975^{+0.069}_{-0.054}$	$9.52^{+0.36}_{-0.31}$	$0.213^{+0.050}_{-0.034}$	0.36	0.12	$0.53^{+0.23}_{-0.28}$
HAT-P-26b	free	$4.23450038^{+0.00000068}_{-0.00000067}$	$6892.590466^{+0.000100}_{-0.000097}$	$0.288^{+0.099}_{-0.111}$	$13.19^{+0.51}_{-0.56}$	$0.0878^{+0.0055}_{-0.0058}$	$0.26^{+0.32}_{-0.19}$	$0.15^{+0.36}_{-0.27}$	$0.30^{+0.11}_{-0.11}$
	fixed	$4.23450039^{+0.00000067}_{-0.00000066}$	$6892.590466^{+0.000099}_{-0.000099}$	$0.290^{+0.099}_{-0.110}$	$13.22^{+0.48}_{-0.52}$	$0.0882^{+0.0051}_{-0.0054}$	0.35	0.12	$0.31^{+0.10}_{-0.10}$
NGTS-5b	free	$3.3569892^{+0.0000024}_{-0.0000024}$	$7740.35267^{+0.00026}_{-0.00026}$	$0.675^{+0.044}_{-0.046}$	$11.16^{+0.31}_{-0.31}$	$0.188^{+0.014}_{-0.014}$	$0.81^{+0.57}_{-0.55}$	$-0.10^{+0.52}_{-0.46}$	$1.07^{+0.52}_{-0.50}$
	fixed	$3.3569890^{+0.0000024}_{-0.0000024}$	$7740.35267^{+0.00026}_{-0.00026}$	$0.691^{+0.041}_{-0.044}$	$11.20^{+0.31}_{-0.31}$	$0.187^{+0.013}_{-0.013}$	0.36	0.12	$1.02^{+0.48}_{-0.46}$

The “LDC" column denotes the fitting strategy of leaving the limb darkening coefficients free or fixing them to a calculation from `ldtk` (Husser et al., 2013; Parviainen and Aigrain, 2015); the adopted strategy for each planet is noted in bold. The mid-transit excess depth δ_{mid} is a derived parameter. Posteriors on the detrending weights are omitted for brevity.

6.3 Results for Individual Planets

WASP-69b

WASP-69b is a Saturn-mass ($0.26 M_\mathrm{J}$), Jupiter-sized ($1.06 R_\mathrm{J}$) planet in a 3.87 day orbit around its K5 host star (Anderson et al., 2014). Its low gravitational potential makes it an excellent target for atmospheric observations. To date, observations of this planet's lower atmosphere have revealed water absorption, sodium absorption, and a Rayleigh scattering slope indicating the presence of hazes (Tsiaras et al., 2018; Murgas et al., 2020; Estrela et al., 2021; Khalafinejad et al., 2021). Additionally, Nortmann et al. (2018) detected helium escaping from the upper atmosphere of WASP-69b with two nights of CARMENES observations. We confirmed the strong absorption reported by these authors in our observation of this planet on UT 2019 Aug 16, which was initially published in Vissapragada, Knutson, Jovanovic, et al. (2020).

Our transit modeling methodology has changed since that initial work, and we therefore re-fit the data to be consistent with the other planets in the sample. We found that the calculated limb darkening coefficients agreed well (within 2σ) with the joint distribution of retrieved quadratic limb darkening coefficients (Appendix 6.7), and the choice does not make much of a difference for the retrieved parameters. Therefore, we adopted the fixed limb darkening coefficient fit for this planet. The best-fit light curve, residual, and Allan deviation plot are shown in Figure 6.2. We find the excess depth at mid-transit to be $0.512^{+0.049}_{-0.048}\%$ in our bandpass, which is consistent with our previous work albeit with slightly larger uncertainty. In our previous work, the detrending model used the best-fit linear combination of comparison star vectors, effectively marginalizing over the detrending vector weights that we fit for in this work, so the previously-reported uncertainties were slightly underestimated.

WASP-52b

WASP-52b is a $0.46 M_\mathrm{J}$, $1.27 R_\mathrm{J}$ planet in a short 1.75 day orbit around its K2 host star (Hébrard et al., 2013). Notably, the system appears to be relatively young: the discovery paper quotes a gyrochronological age of 400^{+300}_{-200} Myr (Hébrard et al., 2013), though this may be an underestimate (Mancini, Southworth, Raia, et al., 2017). Its precarious position–just past the edge of the Neptune desert–was also noted by Owen and Lai (2018). In the high-eccentricity migration framework, which is their preferred scenario for planets at the upper edge of the desert, this planet's position past the edge of the desert suggests that it should have been tidally disrupted. To

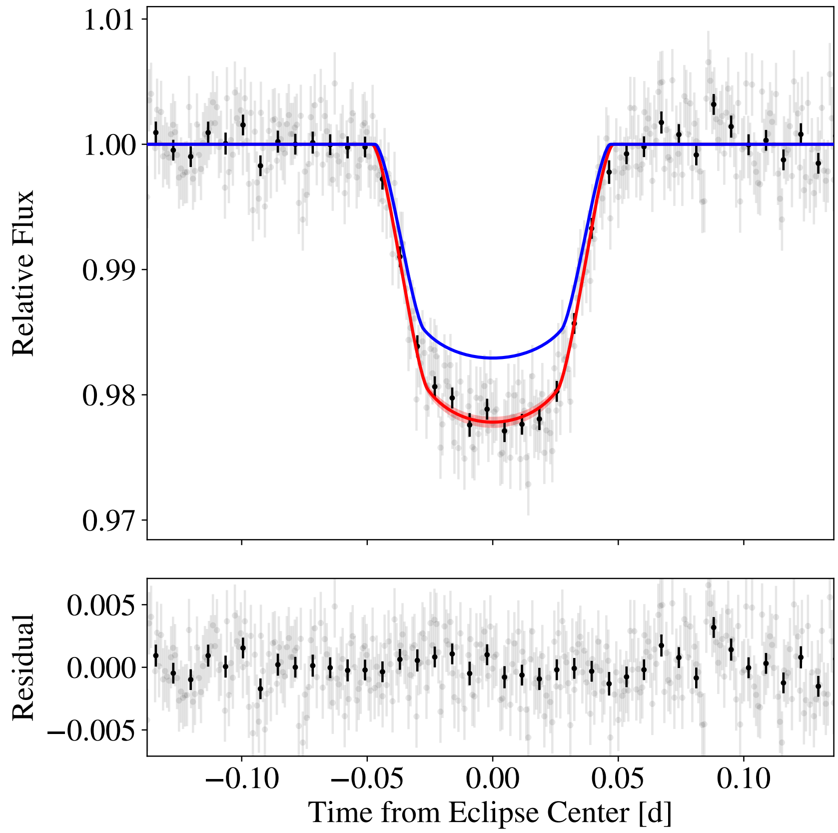

Figure 6.2: Narrowband light curve (top) and residuals (bottom) for WASP-69b. Grey points are detrended data, which are binned to 10 minute cadence in black. The red curve indicates our best-fit model, with 1σ uncertainty indicated by the red shading. The blue curve indicates the nominal light curve model (outside the helium bandpass).

resolve this discrepancy, Owen and Lai (2018) suggest that WASP-52b's radius may have been smaller during migration (with a correspondingly smaller tidal disruption radius), and that it underwent radius inflation only recently. Other published observations of WASP-52b indicate that this planet has a relatively flat transmission spectrum (J. Kirk, P. J. Wheatley, T. Louden, Littlefair, et al., 2016; G. Chen, Pallé, et al., 2017; Tom Louden et al., 2017; Mancini, Southworth, Raia, et al., 2017; Alam et al., 2018; E. M. May et al., 2018), although sodium, potassium, and Hα absorption have all been detected at high spectral resolution (G. Chen, Pallé, et al., 2017; Alam et al., 2018; G. Chen, Casasayas-Barris, et al., 2020).

We first searched for helium in the atmosphere of this planet on UT 2019 Sep 17, and published the results of these observations in Vissapragada, Knutson, Jovanovic, et al. (2020). In this work, we re-fit that light curve jointly with a new observation taken on UT 2020 Aug 04. Observing conditions were worse on the second night, which rendered two faint comparison stars from the first night unobservable, but better positioning of the target star allowed us to add one extra comparison star that was not in the field of view on the first night.

For this planet, we adopted a fixed limb darkening coefficient fit, as we found that the calculated limb darkening coefficients agreed well with the joint distribution of retrieved quadratic limb darkening coefficients (Appendix 6.7), and the choice did not make a difference for the retrieved parameters. In separate retrievals, we constrained the excess absorption to be $0.22^{+0.14}_{-0.13}\%$ on the first night, with a 95th-percentile upper limit of 0.44%, and $1.02^{+0.39}_{-0.41}\%$ on the second night with a 95th-percentile upper limit of 1.68%. When fitting the datasets jointly, we found an excess absorption of $0.29^{+0.13}_{-0.13}\%$, corresponding to a tentative detection at 2.2σ confidence. The joint fit results are shown in Figure 6.3.

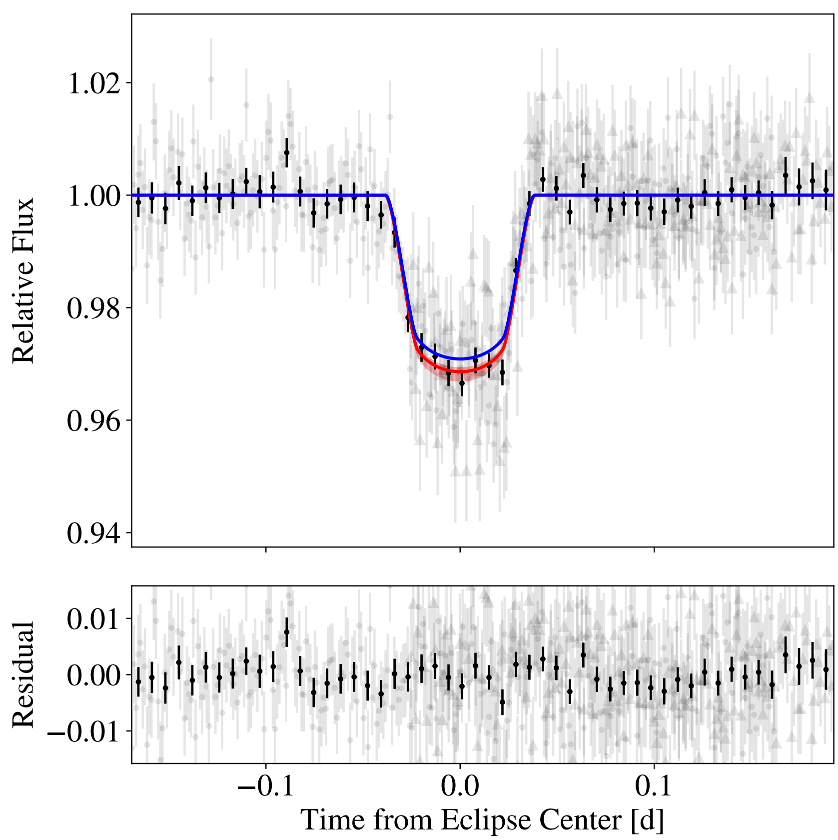

Figure 6.3: Same as Figure 6.2, but for WASP-52b. Points with circular markers indicate the first night of data collection and points with triangular markers indicate the second night.

HAT-P-18b

HAT-P-18b is a Jupiter-sized ($1.00R_{\mathrm{J}}$), low-mass ($0.20M_{\mathrm{Jup}}$) planet in a 5.5 day orbit around its K2 host star (Hartman, Bakos, Sato, et al., 2011). Despite its faintness ($J = 10.8$), the low gravitational potential of this planet makes it amenable to atmospheric characterization, and a Rayleigh scattering slope in HAT-P-18b's transmission spectrum was detected by J. Kirk, P. J. Wheatley, T. Louden, Doyle, et al. (2017). We previously detected a metastable helium signature for this planet in Paragas et al. (2021). The fitting method we employ in this survey is somewhat different from the one in Paragas et al. (2021), so we re-fit the observations here. Rather than fitting jointly with *TESS* observations of the system as we did previously, we fit the WIRC data alone and compare to the precise transit depth from *HST*/WFC3 G141 (Tsiaras et al., 2018). We prefer this approach because the spectrophotometric bin we use from WFC3 (1110.8 nm-1141.6 nm) is narrower and closer to the helium filter bandpass than the *TESS* bandpass (600 nm-1000 nm), and the depth in this bin is more precise than the *TESS* depth. Additionally, in the previous work we reported $(R_{\mathrm{p}}/R_{\star})^2_{\mathrm{WIRC}} - (R_{\mathrm{p}}/R_{\star})^2_{\mathrm{comparison}}$ as the excess absorption, but this is not necessarily equal to the difference in transit depth between the WIRC light curve and comparison light curve, especially when there is strong stellar limb darkening in the helium line (as we infer for HAT-P-18b). To account for this, the comparison light curve should be constructed taking into account limb darkening in the helium bandpass, which we do when obtaining the excess absorption δ_{mid} in this work (see Section 6.2).

For HAT-P-18b, we adopted the free limb darkening coefficient fit. The fixed limb darkening coefficients disagreed with the retrieved coefficients by more than 2σ in the joint posterior (Appendix 6.7), and the choice was consequential for the final fitted parameters, so we choose to adopt the free limb darkening coefficient solution. When fitting each dataset independently, we obtained $(R_{\mathrm{p}}/R_{\star})^2$ values of $2.14^{+0.23}_{-0.24}\%$ and $2.56^{+0.17}_{-0.16}\%$ for the first and second nights, respectively. These are consistent to 1σ with the values obtained by Paragas et al. (2021), who fit the WIRC data together with data from *TESS* to obtain $(R_{\mathrm{p}}/R_{\star})^2$ values of $2.11 \pm 0.25\%$ for the first night and $2.35 \pm 0.14\%$ for the second night. We then fit the WIRC datasets jointly and show the results in Figure 6.4. In the joint fit, we find $(R_{\mathrm{p}}/R_{\star})^2 = 2.46 \pm 0.15\%$, which is about 1σ larger than the result from Paragas et al. (2021) of $2.29 \pm 0.12\%$. Our result for the excess depth is $0.70 \pm 0.16\%$, again slightly larger than our previously-reported signal of $0.46 \pm 0.12\%$.

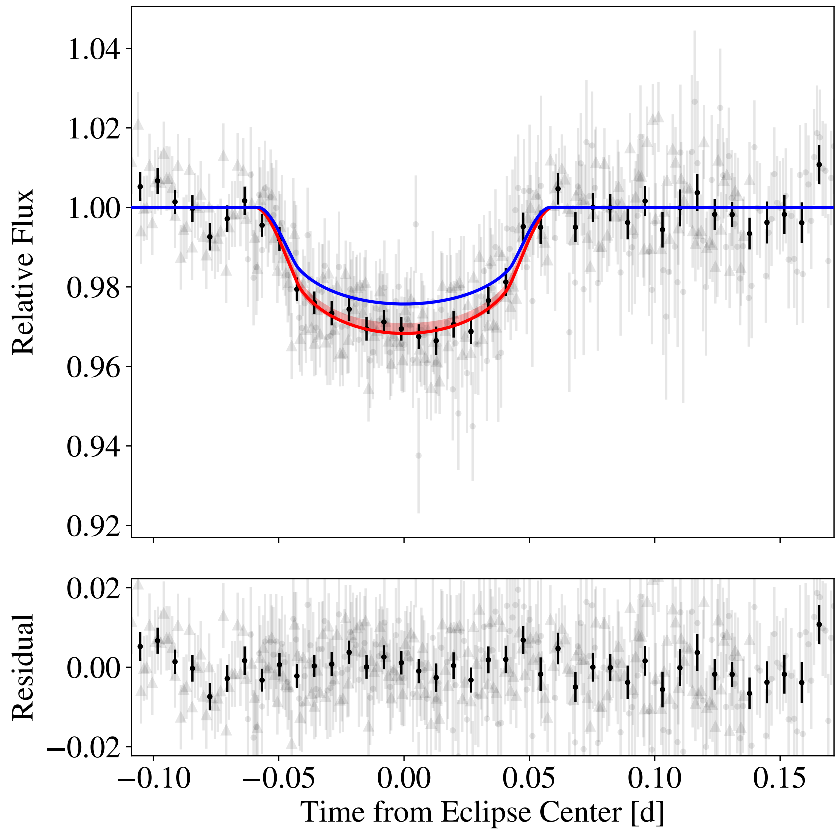

Figure 6.4: Same as Figure 6.2, but for HAT-P-18b. Points with circular markers indicate the first night of data collection and points with triangular markers indicate the second night.

WASP-80b

WASP-80b is a Jupiter-sized ($1.00R_{\rm J}$), $0.54M_{\rm J}$ planet in a 3.07 day orbit around its K7/M0 host star (A. H. M. J. Triaud et al., 2013; Amaury H. M. J. Triaud et al., 2015). At low resolving power, the transmission spectrum of this planet is quite flat (Fukui et al., 2014; Mancini, Southworth, Ciceri, et al., 2014; J. D. Turner et al., 2017; Parviainen, Pallé, et al., 2018; J. Kirk, P. J. Wheatley, T. Louden, Skillen, et al., 2018). Multiple groups running self-consistent wind-launching simulations have reported WASP-80b to be an excellent candidate for mass-loss observations (Salz, Schneider, et al., 2015; Salz, Schneider, et al., 2016; Caldiroli et al., 2021a). However, Fossati et al. (2021) recently obtained four nights of high-resolution data on WASP-80b and did not detect any metastable helium signature, setting an upper limit of 0.7% absorption in the line core.

We observed a full transit of WASP-80b on UT 2020 Jul 09. During the first half of observations the detector started reading large numbers of negative counts relatively infrequently until the issue became more persistent near ingress. The instrument was reset near the middle of the transit, which fixed the problem. Prior to analysis, frames in the first half with $> 0.1\%$ of pixels reading negative counts were discarded. Additionally, the pre-reset data exhibited stronger systematics than the post-reset data, so we treated each of the two halves as separate observations (i.e., allowing each half of the light curve to have different coefficients for the systematics model) and fit them jointly. We optimized the aperture size using the second half of data only, finding an optimized radius of 8 px.

We adopted the fixed limb darkening coefficient fit for WASP-80b, as the calculated limb darkening coefficients agreed well with the joint distribution of retrieved quadratic limb darkening coefficients (Appendix 6.7), and the choice did not make a difference for the retrieved parameters. We did not detect any excess absorption in our data, finding $\delta_{\rm mid} = 0.02^{+0.20}_{-0.20}$ with a 95th-percentile upper limit of 0.35% excess absorption in our bandpass. The fit results are shown in Figure 6.5. Our non-detection agrees with the more sensitive observations from Fossati et al. (2021).

WASP-177b

WASP-177b is a highly-inflated ($1.6R_{\rm J}$), $0.5M_{\rm J}$ planet in a 3.07 day orbit around its K2 host star (O. D. Turner et al., 2019). This planet has an exceptionally low density (similar to WASP-107b), making it a good target for transmission spectroscopy. However, the planetary transit is grazing, which makes it more difficult to extract precise constraints on the wavelength-dependent planet-star radius ratio.

We observed a full transit of this planet on UT 2020 Oct 2. *TESS* also observed this planet (TOI-4521.01) at 2 minute cadence in Sector 42 from UT 2021 Aug – 2021 Sep. Given the grazing nature of the transit and the relatively small number of comparison light curves in the literature, we decided to fit our Palomar/WIRC light curve jointly with the TESS light curve. This allowed us to better capture covariances between the radius ratio, impact parameter, scaled semi-major axis, and limb darkening parameters while also giving us a reference transit depth to which we could compare the WIRC measurement. The *TESS* portion of the fit was carried out similarly to our fit for HAT-P-18b in Paragas et al. (2021); the only additional parameters we included were separate *TESS* limb darkening parameters, the radius ratio in the *TESS* bandpass, and an error re-scaling term.

For a grazing geometry it is difficult to differentiate excess absorption associated with the planet from strong limb darkening, so we first tried a fit with free limb

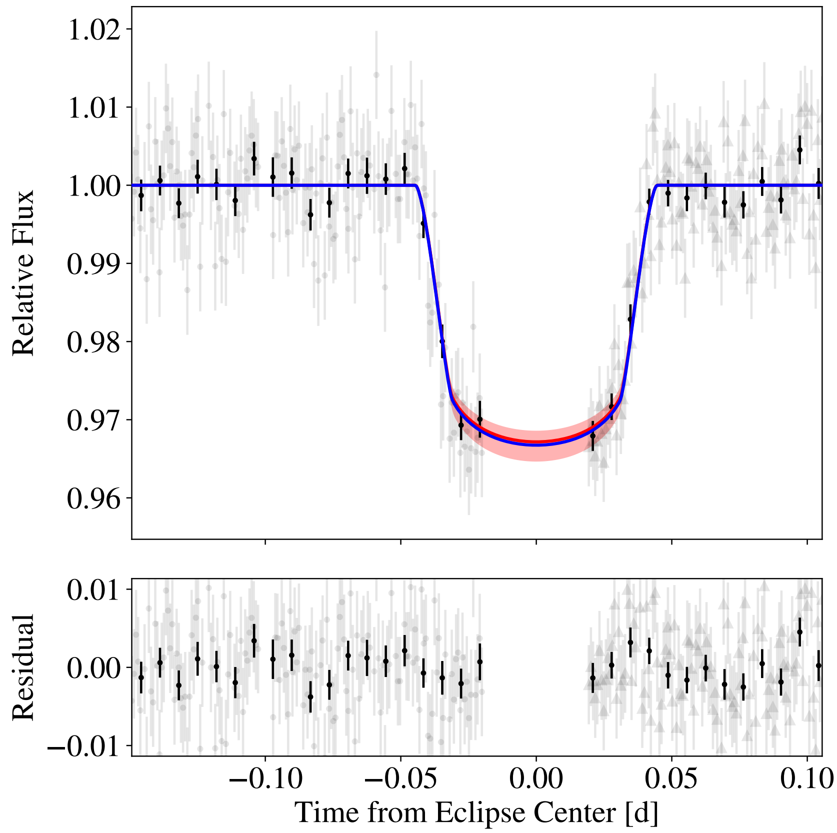

Figure 6.5: Same as Figure 6.2, but for WASP-80b. Points with circular markers indicate the first half of the observations (prior to the instrument reset) and points with triangular markers indicate the second half.

darkening coefficients. However, we found that the data were uninformative on the quadratic limb darkening coefficients (see Appendix 6.7), so we defaulted to using fixed limb darkening coefficients instead. The results of the joint fit are shown in Figure 6.6. The fitted TESS lightcurve is given in Appendix 6.10. Using the *TESS* transit depth as our baseline, we constrain the excess depth to be $0.53^{+0.23}_{-0.28}$%, a non-detection with a 95th-percentile upper limit of 0.90%.

HAT-P-26b

HAT-P-26b resides near the lower edge of the Neptune desert, and is the smallest planet in our sample. With a radius of a $0.57R_\mathrm{J}$ and a mass of $0.059M_\mathrm{J}$, this planet orbits its K1 host star every 4.23 days (Hartman, Bakos, D. M. Kipping, et al., 2011). The Neptune-mass planet has a well-constrained heavy element abundance thanks to the presence of strong water bands in the red-optical and near-infrared (K. B. Stevenson et al., 2016; Wakeford et al., 2017) as well as the potential presence of metal hydride features (MacDonald and Madhusudhan, 2019) and *Spitzer* secondary

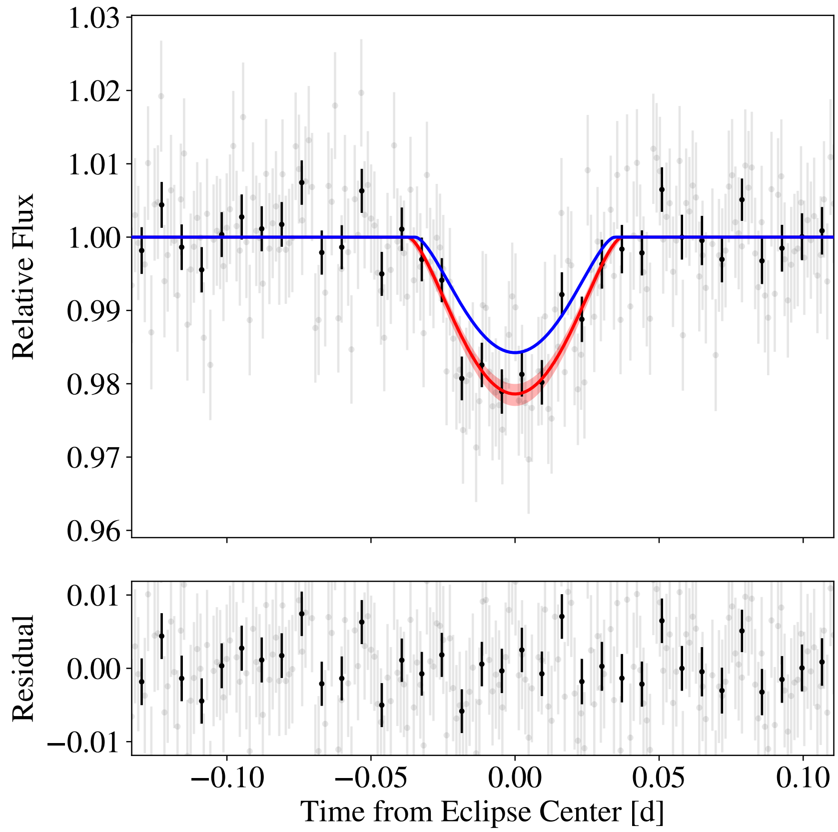

Figure 6.6: Same as Figure 6.2, but for WASP-177b.

eclipse depth ratios (Wallack et al., 2019). At optical wavelengths, HAT-P-26b's alkali features appear to be obscured by a cloud layer (Wakeford et al., 2017; Panwar et al., 2022).

This planet is an excellent target for observations of atmospheric escape. It is larger and less massive than HAT-P-11b (a benchmark planet for metastable helium studies, Allart, Bourrier, Lovis, Ehrenreich, Spake, et al., 2018; Mansfield et al., 2018), and as a result has an inferred H/He envelope fraction approximately twice that of HAT-P-11b (E. D. Lopez and Fortney, 2014). The slightly earlier spectral type of HAT-P-26 (HAT-P-11 is a K4 dwarf) also puts it at the "sweet spot" for metastable helium observations as identified by Antonija Oklopčić (2019). We observed this high-priority target three times: on UT 2021 Feb 18, 2021 May 1, and 2021 May 27. The weather on the first night was relatively poor, and the target was not optimally positioned. Between the first and second nights of observation, we shifted the placement of the target on the detector in order to include an additional comparison star, which greatly increased the final precision.

We do not detect the transit in the first night of data, for which we obtained an overall $R_\mathrm{p}/R_\star = 0.034^{+0.028}_{-0.023}$. As expected, this first night is much noisier than the latter two (Table 4.1): the rms scatter in the unbinned residuals was 1.79% (2.7× the photon noise) in the first observation, whereas it was 0.82% (1.6× the photon noise) and 0.61% (1.4× the photon noise) on the second and third nights, respectively. In order to avoid biasing the final joint fit, we therefore only included the latter two nights of photometry.

After optimizing the set of detrending vectors selected for each of the latter two nights, we obtained mid-transit excess depths of $0.43^{+0.18}_{-0.17}$% and $0.23^{+0.13}_{-0.13}$%. We adopted the fixed limb darkening coefficient fit for HAT-P-26b, as the calculated limb darkening coefficients agreed well with the joint distribution of retrieved quadratic limb darkening coefficients (Appendix 6.7), and the choice did not make a significant difference for the retrieved parameters. The results of our joint fit to the latter two nights are shown in Figure 6.7. We obtained a mid-transit excess depth of $0.31^{+0.10}_{-0.10}$, evidence for helium absorption at 3.1σ confidence.

NGTS-5b

NGTS-5b is a Jupiter-sized ($1.1R_\mathrm{J}$), sub-Saturn-mass ($0.23M_\mathrm{J}$) planet orbiting a K2 dwarf every 3.36 days (Eigmüller et al., 2019). The planet is similar to WASP-69b in mass, radius, orbital period, and stellar host type, so despite the rather faint host star ($J = 12.1$) we identified it as a high-priority target. We observed two full transits of the planet: one on UT 2021 Apr 30 and one on UT 2021 May 27.

This target had only one comparison star available in the field of view, and this along with the faintness of the target star created challenges for our standard systematics model approach. When testing different covariate combinations for the first night of data, the detrending models failed. With relatively poor weather conditions on that first night, the noisy comparison star light curve was severely underweighted in the systematics model when other covariates were included. When included in the joint fit, this underweighted model severely increased the magnitude of the correlated noise. We stress that unlike the first night for HAT-P-26b, which we discarded because there was no transit detected and the noise was nearly 3× the photon noise limit, the transit is clearly detected in this dataset, and the issue stemmed purely from our approach to modeling the systematics. We therefore kept this dataset in the final model, but to avoid the sharp increase in correlated noise we did not use any additional covariates in the systematics model for the first night, and as such we do

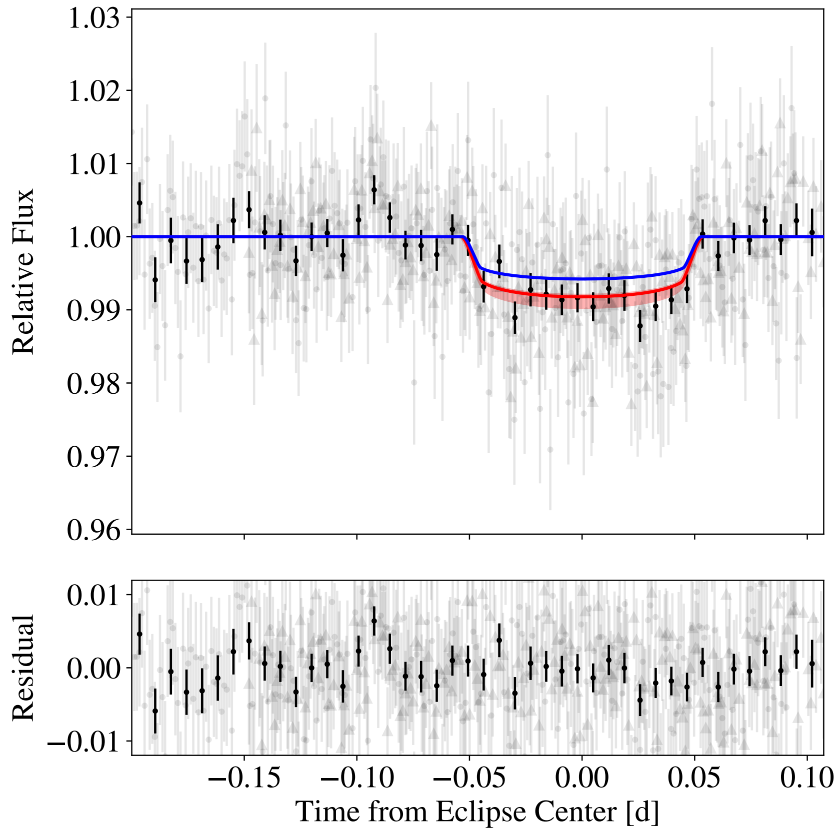

Figure 6.7: Same as Figure 6.2, but for HAT-P-26b. Points with circular markers indicate the second night of data collection and triangular markers indicate the third night. For both the second and third nights, the dashed red lines indicate 1.5× the photon noise.

not report the model selection statistics for this night in Appendix 6.8. Conditions on the second night were more favorable, so the fit was more typical.

We obtained mid-transit excess absorption values of $1.02^{+0.99}_{-0.95}$% and $0.94^{+0.55}_{-0.54}$% for the individual fits to the first and second nights, respectively. We proceeded to fit the datasets jointly, and the results are shown in Figure 6.8. We adopted the fixed limb darkening coefficient fit for NGTS-5b as the calculated limb darkening coefficients agreed well with the joint distribution of retrieved quadratic limb darkening coefficients (Appendix 6.7) and the choice did not make a significant difference for the retrieved parameters. We obtained a final mid-transit excess absorption of $1.02^{+0.48}_{-0.46}$%, a tentative detection at 2.2σ confidence.

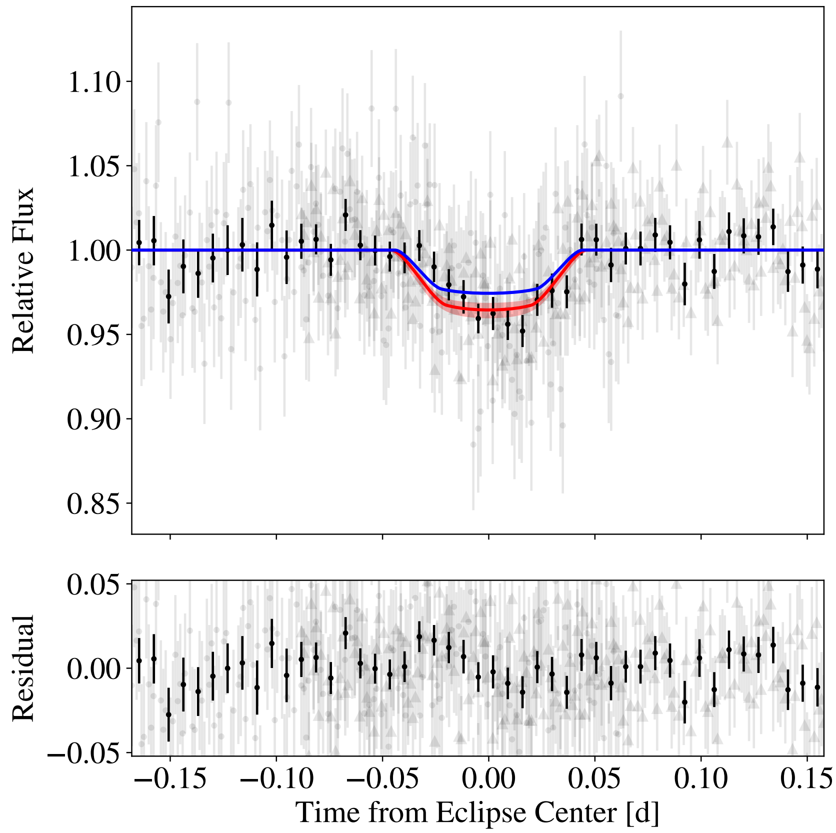

Figure 6.8: Same as Figure 6.2, but for NGTS-5b. Points with circular markers indicate the first night of data collection, and points with triangular markers indicate the second night.

6.4 Mass-Loss Modeling

We can convert the excess depths from Section 6.3 into constraints on planetary mass-loss rates by modeling the outflows with one-dimensional isothermal Parker winds (Antonija Oklopčić and Hirata, 2018; Lampón, López-Puertas, Lara, et al., 2020). In this section, we use the `p-winds` code (dos Santos et al., 2022) to model our observations. Given a mass-loss rate assuming irradiation conditions at the substellar point $\dot{M}_{\rm substellar}$, a thermosphere temperature T_0, and a hydrogen fraction for the outflow $f_{\rm H}$, we first set the density and velocity profiles for the wind. Then, we use a high-energy stellar spectrum to calculate the ionization structure and level populations throughout the outflow. The level populations are used to compute the expected wavelength-dependent absorption signal at high resolving power, which we then convolve with our filter bandpass to compare to the measurements in Section 6.3.

The free parameters in this model are the mass-loss rate, thermosphere temperature, the hydrogen fraction, and the high-energy spectrum. We compute the model over a 50×50 grid of mass-loss rates $\dot{M}_{\text{substellar}} = 10^{10}$ g s^{-1} – 10^{13} g s^{-1} and thermosphere temperatures T_0 = 5000 K−15000 K. The grid was uniformly spaced in $\log(\dot{M}_{\text{substellar}})$ and T_0. We set the hydrogen fraction for all outflows to 0.9, corresponding to a 90-10 hydrogen-helium outflow. Finally, for the high-energy spectra we select proxy stars from the v2.2 panchromatic SEDs from the MUSCLES survey (at 1 Å binning; France et al., 2016; Loyd et al., 2016; Youngblood et al., 2016). We identify three K stars in MUSCLES that appear to be good proxies for our targets: HD 85512, HD 40307, and ϵ Eridani. We model the late K stars ($T_\star \lesssim 4800$ K) in our sample using HD 85512's spectrum, and use HD 40307's spectrum for the early K stars. We use ϵ Eridani's spectrum to model the most active stars in our sample, including WASP-52 ($\log(R'_{\text{HK}}) = -4.4$; Hébrard et al., 2013) and WASP-80 ($\log(R'_{\text{HK}}) = -4.04$; Fossati et al., 2021). We list the spectrum used for each star in Table 6.5. We then scale the MUSCLES spectrum by the stellar radius and planetary orbital distance to obtain the high-energy spectral flux incident at the top of the planet's atmosphere.

Table 6.5: Mass-loss modeling summary.

Planet	MUSCLES spectrum	$\dot{M}(10^{10}$ g s$^{-1}))$	ε	$M_{\text{env}}/\dot{M}$ (Gyr)
WASP-69b	HD 85512	$6.3^{+9.6}_{-4.9}$	$0.43^{+0.66}_{-0.33}$	250^{+830}_{-150}
WASP-52b	ϵ Eridani	$2.7^{+9.0}_{-2.2}$	$0.0079^{+0.0261}_{-0.0065}$	1010^{+4710}_{-780}
HAT-P-18b	HD 85512	$3.7^{+5.6}_{-2.7}$	$0.54^{+0.81}_{-0.39}$	320^{+820}_{-190}
WASP-80b	ϵ Eridani	< 1.4	< 0.046	> 12000
WASP-177b	HD 40307	< 45	< 0.37	> 1300
HAT-P-26b	HD 40307	$9.2^{+25.0}_{-8.0}$	$0.52^{+1.42}_{-0.45}$	$12.2^{+77.6}_{-8.9}$
NGTS-5b	HD 40307	$10.2^{+33.8}_{-9.7}$	$0.16^{+0.52}_{-0.15}$	140^{+2770}_{-100}

After running an initial grid of models, we noticed that many of our winds had sonic points located outside the Roche radius. As discussed in Murray-Clay, Chiang, and Murray (2009), this happens when the tidal gravity term in the momentum equation for the wind is not taken into account. We show in Appendix 6.11 that the tidal gravity term appreciably alters the velocity and density profiles for the planets in our sample, and we update the `p-winds` code (in version 1.3) to account for the effects of the stellar gravity. We then re-calculate our model grids for each planet and use these grids to determine the range of mass-loss rates and thermosphere temperatures that match our observations. Next, we assess which combinations of $\dot{M}_{\text{substellar}}$ and T_0 are energetically self-consistent using the methodology outlined in

Vissapragada, Knutson, dos Santos, et al. (2022). If photoionization is the only heat source, certain combinations do not satisfy energy balance in the isothermal Parker wind, and we omit them from our final results.

Finally, we divide the substellar-point mass-loss rates by a factor of 4 to obtain estimates for the overall mass-loss rate $\dot{M}$. This correction factor accounts for the fact that the planet is only irradiated over π steradians rather than the 4π steradians assumed by our 1D models, so the true mass-loss rates will be about a factor of 4 smaller (Salz, Schneider, et al., 2016; Vissapragada, Knutson, dos Santos, et al., 2022). Other prescriptions to correct for 2D effects exist (e.g. Odert et al., 2020), but they all agree well for outflows from low-gravity planets (like the ones in our sample) that are dominated by adiabatic cooling (Caldiroli et al., 2021b). Performing the radiative transfer using the 1D model rather than a 2D or 3D model also introduces error, but comparisons between 1D and 3D models suggest that this is a minor error term (relative to the uncertainty from the $\dot{M} - T_0$ degeneracy) except in the presence of strong stellar winds (MacLeod and Antonija Oklopčić, 2022; L. Wang and Dai, 2021a; L. Wang and Dai, 2021b).

We show the resulting mass-loss constraints for each planet in Figure 6.9. We used a rejection sampling scheme with this grid of results to generate a list of 100,000 samples for each planet corresponding to the underlying joint distribution of mass-loss rates and thermosphere temperatures. We began by uniformly sampling temperatures from $T_0 \sim \mathcal{U}(5000, 150000)$ and $\log(\dot{M}_{\mathrm{substellar}}) \sim \mathcal{U}(10, 13)$. For each sample, we found the closest point on the grid in Figure 6.9 with corresponding $x\sigma$ discrepancy between the model and the data. We accepted the sample only if $y > \mathrm{erf}(x/\sqrt{2})$, where y is a random draw from $\mathcal{U}(0, 1)$.

With the final list of 100,000 samples in hand for each planet, we marginalize over the thermosphere temperature to obtain distributions for the mass-loss rates, which are summarized in Table 6.5. We evaluate the significance of these mass-loss rates for the expected atmospheric lifetime of each planet by calculating the envelope loss timescale $M_{\mathrm{env}}/\dot{M}$. For HAT-P-26b we adopt an envelope mass fraction of 31.7% (E. D. Lopez and Fortney, 2014). For the other higher-mass gas giants in the sample, we take $M_{\mathrm{env}} \sim M$. We give the resulting envelope loss timescales in Table 6.5.

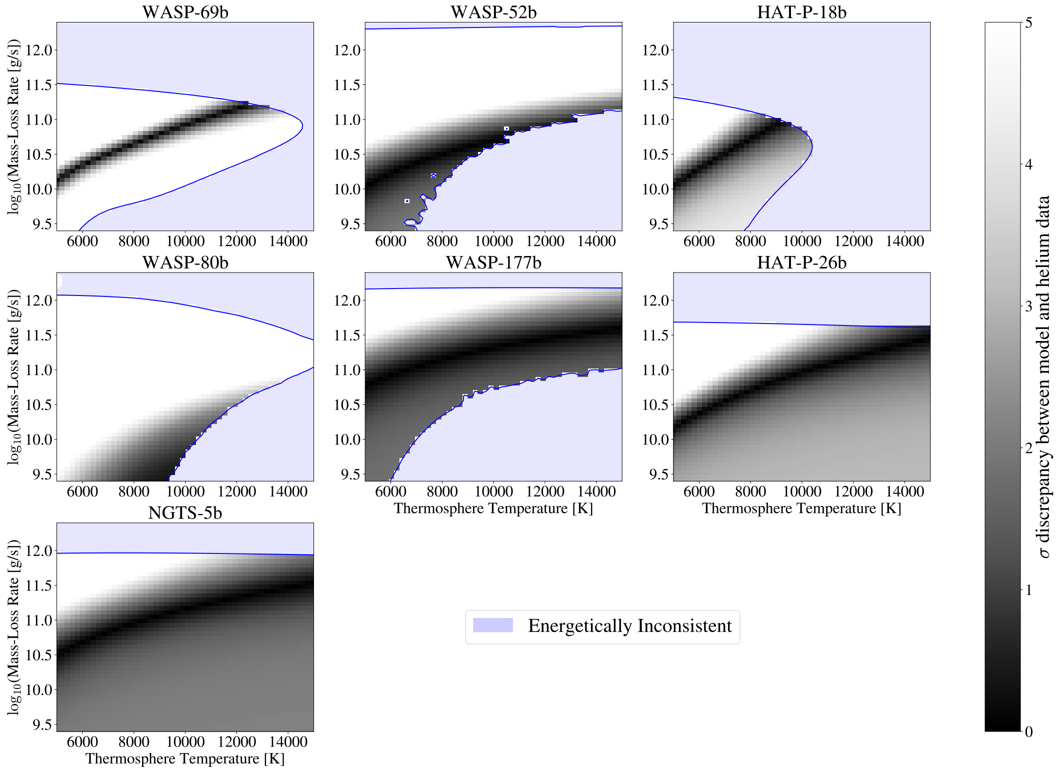

Figure 6.9: Mass-loss models for the seven planets in our sample. The shading gives the σ agreement between the observations and a 1D transonic Parker wind model characterized by the mass-loss rate $\dot{M}$ and thermosphere temperature T_0. Models that violate energy balance (Vissapragada, Knutson, dos Santos, et al., 2022) are rejected (blue shaded regions).

6.5 Discussion

Benchmarking Mass-Loss Models

Self-consistent, one-dimensional mass-loss models like the Pluto-CLOUDY Interface (TPCI; Salz, Schneider, et al., 2015; Salz, Schneider, et al., 2016) and the ATmospheric EScape code (ATES; Caldiroli et al., 2021b; Caldiroli et al., 2021a) are crucial for interpretation of mass-loss-related phenomena in the exoplanet population, but to date there have been relatively few attempts to benchmark their predictions against measurements of present-day mass-loss rates for transiting planets. Here, we compare the inferred mass-loss rates from our seven-planet sample to predictions from the ATES code as a function of the incident XUV flux. Because Caldiroli et al. (2021a) provide analytical approximations for the efficiency as a function of incident XUV flux and gravitational potential, comparisons between the model and the data are simple and do not require expensive computations for each planet.

In order to place all seven planets on the same plot, we need to convert our measured mass-loss rates and XUV fluxes into scaled units that correct for planet-to-planet variations in gravitational potential and Roche radius. Scaled units can be obtained by starting from the energy-limited approximation from the planetary mass-loss rate (e.g. Caldiroli et al., 2021a):

$$\dot{M} = \frac{\varepsilon \pi R_{\rm p}^3 F_{\rm XUV}}{K G M_{\rm p}}, \tag{6.2}$$

where ε is the mass-loss efficiency, $F_{\rm XUV}$ is the incident high-energy flux, and K is the Erkaev et al. (2007) Roche-lobe correction factor. Then, we can rewrite the expression in terms of the planetary density $\rho_{\rm p}$:

$$K\dot{M} = \frac{3\varepsilon}{4G}\frac{F_{\rm XUV}}{\rho_{\rm p}}. \tag{6.3}$$

Planets in the energy-limited regime should therefore exhibit a linear relation between the K-corrected mass-loss rate and the ratio $F_{\rm XUV}/\rho_{\rm p}$ (Caldiroli et al., 2021a).

As the incident XUV flux increases, however, self-consistent models predict that the outflow begins to lose substantial energy to radiative cooling, leading to a sub-linear dependence on $F_{\rm XUV}/\rho_{\rm p}$ beyond a threshold of $F_{\rm XUV}/\rho_{\rm p} \sim 10^4$ erg cm g^{-1}s^{-1} (Murray-Clay, Chiang, and Murray, 2009; Salz, Schneider, et al., 2016; Salz, Czesla, Schneider, and Schmitt, 2016; Caldiroli et al., 2021a). Higher-gravity planets are also predicted to have low overall outflow efficiencies, as the atmospheres are more tightly bound and tend to re-emit more energy locally (Owen and Alvarez, 2016). To an order of magnitude, this happens when the energy liberated by a single photoionization event ($\Delta E \sim 10$ eV $\sim 10^{-11}$ erg) exceeds the particle binding energy, which for a hydrogen atom ($m_{\rm H} \sim 10^{-24}$ g) occurs roughly at a gravitational potential of $\phi_{\rm p} \sim \Delta E/m_{\rm H} \sim 10^{13}$ erg/g (for a more thorough explanation, see Caldiroli et al., 2021a). More sophisticated numerical experiments place this threshold closer to $\phi_{\rm p} \gtrsim 10^{13.2}$ erg/g (Salz, Schneider, et al., 2016; Caldiroli et al., 2021a).

In Figure 6.10 we plot our marginalized and K-corrected $\dot{M}$ distributions as a function of $F_{\rm XUV}/\rho_{\rm p}$, along with the corresponding ATES model prediction for each planet. Immediately, two distinct populations of planets emerge in this parameter space. The first, comprised of HAT-P-18b, WASP-69b, HAT-P-26b, NGTS-5b, and WASP-177b, appear to agree quite well with the ATES predictions. The second group of planets, which includes WASP-80b and WASP-52b, appear to have mass-loss rates that are more than an order of magnitude lower than the model predictions.

We discuss possible explanations for the surprisingly low inferred mass-loss rates of the second group in Section 6.5.

We use a bootstrap averaging method to estimate the mean mass-loss efficiency of planets in the first group. We omit WASP-52b and WASP-80b from this exercise because their helium signals appear to be affected by factors that are not included in our model, such as magnetic fields or stellar winds, as discussed in the next section. For the other planets, we first converted our marginalized $\dot{M}$ distribution for each planet into a distribution on ε using Equation (6.3), and these distributions are summarized in Table 6.5. We then took a random draw from each planet's ε distribution and averaged the draws to get an estimate for the mean efficiency. We repeated this procedure 100,000 times to obtain a final estimate of $\varepsilon = 0.41^{+0.16}_{-0.13}$. We overplot this average ε model in Figure 6.10.

The measured mass loss constraints for all five planets in the first group overlap with the average-ε model at 2σ confidence, and the model is a reasonable approximation to the ATES (Caldiroli et al., 2021a) predictions for our sample as well. ATES also predicts that the mass-loss efficiency should level off with increasing $F_{\mathrm{XUV}}/\rho_{\mathrm{p}}$ as compared to a fixed-ε curve. Unfortunately, the uncertainties in the inferred mass-loss rates for our sample, which are dominated by the degeneracy between mass-loss rate and thermosphere temperature, are too large to differentiate between this model and a constant-ε model. Resolving the line profiles of these planets with high-resolution transmission spectroscopy can help break the degeneracy (e.g. dos Santos et al., 2022).

We can compare our measured efficiency to other giant planets ($R_{\mathrm{p}} > 4R_{\oplus}$) orbiting K stars with reported helium detections in the literature. The reported absorption for WASP-107b (Spake, Sing, et al., 2018; Allart, Bourrier, Lovis, Ehrenreich, Aceituno, et al., 2019; James Kirk et al., 2020; Spake, A. Oklopčić, and L. A. Hillenbrand, 2021) is well-matched by the three-dimensional hydrodynamical models of L. Wang and Dai (2021b), who report a mass-loss rate of approximately 2×10^{11} g s^{-1}. Using the scaled MUSCLES spectrum of ϵ Eridani to calculate the XUV flux, we obtained an outflow efficiency of 0.34, in good agreement with our measured efficiency. The signal observed for HAT-P-11b (Allart, Bourrier, Lovis, Ehrenreich, Spake, et al., 2018; Mansfield et al., 2018) has been modeled using `p-winds` using the scaled MUSCLES spectrum of HD 40307 as a proxy for the stellar XUV spectrum, and dos Santos et al. (2022) report a 1D mass-loss rate of $2.3^{+0.7}_{-0.5} \times 10^{10}$ g s^{-1} (with stellar limb darkening taken into account). Dividing this result by 4 to get the overall mass-loss rate (for consistency with the method outlined in Section 6.4), we obtain an outflow efficiency of $0.170^{+0.052}_{-0.037}$, somewhat smaller than our measured efficiency but consistent within 2σ.

Finally, the signal observed for HD 189733b (Salz, Czesla, Schneider, Nagel, et al., 2018; Guilluy et al., 2020) was modeled using a Parker wind methodology by Lampón, López-Puertas, Sanz-Forcada, et al. (2021). For their 90/10 H/He composition model, they found a mass-loss rate at $T = 12000$ K of about 4×10^9 g s^{-1}, with significant spread due to the $\dot{M} - T_0$ degeneracy. Again dividing by 4 to account for the multidimensional outflow, this corresponds to an efficiency of 0.0023, much smaller than our measured efficiency. A small efficiency is expected: the relatively large mass of HD 189733b puts it in a regime where radiative losses dominate the cooling budget rather than the adiabatic expansion of the atmosphere (Salz, Schneider, et al., 2016; Caldiroli et al., 2021b; Caldiroli et al., 2021a), so the outflow is more similar to WASP-52b and WASP-80b than the other planets in our sample. Similarly to WASP-52b and WASP-80b, the planet has a smaller semimajor axis ($a = 0.031$; Bouchy et al., 2005) and more active host star ($\log(R'_{\rm HK}) = -4.501$; Knutson, Howard, and Isaacson, 2010) than the other planets in our sample. The inferred mass-loss rate for HD 189733b at a 90/10 composition is still at least a factor of a few smaller than predicted by 1D hydrodynamical models, which give mass-loss rates of about $10^{9.5-10.0}$ g s^{-1} for this planet (Salz, Schneider, et al., 2016; Caldiroli et al., 2021b; Caldiroli et al., 2021a). Lampón, López-Puertas, Sanz-Forcada, et al. (2021) resolve this discrepancy by invoking a hydrogen-rich composition for the outflow, but this is not the only factor that can achieve a reduction of the helium signal. In the next section, we consider a range of explanations for the smaller-than-expected helium signals on WASP-52b and WASP-80b that could apply to HD 189733b as well.

Low Mass-Loss Rates for WASP-80b and WASP-52b

We now consider potential explanations for WASP-80b and WASP-52b's low apparent mass-loss rates, which are discrepant with both the ATES model predictions and the rest of the planets in our sample. We note that these two planets have the smallest semimajor axes and the largest $\log(R'_{\rm HK})$ values (Table 6.1) in our sample; this may or may not have anything to do with their low observed mass-loss rates. In this section, we consider five possible explanations: overestimated XUV fluxes, the XUV spectral shapes of their host stars, stronger-than-predicted stellar winds, outflow composition, and magnetic fields.

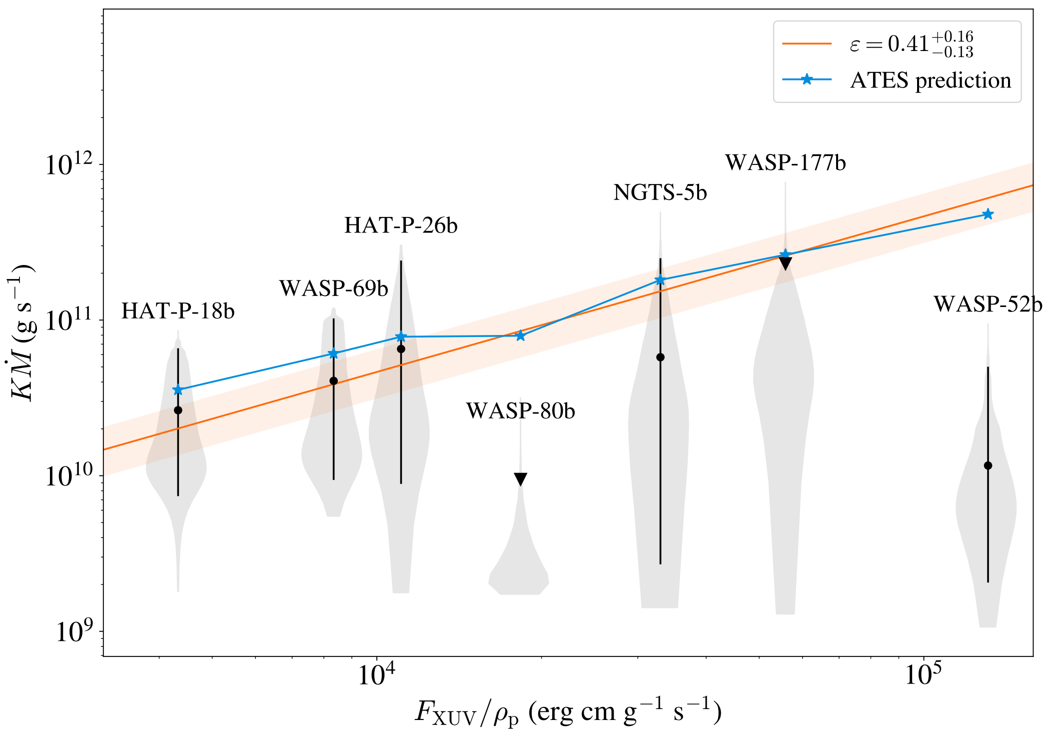

Figure 6.10: K-corrected mass-loss rate $\dot{M}$ as a function of $F_{\rm XUV}/\rho_{\rm p}$ for all the planets in our sample, following Caldiroli et al. (2021a). The shaded violins indicate the marginalized distribution of K-corrected mass-loss rates with the median and 95% confidence interval for the distribution given by the black points and error bars, respectively. The triangle denotes the 95% upper limit for WASP-80. The orange curve indicates the average inferred mass-loss efficiency ε, with the 1σ uncertainty given by the shaded orange region. The blue curve indicates predictions from the ATES code (Caldiroli et al., 2021b; Caldiroli et al., 2021a).

If the XUV flux of the host star was overestimated, it would cause us to overpredict the magnitude of a planet's mass loss rate. To test this effect, we decreased the incident XUV flux by a factor of ten in the `p-winds` models for WASP-52b and WASP-80b and recomputed the mass-loss efficiencies. Averaging the two efficiency parameters using the same bootstrapping method from Section 6.5, we found a mean efficiency of $0.130^{+0.064}_{-0.048}$. This is still smaller than our inferred efficiency for the other five planets, but the distributions overlap at the 2σ level. We conclude that the XUV fluxes would have to be overestimated by at least a factor of ten for the mass-loss efficiencies to come into reasonable agreement with the rest of the sample.

For WASP-80, Fossati et al. (2021) combined archival ROSAT and XMM-Newton observations with a new Gaia distance to calculate a precise X-ray flux measurement of $L_{\rm X} = 4.85^{+0.12}_{-0.23} \times 10^{27}$ erg/s. Scaling this value into the UV yields $F_{\rm XUV} \approx$

6300 erg/cm^2/s, which is close to our adopted value. Two other papers independently measure this star's X-ray flux and find values that are approximately a factor of three smaller (Monsch et al., 2019) and a factor of two larger (Foster et al., 2021) than this value. Despite these methodological differences, factor-of-a-few variations in the XUV flux are not enough to reconcile the tight upper limit on this planet's helium absorption signal with model predictions. For WASP-52, which was observed by Chandra (ACIS), Monsch et al. (2019) found $L_X = 3.1^{+1.2}_{-1.0} \times 10^{28}$ erg/s. Using the X-ray to EUV scaling relation for Chandra (ACIS) from King et al. (2018), we obtain an XUV irradiance of $F_{XUV} \approx 38,000$ erg/cm^2/s. This is quite close to our assumed value. We therefore conclude that, just as with WASP-80, differences in assumed XUV flux are unlikely to explain this planet's low helium absorption signal.

While variations in the integrated XUV flux are unlikely to explain the helium observations for WASP-80b and WASP-52b, the assumed spectral shape may play a role. In order to create a significant population of metastable helium, there must be enough EUV photons to ionize ground-state helium in the outflow, which then recombines into the metastable state (Antonija Oklopčić and Hirata, 2018; Antonija Oklopčić, 2019). As demonstrated by Poppenhaeger (2022), many of the stellar EUV photons that ultimately ionize helium come from coronal iron lines. Iron has a relatively low first ionization potential (FIP), and in very active, low-mass stars, the abundance of species with low FIPs often appear to be diminished (termed the inverse first ionization potential effect, or iFIP; Brinkman et al., 2001; Güdel et al., 2001; Brian E. Wood et al., 2018). WASP-52 and WASP-80 are by far the most active stars in our sample, so they may be affected by this phenomenon. Our assumed proxy star for these two planets, ϵ Eridani, does not exhibit the iFIP effect and has strong coronal iron lines (Poppenhaeger, 2022); this might cause us to overestimate their metastable helium populations in our models.

It is also worth noting that the models we are using in this study assume spherical symmetry, but not all outflows are spherically symmetric. If the outflow is confined into a comet-like shape by a strong stellar wind, it could reduce the magnitude of the helium absorption (e.g., McCann et al., 2019; Carolan et al., 2020; MacLeod and Antonija Oklopčić, 2022). This phenomenon has been directly detected for the hot Jupiter WASP-107b (Khodachenko et al., 2021; Spake, A. Oklopčić, and L. A. Hillenbrand, 2021; L. Wang and Dai, 2021b), and may also explain the relatively weak helium signal measured for the mini-Neptune TOI-560.01 (Zhang et al., 2022). Importantly, both WASP-52 and WASP-80 appear to be relatively young, suggesting that they may have correspondingly enhanced stellar winds. WASP-52 ($v \sin i$ ≈3.6 km/s with a photometric rotation period of 16.4 days, Hébrard et al., 2013) and WASP-80 ($v \sin i$ ≈3.55 km/s, A. H. M. J. Triaud et al., 2013) both rotate rapidly, with estimated gyrochronological ages of less than 1 Gyr (Barnes, 2007; Hébrard et al., 2013; A. H. M. J. Triaud et al., 2013). They are also the two most active stars in our sample, with $B - V$ colors and $\log R'_{\mathrm{HK}}$ values that also suggest ages as young as a few hundred Myr (Mamajek and Lynne A. Hillenbrand, 2008). However, some caution is warranted as stellar angular momenta are known to be affected by giant planets on close in-orbits (e.g. Lanza, 2010; Poppenhaeger and Wolk, 2014; Mancini, Southworth, Raia, et al., 2017).

Fossati et al. (2021) modeled the impact of stellar wind on WASP-80b using a three-dimensional hydrodynamical model (Shaikhislamov et al., 2021; Khodachenko et al., 2021), and showed that it does not suppress the helium signal enough to match their non-detection. They modeled stellar mass-loss rates up to $\sim 10\dot{M}_{\odot}$, but at early times the wind can be even stronger. B. E. Wood et al. (2005) used astrospheric Lyman-α absorption to infer mass-loss rates of $30\dot{M}_{\odot}$ and $100\dot{M}_{\odot}$ for ϵ Eridani and 70 Oph, both relatively young K dwarf stars. We can use the aforementioned X-ray fluxes along with the B. E. Wood et al. (2005) relation to estimate the stellar mass-loss rate for WASP-80. We obtain a mass-loss rate of $\sim 4\dot{M}_{\odot}$, well within the range modeled by Fossati et al. (2021). Using the same relation, we obtain a mass-loss rate of $\sim 35\dot{M}_{\odot}$ for WASP-52. We conclude that a strong stellar wind might suppress the helium signal for WASP-52b, but it is unlikely to explain WASP-80b.

The composition of the outflow could also affect the magnitude of the observed signal. It has been suggested (e.g. Lampón, López-Puertas, Lara, et al., 2020; Lampón, López-Puertas, Sanz-Forcada, et al., 2021) that outflows from giant planets may be depleted in helium, which would suppress both the helium signal and the corresponding inferred mass-loss rate. Fossati et al. (2021) modeled the composition of WASP-80b's outflow and showed that helium depletion (with $n_{\mathrm{He}}/n_{\mathrm{H}} \sim 0.01$) might plausibly explain these data. Previous studies of HD 209458b, HD 189733b, and GJ 3470b have sought to quantify the fractional abundances of hydrogen and helium in planetary outflows by comparing the magnitude of absorption measured in both the Lyman-α and metastable helium lines to Parker wind models (Lampón, López-Puertas, Lara, et al., 2020; Lampón, López-Puertas, Sanz-Forcada, et al., 2021; Lampón, López-Puertas, Czesla, et al., 2021) or 3D hydrodynamical models (Shaikhislamov et al., 2021). However, Lyman-α is a poor tracer for the density distribution in the planetary thermosphere, typically probing above the exobase at high velocities (e.g. Owen, Murray-Clay, et al., 2021). This suggests that anchoring the Parker wind model composition near the wind-launching radius to models of Lyman-α absorption may be inadvisable. A more reasonable route would be to jointly model Hα and metastable helium absorption signals, as suggested by Czesla et al. (2022). Such joint models would be invaluable in resolving this question.

Strong magnetic fields can also confine planetary outflows. For a strongly ionized wind launched in a dipolar planetary magnetic field, equatorial field lines are closed (ionized material traveling along field lines would loop back to the planet), leading to an equatorial "dead zone", while polar field lines remain open (Adams, 2011; Trammell, Arras, and Li, 2011; Owen and Adams, 2014). For close-in planets orbiting exceptionally active stars, the outflows are largely ionized, so material should follow field lines if the planets are magnetized. WASP-80b and WASP-52b have the smallest semimajor axes and their host stars have the largest $\log(R'_{\mathrm{HK}})$ values in our whole sample, making this an attractive explanation.

The ratio of magnetic pressure to ram pressure is a good diagnostic for the influence of magnetic fields (Owen and Adams, 2014), but this ratio depends on the magnetic field strength which is quite uncertain. There are several lines of evidence indicating that the magnetic fields of hot Jupiters may be relatively strong (10-100 G), including the inflated radii of these planets (Batygin and David J. Stevenson, 2010; Yadav and Thorngren, 2017) and evidence for magnetic star-planet interactions in a few systems (SPI; Cauley et al., 2019). Other observations suggest that these planets may have more modest field strengths (1-10 G), including ultraviolet observations of Lyman-α and ionized carbon lines in HAT-P-11b (Ben-Jaffel et al., 2022), and a small inferred hotspot offset in the phase curve of WASP-76b which might be caused by Lorentz drag (Erin M. May et al., 2021; Beltz et al., 2022). Elsasser number scalings also predict more moderate magnetic field strengths (David J. Stevenson, 2003). If the Elsasser number is of order unity, the field strength scales with the square root of the rotation rate; for tidally-locked hot Jupiters, this implies $B \sim 1/\sqrt{P}$. Assuming the fluid densities and conductivities are similar to that of Jupiter, we have $B \sim B_{\mathrm{J}}(P/10\ \mathrm{hr})^{-1/2}$, of order a few G for the planets in consideration here. Even at the lower end of this range, magnetic pressure is expected to dominate over ram pressure near the wind-launching region (Owen and Adams, 2014), suggesting that magnetic fields may indeed play a role in confining the outflows of WASP-80b and WASP-52b.

In summary, inaccuracies in the integrated XUV fluxes are unlikely to explain the helium non-detection for WASP-80b and the small inferred mass-loss rate for WASP-52b, but inaccuracies in the spectral shape could decrease the helium signals for these planets. The stellar wind might also be a contributing factor for WASP-52b, but it is unlikely to explain the non-detection for WASP-80b. Composition and magnetic fields could both play a role in explaining the observations. We propose some observational tests in Section 6.6 that could help to distinguish between these competing hypotheses.

The Upper Neptune Desert Is Stable Against Mass Loss

At the beginning of this work, we hypothesized that if the Neptune desert is indeed cleared by mass loss, then planets at its boundaries should be marginally stable against photoevaporation. We can now test this hypotheses using our measurements and some simple calculations. First, we inspect our observationally-constrained mass-loss rates to evaluate our sample's present-day stability to atmospheric erosion. We expect that close-in giant planets will be destroyed while their host stars are on the main sequence (Hamer and Schlaufman, 2019), so a reasonable timescale for atmospheric stability is $M_{\mathrm{env}}/\dot{M} \sim 4$ Gyr. In Table 6.5, all of the planets in our sample near the upper edge of the desert have predicted atmospheric lifetimes that are much greater than this timescale.

For HAT-P-26b near the lower edge of the desert, our result is inconclusive due to the $\dot{M} - T_0$ degeneracy: if the outflow is hot ($T_0 \gtrsim 10,000$ K) the planet's predicted atmospheric lifetime may be as short as 3.3 Gyr. This is substantially shorter than the envelope mass-loss timescale for HAT-P-11b: using the mass-loss rate from (dos Santos et al., 2022) and the envelope mass fraction of 15.1% from (E. D. Lopez and Fortney, 2014), the mass-loss timescale for HAT-P-11b is ~ 30 Gyr. Importantly, the $\dot{M} - T$ degeneracy for HAT-P-11b is broken by the precise line shape measurement (Allart, Bourrier, Lovis, Ehrenreich, Spake, et al., 2018; dos Santos et al., 2022) and also by energetic arguments (Vissapragada, Knutson, dos Santos, et al., 2022). Both methods suggest the outflow temperature for HAT-P-11b is $T_0 \lesssim 8000$ K, and if this is the case for HAT-P-26b as well, it would have a longer inferred envelope loss timescale. In the future, high-resolution spectroscopy of HAT-P-26b could resolve this degeneracy by measuring the helium line shape and corresponding outflow temperature.

Although the present-day mass-loss rates of the planets in our sample appear to be low, they experienced stronger XUV irradiation (and thus suffered higher mass-loss rates) in the past. We can reconstruct their past mass-loss histories by integrating the energy-limited mass-loss rate back in time (see e.g. Lecavelier Des Etangs, 2007; A. P. Jackson, Davis, and Peter J. Wheatley, 2012; Mordasini, 2020). We first start with the expression:

$$\dot{M} = -\frac{\varepsilon R_{\mathrm{p}}^3 L_{\mathrm{XUV}}}{4a^2 KGM}, \tag{6.4}$$

which is the typical expression for the energy-limited mass-loss rate (Equation 6.2) with the scaled luminosity $L_{\mathrm{XUV}}/(4\pi a^2)$ substituted for the flux F_{XUV}. For this estimate, we assume that the planetary radius is approximately invariant to small changes in the mass. We can do this because the mass-radius relation is nearly flat for the giant planets at the upper edge of the Neptune desert (e.g. J. Chen and D. Kipping, 2017; Owen and Lai, 2018; Thorngren, Marley, and Fortney, 2019). This is because giant planets at the upper edge of the desert are well-approximated by $P \propto \rho^2$ polytropes for which the radius does not depend on mass (D. J. Stevenson, 1982). Additionally, the variations in K with mass are also small and can be ignored. The integral then reads:

$$\int_{M_0}^{M_{\mathrm{p}}} M dM = \int_0^t -\frac{\varepsilon R_{\mathrm{p}}^3 L_{\mathrm{XUV}}}{4a^2 KG} dt, \tag{6.5}$$

where we have introduced the initial planetary mass M_0 and the planet's current age t. To allow for maximum possible mass loss, we assume that the planet has maintained the same mass-loss efficiency for its whole life, even though the efficiency at early times is likely much lower in the recombination limit (Murray-Clay, Chiang, and Murray, 2009; Owen and Alvarez, 2016). Additionally, we assume the planet has remained at its current semimajor axis for its whole life, i.e., that it did not migrate from a more distant location where it experienced lower instellation. Then, defining the integrated stellar XUV luminosity $E_{\mathrm{XUV}} = \int_0^t L_{\mathrm{XUV}} dt$, we obtain the equation:

$$M_{\mathrm{p}}^2 - M_0^2 = -\frac{\varepsilon R_{\mathrm{p}}^3 E_{\mathrm{XUV}}}{2a^2 KG}. \tag{6.6}$$

Finally, writing the current mass of the planet as a fraction $f < 1$ of the initial mass (such that $M_0 = M_{\mathrm{p}}/f$), we obtain:

$$M_{\mathrm{p}} = \frac{1}{a}\sqrt{\left(-\frac{1}{1-\frac{1}{f^2}}\right)\frac{\varepsilon R_{\mathrm{p}}^3 E_{\mathrm{XUV}}}{2KG}} \tag{6.7}$$

This is a line in the $M_{\mathrm{p}} - a$ plane above which planets have lost less than a fraction f of their initial mass, and below which they have lost more. We hereafter take

$f = 0.5$ – a planet losing half of its initial mass – as a metric for marginal stability. To calculate this boundary, we require a prescription for the planetary radii and the integrated stellar XUV flux in addition to our empirically-constrained distribution for ε. For the planetary radii, we use the empirical radius-temperature relation from Equation (1) of (Owen and Lai, 2018) for a typical K dwarf temperature $T_\star = 4700$ K and radius $R\star = 0.8R_\odot$. The spread in the relation is incorporated into our final uncertainties. We note that this relation is only valid for $M_\mathrm{p} \gtrsim 0.2M_\mathrm{J}$; below this mass the planetary radius will change as the planet undergoes photoevaporation. For the integrated XUV flux, a reasonable upper limit for a K dwarf is $E_\mathrm{XUV} \sim 10^{46}$ erg using the fast rotator track from Johnstone, Bartel, and Güdel (2021) as a guide (see their Figure 18).

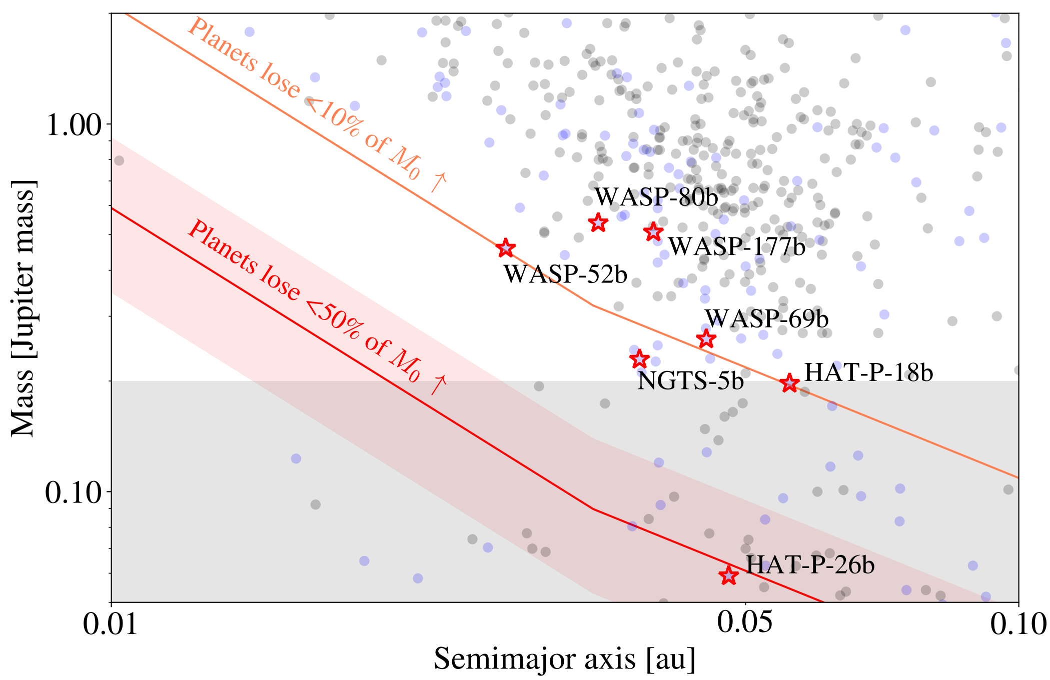

Figure 6.11: $M_\mathrm{p} - a$ plane with marginal stability curves. Planets above the red curve cannot have lost more than 50% of their initial mass M_0 to photoevaporation, even assuming an energy-limited outflow for the entire planetary lifetime. The red shaded region corresponds to the uncertainty on our empirical estimate for the mass-loss efficiency ε with the uncertainty in the empirical radius-temperature relation from Owen and Lai (2018) included as well. The orange curve shows the same for 10% mass loss. Points indicate transiting exoplanets with fractional mass uncertainties of less than 30%; those orbiting stars with 4000 K< T_eff < 5400 K are colored blue, and the seven targets constituting our sample are labeled and outlined with red stars. The gray shaded region indicates $M_\mathrm{p} < 0.2M_\mathrm{J}$ wherein our assumed radii are incorrect.

In Figure 6.11, we draw the $f = 0.5$ boundary on the $M_p - a$ plane for a $R = R_J$ and $K = 0.5$ planet using our empirical efficiency from Section 6.5. For comparison, we also draw the $f = 0.9$ boundary (corresponding to 10% mass loss over the planetary lifetime). We conclude that planets at the upper edge of the Neptune desert have lost less than 10% of their initial masses to photoevaporation. This empirically benchmarked result is in good agreement with previous theoretical calculations by Ionov, Pavlyuchenkov, and Shematovich (2018) and Owen and Lai (2018). HAT-P-26b, near the lower edge of the Neptune desert, is a potential exception – it could have lost $\sim$ 50% of its initial mass if its outflow was energy-limited for the entire planetary lifetime. Although planets like HAT-P-26b along the lower edge of the desert could still be substantially affected by mass loss, we caution that our simplifying assumption that the radius is insensitive to small changes in envelope mass will not hold true for these smaller planets, and a more detailed framework taking into account the core-envelope structure is needed for understanding this part of the population (e.g. Owen and Lai, 2018; Mordasini, 2020).

Throughout this section, we made a number of assumptions to try to estimate the maximum possible mass-loss endured by planets in and near the upper edge of the Neptune desert. In reality, not all planetary host stars will have XUV luminosities as large as those of the most rapidly rotating stellar models from Johnstone, Bartel, and Güdel (2021). We also assumed an energy-limited outflow for the entire planetary lifetime; this is certainly an overestimate at early times, and the efficiency will be much lower during the period of maximum XUV irradiation (Murray-Clay, Chiang, and Murray, 2009; Owen and Alvarez, 2016). Despite this, we still found that the boundary for marginal stability is located well below the actual edge of the desert. We conclude that photoevaporation cannot explain the upper boundary of the Neptune desert.

6.6 Conclusions

In this work, we searched for helium outflows in 7 gas-giant exoplanets orbiting K-type host stars over the course of a 12-night survey with Palomar/WIRC. We summarize our results below:

1. We detected ($> 3\sigma$ confidence) helium absorption from WASP-69b, HAT-P-18b, and HAT-P-26b; tentatively detected ($2 - 3\sigma$) absorption from WASP-52b and NGTS-5b; and did not detect ($< 2\sigma$) absorption from WASP-80b and WASP-177b.

2. When interpreting these signals with a one-dimensional Parker wind model, we found that the six planets in our sample near the upper edge of the desert (WASP-69b, WASP-52b, HAT-P-18b, WASP-80b, WASP-177b, and NGTS-5b) have predicted atmospheric lifetimes $M_{\mathrm{env}}/\dot{M}$ much larger than 10 Gyr. Our result for HAT-P-26b (near the lower edge of the desert) is inconclusive due to the $\dot{M} - T_0$ degeneracy.

3. We compared our empirically measured mass-loss rates to predictions from the one-dimensional, self-consistent hydrodynamics code ATES (Caldiroli et al., 2021b; Caldiroli et al., 2021a). We found that five planets were in good agreement with the ATES predictions: HAT-P-18b, WASP-69b, HAT-P-26b, NGTS-5b, and WASP-177b. The mass-loss rates for these planets are all consistent with a mean outflow efficiency of $\varepsilon = 0.41^{+0.16}_{-0.13}$.

4. We found that WASP-52b and WASP-80b have much lower inferred mass-loss rates than predicted by these models. The measured helium absorption signals for these two planets may be affected by stellar wind confinement, helium depletion, the inverse first ionization potential effect, or magnetic field confinement, although stellar wind confinement appears unlikely for WASP-80b.

5. Our empirically measured mass-loss efficiencies are too small for photoevaporation to sculpt the population of giant planets at the upper edge of the Neptune desert, in agreement with previous work by Owen and Lai (2018) and Ionov, Pavlyuchenkov, and Shematovich (2018).

We conclude that another mechanism besides photoevaporation must be responsible for carving the upper edge of the Neptune desert. Candidate explanations include high-eccentricity migration (Matsakos and Königl, 2016; Owen and Lai, 2018) and *in situ* formation near the magnetospheric truncation radius of the natal protoplanetary disk (Bailey and Batygin, 2018). Although our observations cannot distinguish between these two scenarios, future studies of the functional dependence of the desert's upper boundary on stellar properties may yield more insight into the problem. Additional observations aimed at constraining the presence of long-period planetary companions, for instance with *Gaia* astrometry, could also help to differentiate between these hypotheses.

Our survey also revealed that 1D mass loss models overpredict the metastable helium signatures from WASP-52b and WASP-80b, in agreement with previous work by

Fossati et al. (2021). Although it cannot explain WASP-80b, our estimates suggest that a strong stellar wind might confine the outflow of WASP-52b, similar to what has been proposed for WASP-107b (Spake, A. Oklopčić, and L. A. Hillenbrand, 2021; L. Wang and Dai, 2021b) and TOI-560.01 (Zhang et al., 2022). If the helium line for WASP-52b can be detected with more sensitive observations at higher resolving power, we would expect to see a characteristic blueshifted line profile and/or an extended tail of post-egress absorption in this scenario. If the outflow is instead confined by magnetic fields, the line profile would not be strongly Doppler shifted. We could also test the magnetic confinement explanation for both planets by searching for evidence of star-planet interactions. Cauley et al. (2019) recently demonstrated that close-in planets with strong magnetic fields can affect the stellar chromospheric emission. These magnetic star-planet interactions (SPI) are detected in the Ca II K line, where variations in stellar emission occur on the planetary orbital timescale. Lastly, observations of the Hα absorption signal from both planets could also provide constraints on the outflow composition (Czesla et al., 2022). Hα absorption has already been detected for WASP-52b (G. Chen, Casasayas-Barris, et al., 2020); similar constraints should also be obtained for WASP-80b.

Intriguingly, the *TESS* survey is also beginning to discover planets *within* the Neptune desert, including TOI-849b (Armstrong et al., 2020) and LTT 9779b (Jenkins et al., 2020). Dai et al. (2021) show that these desert-dwellers tend to orbit metal-rich stars and lack planetary companions, suggesting that planets within the desert are more similar to gas giant planets than the rocky, ultra-short period planets below the desert. However, our result confirm that these desert-dwellers are unlikely to be the photoevaporated cores of more massive gas giant planets. In the high-eccentricity migration scenario, these unique planets could be the results of partial tidal disruption as they circularized onto their current orbits (Faber, Rasio, and Willems, 2005; Guillochon, Ramirez-Ruiz, and D. Lin, 2011). Alternatively, Pezzotti et al. (2021) suggest that if TOI-849b had a large initial mass and radius, it may instead have lost its envelope to Roche-lobe overflow (RLO). This process can lead to mass-loss rates far exceeding those from photoevaporation, and is predicted to be consequential for planets on exceptionally short-period orbits (B. Jackson et al., 2017). While it likely plays a role for the closest-in Neptune desert planets, the RLO mass-loss rate drops off precipitously with orbital distance, so it cannot explain the entirety of the desert (Koskinen et al., 2022).

Although these high density desert-dwelling Neptunes likely have very low present-day mass-loss rates, the picture for lower density Neptunes at the lower edge of the desert is somewhat murkier. Previous modeling studies (Kurokawa and Nakamoto, 2014; Lundkvist et al., 2016; Ionov, Pavlyuchenkov, and Shematovich, 2018; Owen and Lai, 2018) concluded that mass loss can be significant for planets near the lower edge of the desert. Our result for HAT-P-26b appears to be consistent with this prediction. *TESS* has identified a large sample of new planets near the lower edge of the desert that are favorable targets for mass-loss measurements, making this a promising area for future investigation. If planetary evolution is dominated by photoevaporation in this mass regime, we also expect the lower boundary of the desert to shift to smaller orbital periods for less luminous late-type stars (e.g. McDonald, Kreidberg, and E. Lopez, 2019; Kanodia et al., 2021). If this prediction can be confirmed observationally, it would constitute additional evidence for the importance of photoevaporation in sculpting the lower part of the desert. With the continued success of *TESS* and the ability to probe mass-loss rates with metastable helium, we now have the means to unveil the divergent evolutionary pathways of planets on either side of the Neptune desert.

6.7 Appendix: Limb Darkening Coefficients

In Figure 6.12, we present the posteriors on the limb darkening coefficients for all stars analyzed in this work alongside calculations for the coefficients with `ldtk` (Husser et al., 2013; Parviainen and Aigrain, 2015).

6.8 Appendix: Detrending Vector Selection

In Table 6.6, we summarize the ΔBIC values obtained when comparing models with different combinations of detrending vectors.

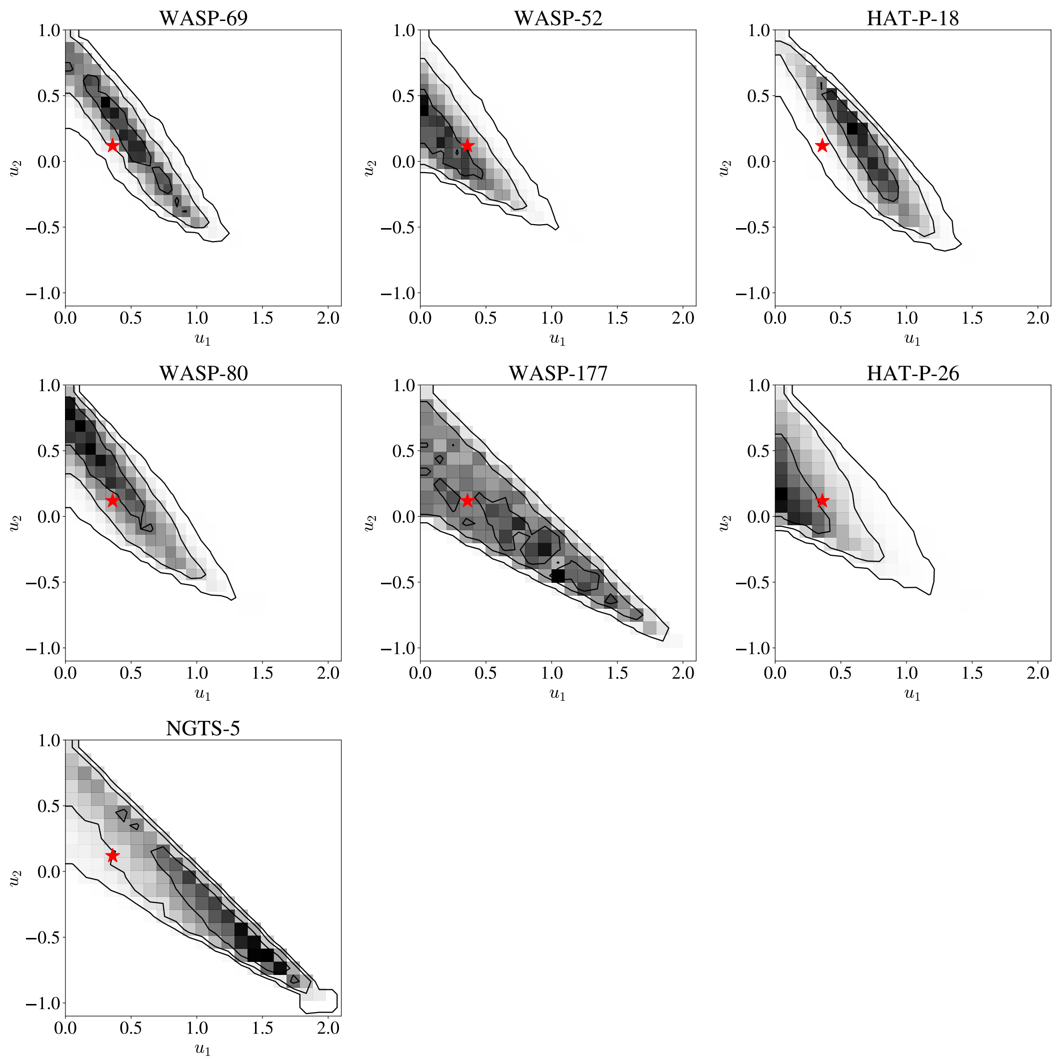

Figure 6.12: Posteriors on the quadratic limb darkening coefficients for all stars analyzed in this work. Contours indicate the 1, 2, and 3σ levels on the posterior mass. The red star on each plot indicates the limb darkening coefficient in the helium bandpass computed using `ldtk` (Husser et al., 2013; Parviainen and Aigrain, 2015).

Table 6.6: Summary of ΔBIC between detrending models in fits with free limb-darkening coefficients.

Planet	Date	LDC	1	2	3	1,2	1,3	2,3	1,2,3
WASP-69b	2019 Aug 16	free	6.27	0.13	-10.11	5.69	-5.19	**-10.22**	-3.61
		fixed	7.18	1.04	**-9.98**	6.09	-3.39	-8.44	-3.30
WASP-52b	2019 Sep 17	free	-5.68	2.58	-0.06	-6.62	**-10.93**	3.51	-5.30
		fixed	-4.23	4.10	2.26	-3.75	**-8.22**	4.75	-3.49
HAT-P-18b	2020 Jun 05	**free**	5.49	3.47	3.62	8.70	8.64	7.83	14.02
		fixed	4.66	1.99	3.15	7.97	9.51	6.86	13.79
HAT-P-18b	2020 Jul 08	**free**	**-1.26**	1.09	3.62	0.25	3.56	7.65	7.10
		fixed	**-0.42**	1.15	3.43	1.90	3.83	6.65	7.40
WASP-80b	2020 Jul 09 (first half)	free	5.43	-23.35	2.26	-19.19	7.65	**-34.50**	-28.68
		fixed	4.76	-22.83	2.73	-17.00	7.35	**-31.85**	-26.11
WASP-80b	2020 Jul 09 (second half)	free	3.21	2.41	3.39	7.00	6.07	7.80	11.96
		fixed	3.52	3.46	2.58	7.59	7.48	8.01	12.14
WASP-52b	2020 Aug 04	free	5.55	**-7.27**	-4.70	-2.55	0.31	-2.43	4.37
		fixed	5.04	**-8.49**	-5.43	-3.01	-0.02	-2.58	2.68
WASP-177b	2020 Oct 02	free	5.06	5.38	5.68	9.67	10.07	7.98	11.76
		fixed	4.94	4.57	4.92	8.97	9.85	7.24	12.80
HAT-P-26b	2021 May 01	free	1.19	**-2.90**	7.10	0.57	6.89	0.15	3.31
		fixed	-0.43	**-5.35**	5.60	-1.79	5.07	-1.38	1.40
HAT-P-26b	2021 May 18	free	3.54	5.80	0.77	10.47	5.60	**-9.22**	-4.17
		fixed	4.53	5.57	0.87	9.92	6.15	**-8.56**	-2.91
NGTS-5b	2021 May 27	free	4.26	**-26.18**	-26.18	-23.46	-22.01	-21.70	-18.07
		fixed	5.29	**-26.87**	-25.87	-22.53	-21.66	-21.31	-18.08

All ΔBIC values are relative to that for no additional detrending vectors, with negative values indicating favored models. Vector 1 corresponds to the centroid offsets, vector 2 corresponds to the water absorption proxy, and vector 3 corresponds to the airmass. Bolded values indicate the adopted detrending model for a given planet; if there are no bolded values then the model with no additional detrending vectors was selected. The “LDC" column denotes the fitting strategy of leaving the limb darkening coefficients free or fixing them to a calculation from `ldtk` (Husser et al., 2013; Parviainen and Aigrain, 2015); the adopted strategy for each planet is noted in bold.

6.9 Appendix: Allan Deviation Plots

In Figure 6.13, we present the Allan deviation plots for all light curves analyzed in this work.

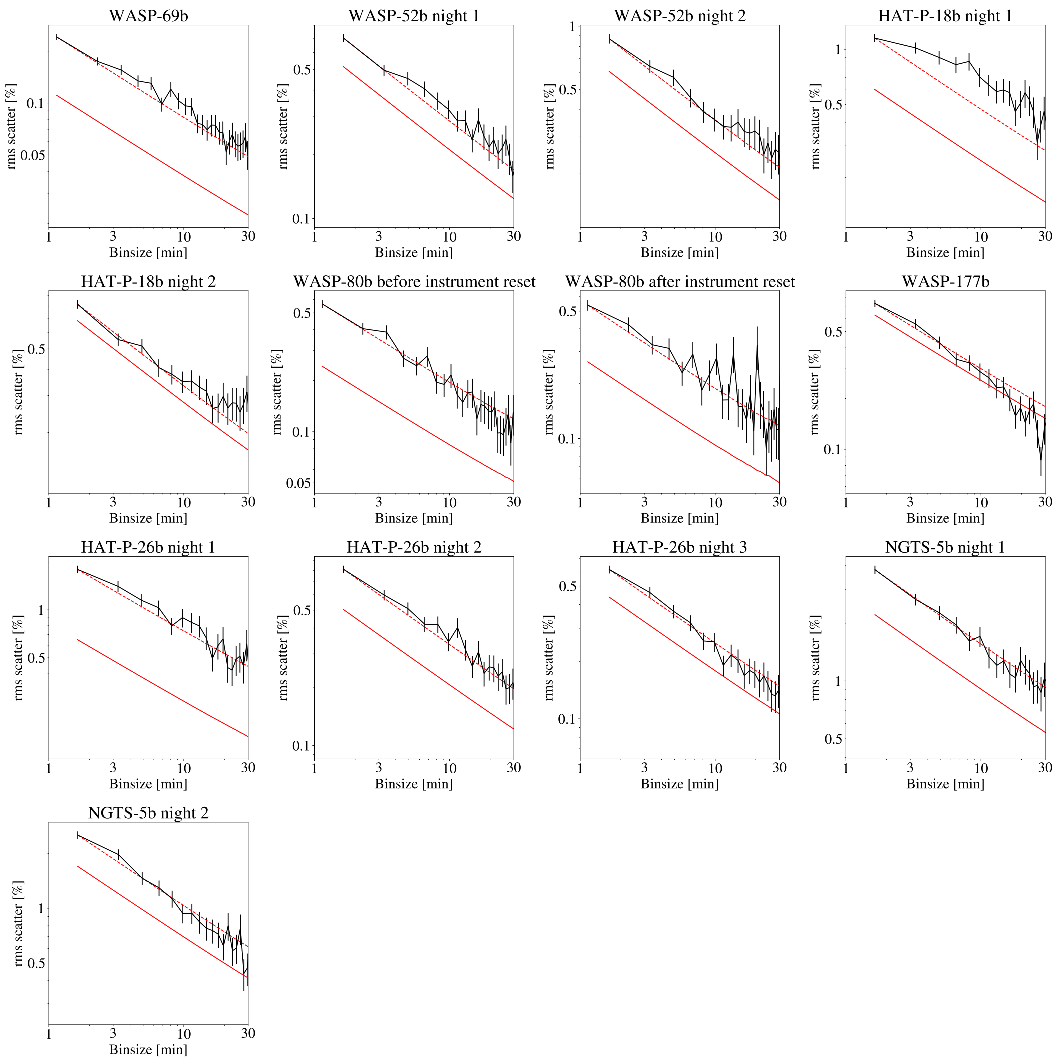

Figure 6.13: Allan deviation plots for all light curves analyzed in this work. The rms of the binned residuals for each light-curve fit are shown with the black curves, the red noise indicates the expectation from photon noise statistics, and the dashed red line is the red line scaled up to match the first point of the black curve. The photon noise values and scaling factors are given in Table 4.1.

6.10 *TESS* Light-Curve Fit

In Figure 6.14, we present the light-curve fit for the WASP-177b *TESS* data. We found a radius ratio in the *TESS* bandpass of $0.187^{+0.054}_{-0.036}$. The rest of the fit parameters are given in Table 6.4 as this was a joint fit with the WIRC data.

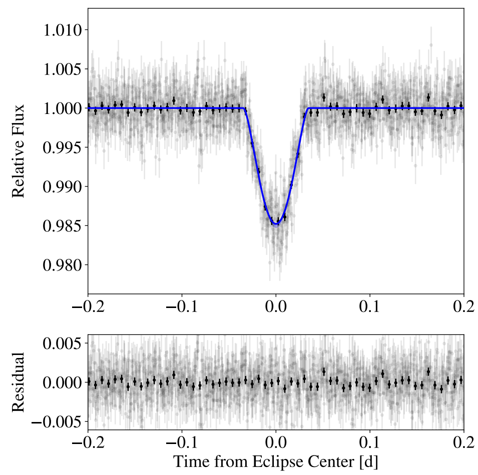

Figure 6.14: Same as Figure 6.2, but for the WASP-177b *TESS* data.

6.11 Appendix: The Parker Wind Model with Tidal Gravity

We demonstrate that a one-dimensional transonic Parker wind model should achieve the sound speed:

$$c_s = \sqrt{\frac{k_B T_0}{\bar{\mu} m_p}} \tag{6.8}$$

within the planetary Roche lobe ($R_s < R_{Roche}$) when the tidal gravity term is considered (Murray-Clay, Chiang, and Murray, 2009; Tang and Young, 2020). Here, M_p is the planet mass, G is the gravitational constant, k_B is the Boltzmann constant, T_0 is the isothermal outflow temperature, $\bar{\mu}$ is the average molecular weight as defined by Lampón, López-Puertas, Lara, et al. (2020), and m_p is the proton mass. The sonic point without considering the stellar gravity is defined as:

$$R_s = \frac{GM_p}{2c_s^2} = \frac{GM\bar{\mu}m_p}{2k_B T_0}. \tag{6.9}$$

To derive the sonic point with tidal gravity considerations, we first write the full momentum equation for the wind (e.g. Equation (2) from Murray-Clay, Chiang, and Murray, 2009):

$$v\frac{dv}{dr} + \frac{1}{\rho}\frac{dP}{dr} + \frac{GM_p}{r^2} - \frac{3GM_\star r}{a^3} = 0. \tag{6.10}$$

As in the original Parker wind solution, we rewrite the pressure gradient term with a density gradient using the derivative of the ideal gas law. We then rewrite the density gradient term as a velocity gradient term using the derivative of the continuity equation (a step-by-step walkthrough of this method is provided in Chapter 3 of Lamers and Cassinelli, 1999). The result is:

$$\frac{1}{v}\frac{dv}{dr} = \frac{1}{v^2 - c_\mathrm{s}^2}\left(\frac{2c_\mathrm{s}}{r} - \frac{GM_\mathrm{p}}{r^2} + \frac{3GM_\star r}{a^3}\right). \tag{6.11}$$

The sonic point is the singular point of Equation (6.11) where the numerator and denominator of the right-hand side both go to zero. The latter condition gives $v = c_\mathrm{s}$, identically to the original Parker wind solution. Requiring the numerator to go to zero gives the cubic:

$$\frac{3GM_\star r^3}{a^3} + 2c_\mathrm{s}^2 r - GM_\mathrm{p} = 0. \tag{6.12}$$

This is the major difference from the Parker wind considered by Antonija Oklopčić and Hirata (2018). Neglecting the tidal gravity term, we obtain the original sonic point solution in Equation (6.9), but the general solution behaves differently:

$$R_\mathrm{s} = a\left(\sqrt[3]{\frac{M_1 + \frac{M_\mathrm{p}}{2}}{3M_\star}} - \sqrt[3]{\frac{M_1 - \frac{M_\mathrm{p}}{2}}{3M_\star}}\right), \tag{6.13}$$

where M_1 is further defined as:

$$M_1 = \sqrt{\left(\frac{M_\mathrm{p}}{2}\right)^2 + \frac{8M_\star^2}{81}\left(\frac{c_\mathrm{s}}{v_\mathrm{K}}\right)^6}, \tag{6.14}$$

and $v_\mathrm{K} = \sqrt{GM_\star/a}$ is the Keplerian velocity. Equation (6.13) agrees with Equation (6.9) in the limit of large sound speed, but the crucial point here is to consider the case where the sound speed is very small, corresponding to cold outflows. Whereas the original sonic point solution would have these outflows fall outside the Roche radius, in this limit $M_1 = M_\mathrm{p}/2$, and substitution into Equation (6.13) yields $R_\mathrm{s} = R_\mathrm{Roche}$.

Therefore, when the sonic point in our original models (which neglected the tidal gravity term) began to venture outside the Roche lobe, it meant that our model was not providing an adequate representation of the density and velocity profiles, which are dominated by the stellar gravity. In general, Equation (6.14) shows that stellar gravity begins to dominate the outflow behavior when:

$$\frac{32}{81}\left(\frac{c_\mathrm{s}}{v_\mathrm{K}}\right)^6\left(\frac{M_\star}{M_\mathrm{p}}\right)^2 \lesssim 1. \tag{6.15}$$

Expanding out the Keplerian velocity term on the left-hand side, this condition scales with $c_s^6 a^3/(M_\star M_p^2)$; therefore the tidal gravity term is important in planets with cool outflows and planets in close proximity to more massive stars. For our sample, the relevant quantities are approximately $v_K \sim 100$ km/s, $c_s \sim 10$ km/s, and $M_p/M_\star \sim 3 \times 10^{-4}$, and Equation (6.15) is nearly satisfied, indicating that the tidal gravity term in the momentum equation appreciably alters our results. The new momentum equation (Equation 6.11) is readily integrated from the sonic point (R_s, c_s) to an arbitrary point $(r, v(r))$ to obtain the velocity profile:

$$\frac{v(r)}{c_s} \exp\left(-\frac{v(r)^2}{2c_s^2}\right) = \left(\frac{R_s}{r}\right)^2 \exp\left[-\frac{GM_p}{c_s^2 r} + \frac{GM_p}{c_s^2 R_s} - \frac{3GM_\star r^2}{2a^3 c_s^2} + \frac{3GM_\star R_s^2}{2a^3 c_s^2} - \frac{1}{2}\right], \tag{6.16}$$

and using the continuity equation we can obtain the density profile:

$$\frac{\rho(r)}{\rho_s} = \exp\left[\frac{GM_p}{c_s^2 r} - \frac{GM_p}{c_s^2 R_s} + \frac{3GM_\star r^2}{2a^3 c_s^2} - \frac{3GM_\star R_s^2}{2a^3 c_s^2} + \frac{1}{2} - \frac{v(r)^2}{2c_s^2}\right]. \tag{6.17}$$

The updated Parker wind structure has been included into the latest release of the `p-winds` code (dos Santos et al., 2022).

References

Adams, Fred C. (Mar. 2011). “Magnetically Controlled Outflows from Hot Jupiters”. In: *ApJ* 730.1, 27, p. 27. DOI: `10.1088/0004-637X/730/1/27`. arXiv: `1101.4234 [astro-ph.EP]`.

Akeson, R. L. et al. (Aug. 2013). “The NASA Exoplanet Archive: Data and Tools for Exoplanet Research”. In: *PASP* 125.930, p. 989. DOI: `10.1086/672273`. arXiv: `1307.2944 [astro-ph.IM]`.

Alam, Munazza K. et al. (Dec. 2018). “The HST PanCET Program: Hints of Na I and Evidence of a Cloudy Atmosphere for the Inflated Hot Jupiter WASP-52b”. In: *AJ* 156.6, 298, p. 298. DOI: `10.3847/1538-3881/aaee89`. arXiv: `1811.00935 [astro-ph.EP]`.

Allart, R., V. Bourrier, C. Lovis, D. Ehrenreich, J. Aceituno, et al. (Mar. 2019). “High-resolution confirmation of an extended helium atmosphere around WASP-107b”. In: *A&A* 623, A58, A58. DOI: `10.1051/0004-6361/201834917`. arXiv: `1901.08073 [astro-ph.EP]`.

Allart, R., V. Bourrier, C. Lovis, D. Ehrenreich, J. J. Spake, et al. (Dec. 2018). "Spectrally resolved helium absorption from the extended atmosphere of a warm Neptune-mass exoplanet". In: *Science* 362.6421, pp. 1384–1387. DOI: 10.1126/science.aat5879. arXiv: 1812.02189 [astro-ph.EP].

Alonso-Floriano, F. J. et al. (Sept. 2019). "He I λ 10 830 Å in the transmission spectrum of HD209458 b". In: *A&A* 629, A110, A110. DOI: 10.1051/0004-6361/201935979. arXiv: 1907.13425 [astro-ph.EP].

Anderson, D. R. et al. (Dec. 2014). "Three newly discovered sub-Jupiter-mass planets: WASP-69b and WASP-84b transit active K dwarfs and WASP-70Ab transits the evolved primary of a G4+K3 binary". In: *MNRAS* 445.2, pp. 1114–1129. DOI: 10.1093/mnras/stu1737. arXiv: 1310.5654 [astro-ph.EP].

Armstrong, David J. et al. (July 2020). "A remnant planetary core in the hot-Neptune desert". In: *Nature* 583.7814, pp. 39–42. DOI: 10.1038/s41586-020-2421-7. arXiv: 2003.10314 [astro-ph.EP].

Bailey, Elizabeth and Konstantin Batygin (Oct. 2018). "The Hot Jupiter Period-Mass Distribution as a Signature of in situ Formation". In: *ApJL* 866.1, L2, p. L2. DOI: 10.3847/2041-8213/aade90. arXiv: 1809.05517 [astro-ph.EP].

Barnes, Sydney A. (Nov. 2007). "Ages for Illustrative Field Stars Using Gyrochronology: Viability, Limitations, and Errors". In: *ApJ* 669.2, pp. 1167–1189. DOI: 10.1086/519295. arXiv: 0704.3068 [astro-ph].

Batygin, Konstantin, Peter H. Bodenheimer, and Gregory P. Laughlin (Oct. 2016). "In Situ Formation and Dynamical Evolution of Hot Jupiter Systems". In: *ApJ* 829.2, 114, p. 114. DOI: 10.3847/0004-637X/829/2/114. arXiv: 1511.09157 [astro-ph.EP].

Batygin, Konstantin and David J. Stevenson (May 2010). "Inflating Hot Jupiters with Ohmic Dissipation". In: *ApJL* 714.2, pp. L238–L243. DOI: 10.1088/2041-8205/714/2/L238. arXiv: 1002.3650 [astro-ph.EP].

Beaugé, C. and D. Nesvorný (Jan. 2013). "Emerging Trends in a Period-Radius Distribution of Close-in Planets". In: *ApJ* 763.1, 12, p. 12. DOI: 10.1088/0004-637X/763/1/12. arXiv: 1211.4533 [astro-ph.EP].

Beltz, Hayley et al. (Jan. 2022). "Exploring the Effects of Active Magnetic Drag in a General Circulation Model of the Ultrahot Jupiter WASP-76b". In: *AJ* 163.1, 35, p. 35. DOI: 10.3847/1538-3881/ac3746. arXiv: 2109.13371 [astro-ph.EP].

Ben-Jaffel, Lotfi et al. (Jan. 2022). "Signatures of strong magnetization and a metal-poor atmosphere for a Neptune-sized exoplanet". In: *Nature Astronomy* 6, pp. 141–153. DOI: 10.1038/s41550-021-01505-x.

Bouchy, F. et al. (Dec. 2005). "ELODIE metallicity-biased search for transiting Hot Jupiters. II. A very hot Jupiter transiting the bright K star HD 189733". In: *A&A* 444.1, pp. L15–L19. DOI: 10.1051/0004-6361:200500201. arXiv: astro-ph/0510119 [astro-ph].

Brinkman, A. C. et al. (Jan. 2001). "First light measurements with the XMM-Newton reflection grating spectrometers: Evidence for an inverse first ionisation potential effect and anomalous Ne abundance in the Coronae of HR 1099". In: *A&A* 365, pp. L324–L328. DOI: 10.1051/0004-6361:20000047. arXiv: astro-ph/0011018 [astro-ph].

Caldiroli, Andrea et al. (Dec. 2021a). "Irradiation-driven escape of primordial planetary atmospheres II. Evaporation efficiency of sub-Neptunes through hot Jupiters". In: *arXiv e-prints*, arXiv:2112.00744, arXiv:2112.00744. arXiv: 2112.00744 [astro-ph.EP].

– (Nov. 2021b). "Irradiation-driven escape of primordial planetary atmospheres. I. The ATES photoionization hydrodynamics code". In: *A&A* 655, A30, A30. DOI: 10.1051/0004-6361/202141497. arXiv: 2106.10294 [astro-ph.EP].

Carolan, S. et al. (Nov. 2020). "The dichotomy of atmospheric escape in AU Mic b". In: *MNRAS* 498.1, pp. L53–L57. DOI: 10.1093/mnrasl/slaa127. arXiv: 2006.13606 [astro-ph.EP].

Cauley, P. Wilson et al. (July 2019). "Magnetic field strengths of hot Jupiters from signals of star-planet interactions". In: *Nature Astronomy* 3, pp. 1128–1134. DOI: 10.1038/s41550-019-0840-x. arXiv: 1907.09068 [astro-ph.EP].

Chen, G., N. Casasayas-Barris, et al. (Mar. 2020). "Detection of Na, K, and Hα absorption in the atmosphere of WASP-52b using ESPRESSO". In: *A&A* 635, A171, A171. DOI: 10.1051/0004-6361/201936986. arXiv: 2002.08379 [astro-ph.EP].

Chen, G., E. Pallé, et al. (Apr. 2017). "The GTC exoplanet transit spectroscopy survey. VI. Detection of sodium in WASP-52b's cloudy atmosphere". In: *A&A* 600, L11, p. L11. DOI: 10.1051/0004-6361/201730736. arXiv: 1703.06716 [astro-ph.EP].

Chen, Jingjing and David Kipping (Jan. 2017). "Probabilistic Forecasting of the Masses and Radii of Other Worlds". In: *ApJ* 834.1, 17, p. 17. DOI: 10.3847/1538-4357/834/1/17. arXiv: 1603.08614 [astro-ph.EP].

Cutri, R. M. et al. (June 2003). "VizieR Online Data Catalog: 2MASS All-Sky Catalog of Point Sources (Cutri+ 2003)". In: *VizieR Online Data Catalog*, II/246, pp. II/246.

Czesla, S. et al. (Jan. 2022). "Hα and He I absorption in HAT-P-32 b observed with CARMENES. Detection of Roche lobe overflow and mass loss". In: *A&A* 657, A6, A6. DOI: 10.1051/0004-6361/202039919. arXiv: 2110.13582 [astro-ph.EP].

Dai, Fei et al. (Aug. 2021). "TKS X: Confirmation of TOI-1444b and a Comparative Analysis of the Ultra-short-period Planets with Hot Neptunes". In: *AJ* 162.2, 62, p. 62. DOI: 10.3847/1538-3881/ac02bd.

Dawson, Rebekah I. and John Asher Johnson (Sept. 2018). "Origins of Hot Jupiters". In: *ARA&A* 56, pp. 175–221. DOI: 10.1146/annurev-astro-081817-051853. arXiv: 1801.06117 [astro-ph.EP].

Dawson, Rebekah I., Ruth A. Murray-Clay, and John Asher Johnson (Jan. 2015). "The Photoeccentric Effect and Proto-hot Jupiters. III. A Paucity of Proto-hot Jupiters on Super-eccentric Orbits". In: *ApJ* 798.2, 66, p. 66. DOI: 10.1088/0004-637X/798/2/66. arXiv: 1211.0554 [astro-ph.EP].

dos Santos, Leonardo A. et al. (Mar. 2022). "p-winds: An open-source Python code to model planetary outflows and upper atmospheres". In: *A&A* 659, A62, A62. DOI: 10.1051/0004-6361/202142038. arXiv: 2111.11370 [astro-ph.EP].

Eigmüller, Philipp et al. (May 2019). "NGTS-5b: a highly inflated planet offering insights into the sub-Jovian desert". In: *A&A* 625, A142, A142. DOI: 10.1051/0004-6361/201935206. arXiv: 1905.02593 [astro-ph.EP].

Erkaev, N. V. et al. (Sept. 2007). "Roche lobe effects on the atmospheric loss from "Hot Jupiters"". In: *A&A* 472.1, pp. 329–334. DOI: 10.1051/0004-6361:20066929. arXiv: astro-ph/0612729 [astro-ph].

Estrela, Raissa et al. (Sept. 2021). "Detection of Aerosols at Microbar Pressures in an Exoplanet Atmosphere". In: *AJ* 162.3, 91, p. 91. DOI: 10.3847/1538-3881/ac0c7c. arXiv: 2106.10292 [astro-ph.EP].

Faber, Joshua A., Frederic A. Rasio, and Bart Willems (May 2005). "Tidal interactions and disruptions of giant planets on highly eccentric orbits". In: *Icarus* 175.1, pp. 248–262. DOI: 10.1016/j.icarus.2004.10.021. arXiv: astro-ph/0407318 [astro-ph].

Ford, Eric B. and Frederic A. Rasio (Feb. 2006). "On the Relation between Hot Jupiters and the Roche Limit". In: *ApJL* 638.1, pp. L45–L48. DOI: 10.1086/500734. arXiv: astro-ph/0512632 [astro-ph].

Foreman-Mackey, Daniel, Rodrigo Luger, Eric Agol, Thomas Barclay, Luke Bouma, et al. (June 2021). "exoplanet: Gradient-based probabilistic inference for exoplanet data & other astronomical time series". In: *The Journal of Open Source Software* 6.62, 3285, p. 3285. DOI: 10.21105/joss.03285. arXiv: 2105.01994 [astro-ph.IM].

Foreman-Mackey, Daniel, Rodrigo Luger, Eric Agol, Thomas Barclay, Luke G. Bouma, et al. (June 2021). *exoplanet: Gradient-based probabilistic inference for exoplanet data & other astronomical time series*. Zenodo. Version 0.5.1. DOI: 10.5281/zenodo.1998447.

Fossati, L. et al. (Dec. 2021). "The GAPS Programme at TNG. XXXII. The revealing non-detection of metastable HeI in the atmosphere of the hot Jupiter WASP-80b". In: *arXiv e-prints*, arXiv:2112.11179, arXiv:2112.11179. arXiv: 2112.11179 [astro-ph.EP].

Foster, G. et al. (June 2021). "Exoplanet X-ray irradiation and evaporation rates with eROSITA". In: *arXiv e-prints*, arXiv:2106.14550, arXiv:2106.14550. arXiv: 2106.14550 [astro-ph.EP].

France, Kevin et al. (Apr. 2016). "The MUSCLES Treasury Survey. I. Motivation and Overview". In: *ApJ* 820.2, 89, p. 89. DOI: 10.3847/0004-637X/820/2/89. arXiv: 1602.09142 [astro-ph.SR].

Fukui, Akihiko et al. (Aug. 2014). "Multi-band, Multi-epoch Observations of the Transiting Warm Jupiter WASP-80b". In: *ApJ* 790.2, 108, p. 108. DOI: 10.1088/0004-637X/790/2/108. arXiv: 1406.3261 [astro-ph.EP].

Gelman, Andrew, Jessica Hwang, and Aki Vehtari (2014). "Understanding predictive information criteria for Bayesian models". In: *Statistics and Computing* 24.997. DOI: 10.1007/s11222-013-9416-2.

Gelman, Andrew and Donald B. Rubin (Jan. 1992). "Inference from Iterative Simulation Using Multiple Sequences". In: *Statistical Science* 7, pp. 457–472. DOI: 10.1214/ss/1177011136.

Güdel, M. et al. (Jan. 2001). "The XMM-Newton view of stellar coronae: X-ray spectroscopy of the corona of <ASTROBJ>AB Doradus</ASTROBJ>". In: *A&A* 365, pp. L336–L343. DOI: 10.1051/0004-6361:20000220.

Guillochon, James, Enrico Ramirez-Ruiz, and Douglas Lin (May 2011). "Consequences of the Ejection and Disruption of Giant Planets". In: *ApJ* 732.2, 74, p. 74. DOI: 10.1088/0004-637X/732/2/74. arXiv: 1012.2382 [astro-ph.EP].

Guilluy, G. et al. (July 2020). "The GAPS programme at TNG. XXII. The GIARPS view of the extended helium atmosphere of HD 189733 b accounting for stellar activity". In: *A&A* 639, A49, A49. DOI: 10.1051/0004-6361/202037644. arXiv: 2005.05676 [astro-ph.EP].

Hamer, Jacob H. and Kevin C. Schlaufman (Nov. 2019). "Hot Jupiters Are Destroyed by Tides While Their Host Stars Are on the Main Sequence". In: *AJ* 158.5, 190, p. 190. DOI: 10.3847/1538-3881/ab3c56. arXiv: 1908.06998 [astro-ph.EP].

Hartman, J. D., G. Á. Bakos, D. M. Kipping, et al. (Feb. 2011). "HAT-P-26b: A Low-density Neptune-mass Planet Transiting a K Star". In: *ApJ* 728.2, 138, p. 138. DOI: 10.1088/0004-637X/728/2/138. arXiv: 1010.1008 [astro-ph.EP].

Hartman, J. D., G. Á. Bakos, B. Sato, et al. (Jan. 2011). "HAT-P-18b and HAT-P-19b: Two Low-density Saturn-mass Planets Transiting Metal-rich K Stars". In: *ApJ* 726.1, 52, p. 52. DOI: 10.1088/0004-637X/726/1/52. arXiv: 1007.4850 [astro-ph.EP].

Hébrard, G. et al. (Jan. 2013). “WASP-52b, WASP-58b, WASP-59b, and WASP-60b: Four new transiting close-in giant planets”. In: *A&A* 549, A134, A134. DOI: 10.1051/0004-6361/201220363. arXiv: 1211.0810 [astro-ph.EP].

Hoffman, Matthew D. and Andrew Gelman (Nov. 2011). “The No-U-Turn Sampler: Adaptively Setting Path Lengths in Hamiltonian Monte Carlo”. In: *arXiv e-prints*, arXiv:1111.4246, arXiv:1111.4246. arXiv: 1111.4246 [stat.CO].

Husser, T. -O. et al. (May 2013). “A new extensive library of PHOENIX stellar atmospheres and synthetic spectra”. In: *A&A* 553, A6, A6. DOI: 10.1051/0004-6361/201219058. arXiv: 1303.5632 [astro-ph.SR].

Ida, S. and D. N. C. Lin (Jan. 2008). “Toward a Deterministic Model of Planetary Formation. IV. Effects of Type I Migration”. In: *ApJ* 673.1, pp. 487–501. DOI: 10.1086/523754. arXiv: 0802.1114 [astro-ph].

Ionov, Dmitry E., Yaroslav N. Pavlyuchenkov, and Valery I. Shematovich (June 2018). “Survival of a planet in short-period Neptunian desert under effect of photoevaporation”. In: *MNRAS* 476.4, pp. 5639–5644. DOI: 10.1093/mnras/sty626. arXiv: 1803.04278 [astro-ph.EP].

Jackson, Alan P., Timothy A. Davis, and Peter J. Wheatley (May 2012). “The coronal X-ray-age relation and its implications for the evaporation of exoplanets”. In: *MNRAS* 422.3, pp. 2024–2043. DOI: 10.1111/j.1365-2966.2012.20657.x. arXiv: 1111.0031 [astro-ph.EP].

Jackson, Brian et al. (Feb. 2017). “A New Model of Roche Lobe Overflow for Short-period Gaseous Planets and Binary Stars”. In: *ApJ* 835.2, 145, p. 145. DOI: 10.3847/1538-4357/835/2/145. arXiv: 1612.04332 [astro-ph.EP].

Jenkins, James S. et al. (Jan. 2020). “An ultrahot Neptune in the Neptune desert”. In: *Nature Astronomy* 4, pp. 1148–1157. DOI: 10.1038/s41550-020-1142-z. arXiv: 2009.12832 [astro-ph.EP].

Johnstone, C. P., M. Bartel, and M. Güdel (May 2021). “The active lives of stars: A complete description of the rotation and XUV evolution of F, G, K, and M dwarfs”. In: *A&A* 649, A96, A96. DOI: 10.1051/0004-6361/202038407. arXiv: 2009.07695 [astro-ph.SR].

Kanodia, Shubham et al. (Oct. 2021). “TOI-532b: The Habitable-zone Planet Finder confirms a Large Super Neptune in the Neptune Desert orbiting a metal-rich M-dwarf host”. In: *AJ* 162.4, 135, p. 135. DOI: 10.3847/1538-3881/ac1940. arXiv: 2107.13670 [astro-ph.EP].

Khalafinejad, S. et al. (Dec. 2021). “Probing the atmosphere of WASP-69 b with low- and high-resolution transmission spectroscopy”. In: *A&A* 656, A142, A142. DOI: 10.1051/0004-6361/202141191. arXiv: 2109.06335 [astro-ph.EP].

Khodachenko, M. L. et al. (May 2021). “Simulation of 10 830 Å absorption with a 3D hydrodynamic model reveals the solar He abundance in upper atmosphere of WASP-107b”. In: *MNRAS* 503.1, pp. L23–L27. DOI: 10.1093/mnrasl/slab015. arXiv: 2101.12504 [astro-ph.EP].

King, George W. et al. (July 2018). “The XUV environments of exoplanets from Jupiter-size to super-Earth”. In: *MNRAS* 478.1, pp. 1193–1208. DOI: 10.1093/mnras/sty1110. arXiv: 1804.11124 [astro-ph.EP].

Kipping, David M. (Nov. 2013). “Efficient, uninformative sampling of limb darkening coefficients for two-parameter laws”. In: *MNRAS* 435.3, pp. 2152–2160. DOI: 10.1093/mnras/stt1435. arXiv: 1308.0009 [astro-ph.SR].

Kirk, J., P. J. Wheatley, T. Louden, A. P. Doyle, et al. (July 2017). “Rayleigh scattering in the transmission spectrum of HAT-P-18b”. In: *MNRAS* 468.4, pp. 3907–3916. DOI: 10.1093/mnras/stx752. arXiv: 1611.06916 [astro-ph.EP].

Kirk, J., P. J. Wheatley, T. Louden, S. P. Littlefair, et al. (Dec. 2016). “Transmission spectroscopy of the inflated exoplanet WASP-52b, and evidence for a bright region on the stellar surface”. In: *MNRAS* 463.3, pp. 2922–2931. DOI: 10.1093/mnras/stw2205. arXiv: 1608.08993 [astro-ph.EP].

Kirk, J., P. J. Wheatley, T. Louden, I. Skillen, et al. (Feb. 2018). “LRG-BEASTS III: ground-based transmission spectrum of the gas giant orbiting the cool dwarf WASP-80”. In: *MNRAS* 474.1, pp. 876–885. DOI: 10.1093/mnras/stx2826. arXiv: 1710.10083 [astro-ph.EP].

Kirk, James et al. (Mar. 2020). “Confirmation of WASP-107b’s Extended Helium Atmosphere with Keck II/NIRSPEC”. In: *AJ* 159.3, 115, p. 115. DOI: 10.3847/1538-3881/ab6e66. arXiv: 2001.07667 [astro-ph.EP].

Knutson, Heather A., Benjamin J. Fulton, et al. (Apr. 2014). “Friends of Hot Jupiters. I. A Radial Velocity Search for Massive, Long-period Companions to Close-in Gas Giant Planets”. In: *ApJ* 785.2, 126, p. 126. DOI: 10.1088/0004-637X/785/2/126. arXiv: 1312.2954 [astro-ph.EP].

Knutson, Heather A., Andrew W. Howard, and Howard Isaacson (Sept. 2010). “A Correlation Between Stellar Activity and Hot Jupiter Emission Spectra”. In: *ApJ* 720.2, pp. 1569–1576. DOI: 10.1088/0004-637X/720/2/1569. arXiv: 1004.2702 [astro-ph.EP].

Kokori, A. et al. (Feb. 2022). “ExoClock Project. II. A Large-scale Integrated Study with 180 Updated Exoplanet Ephemerides”. In: *ApJS* 258.2, 40, p. 40. DOI: 10.3847/1538-4365/ac3a10. arXiv: 2110.13863 [astro-ph.EP].

Koskinen, Tommi T. et al. (Apr. 2022). “Mass Loss by Atmospheric Escape from Extremely Close-in Planets”. In: *ApJ* 929.1, 52, p. 52. DOI: 10.3847/1538-4357/ac4f45. arXiv: 2203.06302 [astro-ph.EP].

Kurokawa, H. and T. Nakamoto (Mar. 2014). “Mass-loss Evolution of Close-in Exoplanets: Evaporation of Hot Jupiters and the Effect on Population”. In: *ApJ* 783.1, 54, p. 54. DOI: 10.1088/0004-637X/783/1/54. arXiv: 1401.2511 [astro-ph.EP].

Lamers, Henny J. G. L. M. and Joseph P. Cassinelli (1999). *Introduction to Stellar Winds*.

Lampón, M., M. López-Puertas, S. Czesla, et al. (Apr. 2021). “Evidence of energy-, recombination-, and photon-limited escape regimes in giant planet H/He atmospheres”. In: *A&A* 648, L7, p. L7. DOI: 10.1051/0004-6361/202140423. arXiv: 2104.08832 [astro-ph.EP].

Lampón, M., M. López-Puertas, L. M. Lara, et al. (Apr. 2020). “Modelling the He I triplet absorption at 10 830 Å in the atmosphere of HD 209458 b”. In: *A&A* 636, A13, A13. DOI: 10.1051/0004-6361/201937175. arXiv: 2003.04872 [astro-ph.EP].

Lampón, M., M. López-Puertas, J. Sanz-Forcada, et al. (Mar. 2021). “Modelling the He I triplet absorption at 10 830 Å in the atmospheres of HD 189733 b and GJ 3470 b”. In: *A&A* 647, A129, A129. DOI: 10.1051/0004-6361/202039417. arXiv: 2101.09393 [astro-ph.EP].

Lanza, A. F. (Mar. 2010). “Hot Jupiters and the evolution of stellar angular momentum”. In: *A&A* 512, A77, A77. DOI: 10.1051/0004-6361/200912789. arXiv: 0912.4585 [astro-ph.SR].

Lecavelier Des Etangs, A. (Jan. 2007). “A diagram to determine the evaporation status of extrasolar planets”. In: *A&A* 461.3, pp. 1185–1193. DOI: 10.1051/0004-6361:20065014. arXiv: astro-ph/0609744 [astro-ph].

Lopez, Eric D. and Jonathan J. Fortney (Sept. 2014). “Understanding the Mass-Radius Relation for Sub-neptunes: Radius as a Proxy for Composition”. In: *ApJ* 792.1, 1, p. 1. DOI: 10.1088/0004-637X/792/1/1. arXiv: 1311.0329 [astro-ph.EP].

Louden, Tom et al. (Sept. 2017). “A precise optical transmission spectrum of the inflated exoplanet WASP-52b”. In: *MNRAS* 470.1, pp. 742–754. DOI: 10.1093/mnras/stx984. arXiv: 1703.09285 [astro-ph.EP].

Loyd, R. O. P. et al. (June 2016). “The MUSCLES Treasury Survey. III. X-Ray to Infrared Spectra of 11 M and K Stars Hosting Planets”. In: *ApJ* 824.2, 102, p. 102. DOI: 10.3847/0004-637X/824/2/102. arXiv: 1604.04776 [astro-ph.SR].

Luger, Rodrigo et al. (Feb. 2019). “starry: Analytic Occultation Light Curves”. In: *AJ* 157.2, 64, p. 64. DOI: 10.3847/1538-3881/aae8e5. arXiv: 1810.06559 [astro-ph.IM].

Lundkvist, M. S. et al. (Apr. 2016). “Hot super-Earths stripped by their host stars”. In: *Nature Communications* 7, 11201, p. 11201. DOI: 10.1038/ncomms11201. arXiv: 1604.05220 [astro-ph.EP].

MacDonald, Ryan J. and Nikku Madhusudhan (June 2019). "The metal-rich atmosphere of the exo-Neptune HAT-P-26b". In: *MNRAS* 486.1, pp. 1292–1315. DOI: 10.1093/mnras/stz789. arXiv: 1903.09151 [astro-ph.EP].

MacLeod, Morgan and Antonija Oklopčić (Feb. 2022). "Stellar Wind Confinement of Evaporating Exoplanet Atmospheres and Its Signatures in 1083 nm Observations". In: *ApJ* 926.2, 226, p. 226. DOI: 10.3847/1538-4357/ac46ce. arXiv: 2107.07534 [astro-ph.EP].

Mamajek, Eric E. and Lynne A. Hillenbrand (Nov. 2008). "Improved Age Estimation for Solar-Type Dwarfs Using Activity-Rotation Diagnostics". In: *ApJ* 687.2, pp. 1264–1293. DOI: 10.1086/591785. arXiv: 0807.1686 [astro-ph].

Mancini, L., J. Southworth, S. Ciceri, et al. (Feb. 2014). "Physical properties and transmission spectrum of the WASP-80 planetary system from multi-colour photometry". In: *A&A* 562, A126, A126. DOI: 10.1051/0004-6361/201323265. arXiv: 1312.4982 [astro-ph.EP].

Mancini, L., J. Southworth, G. Raia, et al. (Feb. 2017). "Orbital alignment and starspot properties in the WASP-52 planetary system". In: *MNRAS* 465.1, pp. 843–857. DOI: 10.1093/mnras/stw1987. arXiv: 1608.02001 [astro-ph.EP].

Mansfield, Megan et al. (Dec. 2018). "Detection of Helium in the Atmosphere of the Exo-Neptune HAT-P-11b". In: *ApJL* 868.2, L34, p. L34. DOI: 10.3847/2041-8213/aaf166. arXiv: 1812.02214 [astro-ph.EP].

Matsakos, Titos and Arieh Königl (Mar. 2016). "On the Origin of the Sub-Jovian Desert in the Orbital-period-Planetary-mass Plane". In: *ApJL* 820.1, L8, p. L8. DOI: 10.3847/2041-8205/820/1/L8. arXiv: 1603.00414 [astro-ph.EP].

May, E. M. et al. (Sept. 2018). "MOPSS. I. Flat Optical Spectra for the Hot Jupiters WASP-4 b and WASP-52b". In: *AJ* 156.3, 122, p. 122. DOI: 10.3847/1538-3881/aad4a8. arXiv: 1807.06561 [astro-ph.EP].

May, Erin M. et al. (Oct. 2021). "Spitzer Phase-curve Observations and Circulation Models of the Inflated Ultrahot Jupiter WASP-76b". In: *AJ* 162.4, 158, p. 158. DOI: 10.3847/1538-3881/ac0e30. arXiv: 2107.03349 [astro-ph.EP].

Mazeh, T., T. Holczer, and S. Faigler (May 2016). "Dearth of short-period Neptunian exoplanets: A desert in period-mass and period-radius planes". In: *A&A* 589, A75, A75. DOI: 10.1051/0004-6361/201528065. arXiv: 1602.07843 [astro-ph.EP].

McCann, John et al. (Mar. 2019). "Morphology of Hydrodynamic Winds: A Study of Planetary Winds in Stellar Environments". In: *ApJ* 873.1, 89, p. 89. DOI: 10.3847/1538-4357/ab05b8. arXiv: 1811.09276 [astro-ph.EP].

McDonald, George D., Laura Kreidberg, and Eric Lopez (May 2019). "The Sub-Neptune Desert and Its Dependence on Stellar Type: Controlled by Lifetime X-Ray Irradiation". In: *ApJ* 876.1, 22, p. 22. DOI: 10.3847/1538-4357/ab1095. arXiv: 2105.00142 [astro-ph.EP].

Monsch, Kristina et al. (Mar. 2019). "The imprint of X-ray photoevaporation of planet-forming discs on the orbital distribution of giant planets". In: *MNRAS* 483.3, pp. 3448–3458. DOI: 10.1093/mnras/sty3346. arXiv: 1812.02173 [astro-ph.EP].

Mordasini, C. (June 2020). "Planetary evolution with atmospheric photoevaporation. I. Analytical derivation and numerical study of the evaporation valley and transition from super-Earths to sub-Neptunes". In: *A&A* 638, A52, A52. DOI: 10.1051/0004-6361/201935541. arXiv: 2002.02455 [astro-ph.EP].

Murgas, F. et al. (Sept. 2020). "The GTC exoplanet transit spectroscopy survey. XI. Possible detection of Rayleigh scattering in the atmosphere of the Saturn-mass planet WASP-69b". In: *A&A* 641, A158, A158. DOI: 10.1051/0004-6361/202038161. arXiv: 2007.02741 [astro-ph.EP].

Murray-Clay, Ruth A., Eugene I. Chiang, and Norman Murray (Mar. 2009). "Atmospheric Escape From Hot Jupiters". In: *ApJ* 693.1, pp. 23–42. DOI: 10.1088/0004-637X/693/1/23. arXiv: 0811.0006 [astro-ph].

Ngo, Henry et al. (Aug. 2016). "Friends of Hot Jupiters. IV. Stellar Companions Beyond 50 au Might Facilitate Giant Planet Formation, but Most are Unlikely to Cause Kozai-Lidov Migration". In: *ApJ* 827.1, 8, p. 8. DOI: 10.3847/0004-637X/827/1/8. arXiv: 1606.07102 [astro-ph.EP].

Ninan, Joe P. et al. (May 2020). "Evidence for He I 10830 Å Absorption during the Transit of a Warm Neptune around the M-dwarf GJ 3470 with the Habitable-zone Planet Finder". In: *ApJ* 894.2, 97, p. 97. DOI: 10.3847/1538-4357/ab8559. arXiv: 1910.02070 [astro-ph.EP].

Nortmann, Lisa et al. (Dec. 2018). "Ground-based detection of an extended helium atmosphere in the Saturn-mass exoplanet WASP-69b". In: *Science* 362.6421, pp. 1388–1391. DOI: 10.1126/science.aat5348. arXiv: 1812.03119 [astro-ph.EP].

Odert, P. et al. (June 2020). "Modeling the Lyα transit absorption of the hot Jupiter HD 189733b". In: *A&A* 638, A49, A49. DOI: 10.1051/0004-6361/201834814. arXiv: 1903.10772 [astro-ph.EP].

Oklopčić, Antonija (Aug. 2019). "Helium Absorption at 1083 nm from Extended Exoplanet Atmospheres: Dependence on Stellar Radiation". In: *ApJ* 881.2, 133, p. 133. DOI: 10.3847/1538-4357/ab2f7f. arXiv: 1903.02576 [astro-ph.EP].

Oklopčić, Antonija and Christopher M. Hirata (Mar. 2018). "A New Window into Escaping Exoplanet Atmospheres: 10830 Å Line of Helium". In: *ApJL* 855.1, L11, p. L11. DOI: 10.3847/2041-8213/aaada9. arXiv: 1711.05269 [astro-ph.EP].

Orell-Miquel, J. et al. (Mar. 2022). "A tentative detection of He I in the atmosphere of GJ 1214 b". In: *A&A* 659, A55, A55. DOI: 10.1051/0004-6361/202142455. arXiv: 2201.11120 [astro-ph.EP].

Owen, James E. (May 2019). “Atmospheric Escape and the Evolution of Close-In Exoplanets”. In: *Annual Review of Earth and Planetary Sciences* 47, pp. 67–90. DOI: 10.1146/annurev-earth-053018-060246. arXiv: 1807.07609 [astro-ph.EP].

Owen, James E. and Fred C. Adams (Nov. 2014). “Magnetically controlled mass-loss from extrasolar planets in close orbits”. In: *MNRAS* 444.4, pp. 3761–3779. DOI: 10.1093/mnras/stu1684. arXiv: 1408.3636 [astro-ph.EP].

Owen, James E. and Marcelo A. Alvarez (Jan. 2016). “UV Driven Evaporation of Close-in Planets: Energy-limited, Recombination-limited, and Photon-limited Flows”. In: *ApJ* 816.1, 34, p. 34. DOI: 10.3847/0004-637X/816/1/34. arXiv: 1504.07170 [astro-ph.EP].

Owen, James E. and Dong Lai (Oct. 2018). “Photoevaporation and high-eccentricity migration created the sub-Jovian desert”. In: *MNRAS* 479.4, pp. 5012–5021. DOI: 10.1093/mnras/sty1760. arXiv: 1807.00012 [astro-ph.EP].

Owen, James E., Ruth A. Murray-Clay, et al. (Nov. 2021). “The fundamentals of Lyman-alpha exoplanet transits”. In: *arXiv e-prints*, arXiv:2111.06094, arXiv:2111.06094. arXiv: 2111.06094 [astro-ph.EP].

Palle, E. et al. (June 2020). “A He I upper atmosphere around the warm Neptune GJ 3470 b”. In: *A&A* 638, A61, A61. DOI: 10.1051/0004-6361/202037719. arXiv: 2004.12812 [astro-ph.EP].

Panwar, Vatsal et al. (Mar. 2022). “A new method to measure the spectra of transiting exoplanet atmospheres using multi-object spectroscopy”. In: *MNRAS* 510.3, pp. 3236–3265. DOI: 10.1093/mnras/stab3646. arXiv: 2112.06678 [astro-ph.EP].

Paragas, Kimberly et al. (Mar. 2021). “Metastable Helium Reveals an Extended Atmosphere for the Gas Giant HAT-P-18b”. In: *ApJL* 909.1, L10, p. L10. DOI: 10.3847/2041-8213/abe706. arXiv: 2102.08392 [astro-ph.EP].

Parviainen, H. and S. Aigrain (Nov. 2015). “LDTK: Limb Darkening Toolkit”. In: *MNRAS* 453.4, pp. 3821–3826. DOI: 10.1093/mnras/stv1857. arXiv: 1508.02634 [astro-ph.EP].

Parviainen, H., E. Pallé, et al. (Jan. 2018). “The GTC exoplanet transit spectroscopy survey. VIII. Flat transmission spectrum for the warm gas giant WASP-80b”. In: *A&A* 609, A33, A33. DOI: 10.1051/0004-6361/201731113. arXiv: 1709.01875 [astro-ph.EP].

Pezzotti, C. et al. (Oct. 2021). “The key impact of the host star’s rotational history on the evolution of TOI-849b”. In: *A&A* 654, L5, p. L5. DOI: 10.1051/0004-6361/202141734. arXiv: 2110.09364 [astro-ph.EP].

Poppenhaeger, K. (May 2022). “Helium absorption in exoplanet atmospheres is connected to stellar coronal abundances”. In: *MNRAS* 512.2, pp. 1751–1764. DOI: 10.1093/mnras/stac507. arXiv: 2202.08838 [astro-ph.EP].

Poppenhaeger, K. and S. J. Wolk (May 2014). “Indications for an influence of hot Jupiters on the rotation and activity of their host stars”. In: *A&A* 565, L1, p. L1. DOI: `10.1051/0004-6361/201423454`. arXiv: `1404.1073 [astro-ph.SR]`.

Rao, Suvrat et al. (July 2021). “Star-planet interactions. VI. Tides, stellar activity, and planetary evaporation”. In: *A&A* 651, A50, A50. DOI: `10.1051/0004-6361/202039965`. arXiv: `2104.07397 [astro-ph.EP]`.

Rasio, Frederic A. and Eric B. Ford (Nov. 1996). “Dynamical instabilities and the formation of extrasolar planetary systems”. In: *Science* 274, pp. 954–956. DOI: `10.1126/science.274.5289.954`.

Rice, Malena, Songhu Wang, and Gregory Laughlin (Feb. 2022). “Origins of Hot Jupiters from the Stellar Obliquity Distribution”. In: *ApJL* 926.2, L17, p. L17. DOI: `10.3847/2041-8213/ac502d`. arXiv: `2201.11768 [astro-ph.EP]`.

Salvatier, John, Thomas V. Wieckiâ, and Christopher Fonnesbeck (Oct. 2016). *PyMC3: Python probabilistic programming framework*. ascl: `1610.016`.

Salz, M., S. Czesla, P. C. Schneider, E. Nagel, et al. (Dec. 2018). “Detection of He I λ10830 Å absorption on HD 189733 b with CARMENES high-resolution transmission spectroscopy”. In: *A&A* 620, A97, A97. DOI: `10.1051/0004-6361/201833694`. arXiv: `1812.02453 [astro-ph.EP]`.

Salz, M., S. Czesla, P. C. Schneider, and J. H. M. M. Schmitt (Feb. 2016). “Simulating the escaping atmospheres of hot gas planets in the solar neighborhood”. In: *A&A* 586, A75, A75. DOI: `10.1051/0004-6361/201526109`. arXiv: `1511.09341 [astro-ph.EP]`.

Salz, M., P. C. Schneider, et al. (Apr. 2015). “High-energy irradiation and mass loss rates of hot Jupiters in the solar neighborhood”. In: *A&A* 576, A42, A42. DOI: `10.1051/0004-6361/201425243`. arXiv: `1502.00576 [astro-ph.EP]`.

– (Jan. 2016). “Energy-limited escape revised. The transition from strong planetary winds to stable thermospheres”. In: *A&A* 585, L2, p. L2. DOI: `10.1051/0004-6361/201527042`. arXiv: `1511.09348 [astro-ph.EP]`.

Schwarz, Gideon (July 1978). “Estimating the Dimension of a Model”. In: *Annals of Statistics* 6.2, pp. 461–464.

Shaikhislamov, I. F. et al. (Jan. 2021). “Global 3D hydrodynamic modelling of absorption in Ly α and He 10830 A lines at transits of GJ3470b”. In: *MNRAS* 500.1, pp. 1404–1413. DOI: `10.1093/mnras/staa2367`. arXiv: `2009.00290 [astro-ph.EP]`.

Spake, J. J., A. Oklopčić, and L. A. Hillenbrand (Dec. 2021). “The Posttransit Tail of WASP-107b Observed at 10830 Å”. In: *AJ* 162.6, 284, p. 284. DOI: `10.3847/1538-3881/ac178a`. arXiv: `2107.08999 [astro-ph.EP]`.

Spake, J. J., D. K. Sing, et al. (May 2018). “Helium in the eroding atmosphere of an exoplanet”. In: *Nature* 557.7703, pp. 68–70. DOI: `10.1038/s41586-018-0067-5`. arXiv: `1805.01298 [astro-ph.EP]`.

Stefansson, Gudmundur et al. (Oct. 2017). "Toward Space-like Photometric Precision from the Ground with Beam-shaping Diffusers". In: *ApJ* 848.1, 9, p. 9. DOI: 10.3847/1538-4357/aa88aa. arXiv: 1710.01790 [astro-ph.IM].

Stevenson, D. J. (Jan. 1982). "Interiors of the Giant Planets". In: *Annual Review of Earth and Planetary Sciences* 10, p. 257. DOI: 10.1146/annurev.ea.10.050182.001353.

Stevenson, David J. (Mar. 2003). "Planetary magnetic fields". In: *Earth and Planetary Science Letters* 208.1-2, pp. 1–11. DOI: 10.1016/S0012-821X(02)01126-3.

Stevenson, Kevin B. et al. (Feb. 2016). "A Search for Water in the Atmosphere of HAT-P-26b Using LDSS-3C". In: *ApJ* 817.2, 141, p. 141. DOI: 10.3847/0004-637X/817/2/141. arXiv: 1511.08226 [astro-ph.EP].

Szabó, Gy. M. and L. L. Kiss (Feb. 2011). "A Short-period Censor of Sub-Jupiter Mass Exoplanets with Low Density". In: *ApJL* 727.2, L44, p. L44. DOI: 10.1088/2041-8205/727/2/L44. arXiv: 1012.4791 [astro-ph.EP].

Tang, H. and E. D. Young (Sept. 2020). "Evaporation from the Lunar Magma Ocean Was Not the Mechanism for Fractionation of the Moon's Moderately Volatile Elements". In: *PSJ* 1.2, 49, p. 49. DOI: 10.3847/PSJ/abb23c.

Thorngren, Daniel P., Mark S. Marley, and Jonathan J. Fortney (Sept. 2019). "An Empirical Mass-Radius Relation for Cool Giant Planets". In: *Research Notes of the American Astronomical Society* 3.9, 128, p. 128. DOI: 10.3847/2515-5172/ab4353.

Trammell, George B., Phil Arras, and Zhi-Yun Li (Feb. 2011). "Hot Jupiter Magnetospheres". In: *ApJ* 728.2, 152, p. 152. DOI: 10.1088/0004-637X/728/2/152. arXiv: 1011.0017 [astro-ph.EP].

Triaud, A. H. M. J. et al. (Mar. 2013). "WASP-80b: a gas giant transiting a cool dwarf". In: *A&A* 551, A80, A80. DOI: 10.1051/0004-6361/201220900. arXiv: 1303.0254 [astro-ph.EP].

Triaud, Amaury H. M. J. et al. (July 2015). "WASP-80b has a dayside within the T-dwarf range". In: *MNRAS* 450.3, pp. 2279–2290. DOI: 10.1093/mnras/stv706. arXiv: 1503.08152 [astro-ph.EP].

Tsiaras, A. et al. (Apr. 2018). "A Population Study of Gaseous Exoplanets". In: *AJ* 155.4, 156, p. 156. DOI: 10.3847/1538-3881/aaaf75. arXiv: 1704.05413 [astro-ph.EP].

Turner, Jake D. et al. (Dec. 2017). "Investigating the physical properties of transiting hot Jupiters with the 1.5-m Kuiper Telescope". In: *MNRAS* 472.4, pp. 3871–3886. DOI: 10.1093/mnras/stx2221. arXiv: 1708.07909 [astro-ph.EP].

Turner, Oliver D. et al. (June 2019). "Three hot-Jupiters on the upper edge of the mass-radius distribution: WASP-177, WASP-181, and WASP-183". In: *MNRAS* 485.4, pp. 5790–5799. DOI: 10.1093/mnras/stz742. arXiv: 1903.06622 [astro-ph.EP].

Valsecchi, Francesca et al. (Nov. 2015). "Tidally-driven Roche-lobe Overflow of Hot Jupiters with MESA". In: *ApJ* 813.2, 101, p. 101. DOI: 10.1088/0004-637X/813/2/101. arXiv: 1506.05175 [astro-ph.EP].

Vehtari, Aki, Andrew Gelman, and Jonah Gabry (2017). "Practical Bayesian model evaluation using leave-one-out cross-validation and WAIC". In: *Statistics and Computing* 27.1413. DOI: 10.1007/s11222-016-9696-4.

Vissapragada, Shreyas, Daniel Jontof-Hutter, et al. (Mar. 2020). "Diffuser-assisted Infrared Transit Photometry for Four Dynamically Interacting Kepler Systems". In: *AJ* 159.3, 108, p. 108. DOI: 10.3847/1538-3881/ab65c8. arXiv: 1907.04445 [astro-ph.EP].

Vissapragada, Shreyas, Heather A. Knutson, Leonardo A. dos Santos, et al. (Mar. 2022). "The Maximum Mass-loss Efficiency for a Photoionization-driven Isothermal Parker Wind". In: *ApJ* 927.1, 96, p. 96. DOI: 10.3847/1538-4357/ac4e8a. arXiv: 2201.09889 [astro-ph.EP].

Vissapragada, Shreyas, Heather A. Knutson, Nemanja Jovanovic, et al. (June 2020). "Constraints on Metastable Helium in the Atmospheres of WASP-69b and WASP-52b with Ultranarrowband Photometry". In: *AJ* 159.6, 278, p. 278. DOI: 10.3847/1538-3881/ab8e34. arXiv: 2004.13728 [astro-ph.EP].

Vissapragada, Shreyas, Gudmundur Stefánsson, et al. (Nov. 2021). "A Search for Planetary Metastable Helium Absorption in the V1298 Tau System". In: *AJ* 162.5, 222, p. 222. DOI: 10.3847/1538-3881/ac1bb0. arXiv: 2108.05358 [astro-ph.EP].

Wakeford, Hannah R. et al. (May 2017). "HAT-P-26b: A Neptune-mass exoplanet with a well-constrained heavy element abundance". In: *Science* 356.6338, pp. 628–631. DOI: 10.1126/science.aah4668. arXiv: 1705.04354 [astro-ph.EP].

Wallack, Nicole L. et al. (Dec. 2019). "Investigating Trends in Atmospheric Compositions of Cool Gas Giant Planets Using Spitzer Secondary Eclipses". In: *AJ* 158.6, 217, p. 217. DOI: 10.3847/1538-3881/ab2a05. arXiv: 1908.00014 [astro-ph.EP].

Wang, Lile and Fei Dai (June 2021a). "Metastable Helium Absorptions with 3D Hydrodynamics and Self-consistent Photochemistry. I. WASP-69b, Dimensionality, X-Ray and UV Flux Level, Spectral Types, and Flares". In: *ApJ* 914.2, 98, p. 98. DOI: 10.3847/1538-4357/abf1ee. arXiv: 2101.00042 [astro-ph.EP].

– (June 2021b). "Metastable Helium Absorptions with 3D Hydrodynamics and Self-consistent Photochemistry. II. WASP-107b, Stellar Wind, Radiation Pressure, and Shear Instability". In: *ApJ* 914.2, 99, p. 99. DOI: 10.3847/1538-4357/abf1ed. arXiv: 2101.00045 [astro-ph.EP].

Watanabe, Sumio (2010). “Asymptotic Equivalence of Bayes Cross Validation and Widely Applicable Information Criterion in Singular Learning Theory”. In: 11.3571.

Wilson, John C. et al. (Mar. 2003). “A Wide-Field Infrared Camera for the Palomar 200-inch Telescope”. In: *Instrument Design and Performance for Optical/Infrared Ground-based Telescopes*. Ed. by Masanori Iye and Alan F. M. Moorwood. Vol. 4841. Society of Photo-Optical Instrumentation Engineers (SPIE) Conference Series, pp. 451–458. DOI: 10.1117/12.460336.

Winn, Joshua N. et al. (Aug. 2010). “Hot Stars with Hot Jupiters Have High Obliquities”. In: *ApJL* 718.2, pp. L145–L149. DOI: 10.1088/2041-8205/718/2/L145. arXiv: 1006.4161 [astro-ph.EP].

Wood, B. E. et al. (Aug. 2005). “New Mass-Loss Measurements from Astrospheric Lyα Absorption”. In: *ApJL* 628.2, pp. L143–L146. DOI: 10.1086/432716. arXiv: astro-ph/0506401 [astro-ph].

Wood, Brian E. et al. (July 2018). “A Chandra/LETGS Survey of Main-sequence Stars”. In: *ApJ* 862.1, 66, p. 66. DOI: 10.3847/1538-4357/aaccf6. arXiv: 1806.05111 [astro-ph.SR].

Yadav, Rakesh K. and Daniel P. Thorngren (Nov. 2017). “Estimating the Magnetic Field Strength in Hot Jupiters”. In: *ApJL* 849.1, L12, p. L12. DOI: 10.3847/2041-8213/aa93fd. arXiv: 1709.05676 [astro-ph.EP].

Youdin, Andrew N. (Nov. 2011). “The Exoplanet Census: A General Method Applied to Kepler”. In: *ApJ* 742.1, 38, p. 38. DOI: 10.1088/0004-637X/742/1/38. arXiv: 1105.1782 [astro-ph.EP].

Youngblood, Allison et al. (June 2016). “The MUSCLES Treasury Survey. II. Intrinsic LYα and Extreme Ultraviolet Spectra of K and M Dwarfs with Exoplanets*”. In: *ApJ* 824.2, 101, p. 101. DOI: 10.3847/0004-637X/824/2/101. arXiv: 1604.01032 [astro-ph.SR].

Zhang, Michael et al. (Feb. 2022). “Escaping Helium from TOI 560.01, a Young Mini-Neptune”. In: *AJ* 163.2, 67, p. 67. DOI: 10.3847/1538-3881/ac3fa7. arXiv: 2110.13150 [astro-ph.EP].

Chapter 7

CONCLUSION

7.1 Synthesis of Results

In this thesis, we described a technique for measuring the mass-loss rates of extrasolar planets using diffuser-assisted narrowband photometry, and we used this technique to survey a population of gas-giant planets near the edge of the Neptune desert. In Chapter 2, we demonstrated the power of diffuser-assisted photometry for ground-based infrared measurements of transit light curves. The photometric precisions we obtain in this work are among the best ever demonstrated from the ground in the infrared. In Chapter 3, we coupled our beam-shaping diffuser to a custom narrowband filter centered on the helium 1083 nm line. We showed that this system could be used to reliably measure helium absorption signals in gas giant planets, and that those signals could be interpreted using a one-dimensional isothermal Parker wind model to obtain mass-loss rates. In Chapter 4, we applied our narrowband photometric technique to three young planets in the V1298 Tau system, and we detected a tentative signal for planet d. In Chapter 5, we refined the interpretation of our absorption signals by considering the energetics of the one-dimension isothermal Parker wind model. We found that many hot, strong outflows that match metastable helium observations violate energy balance; by rejecting these models, we are able to partially resolve the degeneracy between mass-loss rate and thermosphere temperature.

Finally, in Chapter 6, we synthesized all of the observational and theoretical developments from the previous chapters. We used our narrowband photometry technique to survey atmospheric loss in a sample of seven planets. Aided by the energetic constraints from Chapter 5, we proceeded to fit the absorption signals from our study using grids of one-dimensional isothermal Parker wind models, and compared the resulting best-fit models to predictions from self-consistent hydrodynamical code ATES (Caldiroli et al., 2021b; Caldiroli et al., 2021a). We were able to verify the results of the code to within our experimental uncertainties, and we used our results to confirm that mass-loss efficiencies in the Neptune desert are far too small to explain the upper boundary of the Neptune desert. We conclude that this boundary of the exoplanet population is likely to be primordial; either it is a relic of tidal disruption during high-eccentricity migration (Matsakos and Königl, 2016; Owen and Lai, 2018) or it reflects the magnetospheric truncation radii of the natal protoplanetary disks (Bailey and Batygin, 2018).

7.2 New Frontiers

Motivated by the results presented in this thesis, I now present a few ideas that might be interesting avenues for future study.

The Neptune Desert and the Neptune Oasis

The majority of my work has thus far been relevant to the upper boundary of the Neptune desert. This is largely because this region of the desert is far simpler to study than other regions. Planets at the upper boundary of the desert are highly irradiated and large in size with relatively low masses; as a result, they have large atmospheric scale heights and are amenable to transit spectroscopy. It is usually a good idea to study targets with the highest predicted signal-to-noise ratios first, and Chapter 6 is far from unique in this approach (see e.g. the target list from Kirk et al., 2020). There are certainly things left to learn in this high signal-to-noise regime. As suggested in Chapter 6, our knowledge of interactions between the planetary and stellar winds is incomplete, as is our understanding of the planetary magnetic field's influence on the outflow. There are numerous avenues for future studies using the metastable helium line that may clarify these important physical mysteries. We should continue to obtain precise line shape constraints at high-resolution, repeat observations with an aim to constrain variability (due for instance to Kelvin-Helmholtz instabilities at the interface between planetary and stellar winds, Wang and Dai, 2021b), and attempt to observe helium emission from planetary daysides (J. Spake, priv. comm.) in this already-informative sample of high-SNR planets.

At the same time, we are beginning to exhaust the list of good helium targets at the upper boundary of the Neptune desert, at least in the northern hemisphere. TESS will invariably add more targets to the sample, but it seems likely that we will exhaust the pool of potential gas giant targets with detectable helium signatures within the next few years. Additionally, the story emerging from Chapter 6 is that mass loss does not play a consequential role in the evolution of gas giants. Now that our observational techniques have been satisfactorily benchmarked on giant planets, we should expand our studies to include lower-mass planets for which mass loss should be far more consequential (Owen and Lai, 2018). While sub-Neptune planets ($R_\mathrm{p} < 4R_\oplus$) have turned out to be quite challenging targets for mass loss observations in helium (Kasper et al., 2020), sub-Saturn planets ($4R_\oplus < R_\mathrm{p} < 8R_\oplus$) on short orbits ($P < 10$ days) are more observationally favorable and remain relatively unexplored. This definition includes planets at the lower edge of the desert as well as apparent desert-dwellers like TOI-849b (Armstrong et al., 2020) and LTT 9779b (Jenkins et al., 2020).

This proposed direction is timely: over the past three years, *TESS* has completely redefined the Neptune desert sample. To date, it has revealed 51 new Neptune desert candidates with $4R_\oplus < R_\mathrm{p} < 8R_\oplus$ and $P < 10$ d orbiting K-type stars, thought to be the best stellar spectral type for helium observations (Oklopčić, 2019; Wang and Dai, 2021a). I have plotted the new *K* star sample from TESS in Figure 7.1 alongside the sample of previously-known planets in this size and period regime. Only 2 previously-known planets in this region (HAT-P-11b and HAT-P-26b) are bright enough for precise measurements, and both exhibit signs of mass loss (Mansfield et al., 2018; Allart et al., 2018). The large number of high-SNR targets in this sample is quite encouraging. With existing facilities in the northern hemisphere and new spectrographs coming online in the south (such as WINERED; Ikeda et al., 2016), we should be able to hunt for outflows in Neptune desert planets across the night sky.

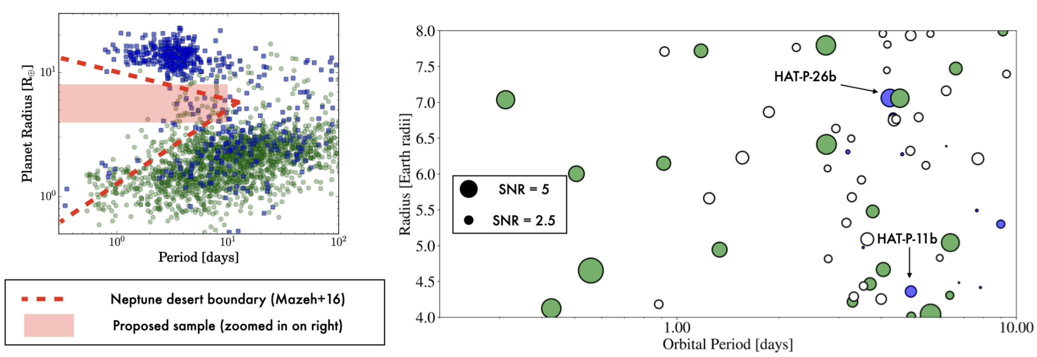

Figure 7.1: (Left) Planetary radius-period distribution from (Owen and Lai, 2018), with Neptune desert boundary from (Mazeh, Holczer, and Faigler, 2016) overplotted in the red dashed line and the proposed Neptune desert sample highlighted in pink. Green points are confirmed planets without measured masses, and blue points are confirmed planets with measured masses. (Right) Proposed sample of close-in Neptune desert planets orbiting K stars, with 11 confirmed planets (blue) and 51 TESS candidates, of which I will observe 20 systems (green). Size corresponds to predicted SNR with WIRC; WINERED SNRs will be a factor of 2 higher.

Alongside this effort, a clearer view of the Neptune desert is certainly needed, especially in the *TESS* era. Of particular importance is answering the question: do the boundaries of the Neptune desert evolve with stellar type? The lower boundary might be expected to change purely because planets orbiting later-type stars are less irradiated than planets orbiting earlier stars. Changes in the upper boundary, on the other hand, may help clarify whether high-eccentricity migration (Matsakos and Königl, 2016; Owen and Lai, 2018) or *in situ* formation near the magnetospheric truncation radius (Bailey and Batygin, 2018) is responsible for this part of the planetary population. Follow-up of *TESS* desert candidates is thus of the utmost importance.

Flare-Driven Mass Loss

Late-type stars flare often, outputting large amounts of energy that can be intercepted by their planets. In Chapter 5, we demonstrated that the second moment of the total heating coefficient limits the efficiency with which intercepted energy is converted to outflow heating. The heating coefficient depends on the neutral density profiles, so efficiency must decrease with increasing incident flux. This is not taken into account in many studies of flare-driven mass-loss (Atri and Mogan, 2021). In fact, because radiative cooling can remove energy from the system at high incident fluxes, the decrease in outflow efficiency is rather precipitous (Murray-Clay, Chiang, and Murray, 2009; Salz et al., 2016; Caldiroli et al., 2021a). The integrated mass loss for a flare event should thus be expected to be sub-linearly dependent on flare energy, which is borne out by model calculations (Wang and Dai, 2021a).

An immediate consequence follows for planets irradiated by flaring stars: if they receive the same integrated XUV luminosity, an atmosphere irradiated by many small flares is less stable against photoevaporation than one irradiated by fewer large flares. The smaller flares are absorbed with better efficiency, so more of the incident flux can power the outflow. This simple argument implies a quantifiable connection between photoevaporation physics and the amplitude and shape of the flare-frequency distribution (FFD) of the host star. Given that the FFD amplitude and shape are quite different for M stars and FGK stars (e.g. Feinstein et al., 2022), flare-driven mass-loss may have left a unique imprint on the population of M-dwarf planets probed by the *TESS* mission. As *TESS* continues to build up this population, both demographic and single-system observational approaches will be crucial for constraining the impact of flares on planetary atmospheres. On the demographic side, we should search for trends in the radius gap and Neptune desert with stellar type and/or flare rates; initial studies from *Kepler* and *K2* already suggest that the M-dwarf radius valley is different than that observed for FGK stars (Cloutier and Menou, 2020). Single-system approaches will also be valuable: by observing outflows in metastable helium in a sample of flaring and non-flaring systems, we may be able to gain insight into the role of flares in driving mass loss.

Atomic Spectroscopy of Exoplanet Atmospheres

We have learned quite a lot from studies of the metastable helium line, but it is not the only atomic tracer of planetary upper atmospheres. At optical wavelengths, Hα can trace the atmospheres at similar altitudes to the helium triplet with most detections being for planets orbiting hot stars rather than cool stars (Czesla et al., 2022). In fact, there are nearly as many Hα detections as there are metastable helium detections in the literature, but the immense scientific value of these observations have gone somewhat unrealized largely because we lack a successful interpretive framework similar to Oklopčić and Hirata (2018) for Hα. The line cores of other Balmer lines (e.g. Wyttenbach et al., 2020) and the optical sodium and potassium features (e.g. Chen et al., 2017) can similarly reach large altitudes when observed at high resolving power. A combined approach to modeling all of these lines would substantially improve our understanding of upper atmospheric physics.

It is also unlikely that we have exhausted the catalogue of observable atomic features in optical and infrared exoplanet spectra. There are likely to be more atomic absorption lines available in public high-resolution datasets waiting to be discovered; an excellent example is the recent discovery of the excited neutral oxygen triplet at 777 nm by Borsa et al. (2021) in archival CARMENES transit spectra of KELT-9b. We have not even exhausted the list of features predicted by the earliest theoretical studies of exoplanet transmission spectra (Seager and Sasselov, 2000), but with the current class of high-throughput, high-resolution spectroscopic facilities, we now have the ability to test their predictions.

Finally, as the field pushes towards characterizing the atmospheres of Earth-sized planets, we will need escape tracers for high mean-molecular weight atmospheres. Volatile element tracers like metastable helium and Hα will not be suitable for these purposes. The optical sodium and potassium lines could possibly trace terrestrial outflows (Gebek and Oza, 2020). Additionally, taking inspiration from its abundance in inner Solar System atmospheres, argon could be an ideal tracer. Argon has two low-lying metastable energy levels similar to the $2\,^3$S state of helium that gives rise to the metastable helium line. The same ionization and recombination processes that produce the metastable helium triplet could thus populate these argon states.

In fact, when the Earth's atmosphere experiences strong irradiation in the form of lightning or aurorae, lines from the metastable states of argon are readily detectable (Wallace, 1964; Burns et al., 2002). If we could observe argon in the atmospheres of transiting exoplanets, we would gain unprecedented insight into the evolution of terrestrial atmospheres.

References

Allart, R. et al. (Dec. 2018). "Spectrally resolved helium absorption from the extended atmosphere of a warm Neptune-mass exoplanet". In: *Science* 362.6421, pp. 1384–1387. DOI: 10.1126/science.aat5879. arXiv: 1812.02189 [astro-ph.EP].

Armstrong, David J. et al. (July 2020). "A remnant planetary core in the hot-Neptune desert". In: *Nature* 583.7814, pp. 39–42. DOI: 10.1038/s41586-020-2421-7. arXiv: 2003.10314 [astro-ph.EP].

Atri, Dimitra and Shane R. Carberry Mogan (Jan. 2021). "Stellar flares versus luminosity: XUV-induced atmospheric escape and planetary habitability". In: *MNRAS* 500.1, pp. L1–L5. DOI: 10.1093/mnrasl/slaa166. arXiv: 2009.04310 [astro-ph.EP].

Bailey, Elizabeth and Konstantin Batygin (Oct. 2018). "The Hot Jupiter Period-Mass Distribution as a Signature of in situ Formation". In: *ApJL* 866.1, L2, p. L2. DOI: 10.3847/2041-8213/aade90. arXiv: 1809.05517 [astro-ph.EP].

Borsa, Francesco et al. (Dec. 2021). "High-resolution detection of neutral oxygen and non-LTE effects in the atmosphere of KELT-9b". In: *Nature Astronomy*. DOI: 10.1038/s41550-021-01544-4. arXiv: 2112.12059 [astro-ph.EP].

Burns, G. B. et al. (Dec. 2002). "Argon auroral emissions". In: *Journal of Atmospheric and Solar-Terrestrial Physics* 64.18, pp. 2013–2017. DOI: 10.1016/S1364-6826(02)00077-9.

Caldiroli, Andrea et al. (Dec. 2021a). "Irradiation-driven escape of primordial planetary atmospheres II. Evaporation efficiency of sub-Neptunes through hot Jupiters". In: *arXiv e-prints*, arXiv:2112.00744, arXiv:2112.00744. arXiv: 2112.00744 [astro-ph.EP].

– (Nov. 2021b). "Irradiation-driven escape of primordial planetary atmospheres. I. The ATES photoionization hydrodynamics code". In: *A&A* 655, A30, A30. DOI: 10.1051/0004-6361/202141497. arXiv: 2106.10294 [astro-ph.EP].

Chen, G. et al. (Apr. 2017). "The GTC exoplanet transit spectroscopy survey. VI. Detection of sodium in WASP-52b's cloudy atmosphere". In: *A&A* 600, L11, p. L11. DOI: 10.1051/0004-6361/201730736. arXiv: 1703.06716 [astro-ph.EP].

Cloutier, Ryan and Kristen Menou (May 2020). "Evolution of the Radius Valley around Low-mass Stars from Kepler and K2". In: *AJ* 159.5, 211, p. 211. DOI: 10.3847/1538-3881/ab8237. arXiv: 1912.02170 [astro-ph.EP].

Czesla, S. et al. (Jan. 2022). “Hα and He I absorption in HAT-P-32 b observed with CARMENES. Detection of Roche lobe overflow and mass loss”. In: *A&A* 657, A6, A6. DOI: 10.1051/0004-6361/202039919. arXiv: 2110.13582 [astro-ph.EP].

Feinstein, Adina D. et al. (Jan. 2022). “Testing Self-organized Criticality across the Main Sequence Using Stellar Flares from TESS”. In: *ApJL* 925.1, L9, p. L9. DOI: 10.3847/2041-8213/ac4b5e. arXiv: 2109.07011 [astro-ph.SR].

Gebek, Andrea and Apurva V. Oza (Oct. 2020). “Alkaline exospheres of exoplanet systems: evaporative transmission spectra”. In: *MNRAS* 497.4, pp. 5271–5291. DOI: 10.1093/mnras/staa2193. arXiv: 2005.02536 [astro-ph.EP].

Ikeda, Yuji et al. (Aug. 2016). “High sensitivity, wide coverage, and high-resolution NIR non-cryogenic spectrograph, WINERED”. In: *Ground-based and Airborne Instrumentation for Astronomy VI*. Ed. by Christopher J. Evans, Luc Simard, and Hideki Takami. Vol. 9908. Society of Photo-Optical Instrumentation Engineers (SPIE) Conference Series, 99085Z, 99085Z. DOI: 10.1117/12.2230886.

Jenkins, James S. et al. (Jan. 2020). “An ultrahot Neptune in the Neptune desert”. In: *Nature Astronomy* 4, pp. 1148–1157. DOI: 10.1038/s41550-020-1142-z. arXiv: 2009.12832 [astro-ph.EP].

Kasper, David et al. (Dec. 2020). “Nondetection of Helium in the Upper Atmospheres of Three Sub-Neptune Exoplanets”. In: *AJ* 160.6, 258, p. 258. DOI: 10.3847/1538-3881/abbee6. arXiv: 2007.12968 [astro-ph.EP].

Kirk, James et al. (Mar. 2020). “Confirmation of WASP-107b’s Extended Helium Atmosphere with Keck II/NIRSPEC”. In: *AJ* 159.3, 115, p. 115. DOI: 10.3847/1538-3881/ab6e66. arXiv: 2001.07667 [astro-ph.EP].

Mansfield, Megan et al. (Dec. 2018). “Detection of Helium in the Atmosphere of the Exo-Neptune HAT-P-11b”. In: *ApJL* 868.2, L34, p. L34. DOI: 10.3847/2041-8213/aaf166. arXiv: 1812.02214 [astro-ph.EP].

Matsakos, Titos and Arieh Königl (Mar. 2016). “On the Origin of the Sub-Jovian Desert in the Orbital-period-Planetary-mass Plane”. In: *ApJL* 820.1, L8, p. L8. DOI: 10.3847/2041-8205/820/1/L8. arXiv: 1603.00414 [astro-ph.EP].

Mazeh, T., T. Holczer, and S. Faigler (May 2016). “Dearth of short-period Neptunian exoplanets: A desert in period-mass and period-radius planes”. In: *A&A* 589, A75, A75. DOI: 10.1051/0004-6361/201528065. arXiv: 1602.07843 [astro-ph.EP].

Murray-Clay, Ruth A., Eugene I. Chiang, and Norman Murray (Mar. 2009). “Atmospheric Escape From Hot Jupiters”. In: *ApJ* 693.1, pp. 23–42. DOI: 10.1088/0004-637X/693/1/23. arXiv: 0811.0006 [astro-ph].

Oklopčić, Antonija (Aug. 2019). “Helium Absorption at 1083 nm from Extended Exoplanet Atmospheres: Dependence on Stellar Radiation”. In: *ApJ* 881.2, 133, p. 133. DOI: 10.3847/1538-4357/ab2f7f. arXiv: 1903.02576 [astro-ph.EP].

Oklopčić, Antonija and Christopher M. Hirata (Mar. 2018). "A New Window into Escaping Exoplanet Atmospheres: 10830 Å Line of Helium". In: *ApJL* 855.1, L11, p. L11. DOI: 10.3847/2041-8213/aaada9. arXiv: 1711.05269 [astro-ph.EP].

Owen, James E. and Dong Lai (Oct. 2018). "Photoevaporation and high-eccentricity migration created the sub-Jovian desert". In: *MNRAS* 479.4, pp. 5012–5021. DOI: 10.1093/mnras/sty1760. arXiv: 1807.00012 [astro-ph.EP].

Salz, M. et al. (Feb. 2016). "Simulating the escaping atmospheres of hot gas planets in the solar neighborhood". In: *A&A* 586, A75, A75. DOI: 10.1051/0004-6361/201526109. arXiv: 1511.09341 [astro-ph.EP].

Seager, S. and D. D. Sasselov (July 2000). "Theoretical Transmission Spectra during Extrasolar Giant Planet Transits". In: *ApJ* 537.2, pp. 916–921. DOI: 10.1086/309088. arXiv: astro-ph/9912241 [astro-ph].

Wallace, L. (Apr. 1964). "The Spectrum of Lightning." In: *ApJ* 139, p. 994. DOI: 10.1086/147833.

Wang, Lile and Fei Dai (June 2021a). "Metastable Helium Absorptions with 3D Hydrodynamics and Self-consistent Photochemistry. I. WASP-69b, Dimensionality, X-Ray and UV Flux Level, Spectral Types, and Flares". In: *ApJ* 914.2, 98, p. 98. DOI: 10.3847/1538-4357/abf1ee. arXiv: 2101.00042 [astro-ph.EP].

– (June 2021b). "Metastable Helium Absorptions with 3D Hydrodynamics and Self-consistent Photochemistry. II. WASP-107b, Stellar Wind, Radiation Pressure, and Shear Instability". In: *ApJ* 914.2, 99, p. 99. DOI: 10.3847/1538-4357/abf1ed. arXiv: 2101.00045 [astro-ph.EP].

Wyttenbach, A. et al. (June 2020). "Mass-loss rate and local thermodynamic state of the KELT-9 b thermosphere from the hydrogen Balmer series". In: *A&A* 638, A87, A87. DOI: 10.1051/0004-6361/201937316. arXiv: 2004.13733 [astro-ph.EP].